RÉPUBLIQUE FRANÇAISE
Liberté Égalité Fraternité

Université de Toulouse

Doctorat de l'Université de Toulouse

préparé à Toulouse INP

Modélisation de parois pour la Simulation aux Grandes Échelles d'écoulements de turbomachines

Thèse présentée et soutenue, le 13 mars 2025 par

Mehdi CIZERON

École doctorale
MEGEP - Mécanique, Energétique, Génie civil, Procédés

Spécialité
Dynamique des fluides

Unité de recherche
CERFACS

Thèse dirigée par
Florent DUCHAINE

Composition du jury
M. Ronan VICQUELIN, Président, CentraleSupélec
M. Xavier GLOERFELT, Rapporteur, ENSAM
M. Alexis GIAUQUE, Rapporteur, École Centrale de Lyon
Mme Maria Vittoria SALVETTI, Examinatrice, Università di Pisa
M. Koen HILLEWAERT, Examinateur, Université de Liège
M. Florent DUCHAINE, Directeur de thèse, Toulouse INP

Membres invités
M. Éric LIPPINOIS, Safran Aircraft Engines
M. Thomas GROSNICKEL, Safran Helicopter Engines

Remerciements

Je tiens tout d'abord à remercier chaleureusement l'ensemble des membres du jury pour avoir accepté d'évaluer mon travail et pour le temps consacré à ma soutenance. Je remercie ceux qui ont fait le déplacement jusqu'à Toulouse, ainsi que ceux qui ont su se rendre disponibles pour participer à distance.

Je suis également reconnaissant aux rapporteurs pour la lecture attentive de mon manuscrit et la qualité de leurs rapports, dont les remarques pertinentes ont enrichi la discussion. Plus généralement, je remercie tous les membres du jury pour les échanges stimulants qui ont eu lieu lors de la soutenance.

Je remercie également Safran pour la confiance qui m'a été accordée tout au long de cette thèse. En particulier, merci à Thomas et Éric pour s'être déplacés à l'occasion de la soutenance, pour le suivi de mes travaux, ainsi que pour la qualité des échanges que nous avons eus, tant lors des réunions que pendant les journées Haida.

Je tiens à remercier mon encadrement, le trio formé par Florent, Laurent et Nicolas. À mon directeur Florent, un grand merci pour tout ce que tu as apporté à cette thèse, et pour m'avoir accueilli au CERFACS il y a maintenant quatre ans, à l'occasion de mon stage en pleine période de COVID. Merci pour ta confiance et pour les opportunités que tu m'as offertes. Pour cela également, merci à Laurent, qui dirige aussi l'équipe E&S du CERFACS. Merci pour ton exigence, ton regard critique et ta hauteur de vue, toujours présents à travers tes retours et tes corrections. Enfin, un grand merci à Nicolas, probablement l'encadrant avec lequel j'ai le plus souvent échangé lorsque je rencontrais des difficultés. Ta porte était toujours ouverte, et tes conseils toujours pertinents. Merci pour tout cela, travailler avec toi a été particulièrement agréable. Je tiens également à remercier Franck pour toutes ses visites au CERFACS et ses nombreux conseils et contributions au cours de la thèse.

Plus généralement, je remercie l'ensemble des membres du CERFACS qui contribuent à créer une ambiance de travail agréable et qui rendent le travail possible dans de bonnes conditions. Notamment, merci à l'équipe administrative pour leur aide précieuse et leur bonne humeur au quotidien. Une pensée spéciale pour Michèle, Brigitte, Philippine, Dimitri et Chantal, avec qui j'ai eu le plus souvent l'occasion d'échanger. Merci également à toute l'équipe CSG, qui en plus d'être d'une efficacité rare et unanimement soulignée est très sympathique. Notamment merci à Fabrice, Isabelle et Gérard qui ont su m'aider plus d'une fois pendant la thèse.

Enfin, un grand merci à tous les doctorants du CERFACS, qui constituent une part essentielle de la vie du laboratoire. Merci à tous ceux que j'ai pu croiser, avec qui j'ai eu l'occasion d'échanger, et à ceux que j'ai côtoyés de plus près, qu'ils soient anciens stagiaires, anciens doctorants, ou encore en train de terminer leur thèse. Merci à Jean-Jacques, qui m'a enrôlé au CERFACS et qui est toujours là. C'est toujours un plaisir de te côtoyer, avec ta bonne humeur et ton accent du Tarn, même s'il s'efface et est moins prononcé que celui de Clo'. Benjamin, camarade

inséparable de Jean-Jacques et conseiller juridique attitré de tous les thésards du CERFACS, c'est un plaisir d'avoir partagé le quotidien du labo avec toi pendant la thèse, et une pensée pour Camille également (et votre Suzie bien sûr). Merci à Francis pour toutes les discussions, tes imitations et accents incroyables, et la démocratisation du BPP, à refaire très vite ! Monsieur Jean Villard, tu es toujours d'un calme remarquable, et toujours rassurant, discuter avec toi est toujours un plaisir. Merci à Éric, amateur éclairé de voitures et détenteur (pour encore un petit moment) du cheat code de la plaque andorrane. Loïc, aussi gentil qu'impressionnant physiquement, un vrai plaisir de t'avoir croisé au CERFACS. Antoine, qui avait des rêves d'espace qu'il a réussi à concrétiser, tout le monde te le dit mais ton rire raisonne encore au CERFACS (même à l'étage). Alexis, ami belge venu chercher la chaleur du sud, spécialiste du numérique d'AVBP (chose rare !), avec qui on peut toujours discuter mécanique. Merci à P.-A. pour tous les moments partagés, notamment autour des discussions du midi. Alex, avec qui on est devenus experts en reconstruction dentaire pendant la thèse — j'espère que ton projet d'éolienne touche à sa fin ! Guillaume, recordman d'ancienneté chez les thésards et fan de F1, je suis heureux d'avoir été témoin de l'aboutissement de ta thèse. Thomas, Nathanaël, Rémi, Arthur, la team rugby de la pause de midi, toujours très précis au pied. Hector, expert de memes en tout genre, et successeur de bureau en E0 (que vous avez bien transformé avec Justin.) Et bien sûr Yann, Clément, Félicia, Alex, Éloïse, Étienne, Antoine, Antony, Lukas, Patrick, Marcos, Carlos, Benoît, Jérôme, Solène, Noémie, Anthony et tous ceux que j'oublie mais avec qui j'ai pu échanger ne serait-ce qu'une discussion ou quelques mots — merci à vous tous de contribuer à cette ambiance unique entre thésards du CERFACS. Enfin, un grand merci à Raphaël, qui a occupé une place particulière tout au long de ces trois années, puisqu'il était assis en face de moi pendant tout ce temps. Blague à part, on s'est bien trouvés dès le début de la thèse pour plein de raisons, et on aura partagé de très bons moments pendant ces trois ans et six mois. Ça nous aura probablement permis de ne pas devenir fous pendant la thèse au CERFACS.

Enfin, merci à tous mes amis et à ma famille pour leur soutien et pour tous les moments qui m'ont permis de penser à autre chose que la thèse pendant ces dernières années. Un merci tout particulier à Aïssa, avec qui j'ai fait un long bout de chemin depuis la classe de CE1 jusqu'à aujourd'hui. On s'est suivis longtemps, et ça compte beaucoup.

Merci aussi à tous mes amis de prépa. Le groupe de colle originel, avec Romain, qui a décidé de partir en backpack à l'autre bout du monde (je n'en attendais pas moins de toi !), et Anna, une présence précieuse pendant ces années, avec qui c'était un plaisir de traverser les colles. Alexis, excellent camarade pour parler cinéma, politique, ou encore dégustation de bière maison, qui se fait actuellement dorer aux Antilles. Thibault, lui aussi à l'autre bout du monde pour le moment, j'espère que tu n'oublies pas les belles années passées à Saint-Étienne avec nous. Sylia, Jihane, merci à vous également. On a su former un groupe soudé pendant ces années de prépa, même si on se voit trop rarement depuis que chacun est parti un peu partout, voire très loin pour plusieurs d'entre vous. Et je ne vous oublie pas

non plus, les 5/2 : William et Adrien, qui comme moi ont compris que la prépa, c'est trois ans. William, qui a soutenu sa thèse avant moi, merci pour tous les fous rires et les rigolades, et pas merci pour m'avoir fait trop manger pendant ces années. Et Adrien, excellent camarade, connu pour sa légendaire ponctualité... ainsi que pour sa chance inouïe quand il s'agit d'éviter les pépins physiques.

Merci à également Kévin, le nordiste qui est venu se perdre à Lyon quelques années. Tu as été une super rencontre à Centrale, tant pour le travail que pour l'a côté. Je vous souhaite le meilleur pour la suite à toi et Alix.

Et en dernier. Merci à ma famille de m'avoir accompagné notamment pendant ces 3 ans et demi de thèse mais pas uniquement. Merci à mes petits frères que je ne vois pas assez souvent mais qui comptent énormément pour moi. Merci à mes parents pour l'éducation qu'ils m'ont donnée, pour m'avoir toujours soutenu et permis de faire les études que je souhaitais de manière sereine. En particulier, merci à mon père, qui, malgré ses plaintes fréquentes de ne jamais être écouté, m'a transmis énormément de choses. Si j'en suis là aujourd'hui, il en porte une importante responsabilité.

Enfin merci à Jessica d'avoir été là depuis 4 ans, un peu plus à l'heure où j'écris ces lignes. Merci de m'avoir supporté, rassuré et remonté le moral dans les moments bas de la thèse. Tu es un exemple pour moi sur plein de sujets, mais en particulier le fait que tu sois passée par la thèse avant moi m'a montré la voie. Merci pour tout, merci d'être à mes côtés et j'ai hâte de la suite avec toi, à commencer par nos vacances qui arrivent vite, les premières depuis un moment !

Contents

Introduction **1**

I Research Background and Bibliographic Context **9**

1 Governing equations **11**
1.1 Navier-Stokes Equations 11
1.1.1 Equation of state 11
1.1.2 Viscous stress tensor 12
1.1.3 Heat flux 12
1.1.4 Turbulence 12
1.2 Boundary Layers 14
1.2.1 Averaged Equations 14
1.2.2 Equilibrium boundary layers 18
1.2.3 Turbulent structures of the boundary layer 22
1.2.4 Energy Equation 23
1.2.5 Non-Equilibrium Effects 25
1.3 Large Eddy Simulation (LES) 32
1.3.1 Introduction to Computational Fluid Dynamics (CFD) and LES 32
1.3.2 LES equations 34
1.3.3 SGS models 35

2 Wall modeling for Large Eddy Simulation **41**
2.1 Motivation for wall modeling 41
2.2 Model Types 45
2.2.1 Algebraic models 45
2.2.2 Ordinary Differential Equations (ODE) models 47
2.2.3 Other models 50
2.3 Wall Modeling Challenges 52
2.3.1 Application limits and domain of validity of wall models . . . 52
2.3.2 RANS/LES coupling 53

II Implementing a wall modeling strategy for turbomachinery **59**

3 Introduction **61**
3.1 Background of the study 61
3.2 Academical Test Cases 62

3.2.1 Turbulent Channel 62
3.2.2 Periodic Hill 65

4 A wall model with pressure gradient effects: the TBLE model 69
4.1 Model description 69
4.1.1 Turbulence model 70
4.1.2 Implementation 74
4.1.3 Intermediate conclusions 78
4.2 Validation on a turbulent channel setup 79
4.3 Validation on a periodic hill setup 83

5 A model for improving wall-model and LES coupling: SGS model stochastic forcing 91
5.1 Background 91
5.2 Description of the model 92
5.2.1 Original stochastic forcing model 93
5.2.2 Improvements to the model 96
5.3 Model validation on a turbulent channel 102
5.3.1 Original model of Blanchard et al. [14] 102
5.3.2 Effect of wall-normal fluctuations 104
5.3.3 Effect of spatial extension of the model 106
5.3.4 Combined effect 108
5.3.5 Compatibility with the TBLE wall model 111
5.4 Periodic Hill test case validation 119

6 Turbomachinery Application 125
6.1 T7.2 Low Pressure turbine 125
6.1.1 Introduction and numerical setup 125
6.1.2 Flow characteristics and results 129
6.2 Fan of the DGEN-180 engine 135
6.2.1 Presentation 135
6.2.2 Flow features 139
6.2.3 Time-averaged results 141

Conclusion 151

Appendix 155

A Applying the fluctuations model on the turbulent channel at different Reynolds numbers 157
A.1 Results with the logarithmic law of the wall 158
A.2 Results with the TBLE wall model 162

B Applying the fluctuations model on the periodic hill at higher Reynolds numbers **167**

C Coupling at a higher point **173**
C.1 LLM Problem 173
C.2 Implementation 173
C.3 Results of the coupling on a turbulent channel 174
C.3.1 Log-Law 174
C.3.2 TBLE 176
C.3.3 Conclusions 177

Bibliography **181**

Introduction

Context

The aviation industry is facing significant challenges in developing the next generation of commercial aircraft to meet a number of stringent environmental, operational, and safety requirements. Engine manufacturers are at the forefront of finding solutions to these demands.

Among the most pertinent subjects is fuel consumption, which is also directly related to CO2 emissions, directly impacting economic and ecological outcomes. Fuel costs typically represent 20-30% of the operational cost for airlines and are therefore a major expense item [2].

Other massive challenges affecting the quality of life, public perception, and regulatory compliance of commercial aviation encompass atmospheric pollution, mainly through nitrogen oxides (NOx) and soot emissions, as well as noise generation, particularly near airports.

Finally, safety is a major cornerstone of commercial aviation. The industry's remarkable safety record is largely attributed to the great reliability of its components, especially the engines. Any future engine design needs to maintain or even improve reliability level while matching the growing environmental and operational demands.

Regulatory bodies, including the International Civil Aviation Organization (ICAO), the European Union Aviation Safety Agency (EASA), and the Federal Aviation Administration (FAA) in North America are imposing stricter limits and pursuing ambitious long-term objectives. For example, the ambitious targets set by the European Union Flightpath 2050 report [93] are to reduce CO2 emissions by 75%, NOx by 90%, and perceived noise levels by 65% relative to the year 2000. In the same way, ICAO's Long-Term Aspirational Goal (LTAG) [76] has set a target of net-zero C02 emissions from aviation by 2050.

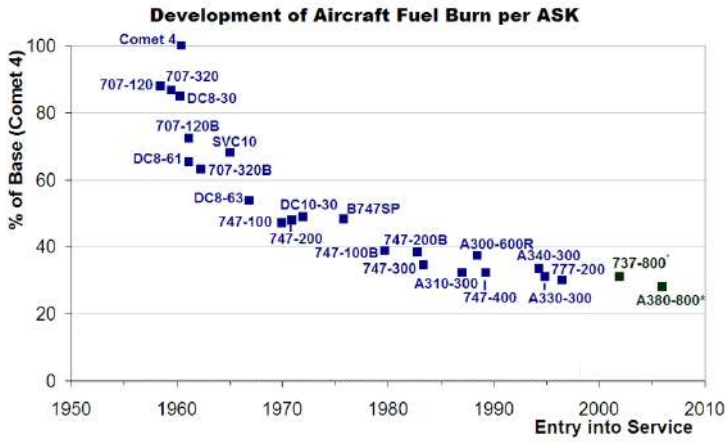

Figure 1: Fuel consumption over the years, from Schaefer [148]

Since the 1960s, improvements in aircraft technology significantly cut fuel consumption and associated CO2 emissions, as shown in Figure 1. The fuel burned per seat was reduced by 70% between the 1960s and 2007. About 40% of this gain in efficiency is due to engine efficiency, and the remaining 30% is due to improvement in airframe efficiencies [131]. A major jump in fuel economy came with the transition from early turbojets to high-bypass turbofans. The adoption of new technologies with advanced materials like titanium and superalloys increased operating temperatures and thereby further improved thermal efficiency. Combustor design similarly included major advances in technology that optimized fuel consumption and emissions.

Recent applications have involved the massive exploitation of composite materials in airframes such as the Boeing 787 and Airbus A350, which greatly reduced their weight and fuel consumption. Besides, advanced engine technologies developed during this period include the latest generation of high-bypass ratio engines like the Pratt & Whitney geared turbofan and the CFM LEAP engine, which have resulted in improved efficiency and performance.

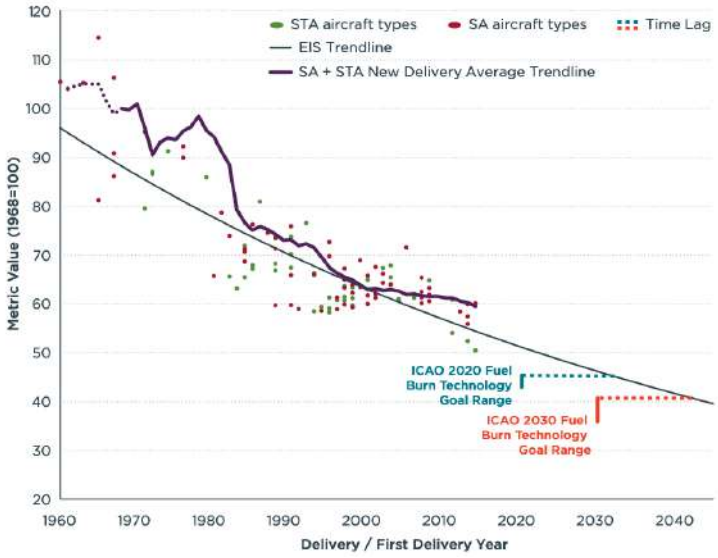

Figure 2: Fuel consumption over the years, from Kharina and Rutherford [89]

Despite these gains in fuel burn, the performance of the current generation of aircraft still falls short of the future ICAO fuel burn goals, as shown in Figure 2. Furthermore, the rate of fuel burn reduction seen today is not sufficient to achieve long-term targets such as those indicated in the EU Flightpath 2050 report or ICAO's LTAG.

This underlines the need for further effort to increase propulsion efficiency. Further research and development in aircraft propulsion, therefore, remains necessary to respond to these challenges by focusing on improving existing engine performance as well as taking further steps in innovative next-generation propulsion system design.

Efficiency of turbomachinery

For an aircraft engine to work at its peak efficiency, three critical stages must be mastered (see the works of Peng [130], Dixon and Hall [44] for more details):

- Efficient Compression: The pressure ratio of the compressor stages should be as high as possible with minimal energy input while staying within surge and stall operability limits to ensure continuous and efficient operation.
- Effective Combustion: The pressure loss and entropy generation through the combustor should be as low as possible while achieving the highest possible exit temperature; complete fuel combustion is needed for maximum energy release. All this has to be done with minimum generation of pollutants like soot and NOx and within the limits of combustion stability.
- Optimal Expansion: The conversion of thermal energy into mechanical work and thrust through the turbine and nozzle should be maximum to ensure high efficiency in energy extraction and propulsion.

When focusing on the turbomachinery components of an engine, which enable the exchange of work between the fluid and the machine through rotating parts—specifically the compressor and turbine stages—several challenges arise. Efficient operation depends largely on minimizing various loss mechanisms that degrade performance. The widely used categorization of losses into profile loss, endwall loss, and leakage loss is retained here (see Denton [42]), understood that most of the time, these mechanisms are interdependent, making precise distinctions difficult or even impossible.

- Profile Loss: This is typically generated at the blade boundary layers away from the hub and shroud walls. It usually includes the losses that occur at the trailing edge of the blade.
- Endwall Loss: Sometimes also referred to as "secondary loss," these occur due to the interaction of hub and shroud boundary layers with the blade row, leading to complex secondary flows. Significant interactions with other loss mechanisms, such as profile and leakage losses, make it challenging to distinctly categorize endwall losses.
- Tip Leakage Loss: Caused by the leakage of flow over the tips of rotor blades or through hub clearances in stator blades, this loss depends heavily on blade design features. In unshrouded compressor blades, strong interactions between leakage and endwall losses often blur the distinction between these two types of losses.

For more details about turbomachinery losses, refer to the detailed work by Denton [42] on loss mechanisms.

These three loss categories are responsible for the majority of entropy generation in turbomachinery. Their relative importance varies with the machine type and specific design parameters such as blade aspect ratio and tip clearance. In most turbomachines, however, these losses are all of the same general order of magnitude, with each loss contributing about one-third of the total loss [42].

Besides these main categories, other loss mechanisms may affect the overall efficiency, although less significantly or less often. For example, shock wave losses occur due to the creation of additional entropy occurring through the formation of shock waves; mixing losses arise due to the mixing of the wakes of upstream airfoils with the downstream flows, resulting in energy dissipation; seal leakage losses can happen due to air escaping through seals between the rotating and stationary parts. Combustion-related inefficiencies—which include instabilities in combustion or incomplete fuel combustion—can also degrade performance.

Design and analysis methods

The design of efficient engines and the quantification of their performance involve a combination of various tools: analytical methods, correlation techniques, experimental testing, and computational fluid dynamics (CFD).

The focus of this thesis is Computational Fluid Dynamics (CFD), a numerical method for the simulation of fluid flow, heat transfer, and associated phenomena by solving the governing equations of fluid mechanics, namely, the Navier-Stokes equations. Various CFD techniques offer different levels of detail, ranging from the less detailed Reynolds-Averaged Navier-Stokes (RANS) methods to the highly detailed Direct Numerical Simulation (DNS), with Large Eddy Simulation (LES) providing an intermediate level of fidelity. In turbomachinery, CFD—mostly RANS simulations during the development phases—is applied to simulate the flow in the different components: compressors, turbines, combustion chambers, and exhaust systems.

CFD offers several advantages in the analysis of turbomachinery design, including:

- Design iteration speed: CFD (RANS) enables multiple design iterations without the actual manufacture of each prototype. This greatly speeds up the design process compared to experimental testing, which is usually time-consuming.
- Extreme conditions capabilities: CFD enables the simulation of conditions that may be unsafe, impractical, or even impossible to realize in a laboratory.
- Non-intrusive data collection: Unlike experimental testing, where probes or sensors can alter flow dynamics, CFD provides data without physically disturbing the flow.
- Parameter exploration: CFD can permit the investigation of a great range of

parameters and conditions that would be impractical or more expensive to reproduce experimentally.

To fully leverage the advantages offered by CFD however, it is essential to be aware of the accuracy achievable with a given approach. Therefore, CFD analyses often include cross-validation of numerical results using methods with different fidelity levels and comparisons with experimental data to ensure reliability.

The focus of this thesis is specifically the use of the Large-Eddy Simulation (LES) of industrial turbomachinery stages such as fans, compressors, and turbines. LES resolves the largest, energy-containing eddies directly while modeling the smallest scales by turbulence models. While this entails a much higher computational cost compared to RANS methods, which model all scales of turbulence, it can offer a more accurate representation of various physical phenomena. These specificities make LES particularly valuable to simulate scenarios involving large-scale unsteadiness or other complex phenomena such as laminar-to-turbulent transition [174], that are more challenging to capture with lower-fidelity RANS approaches. Consequently, in turbomachinery applications, LES is well-suited to investigate the loss mechanisms mentioned above, *off-design* operating conditions involving secondary flows or flow separations, as well as delivering reliable insights into heat transfer and noise predictions.

These conditions and challenges also need to be addressed in exploring all possible future designs, whether they concern hydrogen propulsion systems, electric propulsion systems, ultra-high bypass ratio turbofans, or open rotor configurations. LES is hence a good candidate to address them alongside other validation methods, particularly experimental testing. It is indeed worth recalling here that the accuracy of LES predictions depends on several factors, including the choice of LES models, numerical schemes, and mesh quality and often requires validation to ensure reliability.

Motivation for the thesis and development context

To mitigate the high computational cost associated with LES while maintaining its key advantages in complex, reasonably sized setups relevant for turbomachinery studies, wall modeling can be employed [133]. With this approach, the near-wall behavior is modeled rather than fully simulated. However, such wall models must be carefully designed for their accuracy, relevance, and robustness to be guaranteed. As highlighted in the discussion above about the relevant loss mechanisms and key phenomena within turbomachines, near-wall behavior, and near-wall physics play key roles regarding those processes. In addition, the near-wall region can be particularly complex to model within turbomachinery, since the boundary layers may be subjected to a lot of challenging and non-trivial situations.

The implementation and application of Wall-Modeled LES (WMLES) face challenges related to both physical and numerical aspects. This subject is still an active research topic to provide enhancements to wall models to maintain the credibility,

reliability, and accuracy of LES predictions in various contexts [17, 96]. Central to these discussions is the physical representativeness of the wall models in relation to the specific cases and conditions in which they are applied. In the specific context of turbomachinery flows, this challenge is particularly critical due to the complex geometries and flow conditions, which often involve curvature and pressure gradient effects. Thus, a key motivation of this work is to improve the physical relevance of wall models, which are classically limited to assumptions of flat boundary layers without pressure gradients. More specifically, the work undertaken in this thesis focuses on the implementation of a wall model based on the *Thin Boundary Layer Equations* (TBLE) [9, 23, 58] encompassing the pressure gradient [46] within the massively parallel LES code *AVBP* developed at CERFACS. By enhancing the applicability of the available wall model, this work seeks to exploit the WMLES context to the best of its ability to perform high-fidelity simulations of complex turbomachinery flows.

Additionally, the coupling of the wall model with the LES framework is crucial, as wall models have historically originated from RANS approaches that may not be well-suited for LES contexts. This mismatch can result in discrepancies, such as inconsistencies in velocity profiles [83].

As mentioned above, the work carried out in this thesis is based on the massively parallel AVBP code developed at CERFACS, which solves the compressible and unsteady Navier-Stokes equations. The code enables the LES of reactive flows, two-phase flows, and rotor-stator configurations. It supports fundamental research activities on academic configurations and applied setups in collaboration with industrial partners. Additionally, for post-treatment capabilities, the dedicated Python library Antares [6] is employed.

Organization of the manuscript

The manuscript of the thesis is organized in two parts:

- **Part I** is dedicated to presenting the research background and the bibliographic context in which this work takes place.

  In Chapter 1, the different governing equations of fluid dynamics are presented, with a focus being addressed for the particular case of boundary layers. Finally, the context of Large Eddy Simulation (LES) and its relevant equations are presented in detail.

  In Chapter 2, the framework of wall modeling for LES is detailed, with an overview of the different types of wall models found in literature as well as the challenges they raise.

- **Part II** is dedicated to presenting the implementation strategy followed during the thesis to improve the quality of wall-modeled simulations in the context of the AVBP solver.

Chapter 3 introduces the framework in which the work has been carried out, as well as the academic test cases used throughout the thesis.

Chapter 4 presents the TBLE wall model implemented during the thesis to be able to model pressure gradient effects on the boundary layer with WMLES simulations with AVBP. The model is subsequently tested and validated in the different academic cases.

Chapter 5 then presents the alterations to the coupling between the wall model and the LES solver that have been undertaken to improve the near-wall physics and robustness of the LES framework. The fluctuations model put in place to boost the sub-grid viscosity at the wall when needed which was improved during this PhD work is presented before detailing the validation of the model on the same academic cases.

Finally, Chapter 6 is dedicated to the analysis of two turbomachinery applications, one turbine blade, and one fan stage including the rotor and the stator. Both models are put to the test together in these test cases and the outcomes are discussed.

Part I

Research Background and Bibliographic Context

Chapter 1

Governing equations

This chapter introduces the fundamental equations and conceptual framework necessary to describe fluid motion, with a particular focus on the complexities associated with solid boundaries. It begins by introducing the Navier-Stokes equations, which form the basis for describing the dynamics of viscous fluids. This is followed by the specific properties and governing equations of boundary layers relevant to understanding the characteristics of fluid behavior near solid surfaces. Finally, the framework of Large Eddy Simulation (LES), the methodology used in this thesis to simulate fluid motion, is detailed along with its governing equations.

1.1 Navier-Stokes Equations

The Navier-Stokes equations are the fundamental equations in fluid dynamics that describe the motion of any viscous fluid. The Navier-Stokes equations for compressible flows can be written as such:

$$\boxed{\begin{aligned} \frac{\partial \rho}{\partial t} + \frac{\partial}{\partial x_j}\left(\rho u_j\right) &= 0, \\ \frac{\partial \rho u_i}{\partial t} + \frac{\partial}{\partial x_j}\left(\rho u_i u_j\right) &= -\frac{\partial}{\partial x_j}\left[P\delta_{ij} - \tau_{ij}\right], \\ \frac{\partial \rho E}{\partial t} + \frac{\partial}{\partial x_j}\left(\rho E u_j\right) &= -\frac{\partial}{\partial x_j}\left[u_i\left(P\delta_{ij} - \tau_{ij}\right) + q_j\right]. \end{aligned}} \tag{1.1}$$

Where the Einstein notation has been used, with ρ the density, u_i the velocity components, P the pressure, δ_{ij} the Kronecker symbol defined by $\delta_{ij} = \begin{cases} 0 & \text{if } i \neq j \\ 1 & \text{if } i = j \end{cases}$; τ_{ij} the stress tensor, E the total energy per unit mass, and q_j the heat flux vector.

These equations translate respectively the mass, momentum, and energy conservation in the fluid and result from applying the fundamental conservation laws to a fluid in motion. Some terms need then to be further specified to provide full closure to this set of equations. These terms are detailed in the following subsections.

1.1.1 Equation of state

To close the system of equations formed by the Navier-Stokes equations (1.1), additional relationships in the form of equations of state are required. These equations of state provide relationships between the measurable macroscopic properties of gases. Commonly, the perfect gas equation is used:

$$P = \rho \, r \, T, \tag{1.2}$$

with $r = \frac{\mathcal{R}}{W}$ the gas constant of the mixture which depends on the mean molecular mass of the mixture W and the perfect gas constant $\mathcal{R} = 8.3143$ J/mol K.

1.1.2 Viscous stress tensor

To complete the system of equations (1.1), the viscous terms must be specified as well. The viscous stress tensor is expressed as

$$\tau_{ij} = 2\mu \left(S_{ij} - \frac{1}{3}\delta_{ij} S_{ll} \right), \tag{1.3}$$

with μ the dynamic viscosity and S the strain rate tensor defined as

$$S_{ij} = \frac{1}{2} \left(\frac{\partial u_j}{\partial x_i} + \frac{\partial u_i}{\partial x_j} \right). \tag{1.4}$$

The dynamic viscosity μ can be expressed classically with the Sutherland law

$$\mu = c_1 \frac{T^{3/2}}{T + c_2} \frac{T_{ref} + c_2}{T_{ref}^{3/2}}, \tag{1.5}$$

where the constants T_{ref}, c_1, and c_2 are determined to fit the viscosity of the mixture considered.

1.1.3 Heat flux

The last term needed to provide closure to the Navier-Stokes equations (1.1) is the heat flux vector, which is determined via the Fourier law:

$$q_i = -\lambda \frac{\partial T}{\partial x_i}, \tag{1.6}$$

with the heat conduction coefficient expressed with the Prandtl number Pr, the viscosity and the specific heat capacity at constant pressure of the mixture C_p:

$$\lambda = \frac{\mu \, C_p}{\mathrm{Pr}} \tag{1.7}$$

1.1.4 Turbulence

Under certain conditions, the system of equations of a fluid motion can produce steady, *laminar* solutions. Under these conditions, the fluid motion is dominated by viscous effects and viscous diffusion of its momentum and vorticity. This is however not the case for most of the engineering-relevant applications, where at least some part of the flow is *turbulent*. In that case, the fluid's inertia becomes predominant over its viscosity [184]. A relevant dimensionless quantity to evaluate the turbulent

or laminar state of a flow is the Reynolds number. The Reynolds number is the ratio between inertial and viscous forces, and can be defined as such:

$$\mathrm{Re} = \frac{uL}{\nu} \tag{1.8}$$

where u is the flow speed, L is a characteristic length of the studied setup, and ν is the kinematic viscosity of the fluid. Generally, when the Reynolds number of a flow is small, the flow will be laminar, while a higher Reynolds number implies turbulent conditions, although there is no universally valid threshold Reynolds number to predict the laminar to turbulent transition of a fluid.

Turbulent flows are characterized by irregular conditions under which the various quantities exhibit random variations in time and space coordinates so that statistical averages can be discerned, according to Hinze [70]. Turbulent flows are particularly challenging to predict because they depend on three-dimensional, nonlinear, time-dependent interactions between the different terms of the Navier-Stokes equations.

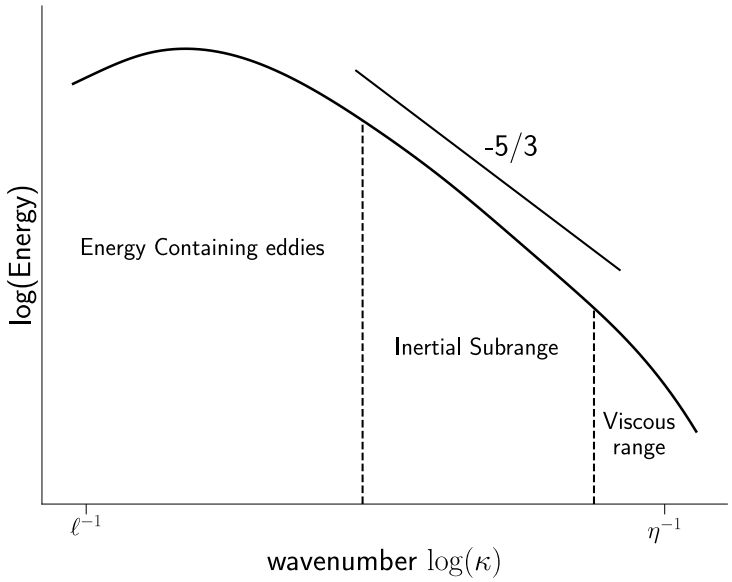

Figure 1.1: Diagram illustrating the turbulent energy spectrum.

One feature of turbulent flows is the presence of *eddies*, which are swirling structures within the flow characterized by their vorticity. Turbulent eddies of various sizes are present in turbulent flows, from the largest eddy size ℓ, to the smallest eddy scale η, known as the Kolmogorov scale [91]. The turbulent eddies are observed to transfer turbulent kinetic energy from the largest sizes to the smallest sizes, with the largest eddies containing most of the turbulent kinetic energy, while the smallest eddies are the scale at which the kinetic energy is dissipated into heat by viscous effects. If the turbulent eddies are grouped by their size, symbolized by a wavenumber κ, and the energy they contain, the classical turbulent energy cascade

shown in Figure 1.1 can be obtained. One thing to note on the turbulent cascade is the wide range of scales over which it spans, if the turbulent Reynolds number $\mathrm{Re}_t = \frac{\kappa^{1/2}\ell}{\nu}$ is high enough $\mathrm{Re}_t \gg 1$, where k is the turbulent kinetic energy.

For more details on turbulence phenomena, the works of Hinze [70], Lesieur [100] or Wilcox [184] can be consulted. However, a few important points can be learned from this brief introduction to turbulence. The structure of a turbulent flow is characterized by random variations of various quantities that are difficult to predict due to the nonlinear, three-dimensional, and time-varying nature of turbulence. In addition, turbulence is characterized by eddy motions that form a cascade of turbulence that can extend over a wide range of scales. Any framework model that attempts to reproduce or predict the behavior of turbulent flows must take these basic principles into account to obtain conclusive results.

The following sections are devoted to first describing the intricacies of the particular case of boundary layer flow, before detailing the Large Eddy Simulation (LES) framework for simulating turbulent flows.

1.2 Boundary Layers

A boundary layer is a thin region adjacent to a solid surface where the fluid velocity changes from zero—as a result of the no-slip condition at the surface—to free flow velocity. This transition zone is the focus of distinct physical phenomena. Understanding and correctly representing the flow dynamics of boundary layers is important for studying wall-bounded flows and flows that develop over surfaces, such as air over an airplane wing or around a turbomachinery blade. Indeed, the frictional forces that occur in the boundary layer have an enormous impact on the performance of these machines. The concept of the boundary layer was introduced by Ludwig Prandtl in 1904 [140]. This work provided a basis for understanding how viscosity affects fluid flow near solid surfaces and introduced a means of simplifying the complicated Navier-Stokes equations in this region. Several factors can affect the behavior and shape of the boundary layer, such as surface curvature, pressure gradients, compressibility, and wall roughness. The following sections are dedicated to the analysis of boundary layers, but are limited to fully developed turbulent boundary layers and exclude the laminar-to-turbulent transition, which is beyond the scope of this study.

1.2.1 Averaged Equations

The analysis of the boundary layer equations typically begins with the mean flow equations for near-wall flows. A detailed analysis and discussion about boundary layers and their equations was recently published in the review of Devenport and Lowe [43]. The Reynolds-Averaged Navier-Stokes (RANS) equations can serve as a useful starting point to study the dynamics of boundary layers. The RANS equations are derived from the Navier-Stokes equations (1.1) by decomposing each flow quantity f into a time-averaged component $\bar{f}$ and a fluctuating component

f'. The Favre average, defined as $\widetilde{f} = \frac{\overline{\rho f}}{\overline{\rho}}$, where each fluid variable is decomposed into a mass-weighted time average $\tilde{f}$ and a fluctuating part f'', can also be used. This allows to simplify the average of the product of two flow quantities f and g as $\overline{\rho f g} = \overline{\rho}(\tilde{f}\tilde{g} + \widetilde{f''g''})$. Time averaging the Navier-Stokes equations with these definitions yields:

$$\boxed{\begin{aligned} \frac{\partial \bar{\rho}}{\partial t} + \frac{\partial \bar{\rho}\widetilde{u}_i}{\partial x_i} &= 0, \\ \frac{\partial \bar{\rho}\widetilde{u}_i}{\partial t} + \frac{\partial}{\partial x_j}\left(\bar{\rho}\widetilde{u}_i\widetilde{u}_j\right) &= -\frac{\partial \overline{P}}{\partial x_i} + \frac{\partial}{\partial x_j}\left[\overline{\tau_{ij}} - \overline{\rho}\widetilde{u_i''u_j''}\right], \\ \frac{\partial \bar{\rho}\widetilde{E}}{\partial t} + \frac{\partial}{\partial x_j}\left(\bar{\rho}\widetilde{E}\widetilde{u_j}\right) &= -\frac{\partial}{\partial x_j}\left[\overline{u_i\left(P\delta_{ij} - \tau_{ij}\right)} + \overline{q_j} + \overline{\rho}\widetilde{E''u_j''}\right]. \end{aligned}} \tag{1.9}$$

An assumption often used in wall-bounded flow studies is the incompressibility of the fluid within the boundary layer. Although this seems a rather restrictive assumption, it holds for a fairly wide range of flow conditions. Notably, as long as the turbulent Mach number remains low, compressibility effects on turbulent flows only affect the flow statistics though average density variations according to Morkovin's hypothesis [113, 162]. In addition to that, the generally observed velocity deficit within the boundary layer results in lower Mach numbers compared to the bulk flow. When this assumption is used, the Favre average is no longer used and the system of RANS equations can be written as:

$$\begin{aligned} \frac{\partial U_i}{\partial x_i} &= 0, \\ U_j\frac{\partial U_i}{\partial x_j} &= -\frac{1}{\rho}\frac{\partial \overline{P}}{\partial x_i} - \frac{\partial \overline{u_i'u_j'}}{\partial x_j} + \nu\frac{\partial^2 U_i}{\partial x_j^2} \\ \frac{\partial}{\partial x_j}\left(\rho\overline{E}U_j\right) &= -\frac{\partial}{\partial x_j}\left[\overline{u_i\left(P\delta_{ij} - \tau_{ij}\right)} + \overline{q_j} + \rho\overline{E'u_j'}\right]. \end{aligned} \tag{1.10}$$

where the convention $\overline{u_i} = U_i$.

To continue discussing the continuity and momentum equations, some geometric parameters are defined and illustrated in Fig. 1.2. The characteristics lengths L, which corresponds to the boundary layer length, and δ, which is the boundary layer thickness, are defined. The characteristic velocity U_e is also defined as the freestream velocity. We then introduce the following non-dimensional variables: $\widehat{U_i} = U_i/U_e$, $\widehat{u_i'} = u_i'/U_e$, $\widehat{x_i} = x_i/L$, $\widehat{x_2} = x_2/\delta$ and $\widehat{P} = P/\rho U_e^2$.

When both the continuity and momentum equations (1.10) are expressed in terms of these non-dimensional variables, they provide useful insight into the behavior of boundary layers. First, the continuity equation is obtained:

$$\frac{\partial \widehat{U_1}}{\partial \widehat{x_1}} + \frac{L}{\delta_o}\frac{\partial \widehat{U_2}}{\partial \widehat{x_2}} + \frac{\partial \widehat{U_3}}{\partial \widehat{x_3}} = 0. \tag{1.11}$$

It is easy to argue that the tangential components of the velocity are of the order

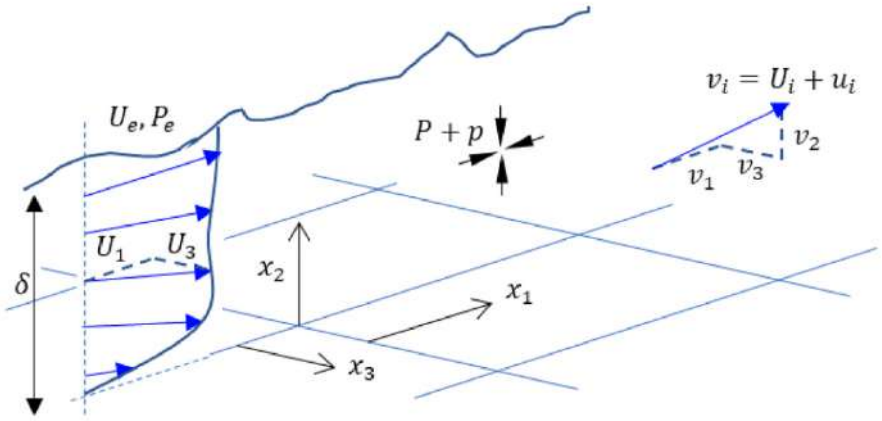

Figure 1.2: Sketch of a boundary layer developing over a flat plate with the non-dimensional quantities' definitions, from [43].

of the free stream velocity [43], which then implies $\widehat{U_1} \sim 1$, $\widehat{U_3} \sim 1$. The continuity equation (1.11) then gives $U_2 \sim U_e \frac{\delta}{L}$.

Applying the non-dimensional variables to the momentum equations in the three directions gives:

$$\begin{aligned}
\widehat{U_1}\frac{\partial \widehat{U_1}}{\partial \widehat{x_1}} + \widehat{U_2}\frac{\partial \widehat{U_1}}{\partial \widehat{x_2}}\frac{L}{\delta} + \widehat{U_3}\frac{\partial \widehat{U_1}}{\partial \widehat{x_3}} &= -\frac{\partial \widehat{P}}{\partial \widehat{x_1}} - \frac{\partial \overline{\widehat{u_1'}^2}}{\partial \widehat{x_1}} - \frac{\partial \overline{\widehat{u_1'}\widehat{u_2'}}}{\partial \widehat{x_2}}\frac{L}{\delta} - \frac{\partial \overline{\widehat{u_1'}\widehat{u_3'}}}{\partial \widehat{x_3}} + \frac{\nu}{U_e L}\left(\frac{\partial^2 \widehat{U_1}}{\partial \widehat{x_1}^2} + \frac{\partial^2 \widehat{U_1}}{\partial \widehat{x_2}^2}\frac{L^2}{\delta^2} + \frac{\partial^2 \widehat{U_1}}{\partial \widehat{x_3}^2}\right), \\
\widehat{U_1}\frac{\partial \widehat{U_2}}{\partial \widehat{x_1}} + \widehat{U_2}\frac{\partial \widehat{U_2}}{\partial \widehat{x_2}}\frac{L}{\delta} + \widehat{U_3}\frac{\partial \widehat{U_2}}{\partial \widehat{x_3}} &= -\frac{\partial \widehat{P}}{\partial \widehat{x_2}}\frac{L}{\delta} - \frac{\partial \overline{\widehat{u_2'}\widehat{u_1'}}}{\partial \widehat{x_1}} - \frac{\partial \overline{\widehat{u_2'}^2}}{\partial \widehat{x_2}}\frac{L}{\delta} - \frac{\partial \overline{\widehat{u_2'}\widehat{u_3'}}}{\partial \widehat{x_3}} + \frac{\nu}{U_e L}\left(\frac{\partial^2 \widehat{U_2}}{\partial \widehat{x_1}^2} + \frac{\partial^2 \widehat{U_2}}{\partial \widehat{x_2}^2}\frac{L^2}{\delta^2} + \frac{\partial^2 \widehat{U_2}}{\partial \widehat{x_3}^2}\right), \\
\widehat{U_1}\frac{\partial \widehat{U_3}}{\partial \widehat{x_1}} + \widehat{U_2}\frac{\partial \widehat{U_3}}{\partial \widehat{x_2}}\frac{L}{\delta} + \widehat{U_3}\frac{\partial \widehat{U_3}}{\partial \widehat{x_3}} &= -\frac{\partial \widehat{P}}{\partial \widehat{x_3}} - \frac{\partial \overline{\widehat{u_3'}\widehat{u_1'}}}{\partial \widehat{x_1}} - \frac{\partial \overline{\widehat{u_3'}\widehat{u_2'}}}{\partial \widehat{x_2}}\frac{L}{\delta} - \frac{\partial \overline{\widehat{u_3'}^2}}{\partial \widehat{x_3}} + \frac{\nu}{U_e L}\left(\frac{\partial^2 \widehat{U_3}}{\partial \widehat{x_1}^2} + \frac{\partial^2 \widehat{U_3}}{\partial \widehat{x_2}^2}\frac{L^2}{\delta^2} + \frac{\partial^2 \widehat{U_3}}{\partial \widehat{x_3}^2}\right).
\end{aligned} \tag{1.12}$$

Once again here, both tangential directions x_1 and x_3 can be treated in the same manner. In that case, following the previous arguments yielded by the continuity equation (1.11), all the convective terms on the left-hand side of the equations are of order 1, as is the pressure gradient term. Let's focus on the x_1 direction equation, keeping in mind that the arguments are similar for the x_3 direction. Regarding the Reynolds stress terms, the first and third one are

$$\frac{\partial \overline{\widehat{u_1'}^2}}{\partial \widehat{x_1}} \sim u'^2/U_e^2;$$

and

$$\overline{\frac{\partial \widehat{u_1'}\widehat{u_3'}}{\partial \widehat{x_3}}} \sim u'^2/U_e^2$$

where u' is a characteristic scale of velocity fluctuations. These terms are **assumed to be negligible** for this analysis.

The second Reynold stress term

$$\overline{\frac{\partial \widehat{u_1'}\widehat{u_2'}}{\partial \widehat{x_2}}}\frac{L}{\delta} \sim (u'^2/U_e^2)(L/\delta)$$

is however **not negligible**.

Regarding the wall-normal component of the momentum equation, the convective terms are

$$\widehat{U_1}\frac{\partial \widehat{U_2}}{\partial \widehat{x_1}} \sim \widehat{U_2}\frac{\partial \widehat{U_2}}{\partial \widehat{x_2}}\frac{L}{\delta} \sim \widehat{U_3}\frac{\partial \widehat{U_2}}{\partial \widehat{x_3}} \sim \frac{\delta}{L} \ll 1$$

and are **here all negligible**.

The Reynolds stress terms for their part are given in equation (1.12) as

$$\overline{\frac{\partial \widehat{u_2'}\widehat{u_1'}}{\partial \widehat{x_1}}} \sim \overline{\frac{\partial \widehat{u_2'}\widehat{u_3'}}{\partial \widehat{x_3}}} \sim u'^2/U_e^2 \ll 1$$

which is **also negligible**, and

$$\overline{\frac{\partial \widehat{u_2}^2}{\partial \widehat{x_2}}}\frac{L}{\delta} \sim \frac{u'^2}{U_e^2}\frac{L}{\delta}$$

which is **in general not negligible**.

The pressure gradient is in general **not negligible** as well:

$$\frac{\partial \widehat{P}}{\partial \widehat{x_2}}\frac{L}{\delta} \sim L/\delta.$$

The viscous terms are then given in Eq. (1.11) as

$$\frac{\nu}{U_e L}\left(\frac{\partial^2 \widehat{U_2}}{\partial \widehat{x_2}^2} + \frac{\partial^2 \widehat{U_2}}{\partial \widehat{x_3}^2}\right) \sim \frac{1}{\mathrm{Re}}\frac{\delta}{L}$$

and

$$\frac{\nu}{U_e L}\left(\frac{\partial^2 \widehat{U_2}}{\partial \widehat{x_2}^2}\frac{L^2}{\delta^2}\right) \sim \frac{1}{\mathrm{Re}}\frac{L}{\delta},$$

where $\mathrm{Re} = \frac{U_e L}{\nu}$ is the Reynolds number. Considering fully turbulent conditions, the high Reynolds number ($\mathrm{Re} \gg 1$) implies that these terms are **also negligible**.

All these considerations allow to simplify the system of equations (1.11), leading to the so-called Thin Boundary Layer Equations (TBLE) [9, 23]:

$$\boxed{\begin{aligned} U_1\frac{\partial U_1}{\partial x_1}+U_2\frac{\partial U_1}{\partial x_2}+U_3\frac{\partial U_1}{\partial x_3} &= -\frac{1}{\rho}\frac{\partial \overline{P}}{\partial x_1}-\frac{\partial \overline{u_1' u_2'}}{\partial x_2}+\nu\frac{\partial^2 U_1}{\partial x_2^2} \\ 0 &= -\frac{1}{\rho}\frac{\partial \overline{P}}{\partial x_2}-\frac{\partial \overline{u_2'^2}}{\partial x_2} \\ U_1\frac{\partial U_3}{\partial x_1}+U_2\frac{\partial U_3}{\partial x_2}+U_3\frac{\partial U_3}{\partial x_3} &= -\frac{1}{\rho}\frac{\partial \overline{P}}{\partial x_3}-\frac{\partial \overline{u_3' u_2'}}{\partial x_2}+\nu\frac{\partial^2 U_3}{\partial x_2^2} \end{aligned}} \tag{1.13}$$

These equations remain quite general for describing the overall flow motion within a boundary layer since they are based only on dimensional arguments concerning the velocity magnitude in a general context. However, they consider only the time-averaged Navier-Stokes equations in fully turbulent conditions ($\mathrm{Re} \gg 1$) and assume incompressibility. For the latter consideration, it can be argued that these conditions are commonly found locally, at least approximately, inside boundary layers since the flow is naturally at reduced velocity and low Mach number near solid boundaries.

1.2.2 Equilibrium boundary layers

Further insight into the physics of boundary layers can be gained by considering equilibrium boundary layers. These are defined by the fact that they are self-similar in their evolution—that is, the shape and structure of the boundary layer is self-preserving in an average sense as it grows. While this imposes some limitations on the conditions under which such a boundary layer may exist, it does allow the general behavior of turbulent boundary layers to be investigated without many complications that come with more complex scenarios. A common starting point seen throughout the literature is the simple case of a boundary layer under the following conditions:

- Fully turbulent flow ($\mathrm{Re} \gg 1$)
- Incompressible flow
- Stationary boundary layer
- Development over a flat surface (essentially two-dimensional)
- Absence of a pressure gradient

Simplifying equations (1.13) under these conditions yields the governing equation:

$$0 = -\frac{\partial \overline{u_1' u_2'}}{\partial x_2}+\nu\frac{\partial^2 U_1}{\partial x_2^2}, \tag{1.14}$$

taking advantage of the fact that the flow is essentially 2D in the streamwise direction, chosen arbitrarily here to be x_1 without altering the generality of the reasoning.

In RANS, which is the formalism chosen in this part, it is common to rewrite the Reynolds stress terms with the Boussinesq closure assumption. This relates the turbulent stresses to the mean flow field using an eddy viscosity concept, where the Reynolds stresses are proportional to the mean strain rate. This writes in the general case:

$$-\overline{u_i' u_j'} = \nu_t \left(\frac{\partial U_i}{\partial x_j} + \frac{\partial U_j}{\partial x_i} \right) - \frac{2}{3} k \delta_{ij} \tag{1.15}$$

with ν_t the turbulent eddy viscosity in question that still needs to be defined, and $k = \frac{1}{2}\overline{u_i' u_i'}$ the turbulent kinetic energy. Replacing $u_1' u_2'$ in equation (1.14) with (1.15) leads to the following expression:

$$\frac{\partial}{\partial x_2} \left[\nu_t \left(\frac{\partial U_1}{\partial x_2} + \frac{\partial U_2}{\partial x_1} \right) + \nu \frac{\partial U_1}{\partial x_2} \right] = 0.$$

Here again, with the same notations as in section 1.2.1, the argument can be made using dimensional analysis that $\frac{\partial U_1}{\partial x_2} \sim \frac{L}{\delta} \frac{\partial U_2}{\partial x_1}$, implying that $\frac{\partial U_1}{\partial x_2} \gg \frac{\partial U_2}{\partial x_1}$. This further simplification leads to the final expression:

$$\boxed{\frac{\partial}{\partial y} \left((\mu + \mu_t) \frac{\partial U_1}{\partial y} \right) = 0,} \tag{1.16}$$

where the wall-normal coordinate x_2 is identified to y. This simple equation accurately describes the behavior of the boundary layer over a flat plate with no pressure gradient, in fully turbulent conditions. In this form, the boundary layer equation allows to highlight the self-similar behavior of the boundary layer when the correct non-dimensional variables are used. These are the inner scaled quantities

$$u^+ = \frac{U_1}{u_\tau}$$

and

$$y^+ = \frac{y u_\tau}{\nu}$$

based on the friction velocity

$$u_\tau = \sqrt{\frac{\tau_w}{\rho}}$$

and the wall friction

$$\tau_w = \mu \left. \frac{\partial U_1}{\partial y} \right|_0 . \tag{1.17}$$

With these variables, self-similar profiles divided into several zones can be established. The two main layers which are the viscous wall region and the log-law region have been described in numerous works like those of Schlichting and Gersten [151], Cebeci and Smith [28], Pope [138] or Wilcox [184]. The behavior of the average flow velocity in these regions is identifiable in Fig. 1.3 with a linear region nearest

to the wall and a logarithmic region farther from it. In fact, the inner layer of the boundary layer can be broken down into three parts:

- **The linear sublayer** ($y^+ < 5$), closest to the wall, where viscous effects dominate and turbulent activity is almost absent. In that region, it is reasonable to assume that $\overline{u_i' u_j'} \underset{y\to 0}{\to} 0$, implying that the turbulent viscosity μ_t can be neglected in this zone, leading to:

$$\mu \frac{\partial U_1}{\partial y} = \text{Cst} = \tau_w.$$

  Using the non-dimensional variables, this becomes:

$$U_1 = \frac{\rho u_\tau^2 y}{\mu} \Leftrightarrow \frac{U_1}{u_\tau} = \frac{y u_\tau}{\nu} \Leftrightarrow \boxed{u^+ = y^+}, \tag{1.18}$$

- **The logarithmic region** or inertial region ($y^+ > 30$), where turbulent transport dominates the flow compared to molecular viscosity. In that region, the turbulent Reynolds stress tensor becomes significant compared to the molecular viscosity translating to $\mu_t \gg \mu$. This leads to the following expression:

$$\mu_t \frac{\partial U_1}{\partial y} = \tau_w \tag{1.19}$$

  To continue developing this equation, a model for the turbulent eddy viscosity needs to be chosen. The mixing length model is typically adopted for this purpose [138, p. 289]:

$$\nu_t = u^* \ell_m = \ell_m^2 \left| \frac{\mathrm{d}U_1}{\mathrm{d}y} \right|, \tag{1.20}$$

  where the turbulent viscosity depends on a characteristic velocity u^* and on the mixing length $\ell_m = \kappa y$, with $\kappa \approx 0.41$ the von Kármán constant. Here, the classical approach uses the friction velocity as the characteristic velocity $u^* = u_\tau$ [138, p.289] leading to:

$$\nu_t = \kappa y u_\tau. \tag{1.21}$$

  From there, the momentum equation yields

$$\rho \kappa u_\tau y \frac{\partial U_1}{\partial y} = \tau_w \tag{1.22}$$

  which can be rearranged as

$$\frac{\kappa \, dU_1}{u_\tau} = \frac{dy}{y}. \tag{1.23}$$

This equation can be written in non-dimensional form and integrated since u_τ is constant with respect to y and $U_1 = u^+ u_\tau$:

$$\kappa \, du^+ = \frac{dy^+}{y^+} \Leftrightarrow \kappa u^+ = \ln(y^+) + c \Leftrightarrow \boxed{u^+ = \frac{1}{\kappa} \ln(y^+) + c'}. \tag{1.24}$$

Where c' is a constant that is commonly admitted to be within 5% of $c = 5.2$ [138, p. 274].

- **The buffer layer**, located between the linear sublayer and the logarithmic region. In this part of the boundary layer, turbulent and molecular diffusion are of comparable scales. This means that no clear scale separation is possible for the analysis of this region. It is generally observed that the maximum production of turbulent kinetic energy occurs in the buffer layer.

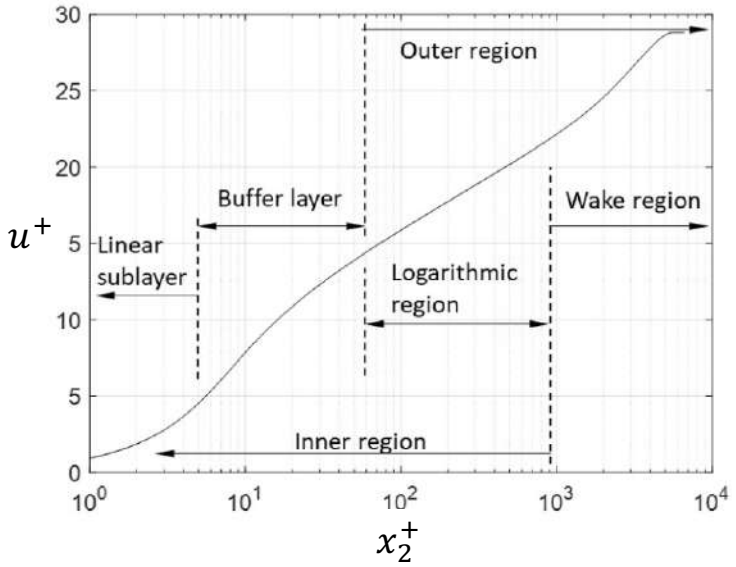

Figure 1.3: Boundary layer velocity profile regions [43, p.6].

This overall behavior is well supported by numerical [73, 186] and experimental data [36, 90, 104]. While this analysis is an important first step, allowing to derive clear trends and conclusions on a simple case, it is important to note that it ignores several complex phenomena that occur in real flows and can affect the shape and dynamics of the turbulent boundary layer. These include unsteadiness, curvature, compressibility, pressure gradients, roughness, and three-dimensional effects.

1.2.3 Turbulent structures of the boundary layer

The observed behavior of a turbulent boundary layer developing over a flat plate, including the mean flow just described and the turbulence statistics, results from complex instantaneous turbulent structures. These structures are well documented in the literature, with the works of Smits [159], Smits et al. [160] or Marusic et al. [109] discussing it at lengths. A commonly accepted classification of the turbulent structures arising near solid boundaries is composed of four main types, as shown in Fig. 1.4. Closest to the wall are sublayer streaks and quasi-streamwise vortices, which occur when $y^+ < 10$ and have a spanwise spacing of about 100 wall units, extending streamwise similarly to the boundary layer thickness ($\sim 1000\nu/u_\tau$).

Next are elongated hairpin vortices, which scale with distance from the wall and are angled at about 45 degrees. At higher Reynolds numbers, these vortices resemble single-legged filaments more than two-legged hairpins, and their distribution becomes more chaotic, as shown by the direct numerical simulations of Schlatter et al. [150].

These are followed by large-scale motions characterized by trains of hairpin vortices extending about 2-3 boundary layer thicknesses (δ) and tilted at shallow angles of 10 to 20 degrees to the wall. Finally, the largest scale structures are the "superstructures", which can be up to ten times longer than hairpins and consist of related groups of smaller structures.

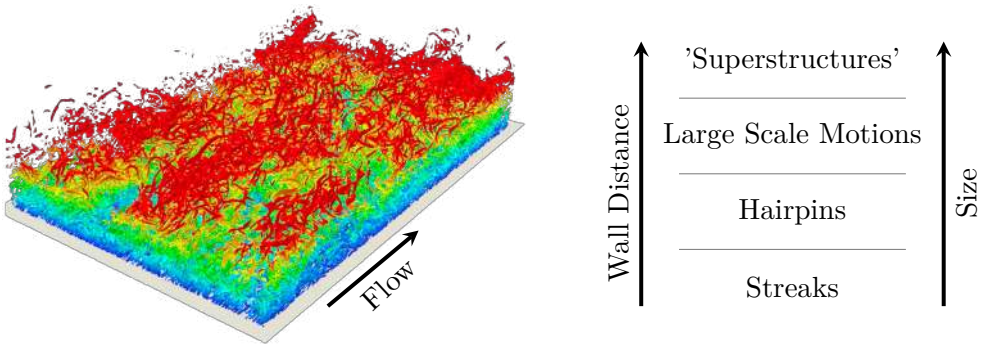

Figure 1.4: Turbulent structures in the boundary layer. Visualization from Schlatter et al. [150].

The various turbulent structures within the boundary layer illustrate well the wide range of length scales over which the turbulent structures span and the interaction between those scales. Strong interactions can happen even between structures located in the near-wall region and motions in the outer region [109]. One additional complexity of the turbulent structure of the boundary layer is that only part of the motions involved scale with the wall shear stress, as first advanced by Townsend [173]. Consequently, the turbulent statistics of even a flat plate boundary layer, such as the intensity of velocity fluctuations, exhibit a dependence on the Reynolds number. The fact that the turbulent velocities plotted for various Reynolds numbers do not collapse is illustrated in Figure 1.5 and is well documented in literature [109, 150, 163].

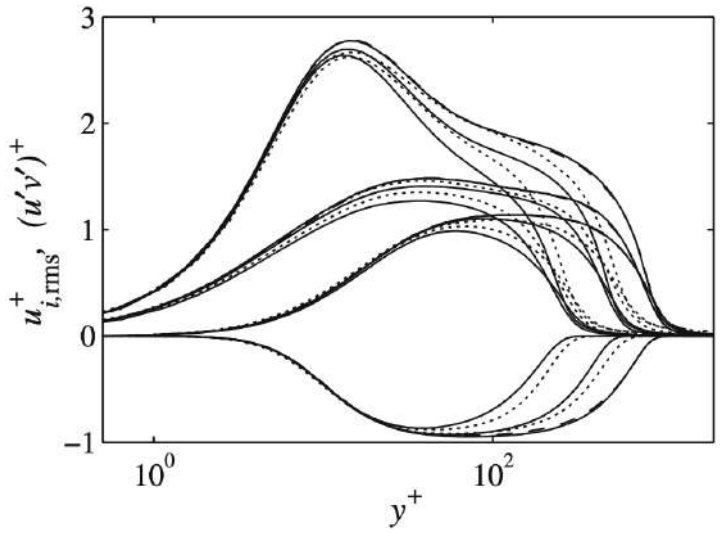

Figure 1.5: Reynolds stresses of a boundary layer over a flat surface at $Re_h = 685$; 1433; 2560 (— Schlatter et al. [150]), $Re_h = 670$; 1410 (····· Spalart [163]) and $Re_h = 1412$; 2512 (- - - Schlatter et al. [149]); from Schlatter et al. [150].

1.2.4 Energy Equation

After discussing the velocity characteristics of the boundary layer, attention is briefly shifted to its temperature and energy characteristics. Although not the primary focus of this thesis, the temperature profiles within the boundary layer show a self-similar behavior similar to the velocity profiles under the same assumptions. This behavior can be described by the non-dimensional temperature

$$\theta^+ = \frac{|T - T_w|}{T_\tau} \tag{1.25}$$

where T_w is the wall temperature and T_τ the friction temperature, defined as

$$T_\tau = \frac{|\overline{q}_w|}{\overline{C_{p_w}}\overline{\rho}_w u_\tau}. \tag{1.26}$$

Here, the subscript w subscripts denotes the wall values of the already defined quantities $\overline{q}$ and C_p. This self-similar behavior has been observed both experimentally [12, 81] and numerically, as demonstrated in the results of Kawamura et al. [85] shown in Fig. 1.6 for various Reynolds and Prandtl numbers.

To support these observations theoretically, a similar approach to that used in part 1.2.2 for the momentum equations can be applied to the RANS energy equation. The energy equation from system (1.10) is:

$$\frac{\partial \rho \overline{E}}{\partial t} + \frac{\partial}{\partial x_j}\left(\rho \overline{E} U_j\right) = -\frac{\partial}{\partial x_j}\left[\overline{u_i\left(P\delta_{ij} - \tau_{ij}\right)} + \overline{q_j} + \rho\overline{E' u'_j}\right].$$

Under the same assumptions as for the momentum equations, examining a zero-

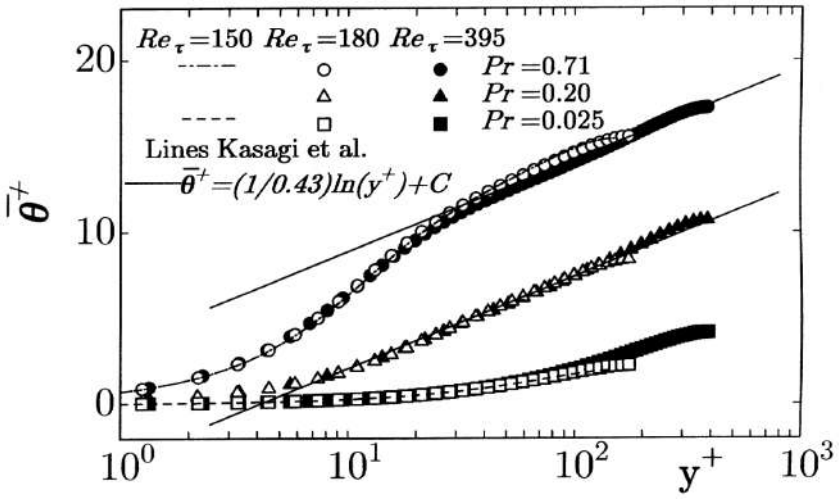

Figure 1.6: Self-Similar temperature profiles obtained in DNS for isothermal walls, from Kawamura et al. [85].

pressure gradient, two-dimensional turbulent boundary layer, the energy equation simplifies to:

$$\frac{\partial}{\partial y}\left[\overline{q_2} + \rho\overline{E' u_j'}\right] = 0,$$

which can be rewritten in terms of the temperature gradient using Fourier's law:

$$\frac{\partial}{\partial y}\left[(\lambda + \lambda_t)\frac{\partial \overline{T}}{\partial y}\right] = 0, \tag{1.27}$$

where the Boussinesq closure introduces the turbulent thermal conductivity λ_t. This turbulent conductivity is typically expressed as a function of the turbulent Prandtl number and turbulent viscosity, in an analogous manner to laminar conductivity: $\lambda_t = \frac{\mu_t \overline{C_p}}{\mathrm{Pr}_t}$. Using the same mixing layer model as in part 1.2.2 for the turbulent viscosity, the turbulent thermal conductivity can be written as:

$$\lambda_t = \overline{\rho}\overline{C_p}\frac{(\kappa y)^2}{\mathrm{Pr}_t}\frac{\mathrm{d}U_1}{\mathrm{d}y}, \tag{1.28}$$

where Pr_t is the turbulent Prandtl number, which can be modeled in various ways [86], but is commonly approximated as a constant value near 0.9 [81]. Integrating equation (1.27) yields:

$$q_w = -(\lambda + \lambda_t)\frac{\partial \overline{T}}{\partial y}, \tag{1.29}$$

with the convention of a wall heat flux directed from the wall to the fluid. Replacing λ_t in this expression gives:

$$\bar{q}_w = -\overline{\lambda}\frac{\partial \overline{T}}{\partial y} - \overline{\rho}\overline{C_p}\frac{(\kappa y)^2}{\mathrm{Pr}_t}\frac{\partial U_1}{\partial y}\frac{\partial \overline{T}}{\partial y}$$

which can be recast in non-dimensional form using eq. (1.25) as:

$$\frac{1}{\mathrm{Pr}}\frac{\partial \theta^+}{\partial y^+} + \frac{(\kappa y)^2}{\mathrm{Pr}_t}\frac{\partial u^+}{\partial y^+}\frac{\partial \theta^+}{\partial y^+} = 1. \tag{1.30}$$

From this equation, two behaviors can be identified similarly to the velocity profile. Near the wall the turbulent contributions can indeed be neglected once again, yielding a linear behavior of the form:

$$\boxed{\theta^+ = \mathrm{Pr}\, y^+}, \tag{1.31}$$

whereas farther from the wall, the turbulent contributions dominate, leading to another simplification:

$$\boxed{\theta^+ = \frac{\mathrm{Pr}_t}{\kappa}\ln y^+ + d}, \tag{1.32}$$

It is important to note here the dependency of the intercept constant d to the fluid's Prandtl number, as also illustrated in Fig. 1.6.

In summary, similar to the velocity profiles, under the same assumptions, the temperature profiles in a boundary layer are self-similar. This self-similarity can be described using a nondimensional temperature scaling that allows to distinguish the linear region near the wall from the logarithmic region farther away. This behavior is well supported by experimental [12, 81] and numerical [85] data and is obtained using a simplified energy equation for a turbulent boundary layer developing over an isothermal flat wall, assuming a zero-pressure gradient scenario.

1.2.5 Non-Equilibrium Effects

After having examined the characteristics of the canonical form of a turbulent boundary layer developing over a flat surface with no pressure gradient, some more complex effects can be discussed. The purpose of the following sections is to discuss some of the phenomena that have been neglected in the analysis presented so far. The effects of surface curvature, compressibility, roughness, and pressure gradient will be considered in sequence.

1.2.5.1 Curvature Effect

The reference study on the influence of geometric wall curvature on the boundary layer is the publication by Patel and Sotiropoulos [129]. To study the influence of curvature, experiments often involve looking at turbulent channels that are curved to approximate a 2D boundary layer as closely as possible. Even in that context, it is not easy to identify the effect of curvature and separate it from the effect of the induced pressure gradient, which is often dominant.

Compared to the classical logarithmic law obtained for boundary layers developing over flat plates, the profile is shifted downward—velocity deficit—for concave walls, and upward—increased velocity—for convex walls—for cases without longitudinal pressure gradient—as shown in Fig. 1.7. These results are often attributed to curvature effects in the outer layer and are less valid in the inner layer, where good agreement with the logarithmic law is observed overall.

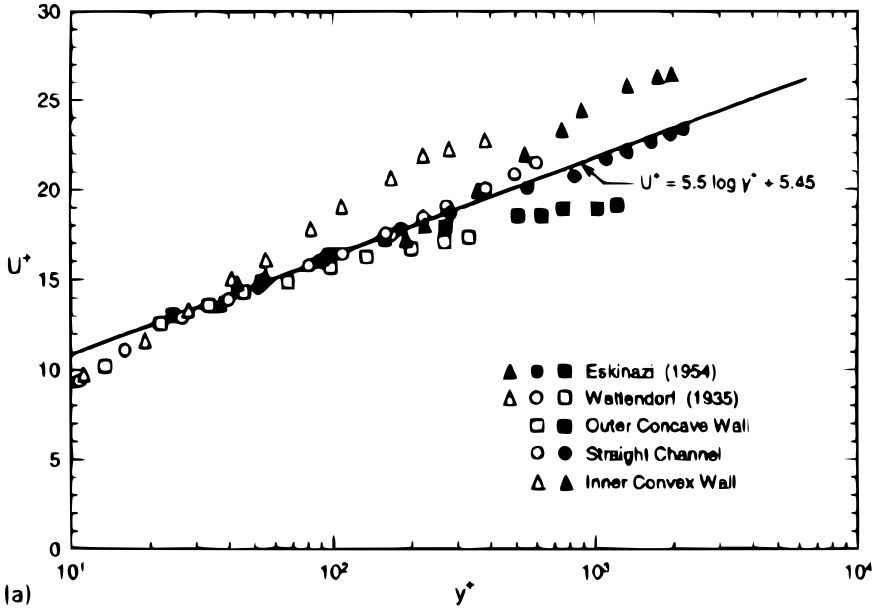

Figure 1.7: Comparison of fully developed channel flow velocity profiles for different convex and concave curvatures [129].

The consistent observations of differences between boundary layers over flat plates and curved surfaces indicate that wall curvature systematically affects the boundary layer. This has led some studies in the literature to adapt the logarithmic law to account for curvature effects using mixed layer arguments [144, 161].

1.2.5.2 Compressibility Effect

Compressibility effects in turbulent boundary layers are significant in high-speed flows where the fluid velocity is a significant fraction of the speed of sound. When the Mach number inside the boundary layer and the compressibility effects cannot be neglected as was done in the sections above, weaker hypotheses than the incompressibility of the boundary layer have to be used. Namely, Morkovin's hypothesis which states that compressibility effects on turbulent flows at reasonable Mach number—typically below 5—only affect the flow statistics though average density variations [113, 162] is used. Experimental data [1] and direct numerical simulations [65, 105, 108] consistently show that the main boundary layer statistics can be accurately predicted by extending the incompressible results to include variable

density. Note that the shock-boundary layer interaction is not discussed here, as it is somewhat outside the scope of this work, although it can significantly alter the boundary layer by affecting its thickness and increasing turbulence intensity due to shock-induced separation and reattachment.

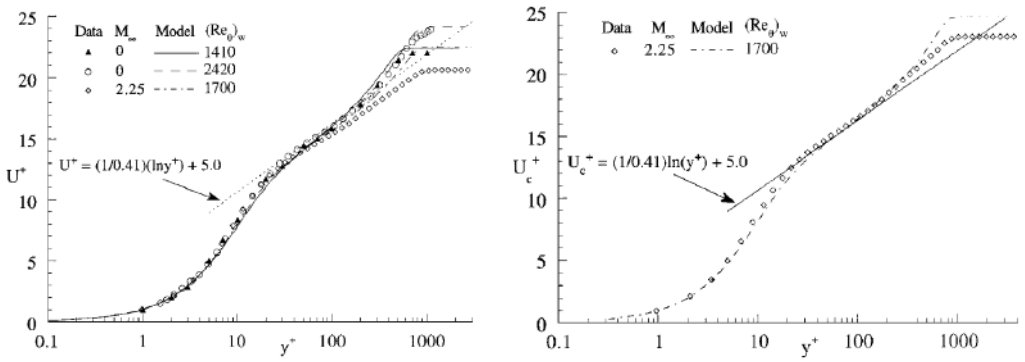

(a) Non-transformed normalized velocity profiles (b) Transformed normalized velocity profiles

Figure 1.8: Velocity profiles for turbulent boundary layers at different Mach numbers, comparing Direct Numerical Simulations data with van Driest model predictions; from So et al. [162].

To accurately predict the main boundary layer characteristics in compressible flows, a transformation can be applied to the self-similar equations derived for an incompressible boundary layer to account for density variations. This transformation is known as the Van Driest transformation [175]. For the logarithmic region, it is expressed as:

$$u_{VD}^{+} = \int_0^{u^+} \left(\frac{\rho}{\rho_w}\right)^{1/2} \mathrm{d}u^+. \tag{1.33}$$

The above transformation converts the boundary layer density fluctuations into modified velocity gradients. With this approximation, velocities in the logarithmic domain are described by a profile that accounts for density fluctuations in the following form:

$$u_{VD}^{+} = \frac{1}{\kappa} \ln y^+ + B_c, \tag{1.34}$$

where B_c is the intercept constant, typically around 5. This essentially means that the transformed velocity follows the same self-similar profile as the incompressible boundary layer. Although this transformation was originally designed for the logarithmic region, both experimental [75] and numerical [75, 162] observations show that the transformed velocity profile near the wall also recovers the linear region. Thus, near the wall, it can be written as:

$$u_{VD}^{+} = y^+. \tag{1.35}$$

This self-similar behavior is well illustrated in Fig. 1.8. On the left, the normalized velocity profiles without the Van Driest transformation show different behaviors depending on the Mach number. On the right, however, the application of the Van Driest transformation retrieves the log-law profile, demonstrating the aforementioned self-similar properties of the transformed velocity profiles.

1.2.5.3 Roughness effect

Generally speaking, surface roughness has a significant effect on boundary layer behavior by inducing an earlier transition from laminar to turbulent flow and by modifying velocity profiles in turbulent boundary layers. Only turbulent boundary layers are considered here, however, and the effect on the transition is not discussed. In this context, rough surfaces disrupt the flow near the wall, invalidating the concept of a linear sublayer. However, if the roughness extends over only a small fraction of the thickness of the boundary layer, then an inner region of the mean velocity profile is still present. In this region, a self-similar velocity profile can be observed. In practice, the same logarithmic profile observed for smooth walls is seen in the inertial part of the inner layer, but with a global velocity shift dependent on the roughness levels. This effect, observed since the works of Clauser [35] and Hama [67], is illustrated in Fig. 1.9 for different roughness levels. In this region, the velocity profile can be described by a modified logarithmic law equation with a velocity shift Δu^+:

$$u^+ = \frac{1}{\kappa} \ln\left(y^+\right) + c - \Delta u^+, \tag{1.36}$$

This equation can also be recast as:

$$u^+ = \frac{1}{\kappa} \ln\left(\frac{y^+}{k_o^+}\right), \tag{1.37}$$

where k_0^+ is the hydrodynamic roughness or roughness length, a scaled version of Nikuradse's sand grain roughness [120] k_s:

$$k_0^+ = k_s \mathrm{e}^{-\kappa(c+3.5)}.$$

The velocity shift Δu^+ is related to k_0^+ by

$$\Delta u^+ = \frac{1}{\kappa} \ln\left(k_0^+\right) + c$$

or to k_s by

$$\Delta u^+ = \frac{1}{\kappa} \ln\left(k_s^+\right) - 3.5.$$

When the roughness Reynolds number $k_g u_\tau/\nu$ is sufficiently high, the wall shear stress is dominated by pressure drag, and both k_0^+ and k_s can be treated as constant fractions of the geometric roughness k_g. This is the "fully rough" regime, which

is achieved when $k_s^+ > 50$. In addition, obtaining wall similarity requires that the roughness does not disrupt the logarithmic layer, which generally occurs when $\delta/k_g > 50$, as suggested by Jiménez [79].

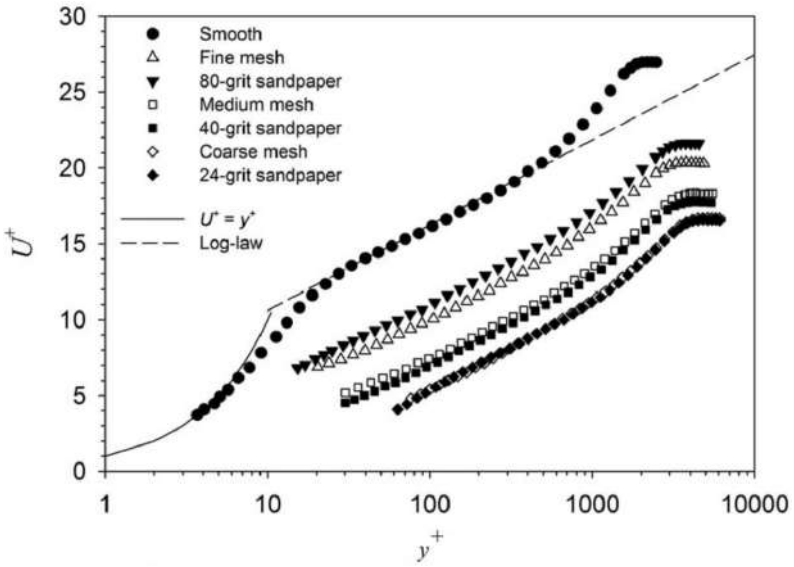

Figure 1.9: Non-dimensional velocity profiles of turbulent boundary layers for several roughness levels, from [52].

In terms of turbulence behavior, the influence of wall roughness on the turbulence stress fields in a boundary layer generally withstands the hypothesis of wall similarity [43]. Outside the immediate roughness layer, turbulence profiles and related quantities are similar in both smooth and rough wall boundary layers when stress levels are normalized with u_τ. Despite concerns that even small roughness could affect the entire flow, as outer region eddies often originate from the buffer layer, experiments have shown that turbulence stresses maintain wall similarity outside the inner region ($y/\delta \gtrsim 0.15$) when roughness is small and meets Jimenez's criterion of $\delta/k_g \leq 50$ [52, 53, 111].

1.2.5.4 Pressure Gradient effect

Pressure gradients can greatly affect the behavior and properties of a turbulent boundary layer. They can change the thickness of the boundary layer, the form of the velocity profiles, or the turbulence intensity. Understanding how pressure gradients affect a turbulent boundary layer is useful to accurately predict and model the flow dynamics in that region. In this context, here, only equilibrium boundary layers—in the sense of Devenport and Lowe [43], *i.e.* boundary layers that are self-preserving—are considered, which imposes some limitations on the conditions under which they can develop, particularly in terms of pressure gradient levels. This limitation, in turn, is useful to focus on the basic effects of pressure gradients without the added complication of non-equilibrium boundary layers.

To identify the conditions under which such equilibrium boundary layers are possible, the non-dimensional variables β and Λ are introduced:

$$\beta = \frac{\delta^*}{\tau_w}\frac{dP}{dx_1} \text{ and } \Lambda = \frac{x_1 - x_0}{U_e}\frac{\partial U_e}{\partial x_1}, \tag{1.38}$$

where β is the Clauser pressure gradient parameter, which is the ratio of the normal forces acting on the boundary layer ($\delta^* \frac{dP_e}{dx_1}$) to the wall shear stress (τ_w). δ^* is the displacement thickness $\delta^* = \int_0^\infty \left(1 - \frac{u}{U_e}\right) dy$, with δ the boundary layer thickness—*i.e.* the height of the boundary layer at which 99% of the edge velocity U_e is reached—and x_0 is the origin (in x_1 direction) of the boundary layer. Finally, Λ is known as the Castillo-George parameter. The first condition for obtaining equilibrium boundary layers with pressure gradients was formulated by Clauser [35] and states that the parameter β should be constant. But even when this condition is satisfied, developing turbulent boundary layers are generally not completely self-similar because of the independent behavior of the inner and outer scales. However, Clauser [35] argued that under this condition, two-dimensional boundary layers are approximately self-similar in the outer region. At higher Reynolds numbers, this approximate similarity includes most of the flow.

In addition, a self-similarity analysis of the momentum boundary layer equations shows that the presence of a pressure gradient can still be compatible with a self-similar behavior of the boundary layer. More details on this can be found in the study by Devenport and Lowe [43], based on earlier work by Rotta [146], Townsend [173] or Castillo and George [25]. These considerations show the existence of equilibrium boundary layers with pressure gradients when the parameter Λ remains constant with x_1. This implies that the edge velocity of the boundary layer must follow $U_e \propto |x_1 - x_0|^{-\Lambda}$ [43, 146]. However, this is not true for all values of Λ; if the boundary layer is slowed down enough, it will quickly separate, violating the assumptions underlying the initial boundary layer equations (1.13). In fact, Devenport and Lowe [43] states that for an equilibrium boundary layer to exist, Λ must be less than 1/3 in all cases, and possibly as low as 0.29 for flows with an adverse pressure gradient.

It should be noted also that studying this type of boundary layer is not an easy task and reproducing such boundary layers is challenging both experimentally and with simulations. Experiments often generate unwanted 3D effects that are difficult to separate from the studied effects. Simulations, on the other hand, are highly sensitive to the way the pressure gradient is imposed and to the initial conditions.

In general, an adverse pressure gradient (APG) slows down the mean flow near the wall, reducing wall friction. If the pressure gradient is strong enough, it can even create an inflection in the velocity profile, leading ultimately to flow separation. When comparing boundary layers with the same wall friction under different pressure gradients, as shown in Figure 1.10, the velocity profiles maintain self-similarity in the logarithmic region, if ignoring the wake region. In the logarithmic region, a stronger pressure gradient leads to a lower non-dimensional velocity, reflecting a velocity deficit at iso-friction level.

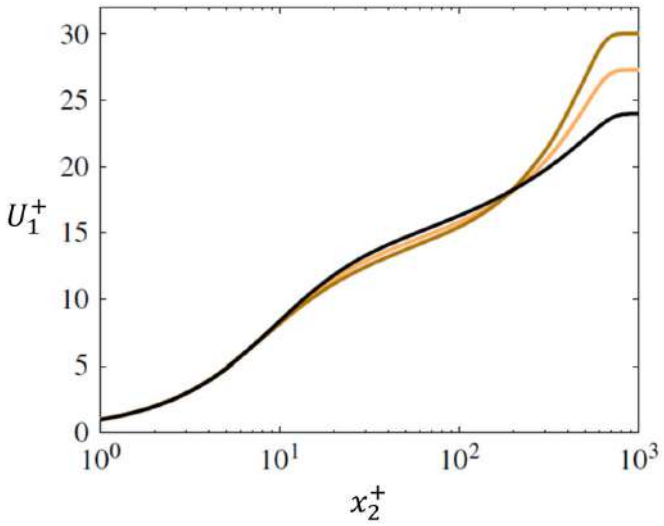

Figure 1.10: Comparison of velocity profiles for boundary layers with adverse pressure gradient with $\beta = 0$ (black), $\beta = 1$ (orange), and $\beta = 2$ (brown) for the same friction $Re_\tau \approx 700$ from Devenport and Lowe [43] and Bobke et al. [15].

In contrast, a favorable pressure gradient (FPG) accelerates the near-wall flow relative to the boundary layer edge, producing a more 'filled-in' velocity profile with less velocity deficit near the wall compared to the outer region. However, the wall friction increases because the FPG steepens the velocity gradient between the wall—at zero velocity— and the accelerated nearby flow.

For turbulent stresses, the following effects of pressure gradients are notable:

- Under an APG, absolute turbulence levels decrease as the pressure gradient increases, but normalized turbulence levels (u'^+, v'^+, w'^+ normalized in wall units) rise because the wall shear stress (τ_w) decreases. In cases of strong APGs, the location of turbulence production may also shift within the boundary layer.

- For an FPG, turbulence levels in the outer region decrease. In some situations, the FPG can even cause relaminarization of the boundary layer, although this phenomenon lies beyond the scope of this work.

After outlining the general equations of fluid motion and examining the specific case of boundary layer flow, the following section will introduce the framework studied and used during this thesis: Large Eddy Simulation (LES).

1.3 Large Eddy Simulation (LES)

1.3.1 Introduction to Computational Fluid Dynamics (CFD) and LES

As mentioned in the introduction, this thesis takes place in the context of computational fluid dynamics (CFD) to simulate numerically the behavior of turbulent flows. The general concept of CFD is to discretize the general flow equations presented in part 1.1 and solve them using numerical schemes to obtain an approximate solution to the problem considered.

As already introduced in part 1.1.4, the presence of turbulence renders the task of CFD methods particularly difficult. Indeed, the non-linear processes at stake, along with the wide range of time and length scales that need to be resolved are particularly challenging.

The CFD method consisting in solving the Navier-Stokes equations for all relevant scales, from the most energetic scale L, to the smallest scale identified by the Kolmogorov length η is called the Direct Numerical Simulation. This method however requires a very high resolution in time and space due to the magnitude of the ratio $\frac{L}{\eta}$, which scales with the Reynolds number of the setup as $Re^{3/4}$ [147]. This method is in practice not usable to simulate reasonable size problems, like turbomachinery setups.

To provide a solution to this scaling problem, several methods of approximation exist in CFD. More details on the different aspects of CFD can be found in the work of Hirsch [71] but two of them which are of interest to this thesis work are briefly acknowledged:

- Solving the Reynolds-Averaged Navier-Stokes (RANS) equations is the first option. This framework already mentioned in the sections above consists of only considering the time average of the solution directly. The solution f is split in a time average $\langle f \rangle$ and a fluctuating part f':

  $$f = \langle f \rangle + f'.$$

  The contribution of the fluctuating part is not directly solved but accounted for through the use of a turbulence model, representative of all the turbulent scales.

- The alternative solution considered here is Large Eddy Simulation (LES). The concept and details of LES are thoroughly discussed in the works of Pope [138], Lesieur et al. [101] and Sagaut [147], but the essential principles are summarized here. Large Eddy Simulation provides a solution for simulating turbulent flows by separating the fluid motion into two parts: large eddies and small eddies. Large eddies are the dominant flow structures in turbulence, contain the majority of the energy, and are explicitly resolved on the computational grid during the simulation. In contrast, small eddies, which represent finer-scale

features responsible for energy dissipation, are not directly resolved. Instead, their effects are approximated using a so-called sub-grid scale (SGS) model. The separation between the large—resolved—and small—modeled—eddies is in practice achieved through a filter in the wavenumber dimension cutting off the higher frequencies, as is visible in Fig. 1.11. The filtering operation is a spatial filtering taking the form:

$$\bar{f}(\underline{x},t) = \int f(\underline{x},t) G_\Delta\left(\underline{x} - \underline{x'}\right) dx', \tag{1.39}$$

with G_Δ the filter of size Δ. In practice, a definite explicit filter is not necessarily used by taking advantage of the grid sampling which acts as a filter.

Using LES, the filtered quantities $\overline{f}$ are solved for, while the remaining quantities $f^{sgs} = f - \overline{f}$ are the sub-grid scale quantities that need to be modeled.

For compressible flows, the Favre filtering is preferably used to account for density fluctuations. The Favre filtering is defined as:

$$\tilde{f} = \frac{\overline{\rho f}}{\bar{\rho}}. \tag{1.40}$$

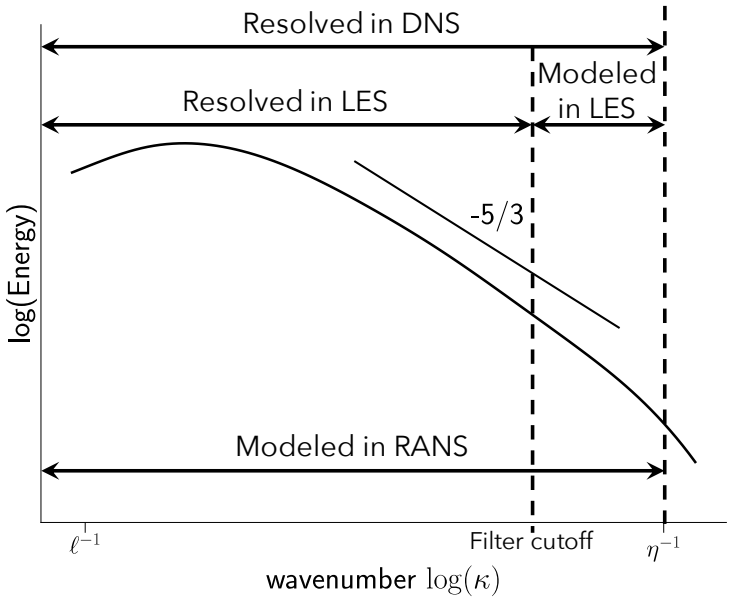

Figure 1.11: Schematic representation of the turbulent energy spectrum and its treatment in DNS, LES, and RANS.

Large Eddy Simulation can be seen as a trade-off between the precision offered by DNS and the cost-effectiveness of RANS simulations, which are extensively used for industrial applications. In DNS, all turbulent scales are resolved, as can be seen in Figure 1.11, while RANS simulations rely entirely on modeling all turbulence. LES is a hybrid approach as it directly resolves the energy-containing part of the turbulence and models the smaller, dissipative scales. This approach makes LES particularly advantageous as it proves to be superior to RANS in a number of scenarios involving large-scale unsteadiness or other complex phenomena such as laminar-to-turbulent transition [174] that are relevant to many turbomachinery applications.

1.3.2 LES equations

The equations governing Large Eddy Simulation (LES) are derived by applying the Favre filter to the Navier-Stokes equations (1.1), yielding:

$$\boxed{\begin{aligned} \frac{\partial \bar{\rho}}{\partial t} + \frac{\partial \bar{\rho}\widetilde{u}_i}{\partial x_i} &= 0, \\ \frac{\partial \bar{\rho}\widetilde{u_i}}{\partial t} + \frac{\partial}{\partial x_j}\left(\bar{\rho}\widetilde{u_i}\widetilde{u_j}\right) &= -\frac{\partial}{\partial x_j}\left[\bar{P}\delta_{ij} - \overline{\tau_{ij}} - \overline{\tau_{ij}}^{sgs}\right], \\ \frac{\partial \bar{\rho}\widetilde{E}}{\partial t} + \frac{\partial}{\partial x_j}\left(\bar{\rho}\widetilde{E}\widetilde{u_j}\right) &= -\frac{\partial}{\partial x_j}\left[\overline{u_i\left(P\delta_{ij} - \tau_{ij}\right)} + \overline{q_j} + \overline{q_j}^{sgs}\right]. \end{aligned}} \tag{1.41}$$

Where the terms can be broken down into three main parts in matrix form:

- the inviscid part,

$$\begin{pmatrix} \bar{\rho}\widetilde{u_i}\widetilde{u_j} + \bar{P}\delta_{ij} \\ \bar{\rho}\widetilde{E}\widetilde{u_j} + \overline{Pu_j}\delta_{ij} \\ \bar{\rho_k}\widetilde{u_j} \end{pmatrix},$$

- the viscous terms,

$$\begin{pmatrix} -\overline{\tau_{ij}} \\ -(\overline{u_i\tau_{ij}}) + \overline{q_j} \\ 0 \end{pmatrix},$$

- and the sub-grid scale terms,

$$\begin{pmatrix} -\overline{\tau_{ij}}^{sgs} \\ \overline{q_j}^{sgs} \\ 0 \end{pmatrix}.$$

For the resolved part of the viscous terms, once again these can be broken down with the following expressions of the stress tensor,

$$\begin{aligned}\overline{\tau_{ij}} &= \overline{2\mu\left(S_{ij} - \frac{1}{3}\delta_{ij}S_{ll}\right)} \\ &\approx 2\bar{\mu}\left(\widetilde{S}_{ij} - \frac{1}{3}\delta_{ij}\widetilde{S}_{ll}\right),\end{aligned} \tag{1.42}$$

with the strain rate tensor,

$$\widetilde{S}_{ij} = \frac{1}{2}\left(\frac{\partial\widetilde{u}_j}{\partial x_i} + \frac{\partial\widetilde{u}_i}{\partial x_j}\right). \tag{1.43}$$

The stress tensor can alternatively be expressed as:

$$\begin{aligned}\overline{\tau_{xx}} &\approx \frac{2\bar{\mu}}{3}\left(2\frac{\partial\widetilde{u}}{\partial x} - \frac{\partial\widetilde{v}}{\partial y} - \frac{\partial\widetilde{w}}{\partial z}\right), \quad \overline{\tau_{xy}} \approx \bar{\mu}\left(\frac{\partial\widetilde{u}}{\partial y} + \frac{\partial\widetilde{v}}{\partial x}\right) \\ \overline{\tau_{yy}} &\approx \frac{2\bar{\mu}}{3}\left(2\frac{\partial\widetilde{v}}{\partial y} - \frac{\partial\widetilde{u}}{\partial x} - \frac{\partial\widetilde{w}}{\partial z}\right), \quad \overline{\tau_{xz}} \approx \bar{\mu}\left(\frac{\partial\widetilde{u}}{\partial z} + \frac{\partial\widetilde{w}}{\partial x}\right) \\ \overline{\tau_{zz}} &\approx \frac{2\bar{\mu}}{3}\left(2\frac{\partial\widetilde{w}}{\partial z} - \frac{\partial\widetilde{u}}{\partial x} - \frac{\partial\widetilde{v}}{\partial y}\right), \quad \overline{\tau_{yz}} \approx \bar{\mu}\left(\frac{\partial\widetilde{v}}{\partial z} + \frac{\partial\widetilde{w}}{\partial y}\right)\end{aligned}$$

The filtered heat flux is in turn,

$$\begin{aligned}\overline{q_i} &= -\bar{\lambda}\overline{\frac{\partial T}{\partial x_i}} \\ &\approx -\bar{\lambda}\frac{\partial\widetilde{T}}{\partial x_i}\end{aligned} \tag{1.44}$$

The sub-grid terms for their part are expressed as follows:

- The subgrid-scale Reynolds stress tensor is

$$\overline{\tau_{ij}}^{sgs} = -\overline{\rho}(\widetilde{u_i u_j} - \widetilde{u}_i\widetilde{u_j}), \tag{1.45}$$

- The subgrid-scale heat flux vector is

$$\overline{q_i}^{sgs} = \bar{\rho}\left(\widetilde{u_i E} - \widetilde{u}_i\widetilde{E}\right) \tag{1.46}$$

1.3.3 SGS models

The sub-grid scale terms presented previously in equations (1.45) and (1.46) need to be modeled to provide closure to the LES equations (1.41). This is applied with the Boussinesq assumption for the Reynolds stress tensor:

$$\overline{\tau_{ij}}^{sgs} = 2\bar{\rho}\nu_{sgs}\left(\widetilde{S}_{ij} - \frac{1}{3}\delta_{ij}\widetilde{S}_{ll}\right), \tag{1.47}$$

where ν_{sgs} is a subgrid-scale viscosity. For the heat diffusion flux, a sub-grid scale thermal conductivity λ_{sgs} is introduced:

$$\overline{q_i}^{sgs} = -\lambda_{sgs}\frac{\partial \widetilde{T}}{\partial x_i}, \tag{1.48}$$

and defined as

$$\lambda_{sgs} = \frac{\mu_{sgs}\overline{C_p}}{\mathrm{Pr}_{sgs}}. \tag{1.49}$$

The parameters of the models are then reduced to the choice of $\nu_{sgs} = \frac{\mu_{sgs}}{\overline{\rho}}$ and Pr_{sgs}. For the SGS Prandtl number, the assumption of a constant value (close to 0.6) can be made and give satisfactory results. The subgrid-scale viscosity ν_{sgs} is for its part the focus of the following sections.

1.3.3.1 Near wall behavior of the SGS models

First, a focus on the appropriate near-wall behavior expected from a sub-grid scale model appears necessary in the context of this thesis which focuses on wall-bounded flows. Accurate representation of the near-wall turbulent behavior by the SGS model is critical to ensure reliable results in such cases. Near walls, the flow is dominated by viscous effects that effectively dampen turbulent fluctuations, causing the Reynolds stress to tend to zero. The literature on this topic is well established and supported by numerical observations [30], suggesting that the Reynolds stress should behave like y^3 as the wall-normal distance y approaches zero.

This expected behavior can be explained by simple considerations on an incompressible boundary layer over a flat surface. In this case, the dominant turbulent contribution is expected to be $\widetilde{uv}$ where u and v are the streamwise and wall-normal velocity components respectively [147]. The velocity components can be expanded at the limit $y \to 0$:

$$\begin{aligned} u &= u_1 y + u_2 y^2 + \mathcal{O}(y^3) \\ w &= w_1 y + w_2 y^2 + \mathcal{O}(y^3), \end{aligned}$$

where u_1, u_2, w_1 and w_2 are functions of space (x and z) and time. The incompressibility assumption gives:

$$-\frac{\partial v}{\partial y} = \frac{\partial u}{\partial x} + \frac{\partial w}{\partial z} = \left[\frac{\partial u_1}{\partial x} + \frac{\partial w_1}{\partial z}\right] y + \mathcal{O}(y^2)$$

Integrating this last equation allows to write:

$$\begin{aligned} u &= u_1 y + u_2 y^2 + \mathcal{O}(y^3) \\ v &= v_2 y^2 + \mathcal{O}(y^3) \\ w &= w_1 y + w_2 y^2 + \mathcal{O}(y^3), \end{aligned} \tag{1.50}$$

with v_2 a function of x, z and time as well. When computing $\widetilde{uv}$, it yields

$$\widetilde{uv} \sim \widetilde{v_2 u_1 y^3 + \mathcal{O}(y^4)} = \mathcal{O}(y^3)$$

This demonstrates that near the wall, the Reynolds stress is predominantly influenced by terms varying with y^3.

As mentioned above, the subgrid-scale eddy viscosity is related to the Reynolds stress by the equation (1.47). The behavior of the strain rate tensor, $\widetilde{S_{ij}}$, can be shown using relations (1.50) to follow $\mathcal{O}(1)$. This results in the subgrid-scale viscosity exhibiting the commonly accepted scaling near solid boundaries of

$$\boxed{\nu_{sgs} \sim y^3}. \tag{1.51}$$

Following the discussion on the theoretical behavior expected from a sub-grid scale (SGS) model near solid boundaries to accurately capture the physical behavior of the flow, the next section provides an overview of several commonly used SGS models that are available in the context of this thesis:

- the Smagorinsky model [158],
- the Wall Adapting Linear Eddy (WALE) model [115],
- the Sigma model (σ model) [118].

The governing equations of each model are detailed, along with the near-wall behavior they induce.

1.3.3.2 The Smagorinsky model

The Smagorinsky model [158] is a historical model that has been extensively used over the years. Smagorinsky proposed a model where the eddy viscosity depends on a length scale that is proportional to the filter size Δ, and is defined as $\ell = C_s\,\Delta$, which leads to the following sub-grid scale viscosity

$$\nu_{sgs} = (C_S\Delta)^2 \sqrt{2\widetilde{S}_{ij}\widetilde{S}_{ij}}, \tag{1.52}$$

where Δ is the filter size of the model (related to grid spacing in practice), $\widetilde{S}_{ij}$ is the filtered strain rate tensor defined by Eq. (1.43), and C_s is a constant of the model known as the Smagorinsky constant, often taken with the value of $C_s = 0.18$ calibrated for isotropic homogeneous turbulence.

The Smagorinsky model assumes that energy is transferred from the large eddies to the smallest turbulent structures, which only dissipate energy without any other transfer or backscatter—*i.e.*, transfer from the smallest scales to larger structures [135]. The Smagorinsky model is simple and computationally inexpensive, making it particularly attractive for large-scale simulations. However, this SGS model has several limitations. First, it relies on a single model constant that can be adjusted but is generally not capable of correctly representing all turbulent flows. To avoid having to define a single value of C_s for the whole domain, an altered version of the Smagorinsky model also exists and is known as the dynamic Smagorinsky model.

As proposed by Germano et al. [59], the subgrid-scale viscosity of the dynamic Smagorinsky model becomes

$$\nu_{sgs} = (C_{S_D}\Delta)^2 \sqrt{2\widetilde{S}_{ij}\widetilde{S}_{ij}}, \tag{1.53}$$

with the only difference with the classical Smagorinsky model being that C_{S_D} is not a constant anymore but this time computed within the simulation. This parameter can be evaluated on the computational grid as proposed by Lilly [102]:

$$C_{S_D}^2 = \frac{1}{2}\frac{L_{ij}M_{ij}}{M_{ij}M_{ij}}, \tag{1.54}$$

with the tensors L_{ij} and M_{ij} defined as

$$M_{ij} = \hat{\Delta}^2\sqrt{2 < \tilde{S}_{ij} >< \tilde{S}_{ij} >} < \tilde{S}_{ij} >; \quad L_{ij} =< \widetilde{u}_i >< \tilde{u}_j > - < \widetilde{u}_i\tilde{u}_j >,$$

where the notion of *test* characteristic length is introduced $\hat{\Delta}$, defined as the cubic root of the volume of all the neighboring cells of the current cell. With this dynamic procedure, a single model constant doesn't need to be user-defined anymore. It does however come at the cost of added complexity to the model.

A notable feature of the Smagorinsky model is that the turbulent viscosity does not vanish for laminar flows, which means that the model can be over-dissipative in inhomogeneous or anisotropic flows and transitional or laminar flows [138, p.602]. The model also assumes isotropy in subgrid dissipation—*i.e.*, in the transfer of energy to the dissipative scales—and thus may be over-dissipative in anisotropic regions.

In terms of near-wall behavior, following the argument developed in section 1.3.3.1 that $\widetilde{S_{ij}} \underset{y\to 0}{\sim} \mathcal{O}(1)$, equations (1.52) or (1.53) imply that $\nu_{\text{smago}} \sim \mathcal{O}(1)$ if the grid size Δ is assumed to have a negligible effect on the variations of ν_{sgs}. This indicates that this model predicts a non-zero subgrid scale viscosity at the walls, which is not the expected physical behavior in the context of LES.

1.3.3.3 WALE model

The Wall-Adapting Local Eddy-Viscosity (WALE) [115] sub-grid scale model was specifically designed to address the shortcomings of other SGS models near walls, especially the Smagorinsky model. The WALE model is specifically formulated to adapt near walls, providing a better representation of turbulence in the near-wall region where the Smagorinsky model tends to over-dissipate energy. The model computes eddy viscosity locally based on the filtered velocity field, making it sensitive to local flow structures.

The WALE model was developed with the introduction of an operator based on the traceless symmetric part of the squared velocity gradient, which is the tensor given by:

$$s_{ij}^d = \frac{1}{2}\left(\tilde{g}_{ij}^2 + \tilde{g}_{ji}^2\right) - \frac{1}{3}\,\tilde{g}_{kk}^2\,\delta_{ij}, \tag{1.55}$$

with, $\widetilde{g}_{ij} = \frac{\partial u_i}{\partial x_j}$ and $\widetilde{g}_{ij}^2 = \widetilde{g}_{ik}\widetilde{g}_{kj}$.

With this operator, the sub-grid scale viscosity model is constructed as follows,

$$\nu_{sgs} = (C_w\Delta)^2 \frac{(s_{ij}^d s_{ij}^d)^{3/2}}{(\widetilde{S}_{ij}\widetilde{S}_{ij})^{5/2} + (s_{ij}^d s_{ij}^d)^{5/4}}, \tag{1.56}$$

with the constant of the model being $C_w = 0.5$.

This wall model recovers proper behavior near the walls when compared to the Smagorinsky model. Using relations (1.50) the operator s_{ij}^d can be shown to behave as $\mathcal{O}(y)$ near walls. Recalling the expression of the SGS model (1.56) and the fact that $\widetilde{S}_{ij} \sim \mathcal{O}(1)$, the correct behavior of $\nu_{\text{wale}} \sim \mathcal{O}(y^3)$ is obtained. In addition to that feature, this model is local and is designed to handle transitional problems and boundary layer flows.

1.3.3.4 The Sigma model (σ model)

The Sigma [118] subgrid-scale model is another approach to modeling turbulence. Like the WALE model, it was designed to address some of the limitations of traditional models such as the Smagorinsky model. The Sigma model is formulated to better capture the anisotropic nature of turbulence, especially in complex flows. To this end, it is designed to produce zero eddy viscosity for any two-dimensional or two-component flow, as well as for axisymmetric and isotropic compressions and expansions. It is also designed to capture the correct behavior in near-wall flows.

The Sigma model is based on the singular values of the filtered strain rate tensor $\widetilde{g}_{ij}$, which provides a measure of the local deformation rate. The singular values are denoted $\sigma_1 \geq \sigma_2 \geq \sigma_3 \geq 0$ and are defined as the square roots of the eigenvalues of the matrix $\mathrm{G} = g^t g$, which are $\lambda_1 \geq \lambda_2 \geq \lambda_3 \geq 0$.

With these singular values, the viscosity model is built as such,

$$\nu_{sgs} = (C_\sigma\Delta)^2 \frac{\sigma_3(\sigma_1 - \sigma_2)(\sigma_2 - \sigma_3)}{\sigma_1^2}, \tag{1.57}$$

with the constant $C_\sigma = 1.5$ of the model.

This model, like the WALE model, has the property of vanishing near solid boundaries with the correct scaling. This can be verified in that case by recalling that the subgrid-scale viscosity ν_{sigma} is constructed from the singular values σ_i of the matrix $G = g^t g$. It can be shown that the eigenvalues of this matrix, using the expansion (1.50), obey the following scaling [118]:

$$\begin{aligned}\lambda_1 &= \mathcal{O}(1)\\ \lambda_2 &= \mathcal{O}(y^2)\\ \lambda_3 &= \mathcal{O}(y^4),\end{aligned}$$

with the convention $\lambda_1 \geq \lambda_2 \geq \lambda_3$. This naturally leads to the scaling of the singular values as $\sigma_1 = \sqrt{\lambda_1} = \mathcal{O}(1)$, $\sigma_2 = \sqrt{\lambda_2} = \mathcal{O}(y)$, and $\sigma_3 = \sqrt{\lambda_3} = \mathcal{O}(y^2)$. Consequently, recalling the SGS model definition (1.57), the near-wall scaling of $\nu_{\text{sigma}} \sim \mathcal{O}(y^3)$ is obtained. This model also has the interesting property of vanishing in various laminar flow configurations (pure shear, pure rotation, pure dilatation/contraction) where no subgrid scale activity is expected.

Chapter 2

Wall modeling for Large Eddy Simulation

2.1 Motivation for wall modeling

As presented in Chapter 1, large eddy simulation is a scale-resolving computational fluid dynamics technique that has become essential for investigating and understanding time-dependent, complex, multi-scale flows. LES provides fine-scale details of the turbulent structures and dynamics within fluid flows while being much less expensive than direct numerical simulations. This can be achieved by directly simulating only the largest and most energetic turbulent scales while relying on models to represent the effects of the smallest scales.

Special consideration, however, must be given to the flow developing near solid boundaries. In this region, quasi-streamwise vortices dominate the near-wall flow. These vortices scale with the viscous length $\delta_\nu = \nu/u_\tau$ [138], meaning they decrease in size as the Reynolds number—and thus the friction velocity—increases. Several studies have estimated the grid requirements for performing LES of wall-bounded flows [29, 33, 187]. Since LES must resolve all the most energetic scales, it imposes quite restrictive conditions on the number of grid points needed. In practice, wall-resolved large eddy simulations (WRLES) typically use a grid resolution of approximately $\Delta y^+ \sim 1$ near walls to capture near-wall dynamics accurately. Here, $y^+ = y\frac{u_\tau}{\nu}$ represents the normalized wall distance, using the notations introduced in Chapter 1. The latest estimate by Yang and Griffin [187] states that the number of grid points required scales with $\mathrm{Re}_{L_x}^{1.86}$, where $\mathrm{Re}_{L_x} = \frac{U_e L_x}{\nu}$ is the Reynolds number, U_e is the freestream velocity, L_x is the streamwise length of the considered boundary layer, and ν is the kinematic viscosity. As a comparison, the number of points required for a direct numerical simulation of the same case is estimated by Yang and Griffin [187] to scale with $\mathrm{Re}_{L_x}^{2.05}$.

This rapid scaling of grid requirements, and consequently computational resources, can make LES prohibitively expensive for various scenarios. This is particularly true for complex, high-Reynolds-number cases, where near-wall refinement demands become excessively high. In contrast, managing grid refinement to a scale comparable to that used in the bulk flow is significantly more cost-effective. If the near wall region is not properly refined, however, not only turbulent structures but also gradients near the wall risk being poorly represented, as shown in Fig. 2.1. This under-resolution leads to inaccurate predictions of the wall flow, which is based on the velocity gradient at the wall $\tau_w = \mu \left.\frac{\partial \tilde{u}}{\partial y}\right|_0$. As a result, incorrect boundary conditions could be applied eventually resulting in a reduction of the overall accuracy of the simulation.

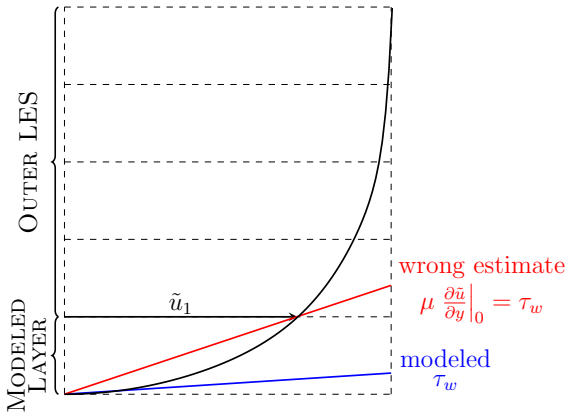

Figure 2.1: Schematic representation of wall stress model correction (adapted from [27]).

To address the computational challenges of performing Large Eddy Simulations (LES) of wall-bounded turbulent flows while preserving the accuracy of near-wall physics, wall models have been developed.

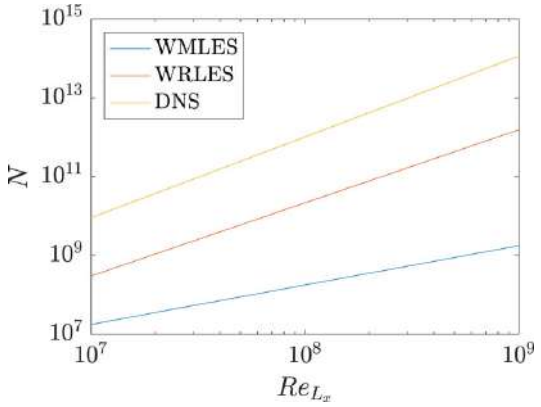

Figure 2.2: Number of points N required to perform the simulation of a flat turbulent boundary layer varying with the Reynolds number (from Yang and Griffin [187]).

These models provide the wall shear stress, and possibly the wall heat flux, based on simplified representations of the complex near-wall region. Instead of resolving the very fine turbulent scales directly at the wall—which would require an extremely refined grid—wall models approximate the influence of these small-scale structures on the larger-scale flow dynamics. The use of wall models allows to significantly reduce the grid point requirements, allowing it to scale with $\mathrm{Re}_{L_x}^{1}$ according to the estimate of Yang and Griffin [187], a substantial improvement compared over the wall-resolved approach. The evolution of grid point requirements with the Reynolds number for Direct Numerical Simulation (DNS), Wall-Resolved LES (WRLES), and Wall-Modeled LES (WMLES) is summarized in Fig. 2.2, highlighting the growing advantage of wall models as the Reynolds number increases. Compared to the fine wall resolution required by WRLES, wall models enable the use of significantly coarser meshes at walls, with a typical resolution in the range of $10 \leqslant \Delta y^+ \leqslant 500$. Figure 2.3 illustrates the contrast in grid resolution between the WRLES and WMLES of even a simple boundary layer at Reynolds number $\mathrm{Re}_b = 20\,000$ based on the boundary layer height δ and bulk velocity U_b.

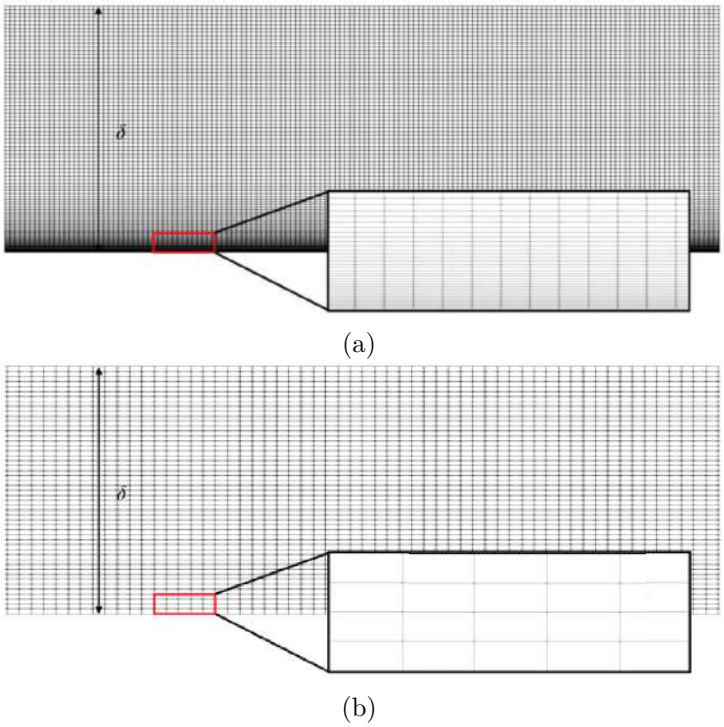

Figure 2.3: Typical grids employed to perform a (a) WMLES and (b) WMLES respectively of a flat plate boundary layer (adapted from Fan et al. [51]).

In practice, wall models are implemented at the boundary conditions of the computational domain to bridge the gap between the wall and the first computational grid point in the LES. The most common type of wall model is the wall stress model. Their purpose is to provide the wall shear stress by solving simplified equations in the near wall region. This approach then allows the closure of the balance equations for the LES equations at the wall using in-flow properties provided by the LES as illustrated in Fig. 2.4. This allows to provide the proper boundary conditions on coarse grids as illustrated in Fig. 2.1. As implied in Fig. 2.4, most wall models require iterations to converge and accurately predict the wall fluxes. Once this is achieved, the wall fluxes are fed back to the LES solver. It is worth noting that the LES solver typically predicts a nonzero wall velocity, u_{slip}, that cannot be corrected due to the Neumann condition already imposed at the boundary. To simultaneously enforce a Dirichlet condition for no slip at the wall, other constraints must be relaxed. This can be achieved, for example, by adjusting the sub-grid scale (SGS) viscosity within the wall cells to accommodate both conditions [78]. For isothermal conditions, a wall model equation for energy is used alongside the momentum equations to provide the heat flux at the wall q_w in addition to the wall stress τ_w.

More details on the actual implementation of such a model can be seen in Fig. 2.5, which illustrates the retrieval of LES data at the first off-wall point. This figure shows how the wall model gathers information from the LES at these nodes to compute wall fluxes and then sends these computed wall fluxes back to the wall nodes, represented on a simple 2D mesh.

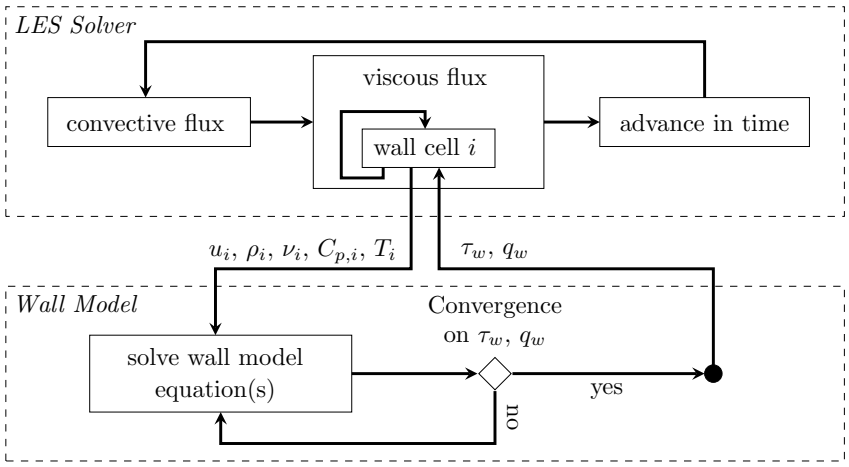

Figure 2.4: Schematic representation of the interactions between an LES solver and a wall stress model (adapted from [24]).

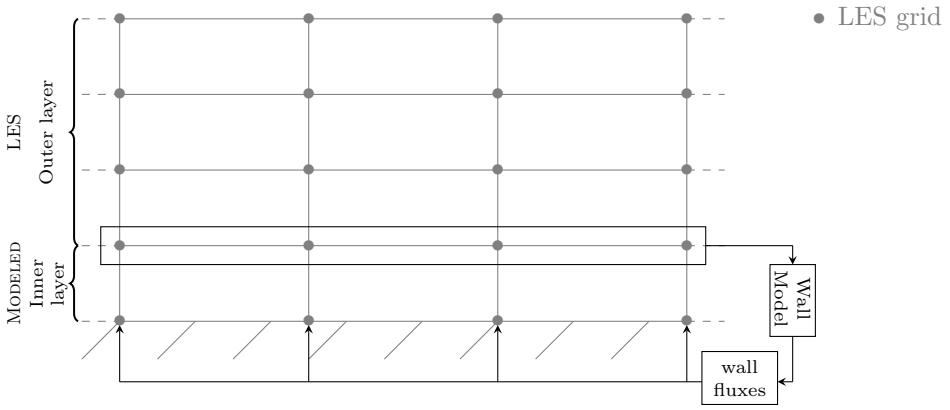

Figure 2.5: Schematic representation of wall stress model on a simple LES grid (adapted from [58]).

To enable optimal operation of the wall model, the input data should be extracted from the inertial zone of the boundary layer where $y^+ \geqslant 50$ and $y/\delta \leqslant 0.1$. This region exhibits self-similarity and contains turbulent structures large enough to avoid under-resolution issues. Additionally, in this range of distance to the wall, a sufficient number of structures are present to allow for statistically representative sampling and to capture their full lifecycle between iterations. This approach enables consideration of average effects only [133] and aligns with the RANS treatment of the boundary layer equations (see Chapter 1) commonly used in wall modeling.

2.2 Model Types

Over the past decades, several types of wall models have been proposed and tested. Several literature reviews that provide a more general understanding of the models are available [18, 96, 133]. The main types of wall models considered in this work are algebraic models and models based on the numerical solution of ordinary differential equations (ODEs). More details on these types of models are provided in the next two sections. The last section presents other wall models that do not fit into the aforementioned groups.

2.2.1 Algebraic models

Algebraic models are among the simplest and most commonly used wall models in LES. These models use algebraic expressions to estimate wall shear stress with local flow quantities such as velocity, density, and viscosity. The primary strength of algebraic models is computational efficiency since they require only the local inversion of simple relations.

Algebraic models are based on the principle of boundary layer self-similarity. As described in part 1.2.2, this self-similarity allows the calculation of wall fluxes based on the knowledge of the flow state at any distance from the wall, provided it is within the inner part of the boundary layer. This method has been used for decades since the pioneering works of Deardorff [41] and Schumann [153].

The simplest and most commonly used algebraic wall models are based on the logarithmic law of the wall, as given by equation (1.24), or two-layer equations (1.18) and (1.24). These models rely on data from a probe point in the LES, typically the first off-wall point, see Fig. 2.5. The appropriate equation is then inverted depending on the wall distance:

$$\boxed{\begin{cases} u^+ = y^+, \text{ for } y^+ < 11.5 \\ u^+ = \frac{1}{\kappa}\ln(y^+) + c, \text{ for } y^+ > 11.5 \end{cases}} \tag{2.1}$$

Given the probing distance y_p, the probed velocity U_p, as well as the density ρ_w and viscosity ν_w at the wall, the relation can be inverted to give the friction velocity u_τ. This process requires an initial guess for the non-dimensional wall distance y_p^+. Since the wall distance depends on the friction velocity u_τ, which is being solved for, the solution process is necessarily iterative until convergence on the friction velocity is achieved. Once the friction velocity u_τ is determined, it directly provides access to the wall friction $\tau_w = \rho_w u_\tau^2$, which can then be fed back into the LES computation at the boundary condition, as illustrated in Fig. 2.5. In practice, the distance to the wall y_p at which the LES data are used is fixed based on the mesh and solver used. The probed LES data are instantaneous values used to invert the model's equations for each wall cell, as shown in Fig. 2.4. This process produces a solution for the wall fluxes that is local and varies at each iteration, as the wall model is solved at each LES solver iteration.

Similar wall laws can be derived for isothermal wall conditions using the self-similar temperature profiles presented in part 1.2.4. The simplest wall model that can be used for the energy equation is defined as follows:

$$\boxed{\begin{cases} \theta^+ = \Pr y^+, \text{ for } y^+ < 11.5, \\ \theta^+ = \frac{\Pr_t}{\kappa} \ln(y^+) + c', \text{ for } y^+ > 11.5. \end{cases}} \tag{2.2}$$

These equations can be used identically to the wall model equations for velocity to compute the wall heat flux, $q_w = \rho_w C_{p,w} u_\tau T_\tau$. Using u_τ computed from the wall stress model, this requires evaluation of $T_\tau = (T_w - T_p)/\theta^+$ where T_p is the probed temperature within the LES field and T_w is the isothermal wall temperature.

Although relatively simple, algebraic models often provide reasonable accuracy for a range of flow conditions at considerably low computational cost, which explains their popularity in practical LES applications [23, 114]. However, their performance may be degraded in complex flow scenarios with strong pressure gradients, separation, or three-dimensional effects—examples where more sophisticated models may be required [23, 133, 183].

Over the years, many studies have refined the simplest algebraic wall models. Among these, the models by Reichardt [143] and Spalding [164] can be noted. The purpose of these laws is to extend the validity of the model to the entire inner region, including the buffer layer—a region not usually well modeled by the standard wall laws. These refined models provide a better representation of the buffer layer and correct the frequent underestimation of friction that is characteristic of standard wall laws.

For compressible flows, as described in part 1.2.5.2, the Van Driest transformation can be applied (Equations (1.34) and (1.35)), taking advantage of the fact that the transformed velocity profile adheres to the canonical self-similar profile. Wall laws using this transformation provide accurate boundary conditions for compressible LES and have been successfully used by Rotta [145], Huang and Coleman [74], and Bocquet et al. [16], among others.

Adapted algebraic laws can also be used to account for the effects of wall roughness in wall models, as explained in part 1.2.5.3. Although wall roughness complicates near-wall physics by introducing perturbations to the flow in the viscous layer, self-similarity of the velocity profile in the inertial layer can still be observed. In general, roughness effects can be accounted for by a modified logarithmic law, which induces a global velocity shift in the inertial layer depending on the roughness level. This velocity shift, denoted Δu^+, is directly expressed in Eq. (1.37). This equation can also be recast in the form:

$$u^+ = \frac{1}{\kappa} \ln\left(\frac{y^+}{k_0^+}\right), \tag{2.3}$$

explicitly linking the velocity profile to geometric roughness through the hydrodynamic roughness or roughness length k_0^+.

Additional research by Afzal [3, 4], Skote and Henningson [157], and Patel [128] incorporates pressure gradient effects with the introduction of the non-dimensional pressure gradient

$$p^+ = \frac{\nu_w}{\rho_w u_\tau^3} \frac{\mathrm{d}\bar{P}}{\mathrm{d}x_1}.$$

These wall laws are strictly valid for constant p^+, which can be too restrictive. As discussed in part 1.2.5.4, self-similarity can be achieved for constant values of the β parameter, a less restrictive condition. These wall laws also often do not significantly improve LES results compared to the classical wall laws as demonstrated in studies like those of Lee and Moser [99] and Skote and Henningson [157]. Moreover, these laws are not valid for favorable pressure gradients ($p^+ < 0$), which raises issues for both physical accuracy and numerical implementation, especially because in an unsteady LES solver localized negative pressure gradients cannot be avoided. In addition, boundary layers can detach under adverse pressure gradients, imposing zero wall friction and thus rendering the non-dimensional velocity given by $u^+ = u/u_\tau$ undefined. These drawbacks can be overcome by using a scaling defined with the pressure gradient, as suggested by Patel [128] and Skote and Henningson [157], using

$$u_p = \left(\frac{u_w}{\rho_w} \frac{\mathrm{d}\bar{P}}{\mathrm{d}x_1} \right)^{1/3} = p^{+1/3} u_\tau.$$

With this, according to Skote and Henningson [157] and Gungor et al. [66], wall laws can be derived as follows:

$$\frac{U_1}{u_p} = \begin{cases} \frac{1}{2} y_p^2 + \gamma^2 y_p \text{ in the linear sublayer} \\ \frac{1}{\kappa} \left(2\sqrt{\gamma^2 + y^p} + \gamma \ln y_p \right) - \frac{2\gamma}{\kappa} \ln \left(\sqrt{\gamma^2 + y_p} + \gamma \right) + C \text{ in the inertial layer} \end{cases} \tag{2.4}$$

where U_1 is the streamwise velocity defined in part 1.2.1, and the usual notations $y_p = y u_p/\nu_w$ and $\gamma = u_\tau/u_p$ are used. Although these wall laws are defined for regions of flow separation, they are not applicable for zero-pressure gradients. To overcome this limitation, Shih et al. [155] introduced a wall law using a scaling based on the friction and the pressure gradient combined $u_c = u_\tau + u_p$ with $u_p = (\nu_w/\rho_w) \left| \frac{\mathrm{d}P}{\mathrm{d}x_1} \right|$. This approach ensures that u_c is always defined and strictly positive, making the wall law valid for both flow separation ($u_\tau = 0$) and zero pressure gradient ($u_\tau = 0$) where it aligns with the classical log law. However, despite its broader applicability, this model does not always agree with typical observations in boundary layers under favorable pressure gradients [26].

2.2.2 Ordinary Differential Equations (ODE) models

Another class of models that is commonly found in the literature relies on solving a set of ordinary differential equations near the walls instead of the LES equations this time. Typically, they use the Reynolds-Averaged Navier-Stokes (RANS)

boundary layer equations (1.9), which are numerically solved on a dedicated near-wall mesh. At each solver iteration, the RANS boundary layer equations are solved using the given LES values and a no-slip wall condition, as illustrated schematically in Fig 2.6. This step provides the velocity and temperature profiles in the near-wall mesh, thus allowing the calculation of the wall fluxes, τ_w and q_w, from an estimate of the velocity and temperature gradients at the wall. Essentially, these models are still wall stress models that work as described in Fig. 2.5, but they require a dedicated mesh and solve differential equations directly.

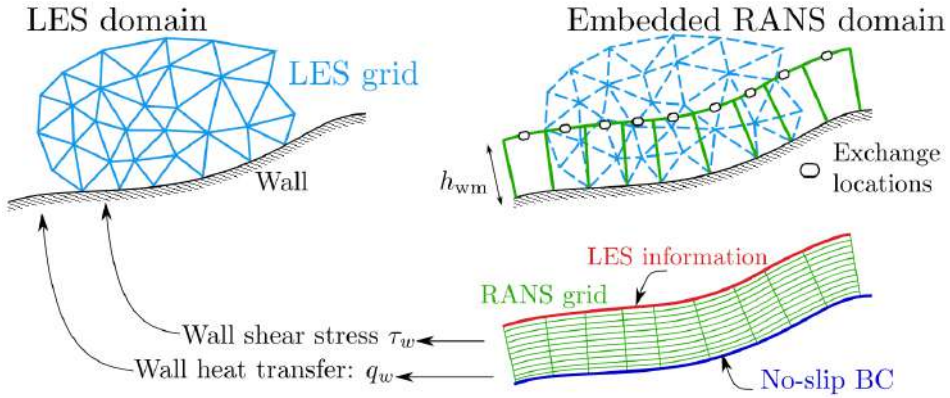

Figure 2.6: Illustration of a full 3D RANS wall model in an unstructured LES solver, from Larsson et al. [96]

Solving the full set of 3D equations (1.9) directly is the most comprehensive and complex approach to this kind of modeling. This method captures most of the physical phenomena relevant to wall-bounded flows, such as pressure gradients and convective fluxes. However, the difficulties of implementing a 3D model and including an embedded mesh in a LES solver, as shown in Fig. 2.6, are major drawbacks. Despite this complexity, the computational cost is still significantly lower compared to wall-resolved LES. This efficiency is mainly due to the larger grid sizes used near the wall in WMLES, which allows larger time steps and thus improves the overall performance. Although these models are complex, they are still used in the literature to explore advanced configurations in LES [18], as evidenced by studies such as those of Kawai and Larsson [84], Park and Moin [125, 126], Yang et al. [190], or Cho et al. [32].

As mentioned above, wall models based on the full 3D RANS equations are complex to implement and integrate into LES solvers. Consequently, simpler versions of these models are also frequently used in the literature. Initial simplifications typically involve assuming incompressibility and stationarity of the boundary layer and neglecting various 3D effects. This effectively approximates the boundary layer as developing over a flat surface. Incompressibility is also a less restrictive condition than it may seem. Indeed, it only requires the boundary layer to be incompressible, which is often the case since the velocity and Mach number in boundary layers are usually small. Under these assumptions, the formulation of the thin boundary layer

equations discussed in part 1.2.1 can be obtained, defined by the equations (1.13):

$$U_1\frac{\partial U_1}{\partial x_1}+U_2\frac{\partial U_1}{\partial x_2}+U_3\frac{\partial U_1}{\partial x_3}=-\frac{1}{\rho}\frac{\partial \overline{P}}{\partial x_1}-\frac{\partial \overline{u_1' u_2'}}{\partial x_2}+\nu\frac{\partial^2 U_1}{\partial x_2^2}$$
$$0=-\frac{1}{\rho}\frac{\partial \overline{P}}{\partial x_2}-\frac{\partial \overline{u_2'^2}}{\partial x_2}$$
$$U_1\frac{\partial U_3}{\partial x_1}+U_2\frac{\partial U_3}{\partial x_2}+U_3\frac{\partial U_3}{\partial x_3}=-\frac{1}{\rho}\frac{\partial \overline{P}}{\partial x_3}-\frac{\partial \overline{u_3' u_2'}}{\partial x_2}+\nu\frac{\partial^2 U_3}{\partial x_2^2}$$

A wall model solving these equations is significantly less complex than solving the full RANS system. However, it still captures important physical effects within the boundary layer, such as pressure gradient effects and the convective transport of momentum. This method has been used in numerous studies, including the early work of Balaras et al. [9] and, more recently, those of Cabot and Moin [23], Wang and Moin [180], and Benarafa et al. [11]. However, solving these equations still requires a mesh with 3D connectivity to compute the velocity and pressure gradients in all directions that appear in the equations, and this remains a significant constraint.

Consequently, further simplifications are often included in the literature to derive one-dimensional ODEs, that can be solved without integrating an embedded 3D mesh within the LES solver. The equations of the model can be solved numerically using a 1D mesh constructed within each cell adjacent to the wall boundaries, as depicted in Fig. 2.7. These simplifications are generally based on the concept of *equilibrium* which, as detailed in section 1.2.2, implies that the boundary layer exhibits self-similar behavior. The most widely used equilibrium TBLE models are based on the premise that the pressure gradient and convective terms in the equations (1.13) cancel out, resulting in the primary equation of the model:

$$\frac{\partial}{\partial y}\left((\mu+\mu_t)\frac{\partial U_1}{\partial y}\right)=0, \tag{2.5}$$

where μ is the viscosity of the fluid and μ_t is its turbulent counterpart, used to model the RANS Reynolds stress $\rho\frac{\partial \overline{u_1' u_2'}}{\partial y}$.

It should be noted that the integration of the equation (2.5) along the wall-normal direction, using usual turbulent eddy models for μ_t, leads to the logarithmic law. This may seem to reduce the usefulness of such methods in practice. However, by numerically solving the full boundary layer equations in the wall-normal direction—from the wall to the coupling or probing location with LES—these methods can simulate flows with spatially non-uniform properties within the first computational cell of the LES. Notably, they can accommodate spatial variations in turbulent viscosity or other complex flow properties that are not analytically integrable but remain solvable numerically. The model equation (2.5) is also valid throughout the entire inner boundary layer and can therefore be applied using a wide range of wall coupling distances. This is particularly beneficial in the buffer layer, where many algebraic models tend to poorly predict wall friction. Nonetheless, it is crucial to avoid using the wall model with a coupling point too close to the wall, even if

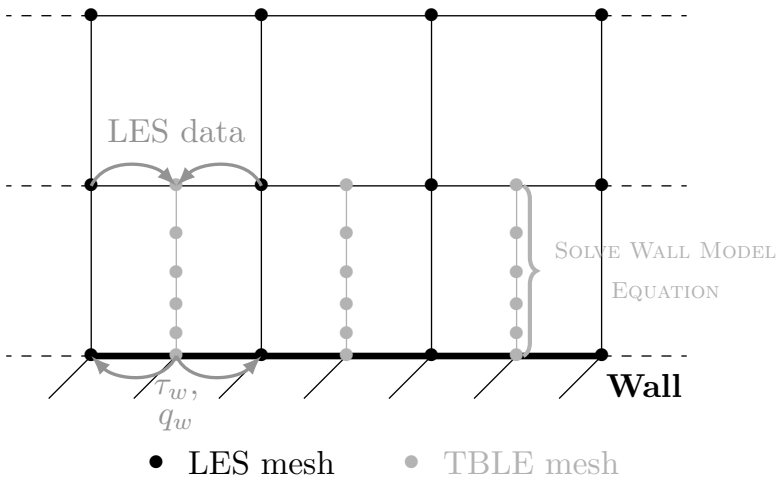

Figure 2.7: Schematic illustration of the implementation of a 1D ODE-based wall model within the first wall cell of an LES solver.

the model's expression is theoretically valid. This precaution should be taken to keep the grid resolution near the wall coarse enough to capture enough turbulent structure per iteration to remain coherent with the RANS equations, as discussed earlier in the introduction to chapter 2.

The primary advantage of such a model is that it provides a framework capable of incorporating more complex physical phenomena, such as compressibility, pressure gradients, and convective terms. This framework has been widely used in the literature over the years [16, 46, 83, 103, 180]. However, to maintain this framework, the inclusion of physical phenomena must be limited to 1D terms, thereby excluding any elements that require 3D connectivity, such as 3D gradients.

Finally, in several cases, the TBLE equation can still be integrated analytically, even when considering some complex phenomena. In such cases, a special class of models based on the TBLE equation is available in the literature. These models use the analytically integrated form of the equation, similar to algebraic laws, and require only numerical inversion to determine the wall fluxes. Such an approach avoids the complications of solving the TBLE on an embedded 1D mesh and minimizes the computational cost. These models are also able to account for pressure gradient effects to some extent, as well as thermal, roughness, and compressibility effects. Examples of models using integral forms of the TBLE equations include the works of Craft et al. [38], Suga et al. [165], Monfort et al. [112], and Catchirayer et al. [27]. These methods, however, are constrained by the requirement to obtain boundary layer equations that are analytically integrable. This in turn limits the range of physical effects that can be modeled and restricts the possible choices of turbulent viscosity models.

2.2.3 Other models

Having discussed the main approaches to wall-stress modeling in LES, alternative models that fall outside the categories already introduced are considered, specifically those that do not directly use RANS equations to relate wall stress to LES variables at some distance from the wall.

Artificial boundary condition models can be mentioned first. These models are based on applying the boundary conditions at some distance from the wall instead of imposing the fluxes directly at the wall. The intent is to impose accurate conditions at a location where the LES flow is correctly resolved—the location where the artificial boundary condition is applied. This approach is based on the premise that WMLES grids are in any case too coarse to accurately capture the inner boundary layer. Historical attempts to use these models include works by Baggett [8], Jimenez and Vasco [80], and Nicoud et al. [116], which reported mixed results, including issues such as artificial pressure fluctuations and transition regions. Recent efforts by Chung and Pullin [34], Inoue et al. [77], and Cheng et al. [31], among others, have further explored this approach using virtual wall boundary conditions. With these models, LES is performed up to a certain distance from the wall, which means that the inner boundary layer is not included in the LES configuration. Instead, it is addressed by solving a form of the TBLE equations discussed in part 2.2.2 to set the correct velocity at the virtual boundary. This method has shown success in turbulent channel flows and detached boundary layers over flat plates. However, applicability to more complex geometries remains unclear [18].

Another model of interest is the dynamic slip wall model of Bose and Moin [17]. This model attempts to provide more consistent boundary conditions to the LES than those using RANS equations. Traditional wall stress models use averaged but spatially unfiltered equations in conjunction with filtered LES variables to determine wall fluxes. In contrast, the dynamic slip model replaces the RANS equations with a filtered equation for the boundary condition that imposes a constraint on the filtered velocity at the wall. This model has demonstrated good performance in turbulent channel flows and simulations of the NACA 4412 airfoil configuration. It has also been further developed and analyzed in subsequent studies [7, 188]. However, a notable drawback of this method is that it formally permits transpiration through the wall, which may compromise mass conservation.

Beyond these models, Nicoud et al. [117] developed an approach based on control theory. In this method, wall friction is determined through an optimization process aimed at minimizing the difference between the resulting velocity profile and a predefined target profile. This approach is however computationally intensive and necessitates the assumption of a target velocity profile. This requirement implies that prior knowledge or assumptions about the simulated flow are needed, which can limit its applicability.

2.3 Wall Modeling Challenges

The use of wall models for LES presents its own set of challenges and difficulties. Broadly speaking, these can be divided into two categories: the inaccuracies of the wall model itself, and the difficulties associated with its coupling to the LES framework.

First, any wall model is designed to work within a range of flow conditions. Therefore, applying a model outside of these conditions can be a source of error. Wall models typically simplify or even neglect many physical phenomena, which means that errors are introduced and depend on how well the assumptions fit the real flow conditions. The magnitude of these errors then depends on the model itself as well as the application.

The second challenge is the integration of wall models into the LES framework. WMLES combines two frameworks that were not originally designed to interact seamlessly, namely RANS equations on one side and LES equations on the other. Ensuring a coherent and accurate interaction between the wall model and the LES is an important requirement to achieve reliable simulations.

2.3.1 Application limits and domain of validity of wall models

The use of any wall model for LES has to be considered with the set of conditions and assumptions applied in the derivation of the model—*i.e.* its approximate domain of validity. If applied outside of this range, the model may deviate due to a mismatch between its theoretical framework and the real flow conditions, which may lead to errors in the simulation.

The simplest wall models described in part 2.2 are based on the assumption of *equilibrium*, as introduced in part 1.2.2. In particular, most of the common models that make use of the logarithmic law of velocity profiles are based on the following assumptions:

- A fully turbulent boundary layer (high Reynolds number)
- Incompressibility of the boundary layer
- Stationarity of the boundary layer
- An essentially 2D boundary layer (neglecting 3D terms and gradients)
- Absence of pressure gradients

Many models have been derived based on the previous assumptions already presented in part 2.2, ranging from simple algebraic models to more complex equilibrium TBLE models.

Part 2.2 also includes models that have been developed to incorporate some physical phenomena that may be relevant, such as compressibility effects or streamwise pressure gradients. However, most of these models are still *equilibrium* models—*i.e.*, they assume that the structure of the boundary layer is self-similar along

its length. This is equivalent to the assumption that the shape and properties of the boundary layer do not vary as it develops downstream, which places strict limits on the physical phenomena that can be considered. In particular, the effects of pressure gradients have been studied and it is shown, as commented in part 1.2.5.4, that self-similar boundary layer conditions are preserved in the presence of a pressure gradient, provided that the boundary layer edge velocity depends on the downstream distance x according to a power law: $U_e \propto |x_1 - x_0|^{-\Lambda}$. There are some more constraints on the exponent Λ, namely that it should not exceed 1/3 for adverse pressure gradients.

In addition to these wall models, there are also variants of the TBLE wall models that deal with non-equilibrium conditions, such as those that consider the pressure gradient. Inner scaling using the pressure gradient in addition to friction is added in these models and is presented in part 2.2 [46, 155]. These models are theoretically capable of producing accurate results for non-equilibrium flows, including separated flows. However, these models still present several limitations. They notably assume a fully turbulent and stationary boundary layer while neglecting three-dimensional effects. These conditions are unlikely to be satisfied in separated boundary layers or flows approaching separation. Three-dimensional effects can actually become important in the presence of strong pressure gradients that lead to these conditions: as the velocity near the wall decreases when approaching separation conditions, the influence of spanwise dynamics becomes significant relative to the streamwise flow. At the same time, the Reynolds number is reduced near separated regions due to the decreased velocity, and the flow is unlikely to be fully turbulent. In addition, strong favorable pressure gradients can induce re-laminarization of the boundary layer, which also takes the model out of its validity range. Despite representing real improvements in terms of the range of applicability, these models are thus not free of some of the limitations associated with equilibrium wall models. In particular, the reliance of wall-models on local near-wall quantities may not be optimal, as recent work by Boxho et al. [19] showed that in separated or strongly adverse pressure gradient flows, wall shear stress correlates poorly with these quantities. This highlights the potential need for more sophisticated models that incorporate non-local information or account for history effects.

It is also worth pointing out that there are in the literature true non-equilibrium models-such as those either based on the full three-dimensional RANS equations (see for example hybrid RANS/LES methods [10, 119, 156, 168]) or models not using the RANS equations at all, such as the models of Nicoud et al. [117], Templeton et al. [170], Bose and Moin [17] or Elnahhas et al. [49]. These models aim to capture complex flow behavior without the traditional constraints of equilibrium assumptions. However, even these models are not free of a number of assumptions. In most cases typically, the boundary layer is assumed to be at least fully turbulent.

2.3.2 RANS/LES coupling

Having discussed the intrinsic difficulties in the construction and use of wall models in different flow configurations, attention must be paid to the difficulties associated with their incorporation into an LES framework. In the usual case, the coupling between the LES solver and the wall model involves many interactions

between the model and the inflow solver, as shown in Fig. 2.8. The first difficulty is the dichotomy between the LES equations on the one hand and the wall models, usually based on RANS equations, on the other. The LES equations take into account the dynamic and fluctuating nature of turbulence at larger scales, whereas the wall models based on RANS are designed around steady-state assumptions and time-averaged quantities. The potential incoherence between the time-averaged approach of the RANS models and the unsteady filtered nature of the LES equations is the main drawback of this approach and can lead to inaccuracies in the overall flow representation.

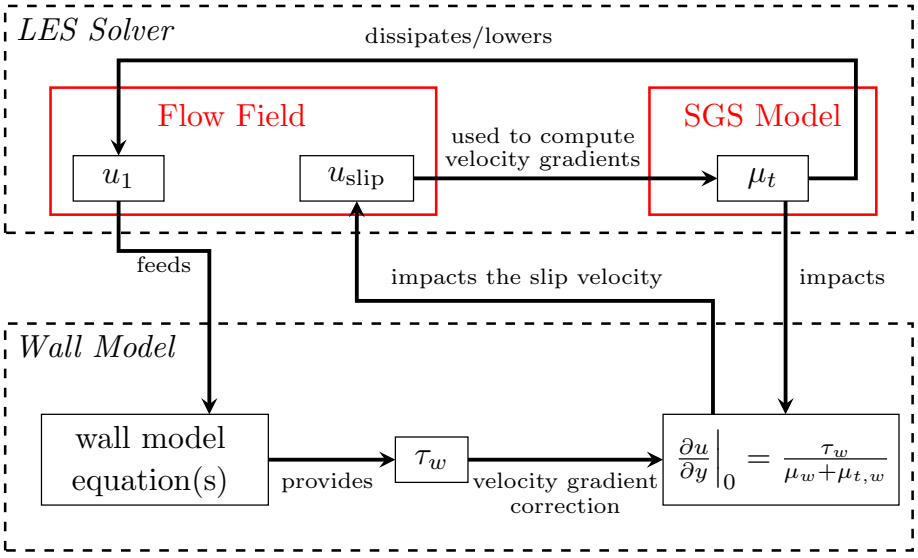

Figure 2.8: Schematic of the coupling between the wall model and the LES solver.

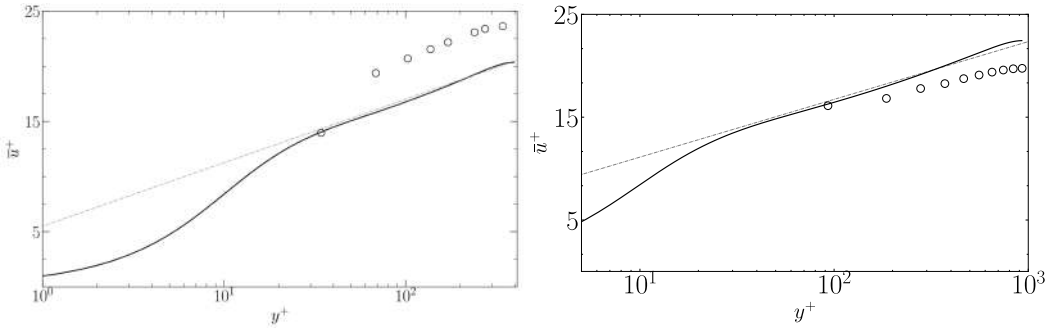

(a) $\mathrm{Re}_\tau = 395$, from Gelain [58]

(b) $\mathrm{Re}_\tau = 547$, WMLES (present work), compared to DNS from Hoyas and Jiménez [73]

Figure 2.9: Illustration of log-layer mismatch on turbulent channel cases under different conditions. — DNS profile; ○ WMLES results; - - - Logarithmic Law.

The main symptom of this issue is the log-layer mismatch, frequently observed in the literature. This phenomenon involves a discrepancy in the observed velocity profiles when using WMLES compared to the expected or reference profiles obtained from higher fidelity approaches such as WRLES or DNS. In such cases, the wall

model typically provides a correct prediction at the matching point—the location where the wall model and LES results are supposed to align. However, discrepancies arise in the velocity profile of the boundary layer above this matching point. This manifests as a shift in the velocity profile, which may appear as an upward shift [83, 134] as illustrated in Fig. 2.9a or, less commonly, a downward shift [98, 117] as in Fig. 2.9b.

Several reasons for this log-layer mismatch have been proposed in the literature, both physical and numerical. In fact, this problem is still under active research, and many studies propose ways to mitigate this mismatch. In the following sections, these propositions will be reviewed, along with the strategies designed to deal with the problem.

2.3.2.1 SGS models and near-wall turbulence

Some of the inconsistencies in WMLES naturally arise from the fact that the wall modeling couples the LES with a RANS framework in the near wall region, two frameworks that use different approaches to turbulence. While LES relies on spatial filtering and subgrid-scale models, RANS methods use time averaging and turbulence models; and neither approach was developed with WMLES as the primary application. One important drawback of the WMLES framework is that the SGS viscosity applied in the near wall region may be unsuitable for the singularities of WMLES calculations.

First, in LES, the SGS models are designed to capture the effects of small turbulent structures with assumed universal behavior, while the larger eddies that carry the majority of the energy are resolved. While this reasoning is well suited to bulk flows or wall-resolved situations, it does not hold when applied to the coarse resolution typically used in WMLES near solid boundaries.

In addition, the velocity gradients on which the computation of the SGS viscosity rely as discussed in part 1.3.3, are also likely to be misevaluated again due to the poor grid resolution near walls. This can be an additional factor to produce inappropriate subgrid scale viscosity.

Therefore, applying the usual SGS models in the near wall region of a WMLES computation can lead to uncertainties and imprecisions. This issue has been identified as a potential cause of inaccuracies in flow field predictions and is a likely contributor to the log-layer mismatch [83, 124].

Another problem that arises from this near-wall treatment is the turbulence structures that develop in the coarse near-wall grid cells. For wall-modeled LES, a direct link is established between the wall stress and the instantaneous velocity at the first grid point, thus creating a too-strong correlation between the instantaneous wall stress predicted and the LES velocity [189]. This artificially high correlation gives the turbulence structures too much coherence compared to what is observed in reality. The existence of unphysical structures can in turn lead to poorly predicted velocity gradients, thus contributing to the log layer mismatch.

For these reasons, there has been a notable effort in the literature to improve the

behavior of SGS models near walls to produce more appropriate behavior for wall-modeled LES computations. Most of the improvements are based on modifications of traditional SGS models [139, 185]. Other approaches have tried to solve the log-layer mismatch by tabulating values obtained in canonical scenarios such as turbulent channels [169] or by ensuring momentum balance in some cells away from the wall [16]. Overall, these methods have proven to be effective, showing that modifying the SGS model to reduce the log-layer mismatch in WMLES is indeed a viable method [58]. However, such modifications must be based on physical principles to be robust and representative: while tuned adjustments to the SGS model may provide the correct solution for specific configurations, they do not always provide a generally robust and justified solution.

Other solutions focus on disrupting the artificial turbulent structures that arise due to the unphysical coherence between wall stress fluctuations and LES velocities. One of the most common methods relies on the stochastic forcing of turbulence near solid boundaries. This has been explored in several studies, notably by Mason and Thomson [110], Piomelli et al. [136], Freire and Chamecki [54], Brasseur and Wei [20], and Blanchard et al. [14]. These works yielded convincing results, proving that stochastic forcing can be successfully used to mitigate the log-layer mismatch. However, there is disagreement as to how the stochastic features should be implemented in terms of location and amplitude [96]. It has been shown that changes in these factors can significantly alter the results, making the development of a consistent and robust stochastic method quite challenging.

2.3.2.2 Temporal filtering

Another look at the discrepancies between the LES framework and the wall models reveals the usefulness of another approach to address the log-layer mismatch: the idea of temporally filtering the LES data before using it for the wall model. This way, as described by Yang et al. [189], instead of using the raw LES velocity $\widetilde{u}$, the wall model uses a temporally filtered velocity u_{wm} computed as follows:

$$u_{wm}^{n} = (1-\epsilon)u_{wm}^{n-1} + \epsilon\widetilde{u}, \tag{2.6}$$

where u_{wm}^{n} is the filtered velocity at the n-th iteration and ϵ is a constant parameter. This expression is actually the definition of an exponential moving average applied to the velocity, which approximates the time average of the LES velocity $\widetilde{u}$ over an averaging time $T_{av} \simeq \frac{\Delta t}{\epsilon}$, with Δt the timestep of the simulation [190]. This approach offers two main advantages. First, the wall model inputs are brought closer to time-averaged quantities as used by the RANS equations. Second, by applying a temporal filter, the strong correlation between wall-stress fluctuations and LES velocity fluctuations—which can lead to unphysical results—is mitigated. This can help reduce inaccuracies in the LES predictions, as already mentioned in part 2.3.2.1. Yang et al. [189] showed that decreasing the constant ϵ —which is equivalent to averaging over a longer time period and smoothing out more fluctuations— leads to a decrease in log-layer mismatch. This method has several intrinsic

advantages, as it requires minimal effort to implement and does not require any prior knowledge of the flow type and/or subgrid-scale model. The value of the ϵ constant may still need to be adjusted on a case-by-case basis however to achieve effectiveness.

2.3.2.3 Coupling point wall distance

Finally, the distance between the wall and the probing point of the LES data—in terms of number of cells—plays a role in the log-layer mismatch. Adjusting this parameter has been studied in the literature.

This approach was first explored by Kawai and Larsson [83]. They comment that, as noted in part 2.3.2.1, the LES data obtained at the first grid point above the wall are mostly unreliable due to numerical and physical errors resulting from the under-resolution of turbulent structures and gradients in the coarse cells near the wall. This problem could be overcome by sampling the LES data from the second, third, or fourth cell above the wall. This method has the additional advantage of decoupling the location where the measurement is made—LES probing—from the location where the correction is applied—wall model prediction. This can be beneficial because, as discussed in part 2.3.2.1, LES data and wall stress fluctuations are artificially over-correlated in WMLES. Probing several cells above the wall can at least reduce the correlation with unphysical structures typically present within the wall cells. In addition, this approach involves modifications solely to the wall model implementation, avoiding changes to SGS or turbulence models and requiring no additional assumptions about the flow type. This method has been regularly applied in the literature with notable success in mitigating the log-layer mismatch [83, 95, 189, 192]. Implementing this strategy, however, may be quite challenging, especially for unstructured and parallel codes, which are common in LES. Additionally, the physical interpretation of the LES results between the wall and the LES probing point remains a matter of concern [103].

Part II

Implementing a wall modeling strategy for turbomachinery

Chapter 3

Introduction

3.1 Background of the study

In the first part of this work, the most relevant equations for performing LES of wall-bounded flows have been presented. The intricacies and challenges associated with the parietal regions of flows have also been presented, highlighting the interest in modeling the near-wall behavior of flows rather than solving it, for cost-effectiveness. The various solutions and challenges in the field of wall modeling have been presented, showing that this topic is still an active area of research, with remaining questions revolving around two main issues:

- The physical representativeness and relevance of the wall model itself
- The association of the wall model framework with the LES equations

The work presented in the following sections is performed in the context of the compressible LES solver AVBP developed at CERFACS. AVBP is a massively parallel compressible LES solver working with unstructured meshes [60, 62, 152]. It solves the compressible LES equations described in part 1.3.2 using either the second order Lax-Wendroff scheme [97] or the third or fourth order two-step schemes TTGC [37] or TTG4A [141]. AVBP is a mature code widely used in the scientific community and industry for complex geometries such as turbomachinery. Although it is well capable of handling wall-resolved simulations [47, 132, 154], the corresponding computational cost remains prohibitive for high Reynolds number complex configurations, as explained in chapter 2. Therefore, AVBP currently includes a classical logarithmic law wall model to put these configurations within reach [78]. However, this model is not well suited to the specific physical phenomena encountered in turbomachinery configurations due to the strong assumptions made when deriving the logarithmic law. In addition, the log-layer mismatch remains a common problem in the use of WMLES and is not the subject of special treatment within the AVBP solver. In this area, however, the recent work of Blanchard et al. [14] has begun to address this issue by introducing SGS model modifications in the near wall region.

The objective of this thesis in that context is to develop, implement, and test a strategy that addresses both of the issues mentioned previously:

- Implementing a wall model more capable of dealing with conditions and physics representative of those encountered in turbomachinery
- Addressing the issue of the log-layer mismatch.

To this end, a wall model based on the TBLE equations presented in parts 1.2.2 and 2.2.2 is implemented to deal with pressure gradient effects. This effect is assumed to be crucial in turbomachinery applications, as it is systematically present and significantly influences boundary layer thickness [182], separation processes, secondary flows [48], laminar-to-turbulent transition or re-laminarization phenomena [43, 177], and ultimately, turbomachinery performance. The TBLE framework is also a candidate to allow further improvements and inclusion of other physical effects in the future. Regarding the log-layer mismatch, the SGS correction model initiated by Blanchard et al. [14] is used and improved, corrected, and made more robust.

These improvements are evaluated across various configurations, both independently and in combination. The initial test cases are academic ones, allowing for verification that the implementation is correctly executed and that the models perform as expected under controlled conditions. These academic test cases are detailed in the following section. Subsequently, the improved models are applied to more complex turbomachinery scenarios, which are discussed in the final section of this thesis.

3.2 Academical Test Cases

This section presents the academic test cases used to evaluate the performance of the models: the turbulent channel and the periodic hill. These are two popular benchmarks within the CFD community as they provide a controlled environment for testing and validating various models such as SGS and wall models. The turbulent channel case is a necessary step in this context: it serves as a basic test to verify that the models can accurately represent wall-bounded flow in the simplest scenario (*i.e.* no curvature and pressure gradient effect). The periodic hill setup, on the other hand, presents more complex flow features caused by the geometry-induced pressure gradient; thus, it challenges the robustness of the models as well as their ability to capture such phenomena as flow separation and reattachment.

3.2.1 Turbulent Channel

As mentioned above, the first test case in this work is the turbulent channel flow illustrated in Fig. 3.1. This scenario meets the usual assumptions of an incompressible flow developing on a surface with no curvature and no pressure gradient and achieving statistical stationarity. Therefore, according to the theory, the average behavior of the boundary layer should follow the classical logarithmic profile. This makes the turbulent channel flow reference scenario where the expected performance of the wall model is known, providing a quick and reliable way to assess model implementation and reliability.

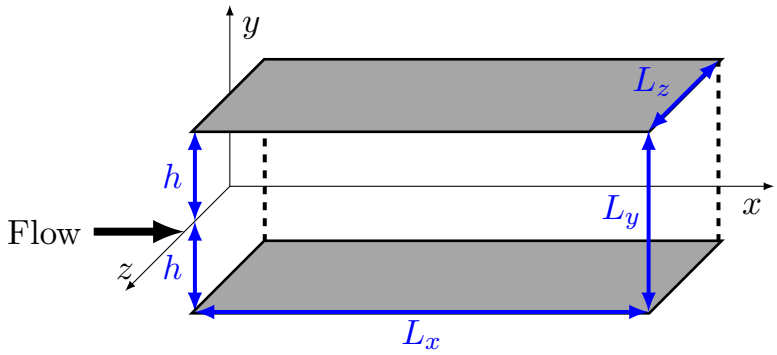

Figure 3.1: Turbulent channel geometry.

This case is also bi-periodic, with only the top and bottom walls being treated with isothermal wall model boundary conditions at 320K. This presents several advantages. The first is simplicity: the only boundary conditions of the case are periodicity and wall laws for the upper and lower walls. The second advantage is that it avoids the need to use turbulence generation methods at the inlet to reproduce fully turbulent conditions. However, this raises the question of how to compensate for friction and ensure continuous flow motion at a constant Reynolds number throughout the domain. In this work, this was achieved by using a source term S_x in the LES momentum equation in the streamwise direction:

$$\frac{\partial \bar{\rho}\widetilde{u_x}}{\partial t} + \frac{\partial}{\partial x_j}\left(\bar{\rho}\widetilde{u_x}\widetilde{u_j}\right) = -\frac{\partial}{\partial x_j}\left[\bar{P}\delta_{xj} - \overline{\tau_{xj}} - \overline{\tau_{xj}}^{sgs}\right] - S_x. \tag{3.1}$$

In order for this source term to balance the friction and ensure a constant Reynolds number, the source term S_x must balance the integral of wall friction:

$$S_x = \frac{\iint_{W_1 \cup W_2} \tau_w \, dS}{V}, \tag{3.2}$$

with W_1 and W_2 the upper and lower walls of the channel, and where V is the volume of the domain and τ_w the target shear stress. In this particular setup, the behaviors of the upper and lower walls are identical, which leads to the simplified equation:

$$S_x = \frac{2\int_0^{L_x}\int_{-L_z/2}^{L_z/2} \tau_w \, dxdz}{V}, \tag{3.3}$$

where the various geometric features can be seen in Fig. 3.1. This equation can be further simplified using the symmetry and periodicities of the problem, as well as statistical stationarity, so that,

$$S_x = \frac{\tau_w}{h}. \tag{3.4}$$

This configuration has been studied many times in literature, which makes it convenient to compare the results obtained with wall models to trusted values and

profiles available. For this work, the direct numerical simulation results of Hoyas and Jiménez [73] are used as a reference. The expected behavior in that case in terms of average velocity profile is well retrieved as illustrated in Fig. 3.2, where the classical linear and inertial regions are clearly identified.

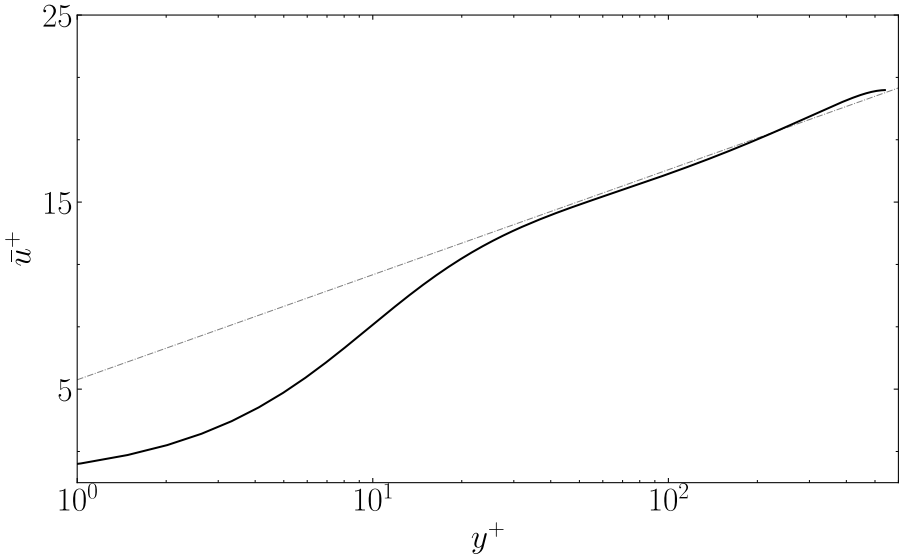

Figure 3.2: Average streamwise velocity profile on the turbulent channel for $\mathrm{Re}_\tau = 547$. — DNS profile from Hoyas and Jiménez [73]; - - - Logarithmic law of the wall.

Three different Reynolds numbers have been selected to be computed, this is to ensure that the wall models are able to reproduce the correct behavior over a reasonable range of friction levels and for different flow conditions. The selected Reynolds numbers are expressed in terms of the friction velocity $\mathrm{Re}_\tau = hu_\tau/\nu$ and summarized in the Table 3.1. The meshes used for the three different configurations are fully hexahedral regular meshes and their properties are presented in Table 3.1 as well.

Re_τ	L_x/h	L_z/h	$N_x \times N_y \times N_z$	Δ_x^+	Δ_y^+	Δ_z^+
547	8 π	4 π	$201 \times 21 \times 101$	68	52	68
934	8 π	3 π	$201 \times 21 \times 101$	117	89	87
2003	8 π	3 π	$201 \times 21 \times 101$	250	191	187

Table 3.1: Turbulent channel mesh characteristics.

Alongside the numerical reference data, empirical correlations can also be used to assess the performance of the numerical simulations performed in this work. Indeed, in this simple scenario, reliable correlations have been established that relate the bulk Reynolds number of the flow to the friction coefficient at the wall $C_f = \frac{\tau_w}{0.5\rho U_b^2}$. Typically, the Kármán-Nikuradse correlation [120] provides a link

between the friction coefficient C_f and the bulk Reynolds number $Re_{b,D_h} = \frac{U_b D_h}{\nu}$ based on the hydraulic diameter $D_h = 2\frac{L_y L_z}{L_y + L_z}$ of the duct:

$$Re_{b,D_h,KN_c} = \left(\frac{C_f}{0.046}\right)^{-1/0.2}. \tag{3.5}$$

This correlation is valid for values of Re_{b,D_h} between 10^4 and 10^6 and can be used to evaluate the performance of the computations using the wall models by comparing the computed bulk Reynolds number to the Reynolds number predicted by the correlation, assuming the friction level is known. Alternatively, the friction coefficient obtained from the simulation can be compared to the friction coefficient predicted by the correlation, provided the bulk Reynolds number is known.

Overall, the turbulent channel test case appears as a necessary prerequisite for testing any implementation of a wall model in LES before moving on to more complex scenarios. It provides a baseline where the performance of different wall models and implementations can be evaluated under controlled conditions. Establishing accuracy in this simpler context is essential before exploring scenarios where variations between models and implementations are expected.

3.2.2 Periodic Hill

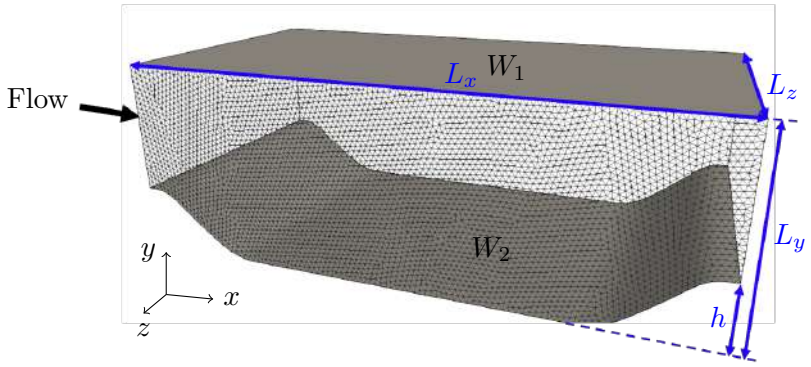

Figure 3.3: Periodic Hill test case geometry and mesh overview.

The channel with periodic constrictions, while still an academic case, is a more complex scenario than the turbulent channel. Originally published by Almeida et al. [5] and publicly available through the ERCOFTAC database, this test case has been used in literature to benchmark LES codes [61, 193] as well as to test wall models [21, 46, 103, 167, 168]. The different key phenomena that develop in this case, namely a strong pressure gradient and flow separation features, are particularly relevant to challenge and discriminate the performance of several wall models. These features, while simpler in this context, are also representative of the complex flow behaviors often encountered in turbomachinery applications. The reference 3D geometry used in this work is that of Fröhlich et al. [55] depicted in Fig. 3.3. This case features two pairs of boundary conditions, on the sides and to

the front and back of the geometry respectively. The top and bottom walls W_1 and W_2 are in this case treated with isothermal wall model boundary conditions at 300K.

The mesh used for the various simulations is a fully tetrahedral unstructured mesh, and remains the same across all operating points. The mesh and geometric properties are summarized in Table 3.2, where N_e represents the number of elements in the domain and N_n indicates the number of nodes. This mesh presents an average of $\langle N_y \rangle = 31$ points between the hill crest and the upper wall, providing sufficient resolution for capturing key flow features. Additionally, the near-wall mesh size is characterized by a wall unit size y^+ at the hilltop varying from approximately 50 for the lower Reynolds number to $y^+ \sim 180$ for the higher Reynolds number, as depicted in Fig. 3.4. These values are satisfying to justify the use of wall-modeled LES.

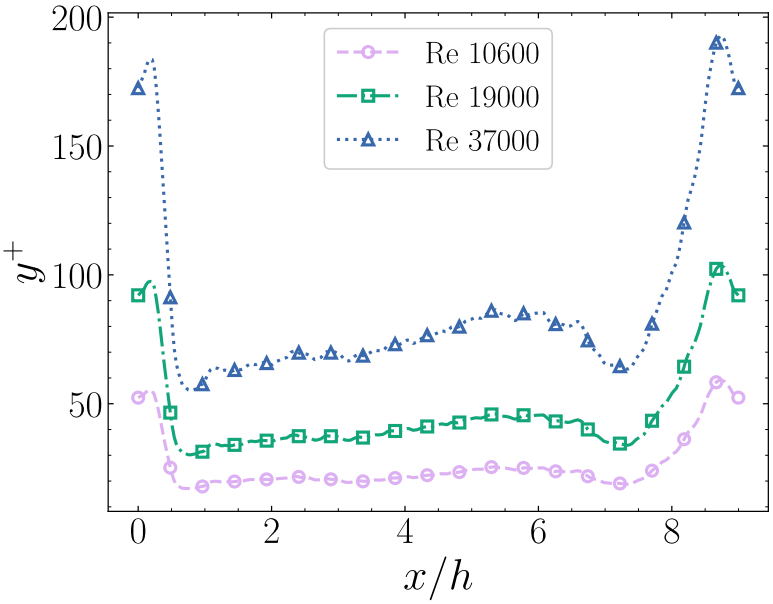

Figure 3.4: Wall unit mesh size y^+ for the three different Reynolds numbers along the bottom wall of the Periodic Hill test case.

Several reference studies of this setup performed recently, including wall-resolved LES (WRLES) as well as DNS [39, 61, 92, 193], are available in the literature along with experiments with PIV or LDA measurements [22, 82, 142]. The availability of these reference data is especially valuable when implementing and testing a wall model, as it offers a reliable benchmark for comparing and evaluating the performance of the various wall models being tested.

The setup is studied at three different Reynolds numbers in this work: $\mathrm{Re}_b = 10\,600$; $19\,000$ and $37\,000$ with the bulk Reynolds number defined at the top of the hill ($x/h = 0$),

L_x/h	L_y/h	L_z/h	$\langle N_y \rangle$	N_e	N_n
9	3.035	4.5	31	1 313 730	236 702

Table 3.2: Periodic hill main geometry characteristics.

$$Re_b = \frac{U_b h}{\nu}, \tag{3.6}$$

with h the hill height and U_b the bulk velocity:

$$U_b = \frac{\int_h^{L_y} \int_0^{L_z} \rho \; u_x \; dydz}{\int_h^{L_y} \int_0^{L_z} \rho \; dydz}. \tag{3.7}$$

Using three different Reynolds number configurations helps to test the performance of the wall models over a range of friction levels, as well as under different pressure gradient conditions and different recirculation bubble lengths and strengths.

Just as in the turbulent channel case, a source term S_x in the streamwise direction x of the momentum equation is needed to balance the wall friction. This source term is a function of the wall friction on the walls W_1 and W_2 depicted in Fig. 3.3:

$$S_x = \frac{\iint_{W_1 \cup W_2} \tau_w \; dS}{V}, \tag{3.8}$$

However, in contrast to the periodic turbulent channel, simplifications cannot be made based on geometry in this setup, which means that the source term must be adjusted during the transient phase until the correct bulk Reynolds number is reached. After such a transient, the source term is kept constant to maintain the desired Re_b.

Chapter 4

A wall model with pressure gradient effects: the TBLE model

This chapter focuses on the details and outcomes of the work conducted in this thesis to address the issue of the physical representativeness of the wall model. This chapter presents the developments made during this thesis to account for the pressure gradient effect in the wall model. To do so, the TBLE framework already introduced in part 2.2.2 is chosen. This allows direct influence of the pressure gradient and enables the possibility of adding further physical contributions in the future.

4.1 Model description

As just presented above, the model implemented during this thesis relies on the TBLE framework. As presented in part 2.2.2, this type of model relies on solving a set of ordinary differential equations. In this work, the 1D form of the TBLE equation is used to integrate seamlessly with the already existing AVBP architecture. Precisely, the implemented wall model is based on solving the 1D Thin Boundary Layer Equation [9, 23] assuming an incompressible, fully turbulent boundary layer with no curvature [43], retaining the pressure gradient effect, leading to the following governing expression:

$$\frac{\partial}{\partial \eta}\left[(\nu+\nu_t)\,\frac{\partial \overline{U}}{\partial \eta}\right] = \frac{1}{\overline{\rho}}\frac{\partial \overline{P}}{\partial \xi}, \tag{4.1}$$

where the streamwise direction is ξ, while the wall-normal direction is η. This equation includes the time-average streamwise velocity $\overline{U}$, time-average streamwise pressure gradient $\frac{\partial \overline{P}}{\partial \xi}$, density $\overline{\rho}$, laminar viscosity ν and a turbulent eddy viscosity ν_t. This model still relies on a one-dimensional equation and neglects the 3D convective terms, which means it should formally be valid for a limited set of conditions corresponding to an equilibrium state of the boundary layer (see part 2.3.1). Although this may not be appropriate for all scenarios [96], it has demonstrated utility in literature, either directly or in integral form, for incorporating pressure gradient effects near the wall [46, 64, 107, 172, 191] with a minimal model complexity.

Although not the focus of this work, the temperature counterpart of the model is also used to resolve the simplest energy equation:

$$\frac{\partial}{\partial \eta}\left[(\lambda + \lambda_t)\frac{\partial \overline{T}}{\partial \eta}\right] = 0, \tag{4.2}$$

This is done to enable the possibility of using the wall model with isothermal walls, as also proposed in the thesis of Gelain [58].

4.1.1 Turbulence model

A crucial aspect of this modeling approach is the selection of the turbulent viscosity ν_t, as well as the turbulent thermal conductivity λ_t for the energy equation.

For the turbulent viscosity, several models can be found in literature in the context of TBLE wall models, most of them using typical mixing length models [16, 23, 83, 180]. However, as discussed in part 2.3.1, the choice of turbulent viscosity ν_t must be consistent with the presence of a pressure gradient. In this work the model introduced by Duprat et al. [46] is employed:

$$\nu_t = \nu\kappa\eta^* \left[\alpha + \eta^* (1-\alpha)\right]^\beta \left[1 - \exp\left(-\frac{\eta^*}{1 + A\alpha^3}\right)\right]^2, \tag{4.3}$$

where ν is the viscosity of the fluid, $\kappa = 0.41$ the von Kármán constant, and $A = 17$, $\beta = 0.78$ are constants of the model. η^* is the non-dimensional wall-normal distance, using the near-wall scaling of Manhart et al. [107],

$$\eta^* = \frac{\eta u_{\tau p}}{\nu}$$

with

$$u_\tau = \sqrt{|\tau_w|/\rho}, \tag{4.4}$$

$$u_p = \left|(\nu/\rho)(\partial P/\partial \xi)\right|^{1/3}, \tag{4.5}$$

and

$$u_{\tau p} = \sqrt{u_\tau^2 + u_p^2}, \tag{4.6}$$

$$\alpha = u_\tau^2 / u_{\tau p}^2. \tag{4.7}$$

Note that the parameter α can in fact serve as an indicator of the pressure gradient's influence on the boundary layer relative to the friction. In particular, $\alpha = 1$ corresponds to a boundary layer without a pressure gradient, while $\alpha = 0$ reflects a separated boundary layer under the influence of a strong pressure gradient, where $\tau_w = 0$. This turbulent viscosity model is designed to be accurate for boundary layers influenced by pressure gradients, offering several important features:

- The viscosity is defined for both positive and negative pressure gradients, even though they affect the viscosity in the same manner due to the absolute value in the definition of u_p.
- The viscosity is defined even in the case of boundary layer separation ($\tau_w = 0$).

In addition to that, when the pressure gradient is zero, $\alpha = 1$ and the turbulent viscosity reduces to

$$\nu_t = \nu\kappa\eta^+ \left[1 - \exp\left(-\frac{\eta^+}{1+A}\right)\right]^2, \tag{4.8}$$

which is very close to the classical dampened mixing length turbulent viscosity model, notably used by Cabot and Moin [23]:

$$\nu_t = \nu\kappa\eta^+ \left[1 - \exp\left(-\frac{\eta^+}{A^+}\right)\right]^2, \tag{4.9}$$

with $A^+ \approx 17$ and $\eta^+ = \frac{\eta u_\tau}{\nu}$. As discussed in part 2.2.2, the use of such a model in the absence of a pressure gradient leads to the recovery of the logarithmic law profile. In addition, the damping function ensures that the model adheres to the correct asymptotic behavior $\mathcal{O}(\eta^3)$ near the wall, as discussed in part 1.3.3.1. This in turn ensures that in scenarios without a pressure gradient, the chosen model can reproduce the expected results of the log-law model, which is a necessary non-regression feature to maintain accuracy and consistency in the simulations.

To ensure the proper behavior of the turbulence model, comparisons can be made for different scenarios, both against reference data and against the more basic turbulence model described in equation (4.9). Evaluating the performance of these two models does not require the full implementation of the wall model within a LES solver. Instead, the wall model equations can be solved independently using a standalone solver. In this thesis, such a solver has been developed within a Python framework. The only inputs required for this solver are the same as those that would be provided by the LES solver in the final implementation. The details of the numerical solving process are consistent with those used in the final implementation described in the next section 4.1.2, and are identical for both turbulent models tested.

The first observation that can be made using the Python solver is a direct comparison of the turbulent viscosity between the two models under consideration defined by Eqs. (4.3) and (4.9). For the case shown in Fig. 4.1, the inputs to the model are a computed boundary layer thickness of $y = 0.0025\,\mathrm{m}$, with a fixed boundary layer velocity at this location of $u = 40\,\mathrm{m/s}$, using standard properties of air at ambient temperature for viscosity and density. This setup corresponds to dimensionless values of $y^+ \approx 335$ and $u^+ \approx 19$. The comparison is made for two cases, one with zero pressure gradient and the other using the value $\frac{\partial \overline{P}}{\partial x} = 5000\,\mathrm{Pa/m}$ or a dimensionless pressure gradient value of $p^+ \simeq 8.5 \times 10^{-3}$ or $\alpha \simeq 0.95$.

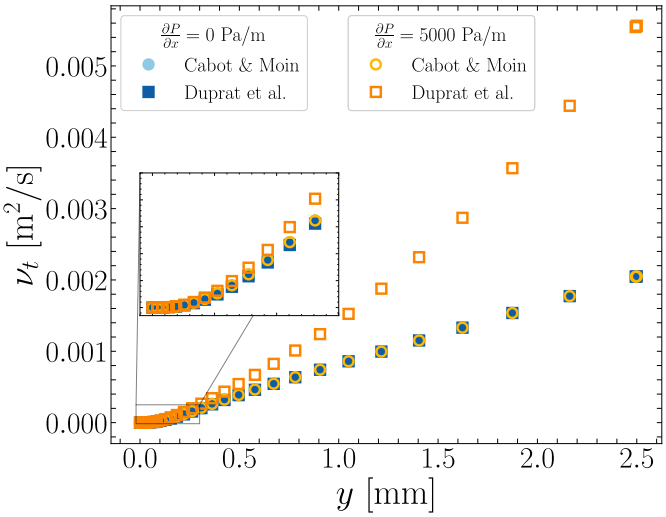

Figure 4.1: Comparison of turbulent eddy viscosity predictions from two models under zero and adverse pressure gradient conditions.

As can be seen in Fig. 4.1, the two models give nearly identical predictions for turbulent viscosity at zero pressure gradient, confirming the non-regression property of the model implemented in this work. However, when a pressure gradient is introduced, the results of the two models begin to diverge significantly. Close to the wall, where small values of turbulent viscosity are expected, the dominant effect of the damping function leads to little or no difference in this region. Further away from the wall, as the turbulent viscosity increases, the results in Fig. 4.1 indicate that the model of Cabot and Moin [23] does not depend on the pressure gradient, as expected from its definition. In contrast, the model from Duprat et al. [46] is very sensitive to the pressure gradient, as would be expected from its construction, and is probably much more physically representative. However, this increase in physical representativeness needs to be validated by comparing the results with actual reference data to establish the reliability of this model.

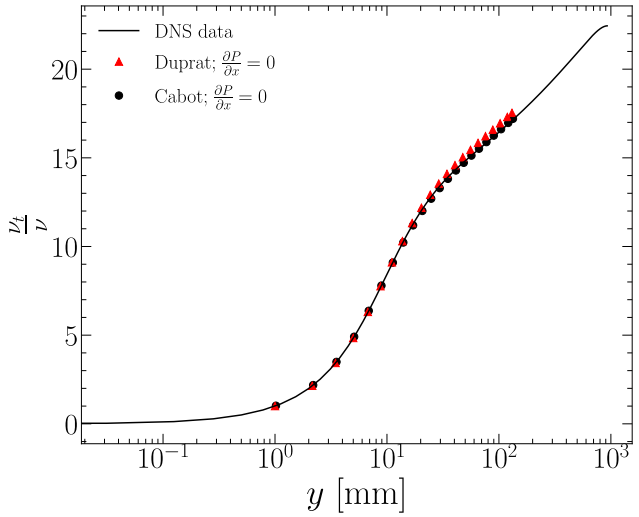

Figure 4.2: Comparison of the non-dimensional velocity profiles produced by the solution of the TBLE model for the two different turbulence models with no pressure gradient. DNS data from Hoyas and Jiménez [73].

When numerically solving the TBLE wall model equation (4.1) for velocity profiles, the first comparison is made with the DNS results of Hoyas and Jiménez [73], who simulated a flat turbulent channel with no pressure gradient, in Fig. 4.2. As expected, good agreement between the two models is observed in this scenario, consistent with the earlier discussion. Both models not only agree well with each other, but also successfully reproduce the DNS results for the turbulent channel, confirming their ability to accurately capture the average flow characteristics in the absence of a pressure gradient.

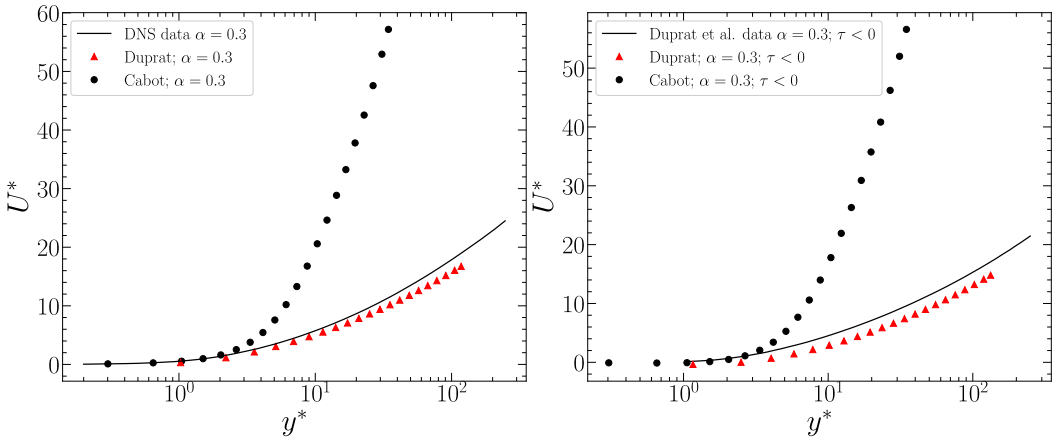

(a) Attached flow conditions ($\tau_w > 0$) (b) Reversed flow conditions ($\tau_w < 0$)

Figure 4.3: Comparison of the non-dimensional velocity profiles produced by the solution of the TBLE model for the two different turbulence models with adverse pressure gradient. DNS data from Duprat et al. [46].

Figure 4.3 provides the comparison of the non-dimensional velocity profiles under the influence of adverse pressure gradient this time, leading to a value of $\alpha = 0.3$. This value can in fact, be obtained under two distinct scenarios: one where the flow is near separation but still attached, and another just after separation ($\tau_w < 0$). Note here that, even though the parameter α is not explicitly included in the model of Cabot and Moin [23], it can be computed a posteriori using the obtained value of friction and the pressure gradient to allow the comparison between the two models under the similar conditions yielding $\alpha = 0.3$, alternatively expressed as $p^+ \approx 3.4$. The results are presented in Figure 4.3a for the attached flow and Figure 4.3b for the separated flow. In both cases, the model of Cabot and Moin [23] produces a radically different velocity profile compared to the model of Duprat et al. [46]. The latter produces a velocity profile in good agreement with the DNS data for these conditions, while the former deviates from the expected behavior. These results confirm the findings presented by Duprat et al. [46].

Moreover, it is important to consider the iterative process required to converge on the wall friction. As already mentioned in part 2.2, this is explained by the fact that some input parameters of the model depend on the friction τ_w, which is indirectly an output of the model. The speed at which this convergence occurs

varies depending on the turbulent viscosity model used. In particular, in the present case for $\alpha = 0.3$ the model of Cabot and Moin [23] required over 5000 iterations to converge for both scenarios. This would be highly impractical in a real LES implementation, especially when considering that convergence must be established for every wall cell in the domain. The model of Duprat et al. [46] on the other hand demonstrated much faster convergence, only requiring between 10 and 100 iterations for $\tau_w > 0$ and $\tau_w < 0$ respectively to respect a criterion of less than 0.1% difference in predicted friction between the last iterations. This further indicates that the turbulent viscosity model of Duprat et al. [46] incorporating pressure gradient effects is better suited for computing boundary layers influenced by pressure gradients.

Regarding the energy equation, the turbulent thermal conductivity λ_t is modeled using a classical turbulent Prandtl model

$$\lambda_t = \mu_t \frac{c_p}{\mathrm{Pr}_t} \tag{4.10}$$

with a turbulent Prandtl number computed as described by Gelain [58] using the model of Weigand et al. [181] as

$$\mathrm{Pr}_t = \frac{1}{\frac{1}{2\,\mathrm{Pr}_{t_\infty}} + C\,\mathrm{Pr}\,\frac{\mu_t}{\mu}\sqrt{\frac{1}{\mathrm{Pr}_{t_\infty}}} - \left(C\,\mathrm{Pr}\,\frac{\mu_t}{\mu}\right)^2 \left[1 - \exp\left(-\frac{1}{C\,\mathrm{Pr}\,\frac{\mu_t}{\mu}\sqrt{\mathrm{Pr}_{t_\infty}}}\right)\right]} \tag{4.11}$$

where the constants of the model are $C = 0.3$ and $\mathrm{Pr}_{t_\infty} = 0.92$.

4.1.2 Implementation

After discussing the details of the physical representativeness of the chosen wall model, the details of the implementation within the LES solver AVBP are presented in this section. The model chosen in this work is based on solving an ordinary differential equation in the near-wall cells. To do so, an embedded mesh needs to be used to provide the necessary discretization of the model equation to solve it numerically. In the present case of a 1D ODE to be solved, the construction of the mesh is in fact sufficiently easy that it can be done only locally within each cell concerned by the wall law—*i.e.* each wall adjacent cell. This general concept is illustrated in Fig. 4.4. In the present implementation, the 1D mesh is constructed so that the distance from the wall to the first point is $\eta^+ = 0.3$ based on an initial guess of the wall friction [87], and with a geometric growth with a constant common ratio of 1.2 for the remaining elements up to η_1, the height of the wall adjacent element. This height is computed as the average height of all the off-wall nodes of the cell.

The boundary conditions of the wall model are zero velocity at the wall and quantities exchanged with the LES at the other end of the 1D mesh. In AVBP, the solutions are available at nodes, while the wall model is computed for each wall cell. This means that an averaging operation has to be applied between the quantities of all the off-wall nodes of each cell to provide the fluid values to the wall model.

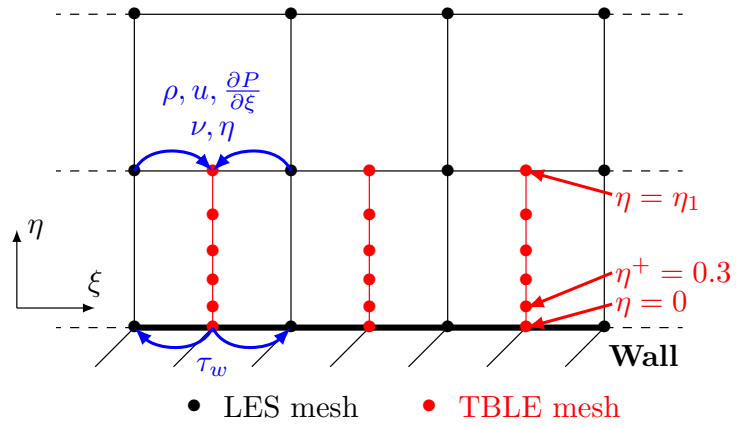

Figure 4.4: TBLE model principle: the equation is discretized in each cell perpendicularly to the wall and solved to yield the wall friction τ_w.

In addition to spatial averaging inside of each cell, temporal averaging is also performed on the pressure gradient term. The current model is indeed sensitive to temporal fluctuations either coming from the velocity field or through the pressure gradient, which will be discussed in the following results. To ensure model robustness in these situations, smoothing of the pressure gradient appears necessary. From literature, this has been described by Zebiri et al. [191] using a spatial smoothing technique that takes advantage of the periodicity of the problem in the spanwise direction. In the present work, a temporal smoothing approach is preferred, such as the one used by Hosseinzade and Bergstrom [72]. To provide temporal smoothing to the pressure gradient term, an exponential moving average (EMA) filter of the form

$$\overline{\frac{\partial P}{\partial \xi}}_{n+1} = \gamma \frac{\partial P}{\partial \xi}_{n} + (1-\gamma)\overline{\frac{\partial P}{\partial \xi}}_{n}, \tag{4.12}$$

is chosen, where the average $\overline{\frac{\partial P}{\partial \xi}}_{n}$ is updated at each iteration n using the instantaneous value $\frac{\partial P}{\partial \xi}_{n}$ and the factor $0 < \gamma < 1$ defines the time constant of the averaging. This temporal filter is chosen for its relatively simple implementation, which minimizes computational and memory footprint. This is achieved because only one algebraic computation is required per timestep, with no extra values to store other than the desired average pressure gradient.

This temporal filter is useful as it filters out high-frequency pressure gradient variations that significantly disrupt wall model predictions in a compressible solver, while still permitting low-frequency fluctuations to allow the model to adjust to slow changes in the unsteady simulation. Note that the time constant of such a filter is usually defined as $T_{av} = \frac{\Delta t}{\gamma}$, with Δt the timestep of the simulation [72, 190]. The higher the factor γ, the lower this time constant will be, which also means that the corresponding time window used to average the data will be small. In the opposite limit, that is, if the time constant is high, the filter tends to give the cumulative

average of data collected since the start of the sampling. The parameter $\gamma = \frac{\Delta t}{T_{av}}$ which appears in Eq. (4.12) is tuned for each simulation so that the averaging time constant is equal to the wall diffusion time scale $T_{av} = h_{wm}/(\kappa u_\tau)$ of each simulation as prescribed by Hosseinzade and Bergstrom [72]. The length scale h_{wm} is the height covered by the wall model, which is here the height of the wall cells, and κ and u_τ are the von Kármán constant and the friction velocity already introduced for Eq. (4.3). It should be noted that alternative estimations of the filtering time-scale, based on convective time scales, can be used as a substitute for the one proposed above, as used notably in the work of Park and Moin [125]. In particular, in setups where the diffusive time-scale is not accessible a priori, assessing a convective time-scale representative of the specific case may be more straightforward. However, for the time-filtering of boundary layer data as is done in this thesis, the findings of Hosseinzade and Bergstrom [72] suggest that the prescribed diffusive time-scale yields superior results, at least for a simple flat plate boundary layer.

After discussing the details of the 1D mesh setup and temporal filtering, the actual solving of the model equations can be described. To do so, recall the equations of the model (4.1) and (4.2) for an isothermal condition, which can be written in the general form:

$$\frac{\mathrm{d}}{\mathrm{d}\eta}\left(D_\Phi \frac{\mathrm{d}\Phi}{\mathrm{d}\eta}\right) = S_\Phi \tag{4.13}$$

with D_Φ the coefficient corresponding to the flow quantity Φ which can be either velocity or temperature, and S_Φ an eventual source term. In the present case, the only source term is the pressure gradient in the equation for velocity. This equation can be discretized in a finite volume manner by first integrating it on a control volume around the i-th node, as detailed in the work of Gelain [58]:

$$\left(D_\Phi \frac{\mathrm{d}\Phi}{\mathrm{d}\eta}\right)_{i+\frac{1}{2}} - \left(D_\Phi \frac{\mathrm{d}\Phi}{\mathrm{d}\eta}\right)_{i-\frac{1}{2}} = \int_{\eta_{i-\frac{1}{2}}}^{\eta_{i+\frac{1}{2}}} S_\Phi d\eta.$$

Then, a second-order centered finite difference is used to write:

$$D_{\Phi,i+\frac{1}{2}} \frac{\Phi_{i+1} - \Phi_i}{\eta_{i+1} - \eta_i} - D_{\Phi,i-\frac{1}{2}} \frac{\Phi_i - \Phi_{i-1}}{\eta_i - \eta_{i-1}} = S_{\Phi,i} \Delta\eta_i,$$

with $\Delta\eta_i = \frac{\eta_{i+1} - \eta_{i-1}}{2}$ the distance between $\eta_{i-\frac{1}{2}}$ and $\eta_{i+\frac{1}{2}}$. Finally, this equation can be recast as,

$$a_i \Phi_{i-1} + b_i \Phi_i + c_i \Phi_{i+1} = d_i, \tag{4.14}$$

with:

$$\begin{aligned} a_i &= \frac{D_{\Phi,i-\frac{1}{2}}}{\eta_i - \eta_{i-1}}, \\ c_i &= \frac{D_{\Phi,i+\frac{1}{2}}}{\eta_{i+1} - \eta_i}, \\ b_i &= -a_i - c_i, \\ d_i &= S_{\Phi,i} \Delta\eta_i. \end{aligned} \tag{4.15}$$

It should be noted as well that the two extremities of the domain, where $i = 0$ and $i = n$, have to be considered as particular cases which are in fact the boundary conditions of the system: Φ_0 and Φ_n are fixed data of the problem.

The coefficients $D_{\Phi,i+\frac{1}{2}}$ and $D_{\Phi,i-\frac{1}{2}}$ can also be computed using a weighted harmonic mean between the values D_i and D_{i+1} with the weights determined by the relative position of $\eta_{i+\frac{1}{2}}$ between i and $i+1$.

$$D_{\Phi,i+\frac{1}{2}} = \left(\frac{\frac{\eta_{i+\frac{1}{2}} - \eta_i}{\eta_{i+1} - \eta_i}}{D_{i+1}} + \frac{\frac{\eta_{i+1} - \eta_{i+\frac{1}{2}}}{\eta_{i+1} - \eta_i}}{D_i} \right)^{-1}$$

$$D_{\Phi,i-\frac{1}{2}} = \left(\frac{\frac{\eta_{i-\frac{1}{2}} - \eta_{i-1}}{\eta_i - \eta_{i-1}}}{D_i} + \frac{\frac{\eta_i - \eta_{i-\frac{1}{2}}}{\eta_i - \eta_{i-1}}}{D_{i-1}} \right)^{-1}$$

leaving no unknown in the expression of coefficients a_i, b_i, c_i and d_i. It should be noted here that the coefficients D_Φ and consequently a_i, b_i, c_i and d_i depend on temperature due to their dependence on μ. In this framework, these coefficients can be recomputed at each iteration using, for example, the Sutherland law (1.5) already used in the LES domain. This approach could be particularly useful in contexts involving high-temperature gradients. However, this feature is not the focus of the present work and it was not tested in that context.

When expressing equation (4.14) for all indices i, this yields the matrix form of the equation,

$$A\Phi = D \tag{4.16}$$

with:

$$A = \begin{bmatrix} b_1 & c_1 & & & 0 \\ a_2 & b_2 & c_2 & & \\ & a_3 & b_3 & \ddots & \\ & & \ddots & \ddots & c_{n-1} \\ 0 & & & a_n & b_n \end{bmatrix} ; \; \Phi = \begin{bmatrix} \Phi_1 \\ \Phi_2 \\ \Phi_3 \\ \vdots \\ \Phi_n \end{bmatrix} ; \; D = \begin{bmatrix} d_1 \\ d_2 \\ d_3 \\ \vdots \\ d_n \end{bmatrix} \tag{4.17}$$

The particular cases of the first and last line of the system can be fixed knowing the boundary values of the system. In particular, for the velocity equation, identifying $U_0 = 0$ and $U_n = U_{\text{LES}}$ yields $b_1 = 1$, $c_1 = 0$, $d_1 = 0$, while $a_n = 0$, $b_n = 1$ and $d_n = U_{\text{LES}}$. For the temperature field, similar considerations give $b_1 = 1$, $c_1 = 0$ and $d_1 = T_w$, as well as $a_n = 0$, $b_n = 1$ and $d_n = T_{\text{LES}}$.

To solve the tri-diagonal system (4.17), the Thomas algorithm is used [127]. This algorithm is highly efficient and resolves the system in a $\mathcal{O}(n)$ complexity. However, as already discussed, in the present case the system needs to be solved iteratively until it produces a converged solution Φ, as the coefficients of the matrix A depend on μ, μ_t and Pr_t which depend on the solution 1D field of $\bar{U}$ and $\bar{T}$.

4.1.3 Intermediate conclusions

In the present thesis, a wall model based on solving the TBLE equations is implemented and subjected to a series of tests. The goal is first to improve the physical representativeness of the wall model present in the AVBP code by considering pressure gradient effects and to evaluate the improvement with academic test cases and turbomachinery configurations. While this approach is not entirely new, as discussed in part 2.2.2, with related past efforts by Wang and Moin [180] and Duprat et al. [46], the methodology treated in this thesis still provides a new angle and useful insights on this method.

First, unlike some previous models that also included pressure gradient effects in the boundary layer equations, see for example Wang and Moin [180], the model developed in this work is combined with a turbulence model that is compatible with these gradient effects, namely the model of Duprat et al. [46]. Although the present implementation is much closer to what was done in Duprat et al. [46], there are still quite significant differences. First, the wall model in Duprat et al. [46] is implemented within an incompressible finite volume framework, whereas the present work operates in the compressible, finite element context of the AVBP solver. More importantly, in the work of Duprat et al. [46], the equation:

$$\frac{\partial U^*}{\partial y^*} = \frac{\text{sign}\left(\frac{\partial P}{\partial x}\right)(1-\alpha)^{3/2}y^* + \text{sign}(\tau_w)\alpha}{\left(1+\frac{\nu_t}{\nu}\right)} \tag{4.18}$$

is numerically integrated to calculate the wall friction. In this thesis, however, the general form of the boundary layer equations is solved using the method outlined in the previous section.

Additionally in this work, the time averaging of the pressure gradient term is implemented, and its impact is tested and discussed. This aspect of wall modeling is rarely addressed in the literature concerning ODE-based wall models, and it was notably absent from the analysis presented in the work of Duprat et al. [46].

In the following sections, the results obtained using the TBLE model with pressure gradient are compared to both reference data and predictions from the standard log-law model. These comparisons are conducted on the two academic test cases introduced in part 3.2: the turbulent channel and the periodic hill case. This first ensures that the model is correctly implemented and offers at least the same quality of predictions on simple cases before offering insight into the effectiveness of the TBLE model in capturing complex flow phenomena, such as pressure gradients and flow separation, and assesses whether the model offers improved physical accuracy compared to the traditional log-law approach.

4.2 Validation on a turbulent channel setup

In this section, the results obtained for the turbulent channel setup, presented in part 3.2.1, are analyzed. This setup is the first test case used to assess the performance of the TBLE wall model. The simple geometry of the channel, coupled with basic boundary conditions and reference data availability, make this setup a particularly suited starting point for testing the TBLE model. Because of these features, such a test case allows for clear comparisons between wall model predictions and reference data, thus ensuring that the TBLE wall model behaves as expected.

All the computations presented in this section are computed using the Lax-Wendroff [97] numerical scheme and the Smagorinsky SGS model [158] available in AVBP.

Re_τ	Case	$Re_{b,Dh}$	$Re_{b,Dh,KNc}$	Error
	Log Law	35520		<1%
547	TBLE	33459	35485	6%
	TBLE EMA	35667		1%
	Log Law	61388		<1%
934	TBLE	58529	61182	5%
	TBLE EMA	61301		1%
	Log Law	142975		<1%
2003	TBLE	138278	150096	3%
	TBLE EMA	144087		<1%

Table 4.1: Wall friction results for the turbulent channel comparing log-law model with current TBLE model with and without temporal smoothing (EMA).

The performance of the wall-modeled simulations can first be assessed by comparing the simulation results with the expected results based on the correlations presented in part 3.2.1. Specifically, Table 4.1 provides the results in terms of the bulk Reynolds number $Re_{b,Dh}$ based on the hydraulic diameter. Recall here that the friction Reynolds number of each case is constant as it is fixed by the source term of the simulation. The comparison of the results thus focuses on the Reynolds number obtained from each simulation relative to the reference Reynolds number, $Re_{b,Dh,KNc}$, calculated using the Kármán-Nikuradse correlation described in part 3.2.1. An accurate simulation with a properly applied wall model should yield a bulk Reynolds number that is sufficiently close to the expected value, as determined by the correlation. A first glance at Table 4.1 shows that the results obtained with the classical log-law are in good agreement with the Kármán-Nikuradse correlation, with error levels below 1% for all the Reynolds numbers considered. However, when using the TBLE model based on instantaneous values of pressure gradient, discrepancies appear between the simulations' Reynolds number and the one based on the correlation. This can be attributed to the sensitivity of the model of Duprat et al. [46] to instantaneous pressure gradient fluctuations. This sensitivity leads to

an underestimation of the observed bulk flow velocity in the simulation, which in turn results in an underestimated Reynolds number. This problem is overcome by using the time-averaged pressure gradient instead of the instantaneous one, thanks to the exponential smoothing technique detailed in part 3.2.1. As described in Section 4.4, the parameter $\gamma = \frac{\Delta t}{T_{av}}$ in Eq. (4.12) is tuned for each simulation. In this simple case, the averaging time characteristic is computed using the diffusive time scale $T_{av} = h_{wm}/(\kappa u_\tau)$ prescribed by Hosseinzade and Bergstrom [72], with h_{wm} representing height covered by the wall model (i.e., the height of the wall cells), while κ and u_τ are the von Kármán constant and the friction velocity already introduced for Eq. (4.3). The results of these calculations are denoted by the suffix *EMA* for Exponential Moving Average in Table 4.1 and confirm that the TBLE model produces the expected results by using this time averaging technique.

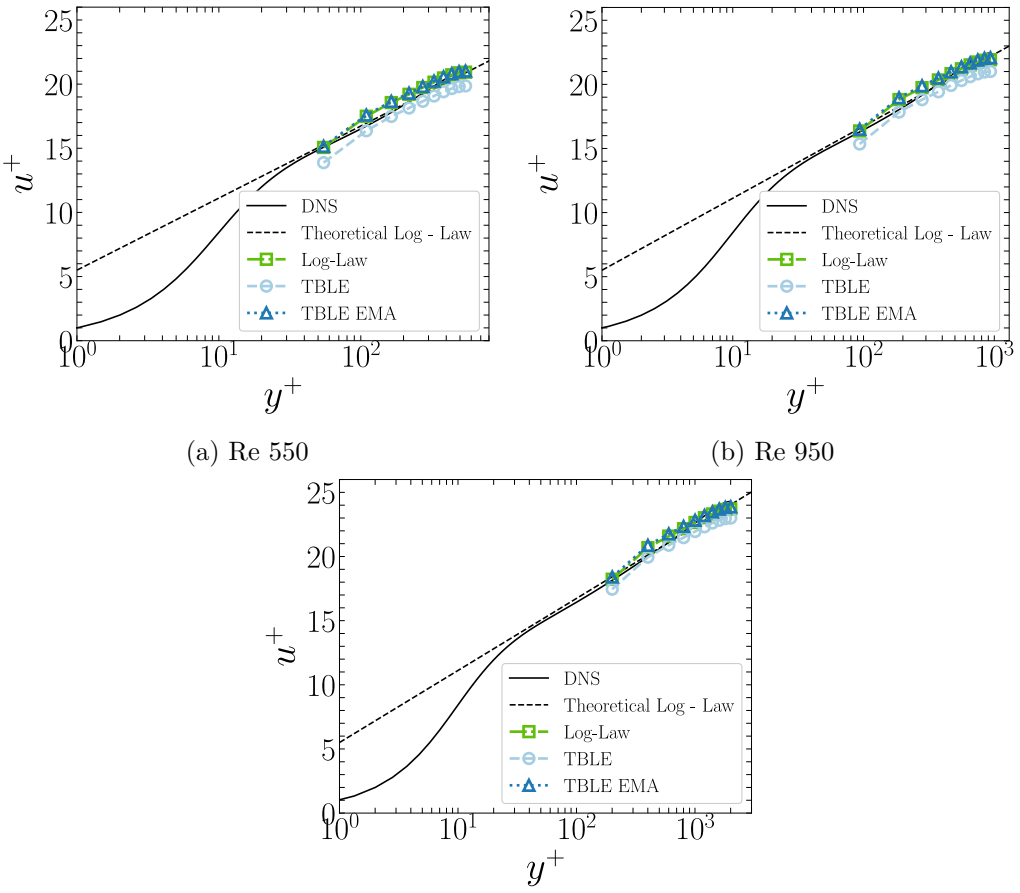

(a) Re 550

(b) Re 950

(c) Re 2000

Figure 4.5: Non-dimensional streamwise velocity profiles of the periodic channel for all operating points compared to the reference DNS [73].

To further evaluate the TBLE wall model performance, the next step is to analyze the average 1D velocity profiles. These profiles are computed by averaging the velocities along the streamwise and spanwise directions (i.e., x and z directions) and are illustrated in Fig. 4.5 for the three Reynolds numbers. The results show discrepancies arising when using the TBLE wall model with an instantaneous

pressure gradient consistent with the observations made regarding the Reynolds numbers. Specifically, for the same given wall friction, the TBLE wall model yields a bulk velocity that is lower than expected and than that of the log-law simulations. However, triggering the exponential moving average of the pressure gradient solves this issue and the resulting velocity profiles match the reference well. This confirms the overall proper behavior of the TBLE model when the pressure gradient is handled appropriately. This method is also robust to Reynolds number variations as it produces accurate results over the three different tested cases. The obtained results also show the particularly sensitive nature of the chosen TBLE wall model to pressure gradient fluctuations, especially in the present case where the pressure gradient is zero on average. Therefore, proper handling of this feature of the model is essential to maintain the physical accuracy of the simulations.

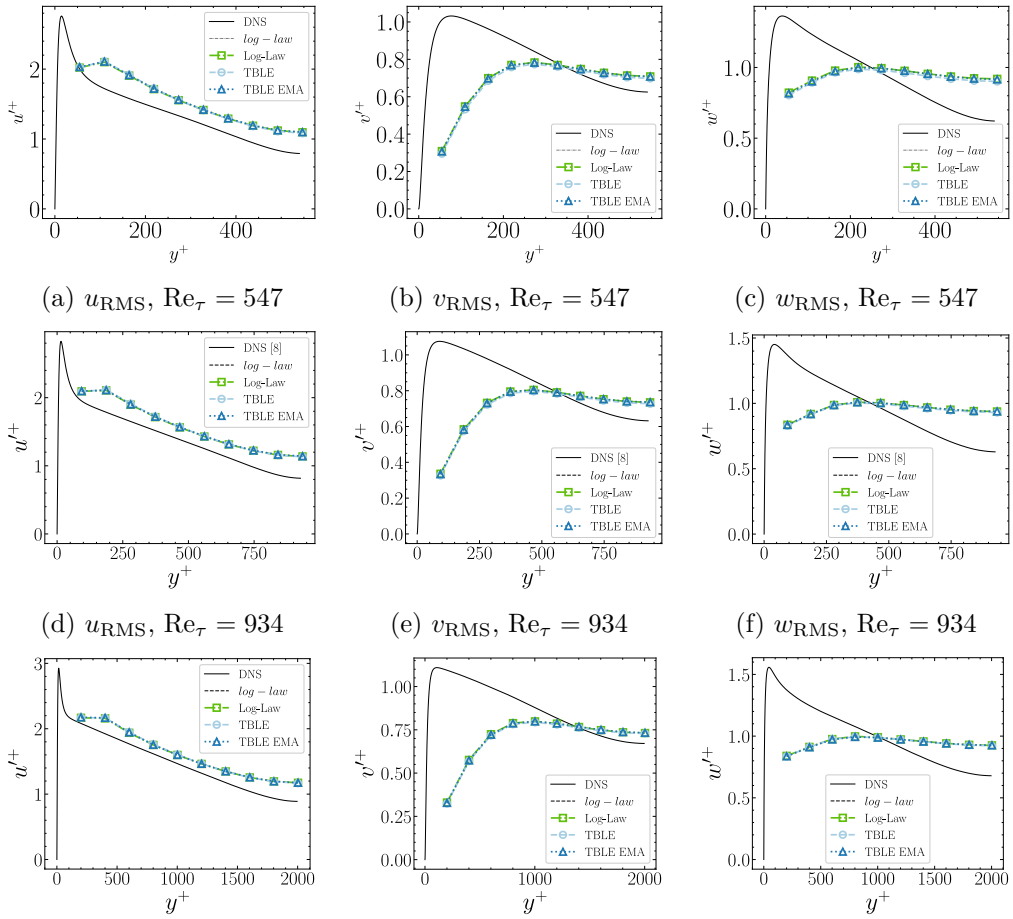

(a) u_{RMS}, $\mathrm{Re}_\tau = 547$ (b) v_{RMS}, $\mathrm{Re}_\tau = 547$ (c) w_{RMS}, $\mathrm{Re}_\tau = 547$

(d) u_{RMS}, $\mathrm{Re}_\tau = 934$ (e) v_{RMS}, $\mathrm{Re}_\tau = 934$ (f) w_{RMS}, $\mathrm{Re}_\tau = 934$

(g) u_{RMS}, $\mathrm{Re}_\tau = 2003$ (h) v_{RMS}, $\mathrm{Re}_\tau = 2003$ (i) w_{RMS}, $\mathrm{Re}_\tau = 2003$

Figure 4.6: RMS velocity components for the turbulent channel flow at three different Reynolds numbers.

Looking at the turbulent velocities in terms of the root mean square (RMS) of each velocity component also provides insight into the behavior of the different wall models relative to the DNS reference data. The RMS results in Fig. 4.6 show no large performance differences between the different wall models in the simulations.

Overall, the wall-modeled simulations produce satisfactory levels of velocity fluctuations. In particular, for the streamwise velocity fluctuations, the models are in quite good agreement with the reference DNS data. However, for the spanwise and wall-normal velocity components, they show a tendency to underestimate the fluctuations close to the wall. These observations are consistent with what is usually produced in literature, except for the fact that the streamwise velocity fluctuations are typically overestimated near the wall in previous studies [23, 46, 88]. This difference can be attributed here to the use of the Smagorinsky SGS model in this work, which is known to be over-dissipative. Overall, the differences observed between the wall-modeled LES and the DNS results can be explained by the rather low grid resolution of WMLES LES grids which are rarely fine enough to capture the detailed dynamics in this region. Given the type of wall models used here, with no specific mechanisms in place to enforce proper behavior for velocity fluctuations, such a result is not surprising.

Re_τ	Case	Simulated convective times $\frac{L_x}{U_b}$	Simulated diffusive times $\frac{h}{u_\tau}$	Cost (core.h)	Add. Cost
547	Log Law	110	148	821.6	
	TBLE EMA	110	148	925.6	11%
934	Log Law	100	125	464.1	
	TBLE EMA	100	125	530.3	13%
2003	Log Law	85	100	174.9	
	TBLE EMA	85	100	202.1	14%

Table 4.2: Summary of the computational cost of the turbulent channel.

At this point, it is also important to note that the computational cost associated with the TBLE wall model is not negligible compared to the classical log-law model. One of the main reasons for this increase in computational complexity is the solution of the ordinary differential equation which is the central part of the TBLE model. Although the tri-diagonal matrix system in itself can be solved with relatively little computational effort, the entire solving procedure requires greater computational resources due to the iterative solution process used to obtain converged values of the wall fluxes. For the current test case, the total additional cost of the simulation is between 10% and 15% compared to the log-law computation, as shown in Table 4.2. However, this additional computational cost remains negligible when compared to the resources that would be needed to perform a wall-resolved LES of the same setup. In addition, this increase in computational cost should be balanced by the expected improvement in physical accuracy, especially in more challenging scenarios where the pressure gradient plays a significant role. It is also important to note that this additional cost depends on several factors, such as the number of wall cells compared to the total number of cells in the domain, the partition load balancing, and the pressure gradient conditions, which can alter the speed at which the wall model converges. In that particular setup, around 10% of the total number of cells of the domain are wall cells.

4.3 Validation on a periodic hill setup

After validating the TBLE wall model implementation in AVBP with the turbulent channel test case, the focus is turned to the periodic hill configuration described in part 3.2. This test case is particularly challenging for wall-model simulations due to the geometry-induced streamwise pressure gradient. The main challenge in this study is the appropriate prediction of the recirculation bubble and its reattachment location on the lower wall. The prediction quality of these features can help highlight the performance differences between the TBLE model and the simpler log-law model. Due to the periodic nature of this test case, the results can be averaged along the spanwise direction to produce 2D fields or 1D profiles that will be analyzed in this section. For the TBLE model, temporal smoothing of the pressure gradient is applied, with a characteristic timescale $T_{av} = h_{wm}/(\kappa u_\tau)$, where h_{wm} is the average cell size above each wall and u_τ is the wall friction velocity estimated at the top of the hill. The reference data to be compared with the present simulations are taken from wall-resolved LES results of Gloerfelt and Cinnella [61]. These have shown good agreement with the experimental results of Rapp and Manhart [142] and other wall-resolved LES studies [193].

All the computations presented in this section are computed using the TTGC [37] numerical scheme and the Smagorinsky SGS model [158] available in AVBP.

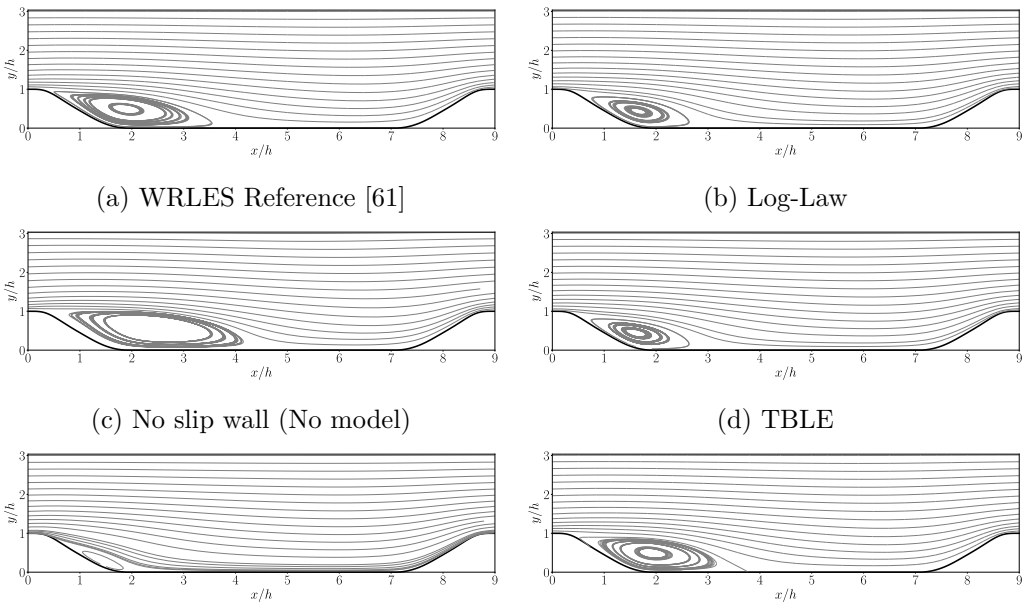

(a) WRLES Reference [61]

(b) Log-Law

(c) No slip wall (No model)

(d) TBLE

(e) Slip wall (No model)

(f) TBLE w/ pressure gradient

Figure 4.7: Average streamlines of the periodic hill ($\mathrm{Re}_b = 10\,600$) for the different models tested.

The first set of results focuses on the average streamlines for the lowest Reynolds number, $Re = 10\,600$, as shown in Fig 4.7. These qualitative visualizations allow us to evaluate the performance of the different simulations by comparing them with the wall-resolved LES (WRLES) results from Gloerfelt and Cinnella [61] shown in Fig. 4.7a, which serve as the reference solution. The results on the LES mesh without wall models (both no-slip and slip boundary conditions) clearly illustrate the necessity of using wall models for LES on these types of meshes. Without wall models, the no-slip condition leads to a vastly overestimated recirculation zone, while the slip wall condition almost completely eliminates recirculation, both of which produce unrealistic results. However, when wall models are used, the predictions are improved, especially in terms of recirculation bubble and reattachment lengths, as shown in Fig. 4.7. Differences in terms of recirculation prediction can also be observed when comparing the performance of the different wall models. The TBLE model with the inclusion of the pressure gradient term performs best, giving results closest to the WRLES reference while the log-law and TBLE without the pressure gradient effects are less accurate. This highlights the relevance of including the pressure gradient effect in the wall model, while the similarity between the log-law model and the TBLE model without pressure gradient effects is in fact expected. Indeed, the TBLE equation without the pressure gradient term reduces to the same behavior as the log-law model in the inertial region, and thus to almost the same prediction.

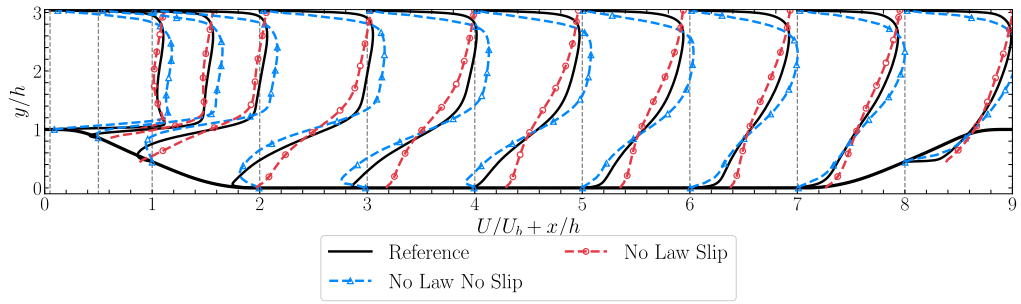

Figure 4.8: Average streamwise velocity over the periodic hill case without wall law compared to WRLES reference [61] for $\mathrm{Re}_b = 10\,600$.

For a more quantitative assessment of the performance of the different wall models, 1D velocity profiles are extracted at various streamwise locations where reference data from Gloerfelt and Cinnella [61] are available. These locations correspond to $x/h = 0.05$, $x/h = 0.5$, followed by evenly spaced locations up to $x/h = 8$. As can be seen from Fig. 4.8, the simulations performed on the WMLES mesh without wall modeling give poor predictions, especially in the vicinity of both the top and bottom walls. Without a proper boundary layer model, the flow dynamics cannot be well captured within the entire domain on such a coarse mesh. The use of wall models improves significantly the results as seen in Fig. 4.9, where differences between wall models also appear. The TBLE model that includes the pressure gradient term shows much better performance compared to models that neglect this effect, as it produces velocity profiles in good agreement with the WRLES data of Gloerfelt and Cinnella [61], especially in the recirculation zone.

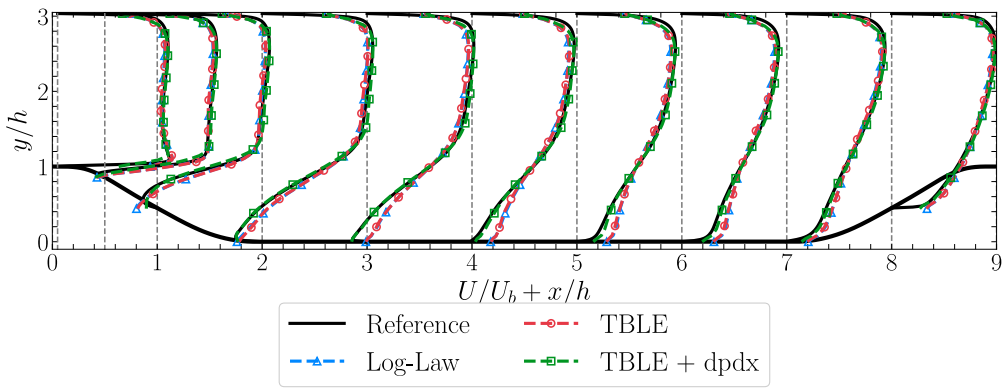

Figure 4.9: Average streamwise velocity over the periodic hill case compared to WRLES reference[61] for $\mathrm{Re}_b = 10\,600$.

The time and spanwise averaged wall friction coefficient, $C_f = \langle\overline{\tau_w}\rangle \,/\, (0.5\rho U_b^2)$ is plotted along both the top (W_1) and bottom (W_2) in Fig. 4.10. The examination of the friction profile along the top wall in Fig. 4.10a shows that unlike in the turbulent channel case, the friction profile is not uniform along the streamwise direction, mainly due to the change in fluid velocity resulting from the change in cross-section. It can also be noted that the pressure gradient influences the friction levels on this top wall, as the results obtained with the TBLE wall model taking the pressure gradient into account differ from the predictions of wall models not considering it. The evolution of the friction coefficient along the bottom wall W_2 in Fig. 4.10b further illustrates the improvement brought by the inclusion of pressure gradient into the TBLE wall model. In the recirculation zone, the wall friction is predicted much more accurately by the TBLE model with pressure gradient effects compared to both the log-law model and the TBLE without the pressure gradient. In particular, the model gives a more representative recirculation zone after the hill for x/h from 1 to 4, as well as an improvement in capturing the friction peak near the second constriction around $x/h = 8.5$. The position of the reattachment point further confirms the superiority of the TBLE wall model with pressure gradient in capturing this flow separation and reattachment. In contrast, the log-law model consistently underpredicts friction levels, especially in the recirculation zone and at the second peak after the geometry constriction. However, while the TBLE model with pressure gradient provides clear improvements in this setup, some of the fine details of the flow feature are still beyond the reach of the WMLES approaches tested here, including the TBLE model. In particular, the WMLES fail to accurately capture the wall friction at the top of the hill. Additionally, none of the models are able to reproduce the minor recirculation that occurs just before the friction peak on the uphill side of the constriction around $x/h = 7$.

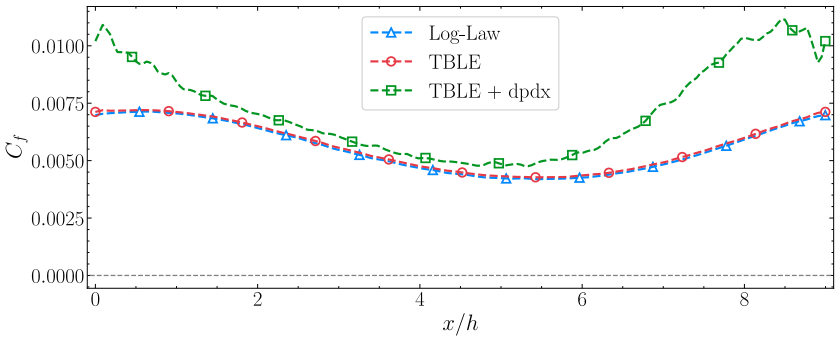

(a) Top wall friction coefficient.

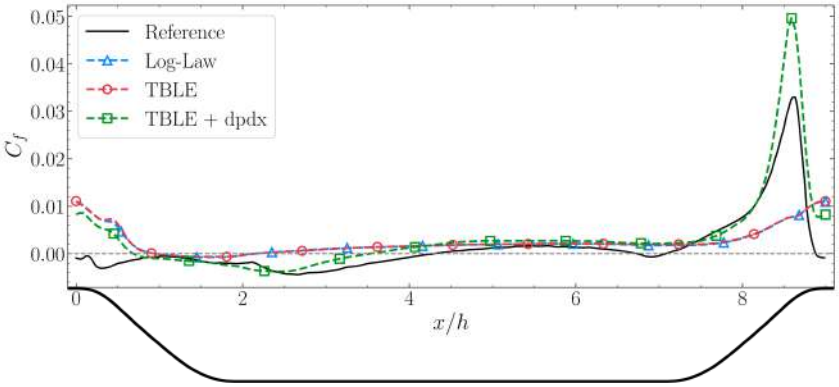

(b) Bottom wall friction coefficient.

Figure 4.10: Comparison of the friction coefficient C_f along the streamwise direction x_h for the different wall models at $Re_\theta = 10600$ in the periodic hill flow.

At higher Reynolds numbers, specifically $\mathrm{Re}_b = 19\,000$ and $37\,000$, the results are consistent with the patterns observed at the lower Reynolds number (Re=10 600).

The 1D velocity profiles, shown in Fig. 4.11, show a close agreement between the predictions from the TBLE wall model and the reference wall-resolved LES from Gloerfelt and Cinnella [61]. In contrast, the log-law model underestimates both the thickness and length of the recirculation bubble, which shows its limitation in accurately treating separated flows subjected to pressure gradients.

The same trend is further evidenced in the friction coefficient profiles along the bottom wall shown in Fig. 4.12. The log-law model struggles to capture the recirculation bubble while the TBLE model with the pressure gradient term recovers its size more accurately, thus illustrating the benefits of incorporating the pressure gradient effects. Examining the wall friction profiles in Fig. 4.12 also reveals that the log-law model underestimates both the magnitude and location of the wall friction peak before the second hill of the setup, just as was the case for the lower Reynolds number setup. On the other hand, the TBLE model recovers both the correct position and a more correct level of friction.

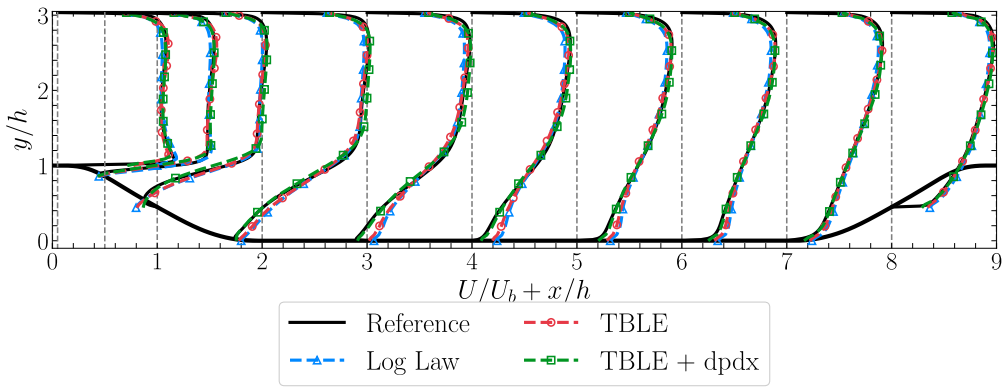

(a) Re 19000

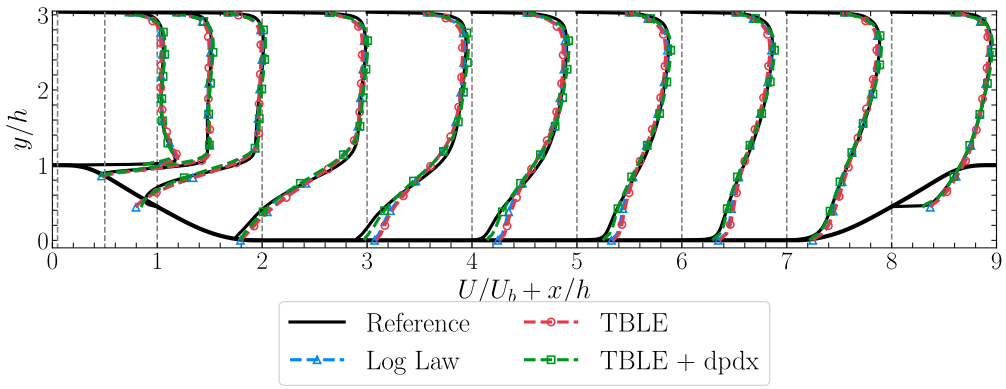

(b) Re 37000

Figure 4.11: Average streamwise velocity over the periodic hill case compared to WRLES reference[61] for higher Reynolds numbers.

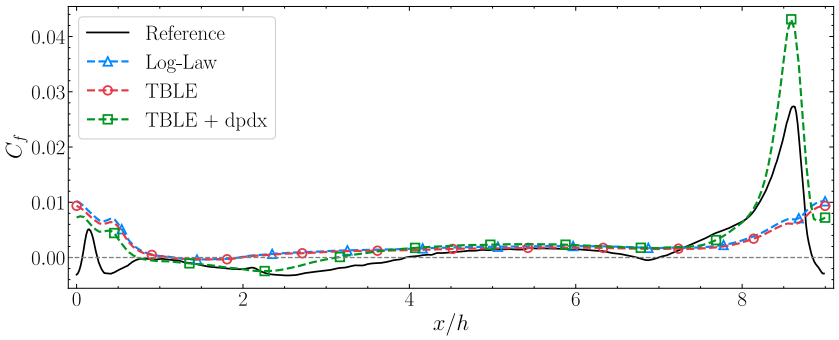

(a) Re_b 19000

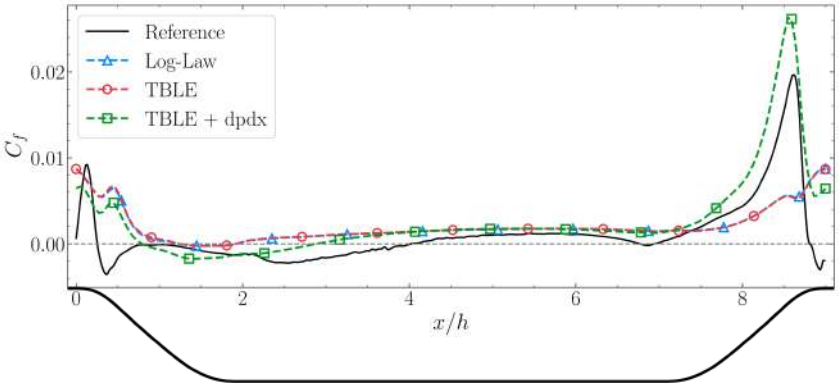

(b) Re_b 37000

Figure 4.12: Friction coefficient on the bottom wall of the periodic hill along the streamwise direction compared to the WRLES reference [61] for higher Reynolds numbers.

Re_b	WRLES [61]	Exp. [142]	Log-Law (Error)	TBLE w/ $\frac{dP}{dx}$ (Error)
10600	4.305	4.21	2.08 (51%)	3.53 (18%)
19000	3.95	3.94	1.94 (50%)	3.12 (21%)
37000	4.0	3.76	1.89 (53%)	2.89 (23%)

Table 4.3: Recirculation zone reattachment length on the Periodic Hill with relative errors computed with respect to the WRLES [61].

The results presented in Table 4.3 summarizing the reattachment lengths strengthen this conclusion. While the TBLE model results do not perfectly match the experimental or WRLES results, its performance is significantly superior to that of the log-law model.

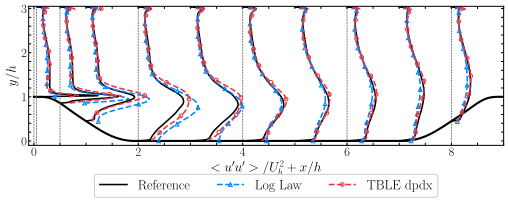

(a) $\mathrm{Re}_b = 10600$; $\langle u'u' \rangle / U_b^2$

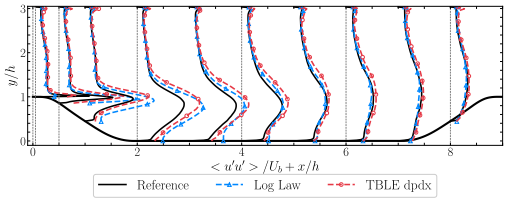

(b) $\mathrm{Re}_b = 19000$; $\langle u'u' \rangle / U_b^2$

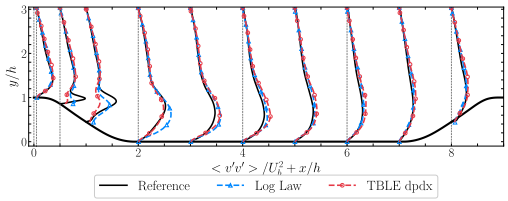

(c) $\mathrm{Re}_b = 10600$; $\langle v'v' \rangle / U_b^2$

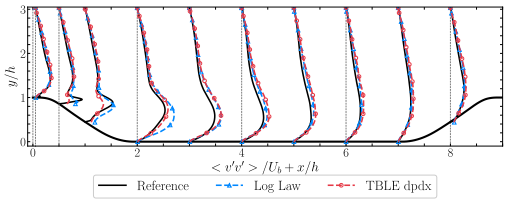

(d) $\mathrm{Re}_b = 19000$; $\langle v'v' \rangle / U_b^2$

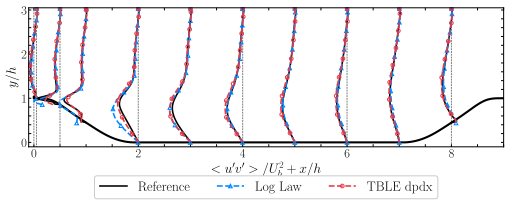

(e) $\mathrm{Re}_b = 10600$; $\langle u'v' \rangle / U_b^2$

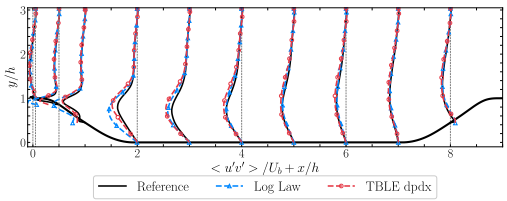

(f) $\mathrm{Re}_b = 19000$; $\langle u'v' \rangle / U_b^2$

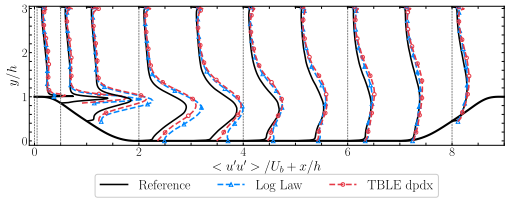

(g) $\mathrm{Re}_b = 37000$; $\langle u'u' \rangle / U_b^2$

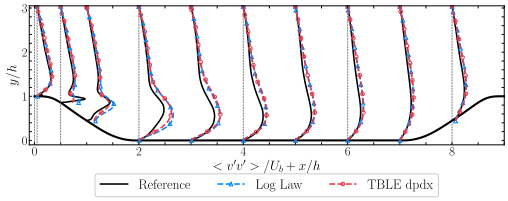

(h) $\mathrm{Re}_b = 37000$; $\langle v'v' \rangle / U_b^2$

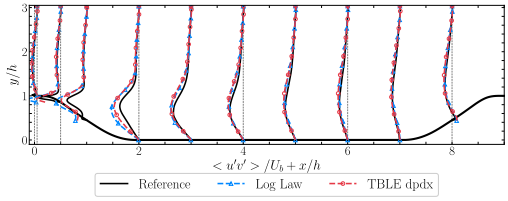

(i) $\mathrm{Re}_b = 37000$; $\langle u'v' \rangle / U_b^2$

Figure 4.13: Turbulence intensities over the periodic hill setup compared to reference WRLES [61].

Higher order statistics of the velocity profiles shown in Fig.4.13 provide further quantifiable insight. When comparing the log-law model with the TBLE wall model, some differences can be observed especially in the region with the highest shear levels, although no significant trend can be drawn. This is expected since no specific treatment is applied in these models to ensure accurate physical turbulence predictions. This outcome is also consistent with the findings for the turbulent channel case presented in part 4.2. This conclusion holds for all three Reynolds numbers tested in this thesis. It is also important to note that the prediction of turbulent intensities is sensitive to the grid resolution and the SGS model used, as highlighted by Gloerfelt and Cinnella [61]. This aspect is not specifically addressed here and the use of the Smagorinsky SGS model, together with the relatively coarse grid designed for wall-modeled LES, means that perfect agreement with the reference wall-resolved LES is not expected.

Re_b	Case	Simulated convective times	Cost (core.h)	Add. Cost
10600	Log Law	50	696	
	TBLE ($\partial P/\partial x$ EMA)	50	892.3	22%
19000	Log Law	50	391.8	
	TBLE ($\partial P/\partial x$ EMA)	50	544.4	28%
37000	Log Law	85	274.5	
	TBLE ($\partial P/\partial x$ EMA)	85	434.8	37%

Table 4.4: Computational cost of the periodic hill.

As in the turbulent channel case, the use of the TBLE wall model induces an additional computational cost in this periodic hill setup. Table 4.4 provides a summary of the computational cost for simulations with the TBLE model including pressure gradient effects compared to the classical log-law computations. The results show an additional cost ranging from 22% to nearly 40% more than the log-law computations. This is slightly higher than the additional cost observed in the turbulent channel case. As already explained, the computational cost induced by the TBLE wall model can be influenced by several parameters. Although in that case, wall cells represent only about 2% of the total number of cells, partition load balancing also plays a significant role in the wall model's computational cost. In addition, pressure gradient conditions also have an impact on the convergence time of the wall model, further impacting its cost. Despite the non-negligible cost increase, the significant improvements in prediction accuracy provided by the TBLE wall model justify this trade-off. Besides, future efforts to optimize the wall model code may be able to mitigate this added computational cost.

Chapter 5

A model for improving wall-model and LES coupling: SGS model stochastic forcing

5.1 Background

Following the presentation of the TBLE model for addressing the physical modeling challenges in WMLES, attention is directed to the issue of log-layer mismatch. As discussed in part 2.3.2, coupling LES frameworks with wall models is not inherently straightforward, and challenges like log-layer mismatch frequently arise. This issue is particularly evident in the turbulent channel test case studied earlier using the AVBP solver. The problem is first analyzed in the context of the logarithmic law of the wall, before evaluating the proposed solution using the TBLE model in subsequent sections (starting from Section 5.3.5). A notable feature of the turbulent channel case is the dependence of results on the choice of the subgrid-scale (SGS) model. Figure 5.1 demonstrates this dependency when employing the logarithmic law wall model. The Smagorinsky SGS model exhibits the best overall agreement with reference data, whereas the Sigma and WALE models, previously introduced in section 1.3.3, show a log-layer mismatch, inducing poorer performance in this context.

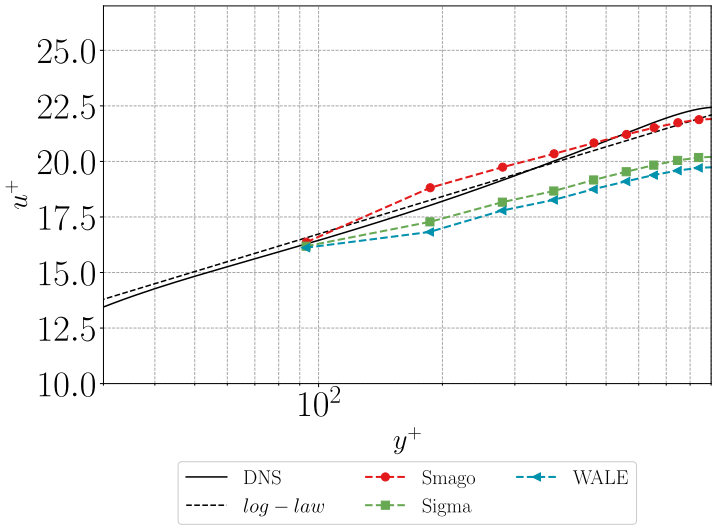

Figure 5.1: Average velocity profiles on the turbulent channel at $\mathrm{Re}_\tau = 934$ for different SGS models obtained with the log-law; DNS data from Hoyas and Jiménez [73].

The effect of this mismatch can be quantified in terms of errors in the bulk Reynolds number, compared against the expected value obtained from the Kármán-Nikuradse correlation (detailed in part 3.2.1). These results are summarized in Table 5.1 and confirm that the WMLES simulations performed with the Sigma and WALE SGS models yield less accurate bulk Reynolds numbers compared to those obtained using the Smagorinsky model.

Re_τ	Case	$Re_{b,Dh}$	$Re_{b,Dh,KNc}$	Error
	Smago	35520		<1%
934	Sigma	33458	35485	11%
	WALE	35667		1%

Table 5.1: Wall friction results for the turbulent channel comparing the different SGS models

This discrepancy highlights the lack of robustness of WMLES when moving from one LES context and SGS model to another. It underlines the need for refining the behavior of SGS models in near-wall regions to improve reliability. In particular, this is crucial to take full advantage of the better properties of the Sigma and WALE models, discussed in section 1.3.3. To this end, the work conducted in this thesis focuses on developing and enhancing a stochastic forcing approach to modify SGS behavior near walls, building upon the methodology introduced by Blanchard et al. [14].

5.2 Description of the model

As exposed above, the work done in this thesis to improve the coupling between the SGS models and the wall models is based upon the previous work of Blanchard et al. [14]. Their model addresses the log-layer mismatch observed in turbulent channel simulations when using the Sigma or WALE SGS models instead of the Smagorinsky model. This is first examined in the context of the use of the logarithmic law wall model.

Figure 5.2 illustrates the different behavior of each SGS model tested in this context, showing a clear deviation of the Sigma and WALE models from the Smagorinsky model. This difference is expected since, as laid out in part 1.3.3.1, only the WALE and Sigma models were built to reproduce the turbulence's correct near-wall behavior. However, this holds true only when simulations are well resolved, and the near-wall cells are entirely within the viscous sublayer, where turbulent activity decays as described in part 1.3.3.1. In the WMLES context, however, the near-wall grid is typically too coarse to ensure that the turbulence is correctly resolved. Additionally, the first near-wall cell often spans over several orders of magnitude in y^+, with a significant portion located in the logarithmic region. In this region, the SGS model must predict a non-zero turbulent viscosity. The absence of this adjustment explains why the Smagorinsky model performs better in WMLES, while the Sigma and WALE models exhibit a pronounced log-layer mismatch.

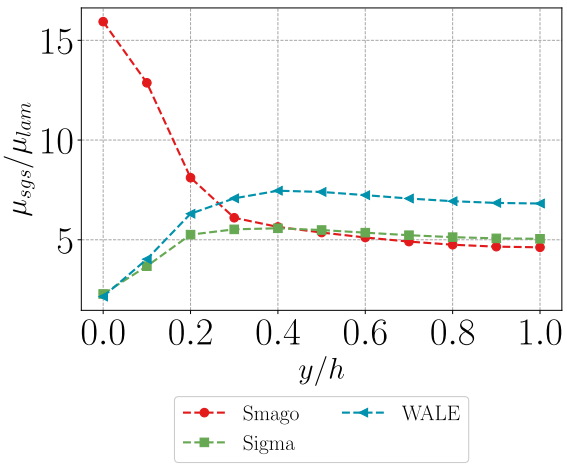

Figure 5.2: Sub-Grid viscosity profiles on the turbulent channel at $\mathrm{Re}_\tau = 934$ for different SGS models.

The log-layer mismatch observed here appears in fact as an artifact of how the SGS models behave near the wall. The Sigma and WALE models were designed to predict near-zero SGS viscosity in near-wall cells, which is appropriate for wall-resolved LES but incorrect in the WMLES context. These observations call for a correction to the Sigma and WALE models when applied to WMLES.

5.2.1 Original stochastic forcing model

The approach proposed by Blanchard et al. [14] modifies the computation of the turbulent viscosity exclusively in near-wall cells, while the behavior of the SGS models in the rest of the domain remains unchanged. The method introduces artificially generated turbulent activity within the near-wall cells through stochastic forcing of the velocity gradients. This method takes advantage of the general form of the viscosity shared by all the SGS models of AVBP discussed here:

$$\nu_{sgs} = (C_m \Delta)^2 \mathrm{OP}_m \tag{5.1}$$

where C_m is a model-specific constant, Δ represents the filter width related to the grid size, and OP_m is a model-specific operator that depends on the velocity gradients, as detailed in part 1.3.3. Because OP_m inherently relies on velocity gradients, introducing a stochastic forcing to these gradients directly influences the SGS viscosity ν_{sgs}.

The purpose of this stochastic forcing is to give the SGS models more representative velocity gradients. The predicted velocity gradients in WMLES in coarse near-wall cells are not necessarily representative of the true turbulent activity. Instead, with the introduction of stochastic perturbations, the SGS models can estimate u_{sgs} better and improve the physical accuracy of the simulation. It is important to emphasize here that this stochastic forcing only affects the computation of the SGS

viscosity, while the rest of the flow parameters, such as the actual resolved velocity gradients, remain unchanged, ensuring that the stochastic adjustment is limited to the SGS model computations.

The core principle of the model lies in modifying the velocity gradients used by the SGS model according to the following equation:

$$\left(\frac{\partial \widetilde{u}_i}{\partial x_j}\right)_{\text{corr}} = \left(\frac{\partial \widetilde{u}_i}{\partial x_j}\right)_{LES} + \left(\frac{\partial u_i'}{\partial x_j}\right) \tag{5.2}$$

where

- $\left(\frac{\partial \widetilde{u}_i}{\partial x_j}\right)_{\text{corr}}$ is the corrected velocity gradient used in the computation of the SGS viscosity.
- $\left(\frac{\partial \widetilde{u}_i}{\partial x_j}\right)_{LES}$ represent the resolved velocity gradients of the LES.
- $\left(\frac{\partial u_i'}{\partial x_j}\right)$ is the stochastic fluctuation in the velocity gradients introduced by the model.

In this approach, the fluctuations $\left(\frac{\partial u_i'}{\partial x_j}\right)$ are prescribed at each iteration using random number generation. To ensure physical relevance, the statistical properties of these random fluctuations must be defined over time. Specifically:

- The mean of the fluctuations: it is set to zero, ensuring that the stochastic component only introduces variability around the unmodified LES velocity gradients without biasing the results.
- The standard deviation $\sigma = \sqrt{\overline{\left(\frac{\partial u_i'}{\partial x_j}\right)^2}}$. It quantifies the intensity of the fluctuations.

To prescribe a physically relevant standard deviation σ, a link between the turbulent kinetic energy and the external LES velocity is established. First, in the RANS context used in the wall model framework, the mixing length model for turbulent viscosity [138, p. 289] writes:

$$\nu_t = \ell_m^2 \left|\frac{\mathrm{d}\overline{u}}{\mathrm{d}y}\right|, \tag{5.3}$$

where the mixing length ℓ_m can be written $\ell_m = \kappa y$ within the logarithmic and overlap regions [176] and where $\kappa = 0.41$ is the von Kármán constant. It is also known that, within the logarithmic zone of the boundary layer, $\frac{\partial u}{\partial y} = \frac{u_\tau}{\kappa y}$, which means that the turbulent viscosity can be written as

$$\nu_t = u_\tau \kappa y. \tag{5.4}$$

Alternatively, the turbulent viscosity can also be modeled using the turbulent kinetic energy k [138, p. 369]:

$$\nu_t = C_\mu^{1/4}\sqrt{k}\ell_m \tag{5.5}$$

where the constant of the model is $C_\mu = 0.09$.

When combining equations (5.4) and (5.5), the following expression is obtained:

$$u_\tau \kappa y = C_\mu^{1/4}\sqrt{k}\ell_m, \tag{5.6}$$

which can be recast as:

$$k = \frac{u_\tau^2}{\sqrt{C_\mu}} = \frac{\tau_w}{\rho\sqrt{C_\mu}}. \tag{5.7}$$

To relate the turbulent kinetic energy to the velocity gradients, a model for the dissipation rate ε [138, p. 370] can be used:

$$\varepsilon = \frac{C_\mu k^2}{\nu_t}. \tag{5.8}$$

This expression is valid within the logarithmic region of the boundary layer and can be rewritten using eq. (5.4):

$$\varepsilon = \frac{C_\mu k^2}{u_\tau \kappa y} = \frac{C_\mu k^2}{\kappa \nu_w y^+}, \tag{5.9}$$

where y^+ is the wall distance in wall units and ν_w the laminar viscosity at the wall.

To relate the kinetic energy dissipation rate ε with the velocity gradients, the assumption of homogeneous isotropic turbulence (HIT) was used in the work of Blanchard [13]. Although being a strong assumption and not necessarily true within the entire height of the boundary layer, which is subject mainly to shear effects, it can still be justified under certain conditions. In particular, Schlichting and Gersten [151] argue that the expression for the dissipation rate ϵ derived under HIT assumptions remains valid in cases where the turbulence is locally isotropic and characterized by significant velocity gradient fluctuations $\partial u_i'/\partial x_j$. These conditions are typically encountered in the inertial region of the boundary layer. Under these conditions, the expression of Taylor [166] can be used:

$$\varepsilon = 15\nu\overline{\left(\frac{\partial u'}{\partial x}\right)^2}. \tag{5.10}$$

Finally, combining equations (5.9) and (5.10) allows to write:

$$15\nu\overline{\left(\frac{\partial u'}{\partial x}\right)^2} = \frac{C_\mu k^2}{\kappa \nu_w y^+}, \tag{5.11}$$

which can be recast using eq. (5.7) as

$$\overline{\left(\frac{\partial u'}{\partial x}\right)^2} = \frac{\tau_w^2}{15\mu_w^2 \kappa y^+}. \tag{5.12}$$

In the context of HIT, Taylor [166] also demonstrated that

$$\overline{\left(\frac{\partial u'}{\partial x}\right)^2} = \frac{1}{2}\overline{\left(\frac{\partial u'}{\partial y}\right)^2} = \frac{1}{2}\overline{\left(\frac{\partial u'}{\partial z}\right)^2}, \tag{5.13}$$

$$\overline{\left(\frac{\partial u'}{\partial x}\right)^2} = \overline{\left(\frac{\partial v'}{\partial y}\right)^2} = \overline{\left(\frac{\partial w'}{\partial z}\right)^2}, \tag{5.14}$$

implying the following expressions:

$$\sigma_{ij} = \sqrt{\overline{\left(\frac{\partial u_i'}{\partial x_j}\right)^2}} = \frac{\tau_w}{\sqrt{15\kappa y^+ \mu_w}} \quad \text{for i} = j, \tag{5.15}$$

$$\sigma_{ij} = \sqrt{\overline{\left(\frac{\partial u_i'}{\partial x_j}\right)^2}} = \sqrt{2}\frac{\tau_w}{\sqrt{15\kappa y^+ \mu_w}} \quad \text{for i} \neq j. \tag{5.16}$$

Equations (5.15) and (5.16) constitute the standard deviation of the fluctuations of each velocity gradient component needed to complete the model.

In summary, the model developed by Blanchard et al. [14] aims at altering the SGS model's behavior in the near-wall cells by increasing the turbulent activity within these cells. The model relies on stochastic fluctuations applied at every iteration to each velocity gradient component that are designed to follow a normal distribution with zero mean. In order to compute these fluctuations, a random number ζ uniformly distributed between 0 and 1 is first calculated. This random number is then transformed by the inverse cumulative distribution function associated with the normal distribution, using the standard deviation σ_{ij} derived previously. The inverse cumulative function can be written with the error function, erf, so that the fluctuations generated at each iteration are given by:

$$\left(\frac{\partial u_i'}{\partial x_j}\right)(\zeta) = \frac{\tau_w}{\sqrt{15\kappa y^+ \mu_w}}\sqrt{2}\text{erf}^{-1}(2\zeta - 1) \quad \text{for i} = \text{j} \tag{5.17}$$

$$\left(\frac{\partial u_i'}{\partial x_j}\right)(\zeta) = \frac{\tau_w}{\sqrt{15\kappa y^+ \mu_w}}2\text{erf}^{-1}(2\zeta - 1) \quad \text{for i} \neq j. \tag{5.18}$$

As already laid out, these fluctuations are then added to the computed LES velocity gradients according to equation (5.2) for the computation of the SGS model viscosity to increase the levels of viscosity for the Sigma and WALE model to better represent the actual turbulent state of the boundary layer.

5.2.2 Improvements to the model

After presenting the foundations of the model developed by Blanchard et al. [14], this thesis introduces enhancements aimed at improving its performance and applicability. These contributions are guided by an analysis of results from turbulent channel simulations (to be detailed in the following section) and theoretical considerations. The proposed enhancements are twofold:

- Selective activation of the model on the wall-normal velocity gradient component only
- Spatial extension of the model activation range in cells not adjacent to the wall

The first modification aims at focusing the stochastic forcing to act only on the fluctuations of the wall-normal velocity gradient component. The wall-normal component of velocity, v, is indeed directly constrained by the no-penetration Dirichlet condition at the wall, where both its magnitude and fluctuation are drastically diminished in the near-wall region. In contrast, the streamwise (u) and spanwise (w) velocity components are less affected because the wall model employs a slip-wall condition for tangential velocity. This phenomenon can be analyzed through the dissipation term of the Reynolds stress budget equation [73]:

$$\epsilon_{ij} = -2\nu \left\langle \frac{\partial u_i'}{\partial x_k} \frac{\partial u_j'}{\partial x_k} \right\rangle \tag{5.19}$$

where $\langle \cdot \rangle$ denotes temporal and spatial averaging in the directions parallel to the wall. Specifically, the diagonal terms of the dissipation tensor can be expressed as:

$$\epsilon_{11} = -2\nu \left\langle \frac{\partial u'^2}{\partial x_k^2} \right\rangle ; \epsilon_{22} = -2\nu \left\langle \frac{\partial v'^2}{\partial x_k^2} \right\rangle ; \epsilon_{33} = -2\nu \left\langle \frac{\partial w'^2}{\partial x_k^2} \right\rangle \tag{5.20}$$

In the LES computations, an approximation of the diagonal terms of this ϵ matrix can be obtained by computing the root mean square (RMS) of the velocity gradients, expressed as:

$$\tilde{\epsilon}_{11} = -2\nu \left\langle \left(\frac{\partial u}{\partial x_k} \right)'^2 \right\rangle ; \tilde{\epsilon}_{22} = -2\nu \left\langle \left(\frac{\partial v}{\partial x_k} \right)'^2 \right\rangle ; \tilde{\epsilon}_{33} = -2\nu \left\langle \left(\frac{\partial w}{\partial x_k} \right)'^2 \right\rangle \tag{5.21}$$

These terms can be seen plotted in Figure 5.3 along the wall-normal direction of the turbulent channel presented in part 3.2.1 in WMLES. This figure highlights a significant reduction in wall-normal velocity fluctuations (ϵ_{22}) compared to the fluctuations in the wall-tangent directions (ϵ_{22} and ϵ_{33}) whereas the DNS results of Hoyas and Jiménez [73] in Figure 5.4 show smaller differences in fluctuation levels between the wall-normal and wall-tangent directions within the logarithmic region. The several orders of magnitude difference observed in the LES computations (Figure 5.3) suggest that the wall-normal velocity component requires additional fluctuations to correct the underestimation and produce accurate levels of SGS viscosity while the fluctuation levels in the wall-tangent components of the velocity gradients are already sufficient. This strategy is further validated by observations from turbulent channel results obtained using different versions of the model, which are detailed in the following sections.

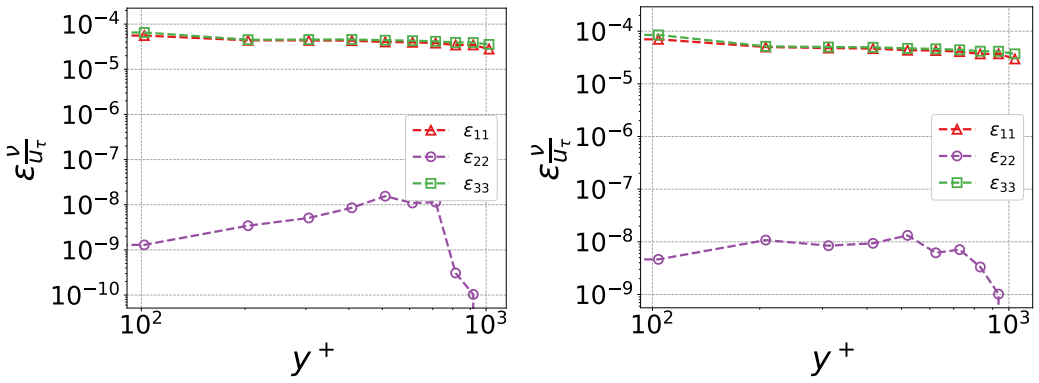

(a) Sigma (b) WALE

Figure 5.3: Approximated dissipation rate of turbulent kinetic energy computed with the RMS of the velocity gradients for the LES computation of a turbulent channel flow at $\mathrm{Re}_\tau = 934$.

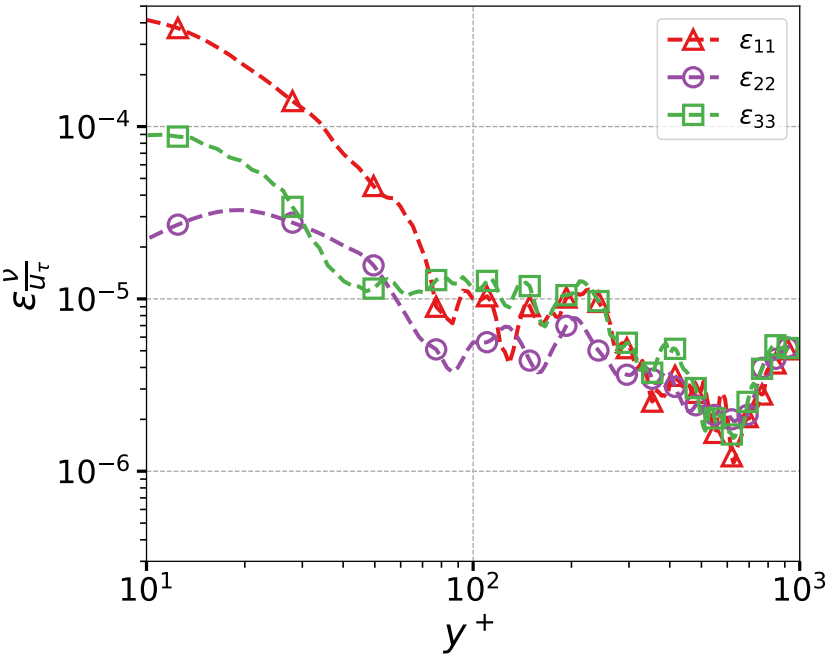

Figure 5.4: Dissipation rate of turbulent kinetic energy computed in the DNS of a turbulent channel flow at $\mathrm{Re}_\tau = 934$, from Hoyas and Jiménez [73].

In practice, this selective activation requires modifying equations (5.17) and (5.18) as follows:

$$\left(\frac{\partial u_i'}{\partial x_j}\right)(\zeta) = \frac{\tau_w}{\sqrt{15\kappa y^+}\mu_w}\sqrt{2}\mathrm{erf}^{-1}(2\zeta - 1) \quad \text{for i} = 2 = \text{j}, \tag{5.22}$$

$$\left(\frac{\partial u_i'}{\partial x_j}\right)(\zeta) = \frac{\tau_w}{\sqrt{15\kappa y^+}\mu_w}2\mathrm{erf}^{-1}(2\zeta - 1) \quad \text{for i} = 2 \neq j, \tag{5.23}$$

$$\left(\frac{\partial u_i'}{\partial x_j}\right)(\zeta) = 0 \quad \text{for i} \neq 2, \tag{5.24}$$

where x_2 is the wall-normal direction, that has to be identified for each wall cell, and x_1 and x_3 are the wall tangent directions.

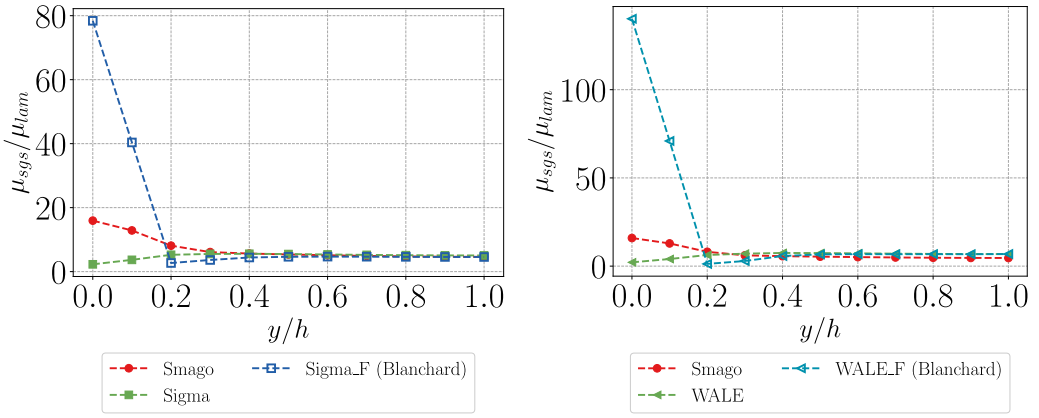

(a) (b)

Figure 5.5: Results of the fluctuations model on the turbulent channel (Re_τ = 934) in terms turbulent eddy viscosity for (a) Sigma and (b) WALE and added fluctuations Sigma_F and WALE_F.

The second modification of the model is designed to extend the spatial application of the fluctuation model beyond the first cell immediately adjacent to the wall. In its original form, the model imposes fluctuations in a very localized manner, resulting in abrupt transitions in sub-grid scale viscosity at the boundary between the first cell and those further from the wall. This behavior is illustrated in Figure 5.5 where the discontinuity created by the model dynamics at the third point away from the wall is clearly visible. The third point indeed corresponds to the first cell which is not directly touching the wall and thus the first cell which is not affected by the fluctuation model, which explains the sharp change in slope of the SGS viscosity profile in this location. This behavior can introduce non-physical features in the flow dynamics in this region. Additionally, the cells located directly above the first wall cell still fall within the logarithmic layer and also suffer from mesh under-resolution. It is hence justified to apply the fluctuation model in these cells

as well. The modification of the model proposed here smooths out the application of fluctuations over a larger area, avoiding undesirable effects reported above, and leading to better continuity for the model in the near-wall region, ensuring results that are more robust and physically consistent.

To apply the fluctuation model in an extended region above the wall, some adaptations to the model's implementation are necessary. To compute the fluctuations used in the SGS model according to equations (5.22) and (5.23) the knowledge of quantities such as y^+, τ_w, and the wall-normal direction is required. However, by default in AVBP, these values are only available at the wall-bounded cells. A searching and matching algorithm has then been developed in this thesis to make the required data available within the entire LES domain. The principle of this algorithm, illustrated in Figure 5.6, is as follows:

- For each node in the LES domain, the nearest node on a wall boundary is identified, and this matching is stored.
- The wall distance, defined as the distance between the current node and the nearest wall node, denoted y_w, is computed and assigned to the current node. Additionally, the wall normal components are stored if needed.

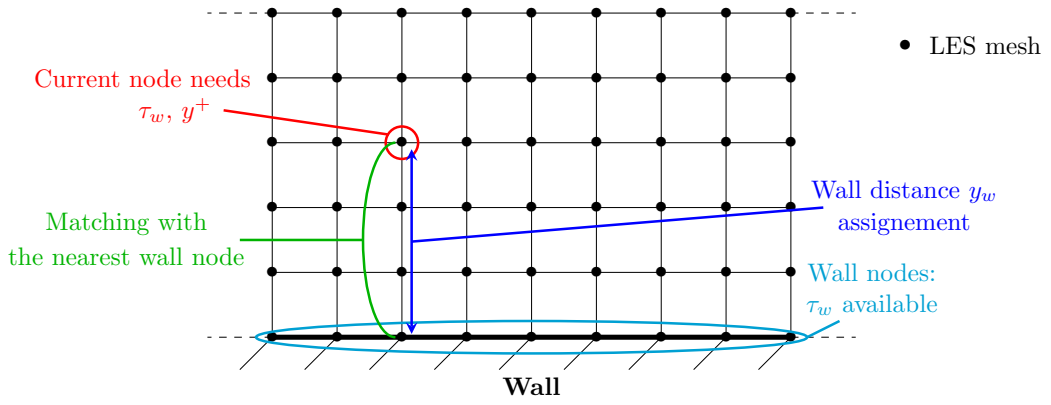

Figure 5.6: Illustration of the mesh node matching to the nearest wall for a structured mesh.

This algorithm also works for unstructured meshes, which are primarily used in AVBP, with the distance to the closest wall node being an approximation of the real wall distance, as visible in Fig. 5.7.

This process is performed once during the pre-processing phase to minimize the computational cost of this modification. Once this has been achieved, the LES computation can be carried out as usual except for the fluctuation model. To use the fluctuation model properly, it is necessary to fetch the wall friction τ_w from the flagged wall node during the pre-processing. This has to be done at every iteration because the wall friction τ_w is a time-varying quantity. With this data and the already calculated wall distance y_w, the value of y^+ can be computed as well.

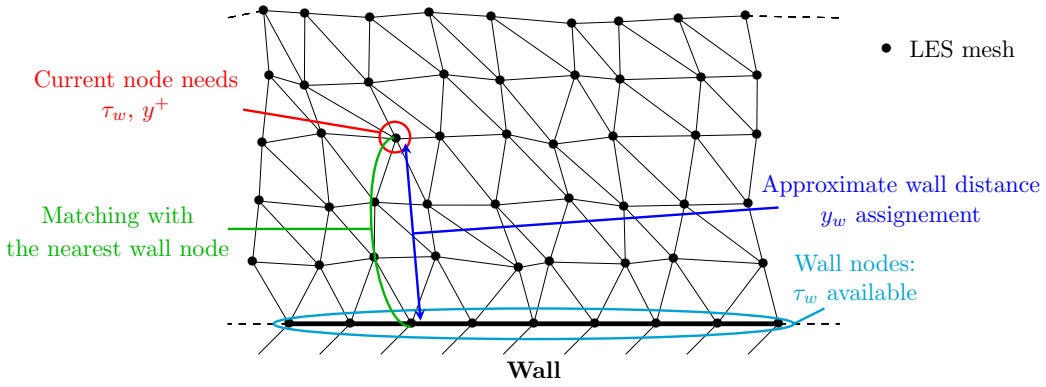

Figure 5.7: Illustration of the mesh node matching to the nearest wall for an unstructured mesh.

With these modifications, the fluctuation model can be applied to an arbitrary area of the domain. However, its application to the whole domain would be both inefficient and irrelevant. Two approaches have been implemented to define the area of application of the near-wall model:

- Application to the first two near-wall cells: This method smoothens the effects of the model by extending it to an additional cell compared with the initial version.
- Limitation by a maximum value of y^+: The model is applied in a zone defined by a maximum y^+. In this work, the limit is fixed to correspond to roughly four cells above the wall for the turbulent channel cases tested.

It is also worth noting that in all cases, the intensity of the fluctuations decreases progressively with increasing distance from the wall, in line with the $1/\sqrt{y^+}$ decay described in the model equations (5.22) and (5.23). This feature of the model ensures that it remains effective where it is most needed while reducing disruptive effects in areas where it becomes less relevant, away from walls.

The two model modifications implemented in this thesis produce the sub-grid viscosity profiles shown in Figure 5.8, where both limitations of the zone of application of the model have been tested on a turbulent channel case. The tested fluctuations model profiles appear in shades of purple, denoted in the legend by the notation $_F$, with the mention (V) indicating that it is applied only in the wall-normal direction, followed by the spatial range on which it is applied. As anticipated, reducing the fluctuation activity by restricting it to the normal component of the velocity gradients leads to a decrease in sub-grid viscosity near the wall compared with the initial model. The second modification, which extends the application of fluctuations to additional cells farther from the wall, results in an increased sub-grid viscosity in those regions. Furthermore, the activity of the sub-grid scale model associated with these fluctuations diminishes progressively with increasing distance from the wall, consistent with the $1/\sqrt{y^+}$ decay described in the model equations.

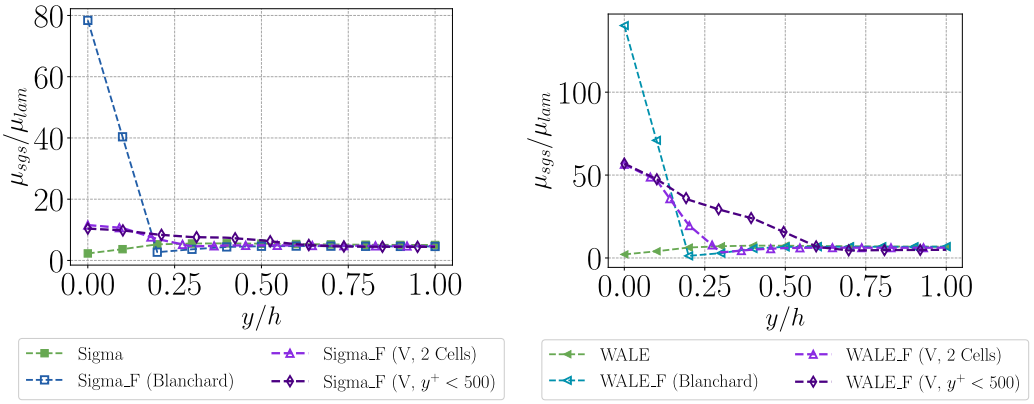

(a) (b)

Figure 5.8: Results of the improved versions of the fluctuations model on the turbulent channel ($\mathrm{Re}_\tau = 934$) in terms of turbulent eddy viscosity for (a) Sigma and (b) WALE.

Note that the behaviors of the Sigma and WALE models are different because the nature of the non-linear operators OP in equation (5.1) changes with the model. However, the modifications carried out in this work result in smoother and more realistic sub-grid viscosity profiles than those obtained with the original version, without the discontinuities present in the latter visible in Figure 5.5. These profiles are more physically realistic, and the improvement in the general performance of the model is discussed in the next section.

5.3 Model validation on a turbulent channel

Following the detailed presentation of the fluctuation model and its modifications in the previous section, its validation is performed using the turbulent channel configuration introduced in part 3.2.1. The turbulent channel serves as a robust benchmark thanks to its simple geometry, its frequent use in evaluating wall models, and the availability of high-fidelity DNS data. Because of these properties, it stands as an excellent test case to assess the performance and improvements brought by the proposed fluctuation model. The model is tested first using the logarithmic law of wall, before applying it with the TBLE wall model in Section 5.3.5.

5.3.1 Original model of Blanchard et al. [14]

To begin the validation, the assessment of the original fluctuation model introduced by Blanchard [13] is performed. This evaluation focuses on the streamwise velocity profiles over the channel for the intermediate Reynolds number $\mathrm{Re}_\tau = 934$, as presented in Figure 5.9.

The first thing to note is that the model fulfills its main function of mitigating log-layer mismatch. The velocity profiles are in better agreement with the

reference DNS data, confirming the effectiveness of the model in addressing this critical issue. This is further confirmed by the data of Table 5.2, comparing the bulk Reynolds number for each case and SGS model to the value predicted by the Kármán-Nikuradse correlation, as explained in chapter 4. The consequence of reducing the log-layer mismatch is directly reflected in a reduction of the bulk Reynolds number error from approximately 10% to a much more acceptable range.

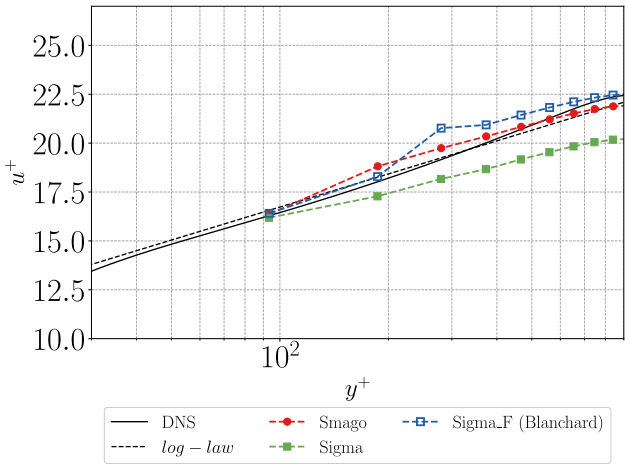

(a)

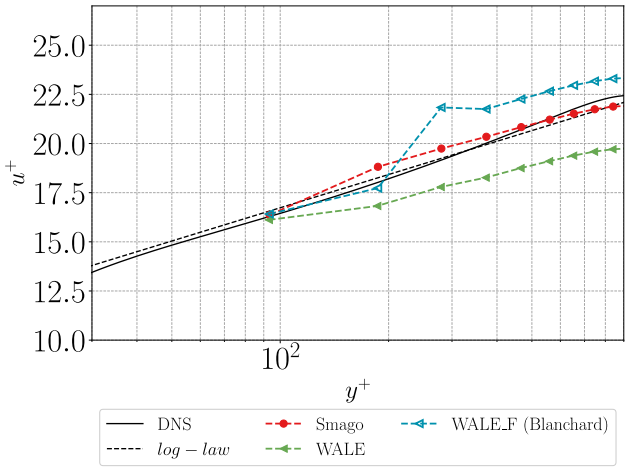

(b)

Figure 5.9: Average velocity profiles obtained on the turbulent channel (Re_τ = 934) with (a) Sigma and (b) WALE SGS models and with the fluctuations model (Sigma_F and WALE_F).

Re_τ	Case	$Re_{b,Dh}$	$Re_{b,Dh,KNc}$	Error
	Smago	61388		<1%
	Sigma	55560		9%
934	WALE	54235	61182	11%
	Sigma_F	63197		3%
	WALE_F	65053		5%

Table 5.2: Wall friction results for the turbulent channel at $Re_\tau = 934$ comparing the different SGS models with and without the fluctuations model.

On the other hand, despite these strengths, the original model also displays some weaknesses. One of them, as developed in the previous section, is the discontinuity in the sub-grid viscosity across the first cell off the wall, where the fluctuation model is on, and the neighboring cells, further away from the wall, where the model is not applied. The resulting discontinuity produces an unphysical behavior, which can be seen as a stall in the velocity profile at the third grid point from the wall. This problem is exacerbated by the too-large amplitude of fluctuations imposed in the first cell, since, as shown earlier, only the wall-normal component of fluctuations is really needed. In addition, the model response also differs among the two considered SGS formulations. The performance of the WALE model is poorer overall as it generates unphysically high velocity levels even beyond the third point above the wall.

To address the issues and discrepancies observed in the velocity profiles with the original fluctuation model, the enhanced version developed in this work, as described in part 5.2.2, has been implemented. This improved model is tested here on the turbulent channel case to establish if it is able to provide results that are closer to the reference data. To evaluate the impact of the various improvements, each modification is applied separately. This provides insight into the relative contribution of each improvement and whether both are necessary to achieve the desired performance.

5.3.2 Effect of wall-normal fluctuations

First, the modification that limits the impact of the fluctuation model to the wall-normal component of the velocity gradient is tested (Eqs. (5.22) to (5.24)). The velocity profiles, presented in Figure 5.10, indicate that this modification (plotted in orange), enhances the performance of both the Sigma and WALE SGS models over the original fluctuation model. While there is significant improvement, these changes are not enough on their own. The SGS viscosity profiles presented in Fig. 5.11 still experience an abrupt discontinuity, which is also reflected in a velocity profile discontinuity at the second or third grid point off the wall. This discontinuity is weaker than that in the original model —*i.e.* modifying the gradients of the three velocity components— but still unphysical, calling for further refinement.

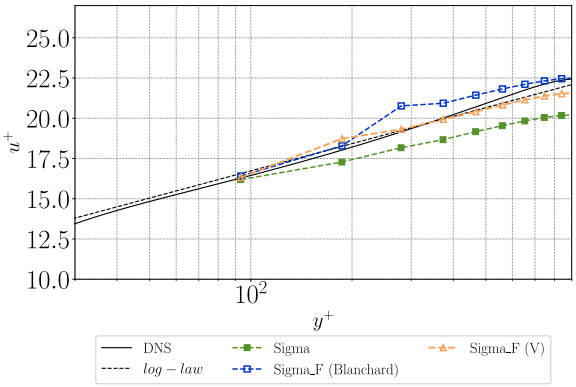

(a)

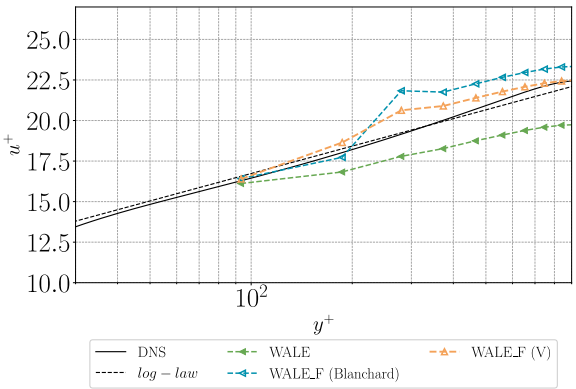

(b)

Figure 5.10: Average velocity profiles obtained on the turbulent channel ($Re_\tau = 934$) with (a) Sigma and (b) WALE SGS models and with the fluctuations model applied only to the wall-normal component.

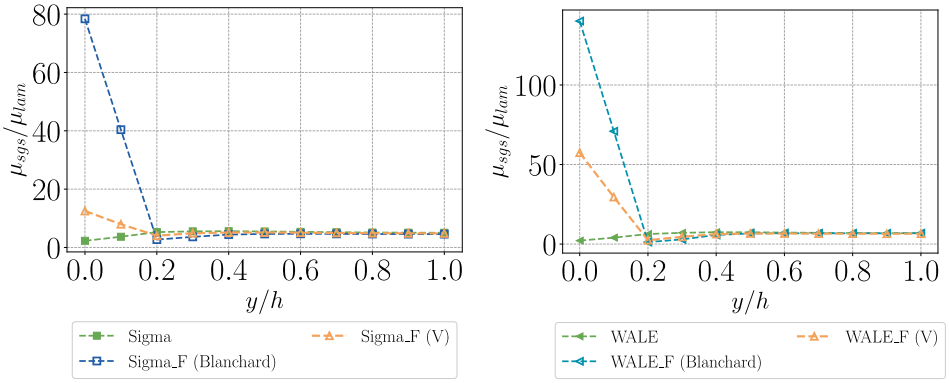

(a) (b)

Figure 5.11: Turbulent viscosity profiles obtained on the turbulent channel ($Re_\tau = 934$) with (a) Sigma and (b) WALE SGS models and with the fluctuations model applied only to the wall-normal component.

5.3.3 Effect of spatial extension of the model

Second, the impact of extending the application of the model to a wider region above the walls is evaluated. Specifically, the quality of the results produced is assessed when applying the fluctuation model up to $y^+ = 500$ or to the first two cells above the walls. The velocity profiles are shown in Figure 5.12, with the present implementation of the model plotted in shades of orange. These results demonstrate that this version of the model produces smoother velocity profiles compared to the original fluctuation model. However, this modification is not sufficient to produce a fully satisfying behavior. The velocity profiles still contain unphysical behavior, mainly in the near-wall region. While the velocity is underpredicted within the cells closer to the wall, it becomes overpredicted near the center of the channel. This is also reflected in the SGS viscosity profiles in Fig. 5.13. On the one hand, the too-high fluctuations applied within the first cells result in too high a viscosity near the wall, while abrupt changes in viscosity can still appear at the location where the fluctuation model is switched or cut off. Such a discontinuity participates in the production of the unphysical behavior observed on the velocity profiles.

In conclusion, although the two modifications proposed for the fluctuations model are capable of achieving acceptable integral results—evidenced by the correlation between Reynolds number and wall friction levels in Table 5.3—neither modification alone significantly improves the velocity profiles or SGS viscosity profiles to a level that can be considered physically realistic. Therefore, a combination of the two enhancements appears necessary to achieve consistent and accurate results.

Re_τ	Case	$Re_{b,Dh}$	$Re_{b,Dh,KNc}$	Error
	Smago	61388		<1%
	Sigma	55560		9%
	WALE	54235		11%
	Sigma_F (V component)	60279		1%
934	WALE_F (V component)	63128	61182	3%
	Sigma_F (2 cells)	61788		1%
	WALE_F (2 cells)	62203		1%
	Sigma_F ($y^+ < 500$)	62084		1%
	WALE_F ($y^+ < 500$)	60071		1%

Table 5.3: Wall friction results for the turbulent channel at $\mathrm{Re}_\tau = 934$ comparing the different SGS models with and without the different enhancements of the fluctuations model.

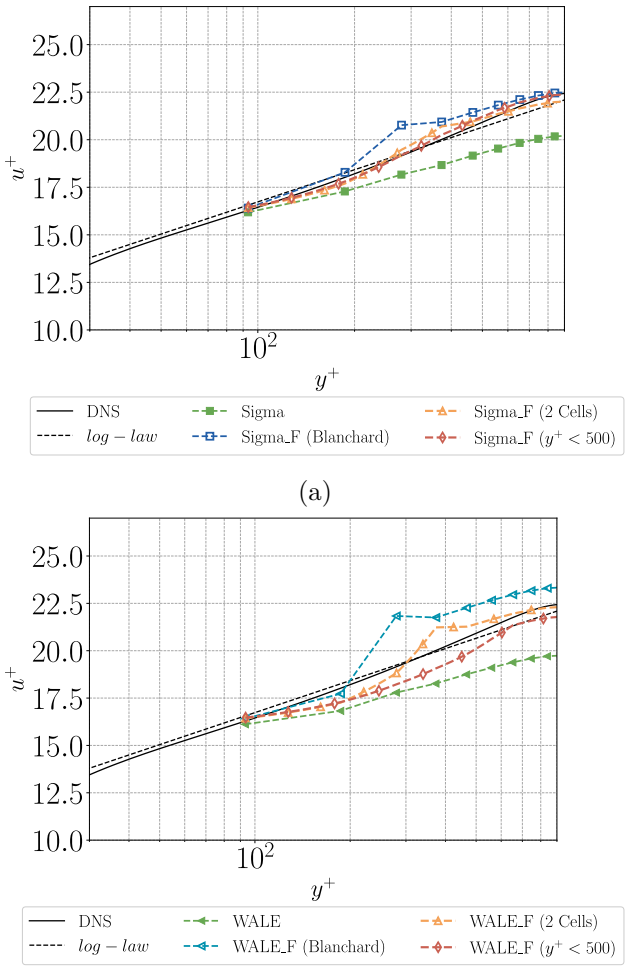

Figure 5.12: Average velocity profiles obtained on the turbulent channel ($Re_\tau = 934$) with (a) Sigma and (b) WALE SGS models and with the fluctuations model applied to a wider range of cells.

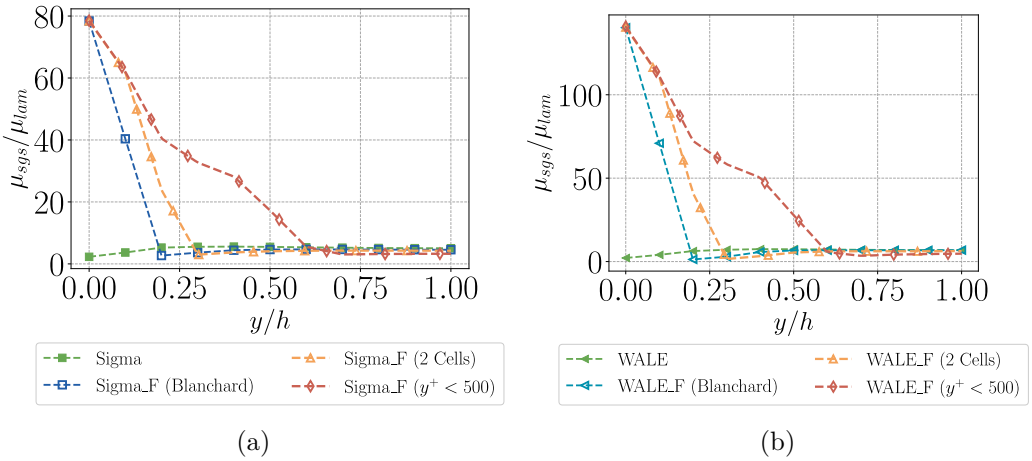

Figure 5.13: Turbulent viscosity profiles obtained on the turbulent channel ($Re_\tau = 934$) with (a) Sigma and (b) WALE SGS models and with the fluctuations model applied to a wider range of cells.

5.3.4 Combined effect

Finally, combining the two proposed improvements yields the most satisfactory results. First, as shown in Table 5.4, the modified fluctuation model successfully maintains the ability to recover a strong correlation between the expected Reynolds number at the given friction levels and the actual Reynolds number obtained from the computations.

Re_τ	Case	$Re_{b,Dh}$	$Re_{b,Dh,KNc}$	Error
	Smago	61301		<1%
	Sigma	55560		9%
	WALE	54235		11%
934	Sigma_F (V component, $y^+ < 500$)	60966	61182	<1%
	WALE_F (V component, $y^+ < 500$)	62742		2%
	Sigma_F (V component, 2 cells)	60105		1%
	WALE_F (V component, 2 cells)	61825		1%

Table 5.4: Wall friction results for the turbulent channel at $\mathrm{Re}_\tau = 934$ comparing the different SGS models with and without the fluctuations model.

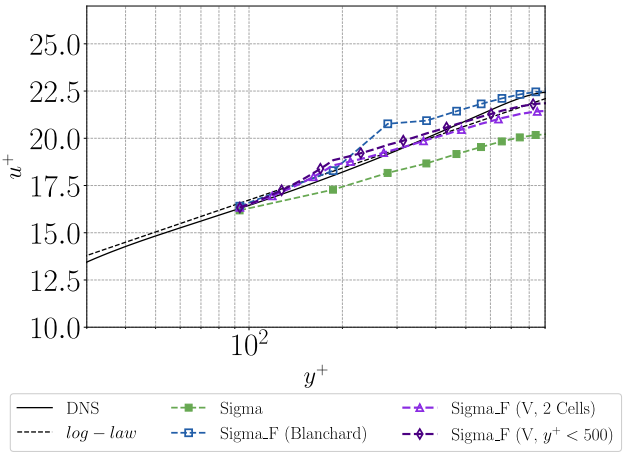

(a)

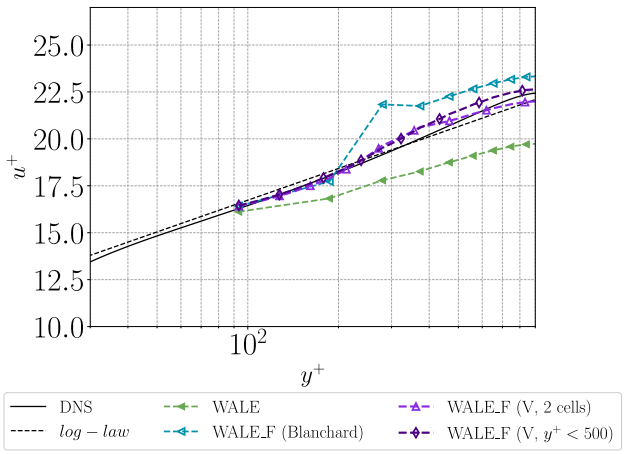

(b)

Figure 5.14: Average velocity profiles obtained on the turbulent channel ($\mathrm{Re}_\tau = 934$) with (a) Sigma and (b) WALE SGS models and with the fluctuations model applied to a wider range of cells and on the wall-normal component only.

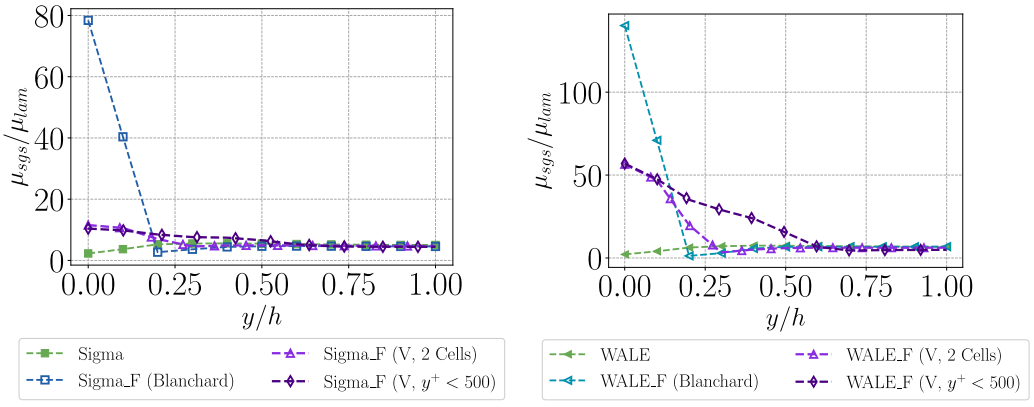

(a) (b)

Figure 5.15: Turbulent viscosity profiles obtained on the turbulent channel ($\mathrm{Re}_\tau = 934$) with (a) Sigma and (b) WALE SGS models and with the fluctuations model applied to a wider range of cells and on the wall-normal component only.

The velocity profiles plotted in Figure 5.14, with the present implementation in shades of purple, evidence that the model maintains its capability to reduce the log-layer mismatch. At the same time, the combined improvements yield more physically realistic velocity profiles than the original model. The modifications developed in this thesis are quite effective in controlling the fluctuations to yield smoother and consistent SGS viscosity profiles with well-suited intensity over the channel height as evidenced in Fig. 5.15. This improved behavior removes the discontinuities and unphysical artifacts that were seen in the earlier versions, which constitutes a major advance in the performance of the model.

In terms of RMS velocity, the impact of the fluctuation model is illustrated in Figure 5.16. These results can be analyzed as follows:

First, when compared to the Sigma or WALE models without fluctuations, all versions of the fluctuation model improve the RMS levels near the wall in the wall-tangent directions. This improvement addresses the excessively high RMS levels on the streamwise component observed in the default Sigma and WALE models, which are linked to the very low SGS viscosity near the wall. By introducing higher viscosity values via the fluctuation model, the velocity fluctuations are brought closer to the reference data, particularly in the regions where the default models fall short.

It should be underlined that, as slip wall conditions are used in this case, the values of velocity fluctuations at the wall should not be considered in the present analysis. The simulations performed with the Sigma model and the improved fluctuation model developed in the present work show a good agreement with the reference DNS data starting from the first point away from the wall for the u' component. Notably, the slope of the velocity fluctuations is well captured. However, this level of agreement is not consistently observed for all velocity components or for the WALE SGS model.

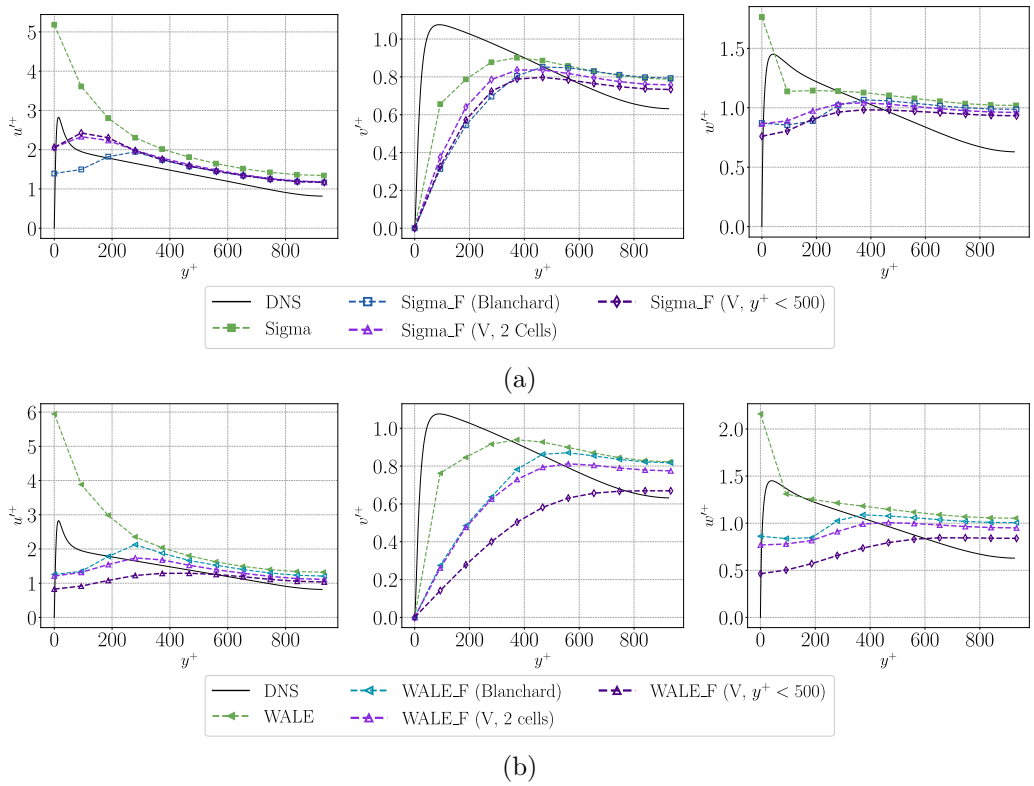

Figure 5.16: RMS velocity profiles for the turbulent channel at $\mathrm{Re}_\tau = 934$ and with the enhanced fluctuations model with the (a) Sigma or (b) WALE SGS model.

When used with the WALE SGS model, all the fluctuation models give reasonable velocity fluctuation magnitudes for all components and do not show large differences among the versions. A notable exception is found in the case where the fluctuation model is applied up to $y^+ = 500$. In that case, the implementation of the model that applies the fluctuations only to the first two cells better captures the RMS velocity profiles. This can be interpreted as a consequence of the specific response of the WALE viscosity to the induced velocity fluctuations, which is stronger than in the Sigma model. This in turn leads to reduced levels of velocity fluctuations within the domain.

Finally, the primary differences between the computations and the reference DNS data occur in the very near-wall region, where the RMS fluctuation peak is underpredicted. This outcome is expected due to the coarse resolution of the LES fields and gradients near the walls, with the RMS peak entirely located within the first computational cell. Achieving such fine precision is beyond the scope of WM-LES computations, where the effect of these peaks is intended to be modeled within the SGS and wall models. Nevertheless, the overall results remain satisfactory: fluctuation levels farther from the wall align well with the reference, and the average velocity profiles, as previously discussed, are also in good agreement with the DNS data.

In conclusion, this turbulent channel case illustrates the good performance of the proposed modifications to the fluctuation model in preventing several shortcomings of the original model: spurious discontinuities in the SGS viscosity and unphysical features in the velocity profile. The modified model performs better when compared against the reference DNS data. When the two improvements developed in this thesis—restricting the fluctuations to the wall-normal component and extending their application to a wider region—are applied together, the model yields physically realistic results: smoother velocity profiles and better monotonicity of SGS viscosity along the channel height. While the RMS of the velocity profiles do not perfectly capture the peak near the wall, because of the WMLES inherent limitations, they are in reasonable agreement with the DNS further away from the wall. Notably also, the improvements noted for the intermediate Reynolds number $\mathrm{Re}_\tau = 934$ are consistent with the results obtained for the two other Reynolds numbers tested in this study. The details of the analysis for these additional cases are given in the Appendix A.

5.3.5 Compatibility with the TBLE wall model

After having tested the performance of the fluctuation model with the classical analytical wall model, the compatibility with the TBLE wall model implemented within this thesis (see Chapter 4) is investigated. This primary objective is to ensure the consistency of results when using the TBLE wall model with the fluctuation model. Regarding the turbulent channel tested here, which has no average pressure gradient, the TBLE model, when coupled to the exponential moving average (EMA) of the pressure gradient, should give similar results compared to the logarithmic law of the wall. This is indeed demonstrated in part 4.2, where the TBLE model used with the Smagorinsky SGS model yields results that are in close agreement with the logarithmic law. For this configuration, the pressure gradient is averaged with the EMA algorithm presented in part 4.1.2. The time averaging factor, γ, is chosen to produce an averaging characteristic time based on a diffusive time, given by

$$T_{av} = h_{wm}/(\kappa u_\tau), \tag{5.25}$$

where h_{wm} represents the height of each wall cell, κ the von Kármán constant and u_τ the friction velocity (see part 4.2). In the simulations conducted during this work, this time characteristic T_{av} computed with Eq. (5.25) is of the order of 0.1 total diffusive times

$$T_d = h/u_\tau, \tag{5.26}$$

where h is the height of the channel. This setup ensures that the TBLE wall model behaves similarly to the logarithmic law of the wall, enabling a comparison of the results obtained with the fluctuation model in both wall model frameworks.

Table 5.5 presents a summary of the results obtained for the turbulent channel using the TBLE wall model. The first observation that can be made is that

the discrepancies between the expected Reynolds number and the values obtained with the TBLE model, when coupled to the Sigma or WALE models (without the fluctuations model), are higher than those observed with the logarithmic law of the wall.

Re_τ	Case	$Re_{b,Dh}$	$Re_{b,Dh,KNc}$	Error
	TBLE Smago	61301		<1%
	TBLE Sigma	45789		25%
934	TBLE WALE	45442	61182	25%
	TBLE Sigma (γ/1000)	55914		9%
	TBLE WALE (γ/1000)	54892		10%

Table 5.5: Wall friction results for the turbulent channel computed with the TBLE wall model at $\mathrm{Re}_\tau = 934$ comparing the different SGS models and without the fluctuations model.

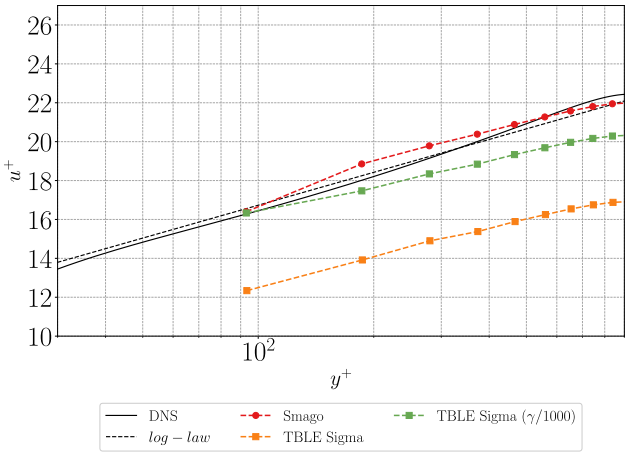

(a)

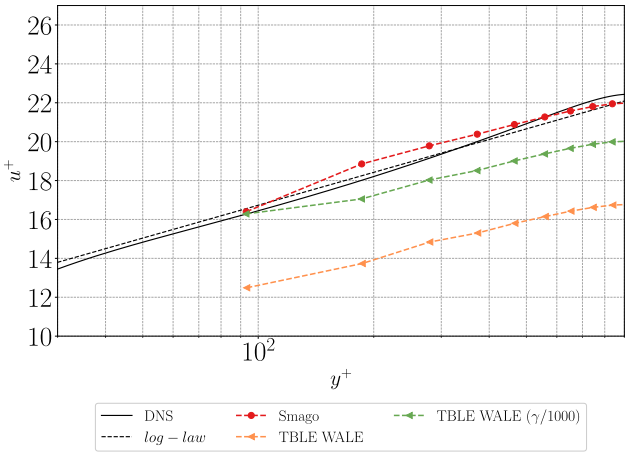

(b)

Figure 5.17: Average velocity profiles on the turbulent channel at $\mathrm{Re}_\tau = 934$ computed with the TBLE wall model for (a) Sigma and (b) WALE SGS models and without the fluctuations model.

An immediate explanation for this can be found by looking at the velocity profiles in Figure 5.17. In fact, the profiles obtained when using Sigma or WALE models show a velocity deficit from the very first point, which is predicted by the wall model. This result is similar to what was observed in part 4.2 without averaging the pressure gradient. Here, the level of averaging that was sufficient with the Smagorinsky model is not high enough for the Sigma or WALE models. This discrepancy appears because both the Sigma and WALE models yield a much lower level of SGS viscosity near the wall than is obtained when using the Smagorinsky model; hence, more intense levels of pressure fluctuations are fed into the TBLE model.

This argument is supported by the observations of the α factor, defined as

$$\alpha = u_\tau^2 / u_{\tau p}^2,$$

where

$$u_{\tau p} = \sqrt{u_\tau^2 + u_p^2}$$

and

$$u_p = \left| (\nu/\rho)(\partial P/\partial x_1) \right|^{1/3},$$

which quantifies the pressure gradient level seen by the TBLE model. When $\alpha = 1$, no pressure gradient is fed to the TBLE model, which corresponds to the expected scenario for this setup. Instantaneous snapshots of α for the channel walls, shown in Figure 5.18 reveal that both Sigma and WALE models generate higher levels of pressure gradient fluctuations. These fluctuations are not adequately dampened by the exponential moving average before being used by the TBLE model. In contrast, with the Smagorinsky model, the pressure gradient fluctuations are well-controlled, and the values of α are concentrated near 1, as expected (see Figure 5.20).

To address this issue, it was found that the pressure gradient requires more time-averaging when using the Sigma and WALE models. This is confirmed by decreasing the averaging factor γ by a factor of 1000 —*i.e.* performing the exponential average over a time T_{av} 1000 times longer— which led to the pressure gradient being dampened to expected levels. In that particular case, this modification means that the time characteristic of the exponential filter is of the order of 100 diffusive times T_d (defined in Eq. (5.26)), while a T_{av} of the order of $0.1T_d$ is sufficient with the Smagorinsky SGS model. As shown in Figures 5.19 this adjustment brought the distribution of α values closer to 1, which is in line with the expected values in this setup. Figure 5.20, presenting the probability density functions (*P.D.F.*) of the values of α across the walls of the turbulent channel is a further indication that the increase in time averaging brings α closer to one. Consequently, the results presented in Table 5.5 show that the error between the expected Reynolds number (calculated using the Kármán-Nikuradse correlation) and the actual Reynolds number computed is reduced, returning to the same level that was observed with the logarithmic law of the wall.

Further evidence is provided in Figure 5.17, where velocity profiles obtained with the TBLE model and the increased pressure gradient averaging no longer show the abnormal velocity deficit (green line). However, a velocity deficit similar to the log-layer mismatch observed with Sigma and WALE models using the logarithmic law is still present. This mismatch, as with the log-law model, should be corrected by the fluctuations model, ensuring consistent and physically realistic results.

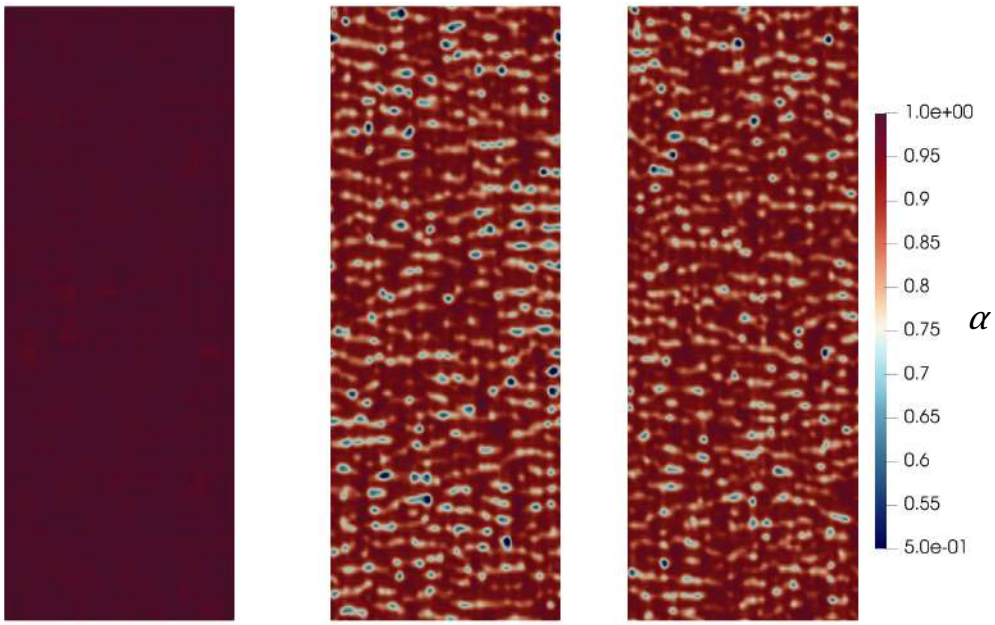

(a) Smagorinsky (b) Sigma (c) WALE

Figure 5.18: Instantaneous snapshot of the factor α on the turbulent channel walls computed with the TBLE wall model at $\mathrm{Re}_\tau = 934$ with different SGS models (without the fluctuations).



(a) Smagorinsky (b) Sigma (c) WALE

Figure 5.19: Instantaneous snapshot of the factor α on the turbulent channel walls computed with the TBLE wall model with 1000 times more averaging of the pressure gradient at $\mathrm{Re}_\tau = 934$ with different SGS models (without the fluctuations).

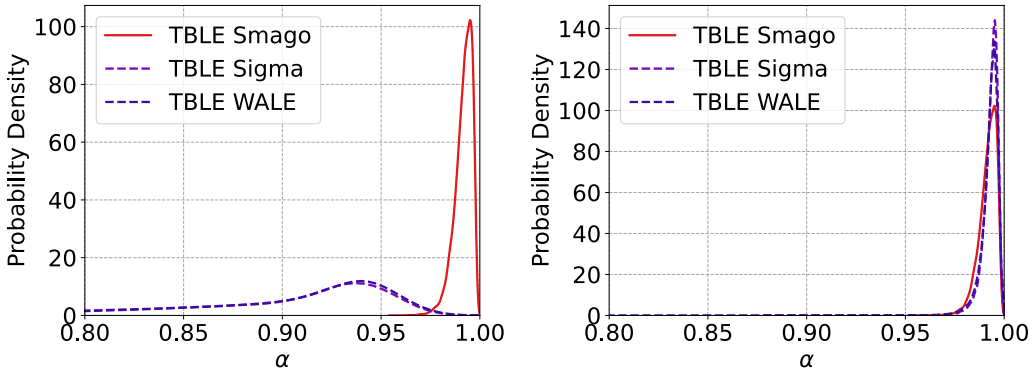

(a) Normal (Eq. (5.25)) pressure gradient averaging

(b) Increased ($\gamma/1000$) pressure gradient averaging

Figure 5.20: Probability Density Function (*P.D.F.*) of the factor α values on the turbulent channel walls, computed using the TBLE wall model at $\mathrm{Re}_\tau = 934$ with the different SGS models.

Re_τ	Case	$Re_{b,Dh}$	$Re_{b,Dh,KNc}$	Error
	TBLE Smago	61301		<1%
	TBLE Sigma ($\gamma/1000$)	55914		9%
	TBLE WALE ($\gamma/1000$)	54892		10%
	TBLE Sigma_F	63420		3%
934	TBLE WALE_F	65354	61182	6%
	TBLE Sigma_F_V_yp	61078		<1%
	TBLE WALE_F_V_yp	63227		3%
	TBLE Sigma_F_V_2C	60129		1%
	TBLE WALE_F_V_2C	62096		1%

Table 5.6: Wall friction results for the turbulent channel at $\mathrm{Re}_\tau = 934$ comparing the different SGS models with and without the fluctuations model.

When the fluctuations model is applied, with the time-averaging defined in Eq. (5.25), both the original model of Blanchard et al. [14] and the improved version developed in this thesis recover the performance obtained with the log-law wall model, as evidenced in Table 5.6. This is also supported by the velocity profiles shown in Figure 5.21, for which the same behavior found with the log-law is reproduced:

- A reduced log-layer mismatch with the original model of [14], although with unrealistic profiles due to the discontinuity at the third point in the channel (blue lines).
- Significantly better results with the modified model developed in this thesis, giving more physically realistic velocity profiles while still reducing the log-layer mismatch (in shades of purple).

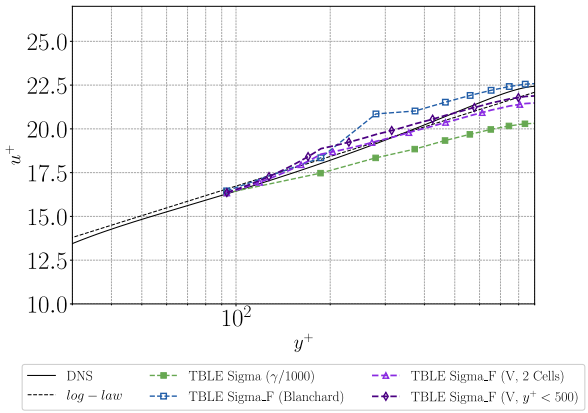

(a)

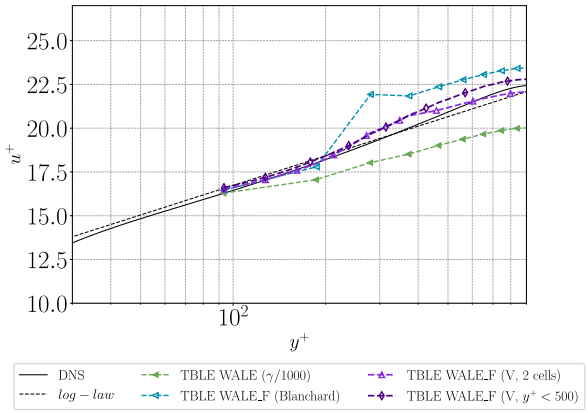

(b)

Figure 5.21: Average velocity profiles obtained on the turbulent channel ($Re_\tau = 934$) with the TBLE wall model and (a) Sigma and (b) WALE SGS models with the enhanced fluctuations model.

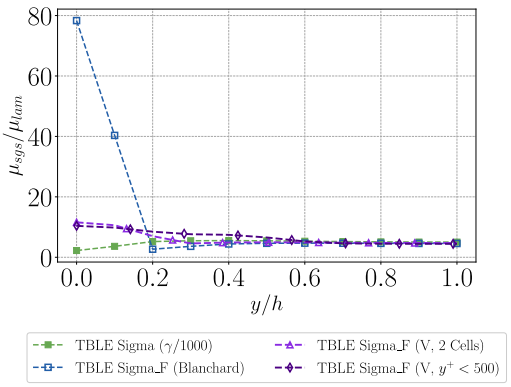

(a)

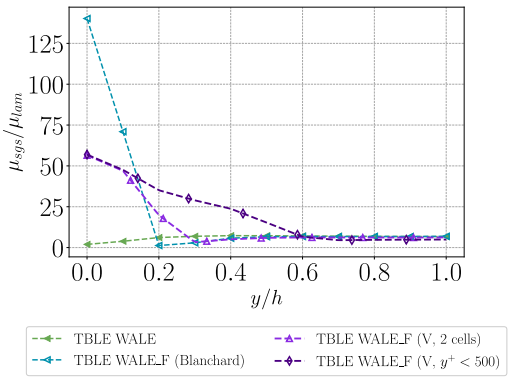

(b)

Figure 5.22: Turbulent viscosity profiles obtained on the turbulent channel ($Re_\tau = 934$) with the TBLE wall model and (a) Sigma and (b) WALE SGS models with the enhanced fluctuations model.

These improvements can be attributed to two factors. First, the fluctuations model itself, which, as with the logarithmic law of the wall, produces results that are consistent with the expected behavior (see Fig. 5.22). Second, the side-effect of increased SGS viscosity near the walls, which has a positive impact on the pressure gradient fluctuations. The higher SGS viscosity near the walls, comparable to the levels seen with the Smagorinsky model, leads to reduced levels of pressure gradient fluctuations. This, in turn, helps to achieve the expected results with the TBLE model, using the same time-averaging of the pressure gradient applied with the log-law model —*i.e.* with a γ parameter defined to produce the time average characteristic of Eq. (5.25).

Regarding the turbulence, the same conclusions drawn with the log-law wall model also apply when using the TBLE wall model. The overall levels of the RMS of the different velocity components are satisfactory with both the original fluctuations model of Blanchard et al. [14] and the enhanced fluctuation model developed in this thesis, as shown in Figures 5.23 and 5.24. However, the very near-wall peaks of fluctuations remain unresolved on such coarse meshes. Additionally, as observed previously, when using the WALE model, the enhanced fluctuations model, applied to the first two cells only, provides the best performance in terms of RMS velocity fluctuations when compared to the implementation which imposes fluctuations up to $y^+ = 500$.

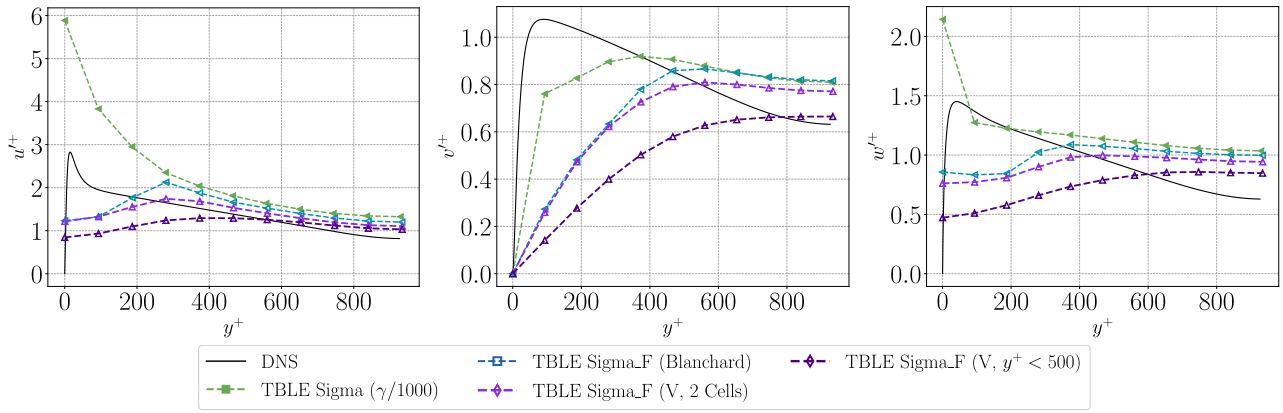

Figure 5.23: RMS velocity profiles obtained on the turbulent channel ($\mathrm{Re}_\tau = 934$) with the TBLE wall model and Sigma SGS viscosity with or without the different versions of the fluctuations model.

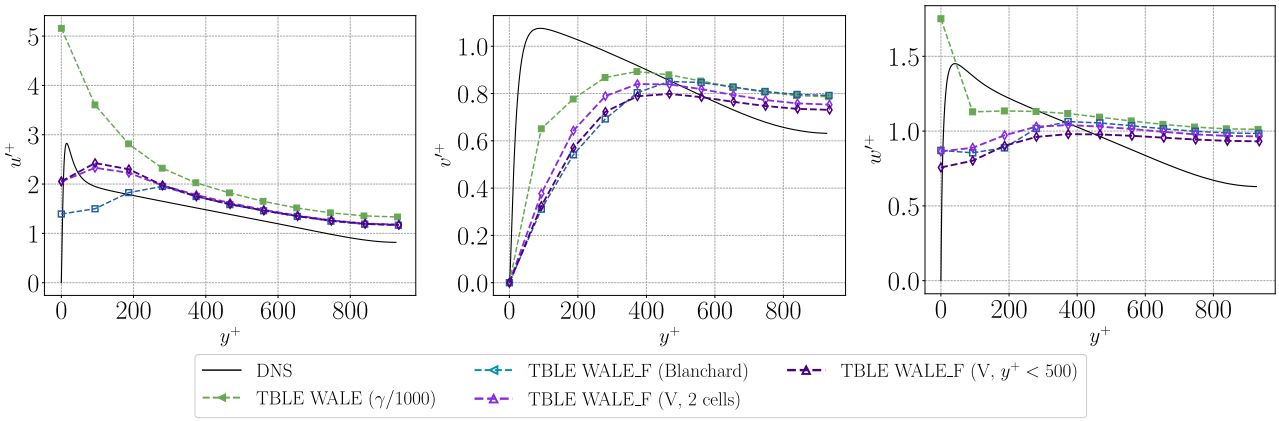

Figure 5.24: RMS velocity profiles obtained on the turbulent channel ($\mathrm{Re}_\tau = 934$) with the TBLE wall model and WALE SGS viscosity with or without the different versions of the fluctuations model.

Additionally, when the fluctuations model is applied in combination with the TBLE model, the same satisfactory results are obtained for the other two Reynolds numbers tested. The consistent performance of these results for a range of flow conditions is further developed in Appendix A. These provide further support for the validity and robustness of the model.

To conclude on the validation of the fluctuations model and the improvements introduced in this thesis, they were tested on the turbulent channel test case. The obtained results demonstrated that the fluctuations model effectively reduces the log-layer mismatch when used with both Sigma and WALE SGS viscosity models. Furthermore, compared to the original model of Blanchard et al. [14], significant improvements were observed when using the versions of the model developed in this work, with more physically consistent velocity profiles and better-aligned SGS viscosity profiles produced by the altered model.

The fluctuations model also proved to be compatible with the TBLE model, which incorporates the pressure gradient, as implemented in this thesis. An important side-effect of the fluctuations model was identified: the increased sub-grid viscosity resulting from its application helps mitigate pressure gradient fluctuations, allowing the TBLE model to be used effectively with both Sigma and WALE models. Without the fluctuations model, however, the pressure gradient fluctuations would require longer time-averaging —with a time characteristic several orders of magnitude larger— when used with Sigma and WALE than when paired with the Smagorinsky model.

5.4 Periodic Hill test case validation

After validating the framework of the fluctuations model on the turbulent channel test case, the enhanced fluctuations model developed in this thesis —denoted by the suffix "_F" and specified as (V) for the wall-normal component and (2 cells) or ($y+ < 500$) for the different implementations of the spatial extension— is now tested on the more complex periodic hill configuration. This test case, described in detail in part 3.2.2, features a recirculation bubble developing under the influence of the pressure gradient as well as regions of high friction. This makes the periodic hill setup a more challenging environment for evaluating the performance of the fluctuations model. The periodic hill case has already been used to benchmark the TBLE model in section 4.3, showing significant improvements over the classical logarithmic law when combined with the Smagorinsky SGS viscosity model. This section includes the results obtained using the TBLE model with the time-averaged pressure gradient and Smagorinsky model, as previously presented in Section 4.3. The analysis is further extended to include results from with the Sigma model, both without and with the fluctuation model, as developed in this thesis and detailed in section 5.2.2.

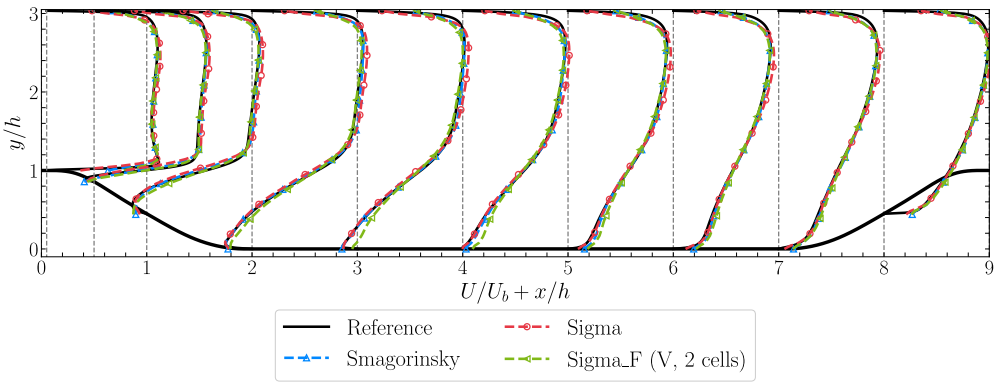

(a)

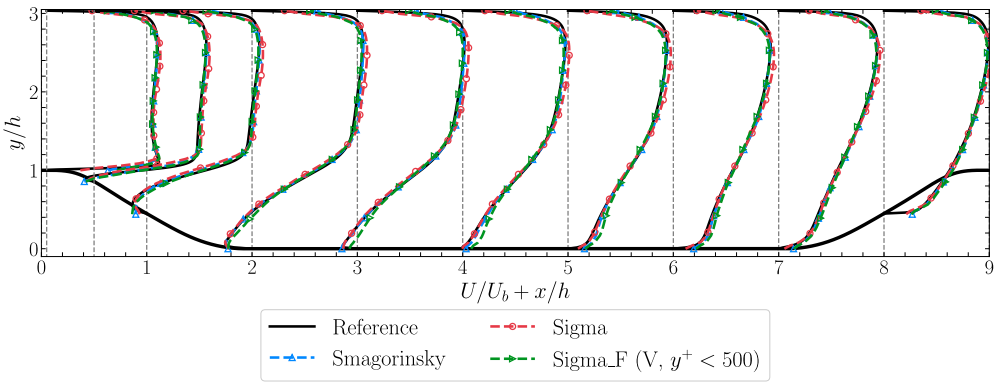

(b)

Figure 5.25: Average streamwise velocity over the periodic hill case ($\mathrm{Re}_b = 10\,600$) computed with the TBLE wall model and without or with the fluctuations model implemented in (a) two neighboring cells above the walls or (b) in the cells where $y^+ < 500$, compared to WRLES reference [61].

First, the average streamwise velocity profiles at various streamwise locations are plotted in Figure 5.25. Again, the two versions of the fluctuations model tested in this thesis appear, with the results of the application of the model on the first two cells above the wall in Fig. 5.25a and the results of the model applied up to $y^+ = 500$ (roughly 10 cells above the wall) in Fig. 5.25b. The results indicate that the Sigma SGS model combined with the TBLE wall model produces velocity profiles that are in good agreement with both the Smagorinsky SGS model results and the reference WRLES data from Gloerfelt and Cinnella [61]. However, when the fluctuations model is applied, it leads to overestimated velocity profiles in the recirculation region on the bottom wall and in the wake of the recirculation.

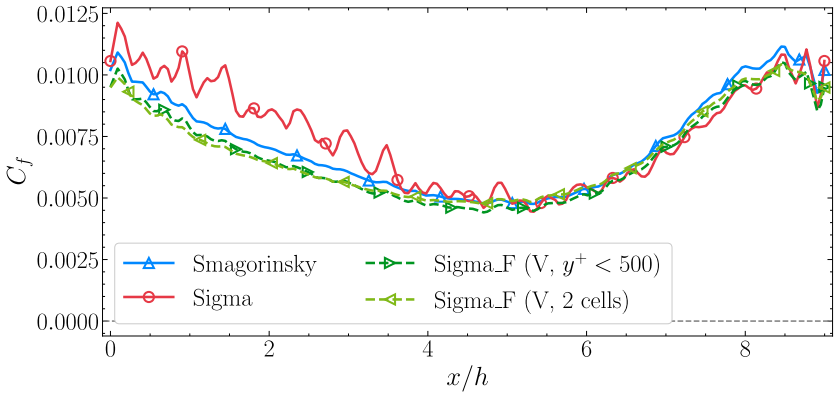

(a) Top Wall

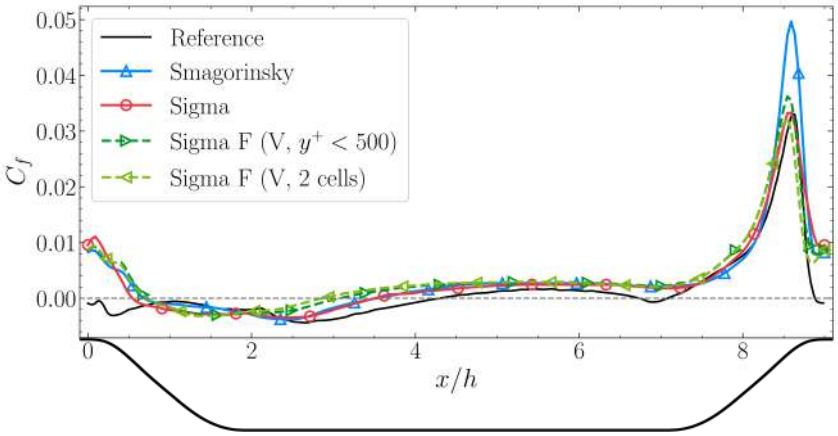

(b) Bottom Wall compared to the WRLES reference [61]

Figure 5.26: Friction coefficient over the periodic hill ($\mathrm{Re}_b = 10600$) computed with the TBLE wall model and with or without the enhanced fluctuations model along the streamwise direction.

This trend is further demonstrated in the friction coefficient C_f profile plotted along the bottom wall in Figure 5.26b. It can be seen that the size of the recirculation zone is underestimated when the fluctuations model is used compared to the cases without the fluctuations model and the reference data. The reattachment

length of the recirculation zone given in Table 5.7 confirms this trend, underlining again that the adopted fluctuations model has drawbacks in predicting the flow separation and its reattachment location for such configuration.

Re_b	Case	WRLES [61]	Exp. [142]	TBLE (Error)
10600	Smagorinsky	4.305	4.21	3.53 (18%)
	Sigma			3.48 (19%)
	Sigma_F (V, 2 cells)			2.89 (32%)
	Sigma_F (V, $y^+ < 500$)			3.07 (28%)

Table 5.7: Recirculation zone reattachment length on the Periodic Hill with relative errors computed with respect to the WRLES [61].

In other regions of the flow, however, the application of the fluctuations model does not compromise the quality of the computation. This is particularly evident in areas where the Reynolds number (based on the friction $Re_\tau = hu_\tau/\nu$) is higher and more representative of fully turbulent conditions, such as near the friction peak. In that location, it can be noted that the use of the Sigma SGS model, with or without the fluctuations model, achieves friction levels closer to those observed in the WRLES of Gloerfelt and Cinnella [61] compared to the results obtained with the Smagorinsky SGS model.

Similarly, on the top wall, where friction levels are higher than on the bottom wall, the activation of the fluctuations alongside the TBLE wall model produces convincing results in Fig. 5.26a. The fluctuations model helps recover a smooth friction profile (in shades of green) in contrast with the noisier profiles obtained with the Sigma SGS model alone. This difference is linked to the noise in the pressure gradient input to the TBLE model already observed in the turbulent channel when using the Sigma SGS model alone (see part 5.3.5). The observation of the pressure gradient profiles in Fig. 5.27a evidence that the use of the fluctuations model once again leads to smoother and more suitable levels of pressure gradient, as a result of the modification of the near-wall SGS viscosity. On the bottom wall however, the pressure gradient levels observed in Fig. 5.27b are generally higher than those observed on the top wall and appear less noisy and less affected by the activation of the fluctuations model.

Additionally, in the bulk flow region, as shown in Figure 5.25, the Sigma SGS model without the fluctuations model slightly overestimates the average velocity. This appears to be coupled with an altered mass flow distribution over the height of the channel. However, when the Sigma model is used in conjunction with either version of the fluctuations model, the predicted velocity levels are in better agreement with the reference data. This overestimation in the bulk flow is also associated with an underprediction of velocity in the near-wall region on the upper wall, which is corrected by the fluctuations model. This behavior aligns with the observations made in the turbulent channel setup and is consistent with the similarities between the upper wall region of the periodic hill setup and a channel flow configuration.

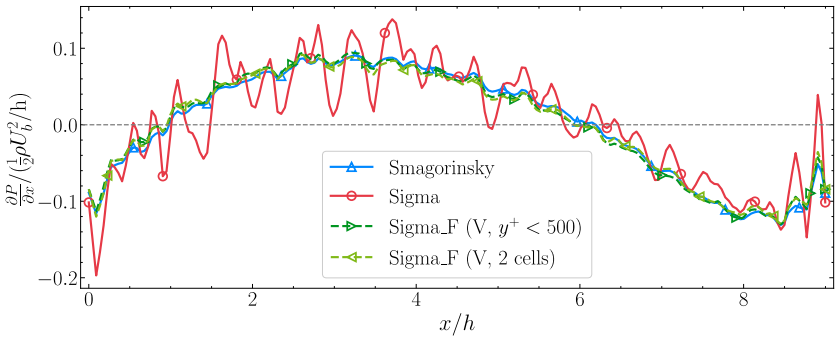

(a) Top Wall

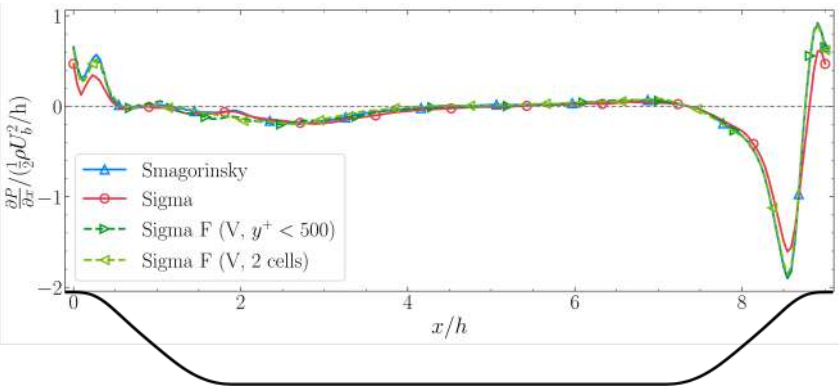

(b) Bottom Wall

Figure 5.27: Non-dimensional pressure gradient ($\frac{\partial P}{\partial x}/(0.5\rho U_b^2/h)$) evolution along the streamwise direction of the periodic hill simulated with the TBLE wall model at $\mathrm{Re}_b = 10600$.

The results concerning velocity fluctuations can be analyzed by examining Figure 5.28. A notable observation in the case with the Sigma SGS model is the significant overprediction of the axial component u' near the top wall. This issue is once again corrected when applying the fluctuation model both on cells above the wall or on all cells where $y^+ < 500$, which produces u' levels that align well with the reference WRLES in this region. Given the similarity of this region to the turbulent channel setup, the explanation is consistent with the former case: the Sigma model predicts excessively low levels of SGS viscosity, and the application of the fluctuation model increases the viscosity, thereby reducing the levels of velocity fluctuations. Beyond this clear improvement, no other major trends emerge in this setup, where the velocity fluctuation levels are quite similar across all tested models. One notable exception is observed in the cross-correlation of fluctuations, $u'v'$, in the shear layer immediately downstream of the hill. Here, the Sigma model—whether or not the fluctuations model is activated—yields fluctuation levels that better match the reference WRLES than the Smagorinsky model. This difference can be attributed to the known over-dissipative nature of the Smagorinsky model compared to the Sigma model, as discussed in part 1.3.3. However, since this improvement is confined to a very localized region of the domain, it does not allow for broader conclusions to be drawn.

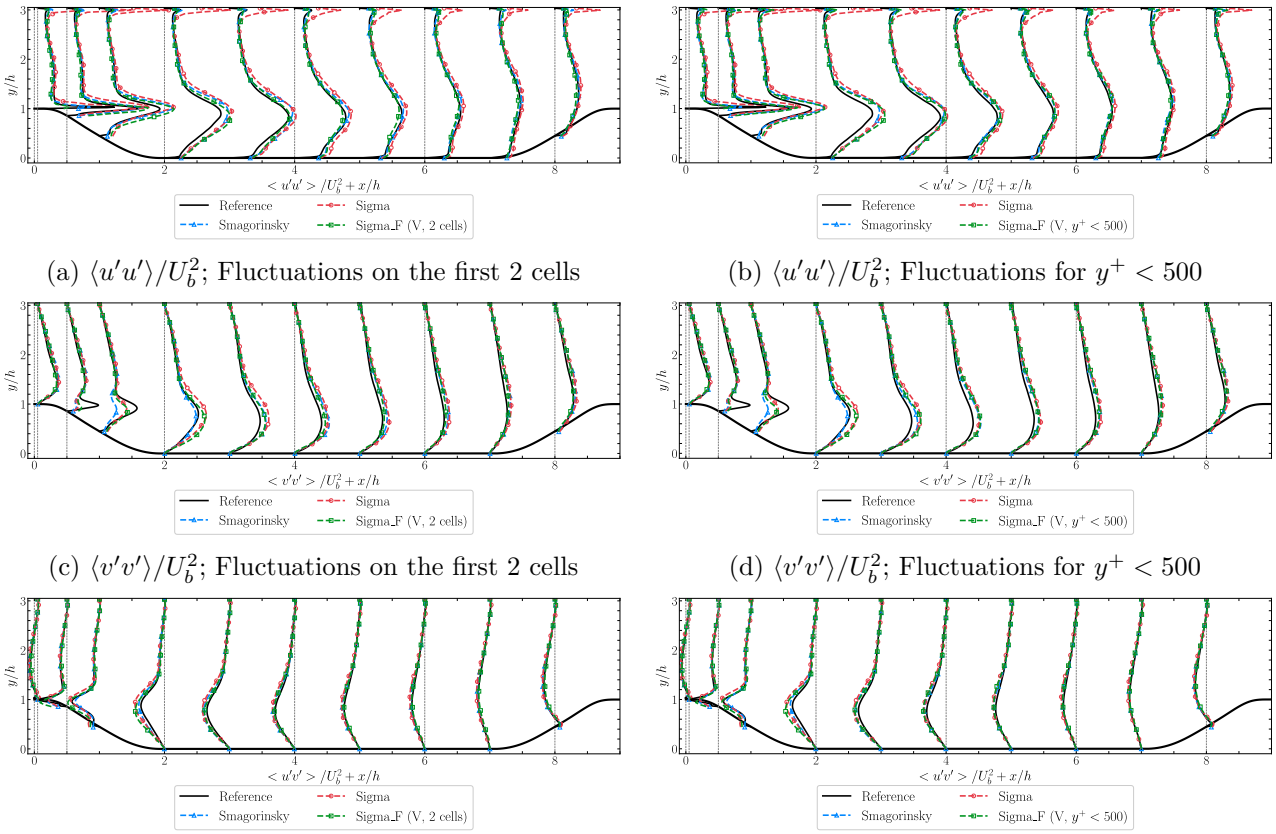

(a) $\langle u'u' \rangle / U_b^2$; Fluctuations on the first 2 cells

(b) $\langle u'u' \rangle / U_b^2$; Fluctuations for $y^+ < 500$

(c) $\langle v'v' \rangle / U_b^2$; Fluctuations on the first 2 cells

(d) $\langle v'v' \rangle / U_b^2$; Fluctuations for $y^+ < 500$

(e) $\langle u'v' \rangle / U_b^2$; Fluctuations on the first 2 cells

(f) $\langle u'v' \rangle / U_b^2$; Fluctuations for $y^+ < 500$

Figure 5.28: RMS velocity profiles obtained over the periodic hill setup at $\mathrm{Re}_b = 10\,600$ computed with the TBLE wall model and with or without the enhanced fluctuations model compared to reference WRLES [61].

All these observations made on the periodic hill setup at this Reynolds number of $Re_b = 10\,600$ are consistent with those obtained at the two higher Reynolds numbers examined in this work. Similar trends are observed, with the fluctuations model improving predictions in high Reynolds number regions, such as near the top wall, while causing a deterioration in low Reynolds number zones, such as the recirculation regions. These consistent results across different flow conditions reinforce the conclusions drawn in this section. Full details of the higher Reynolds number cases are presented in Appendix B.

Overall, considering the performance and enhancements given by the fluctuations model developed and implemented during this thesis on the periodic hill setup, two main conclusions arise:

- Performance in low friction regions: The fluctuations model worsens the predictive quality of the simulations in regions of low velocity, such as the recirculation zone and its wake. It yields velocity and friction profiles further away from the reference data compared to simulations without the fluctuations model.

- Performance in high friction regions: In regions of higher velocity and friction such as near the top wall, the fluctuations model improves the averaged velocity fields as well as the velocity fluctuation level predictions, compared to the use of the Sigma model alone. In other high friction regions, for instance, in the area of maximum friction along the bottom wall, the performance of the Sigma model is satisfying and superior to the Smagorinsky model, whether fluctuations are activated or not.

These results can be explained by the fact that the fluctuations model is designed specifically for fully turbulent applications. In regions of low Reynolds numbers, the fluctuations model unrealistically excites the SGS viscosity model and consequently results in excessive levels of SGS viscosity that further deteriorate the flow predictions.

The behavior of the fluctuations model could be improved in the future by conditionally activating the fluctuations model, based on the local friction Reynolds numbers being sufficiently high. Such a method would help to ensure that the model remains active where the flow is sufficiently close to fully turbulent conditions, helping improve the performance of the Sigma or WALE model near walls but without detrimental side effects in low-velocity regions where it is not needed.

Chapter 6

Turbomachinery Application

Following the implementation and validation on academic test cases of the models used during this thesis to improve the behavior of wall-modeled LES, it is now time to apply them to more practical turbomachinery scenarios. This involves investigating two distinct setups of both turbine and compressive components. The first one consists of a low-pressure turbine blade cascade, followed by a study of a rotor-stator fan stage sector.

6.1 T7.2 Low Pressure turbine

6.1.1 Introduction and numerical setup

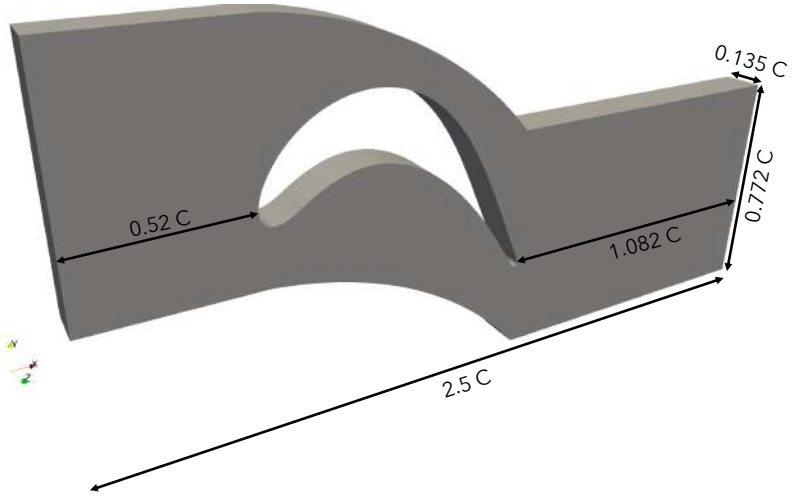

Figure 6.1: Sketch of the geometry and computational domain of the T7.2 turbine setup.

The first turbomachinery configuration analyzed in this work is a linear cascade of the T7.2 turbine blade design, introduced as part of the European project on Aerothermal Investigations on Turbine Endwalls and Blades (AITEB) [50, 68]. This blade profile has been extensively studied to investigate the effects of film cooling and thermal loads, using both experiments [94] and Large-Eddy Simulations (LES) [45, 106].

The T7.2 turbine blade is a highly loaded, low Mach number configuration, characterized by a large recirculation bubble on its pressure side on the one hand,

and an adverse pressure gradient on the suction side leading to separation and transition to turbulence on the other hand. In the context of WMLES, these features are especially relevant because they provide a challenging test case to assess the accuracy and robustness of different wall models. Both regions are dominated by pressure gradient effects which make them key regions for evaluating the TBLE wall-model performance, although the suction side is a more challenging area due to the laminar-to-turbulent transition being outside of the scope of the model. This turbine blade has been studied experimentally for different Reynolds numbers and inlet turbulence intensities.

In this work, the configuration is analyzed at a Reynolds number of 150 000 based on the chord length C and exit velocity, with no turbulence injection applied. This choice avoids introducing the complexity of handling turbulence injection in LES and simplifies the analysis. The results are compared to the experimental data corresponding to the lowest turbulence level, given that this level—1.6%—is small enough to have a negligible influence on the outcome.

The numerical setup studied here is presented in Fig. 6.1 along the geometric definitions of the domain, with C denoting the chord length. Two simulation frameworks are used in this thesis: a Wall-Resolved LES (WRLES) to provide high-fidelity reference data and two Wall-Modeled LES (WMLES) for evaluating wall models under similar numerical conditions. The WMLES simulations compare the log-law wall model and the TBLE model, which incorporates the pressure gradient with temporal smoothing. All simulations use the Sigma SGS model, while the TBLE model is further evaluated with and without the fluctuation model developed in this thesis, implemented with activation in the two cells directly above the wall.

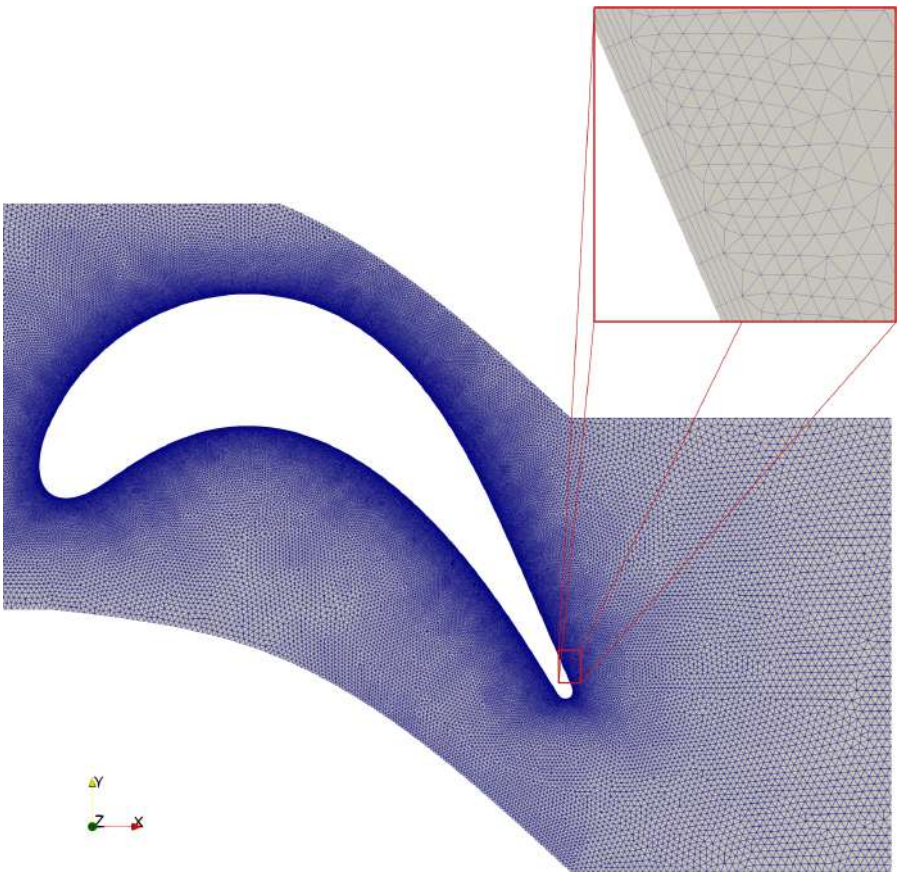

Figure 6.2: Side cut of the wall resolved LES mesh of the T7.2 turbine configuration.

The WRLES relies on a mesh of 54 832 097 elements, predominantly tetrahedra, supplemented by a near-wall layer of prismatic cells to capture the boundary layer behavior more accurately. This mesh originates from a previous study that notably examined the effects of mesh resolution. The wall-normal resolution is set to achieve $y^+ \approx 1$ to capture the viscous sublayer dynamics and justify the wall-resolved nature of the simulation. Figure 6.2 presents the features of the WRLES mesh, and Figure 6.4 illustrates the actual wall resolution in wall units around the blade profile, indicating that the resolution target was met.

In contrast, the WMLES uses a coarser mesh, as illustrated in Figure 6.3, that consists of 1 621 281 uniformly sized tetrahedral elements. This setup yields a near-wall resolution of $y^+ \sim 100$, as can be seen from Figure 6.4. At this resolution, the first cell is located well within the logarithmic region of the boundary layer, which is appropriate for the use of wall models.

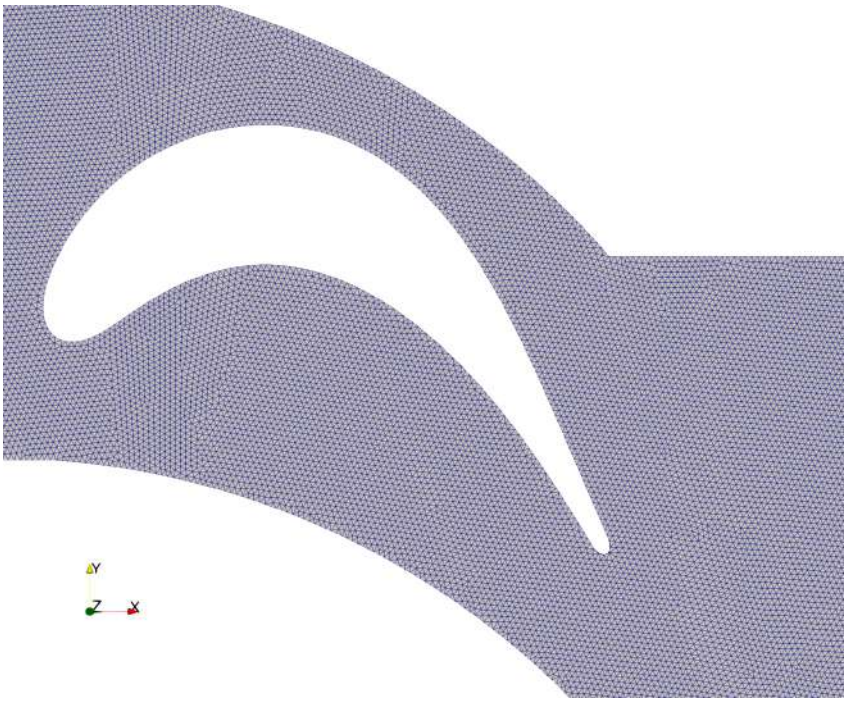

Figure 6.3: Side cut of the wall modeled LES mesh of the T72 turbine configuration.

To evaluate the performance of the different wall models in this setup, the analysis focuses on the near-wall regions, since these are the most directly affected by the choice of wall modeling approach. Although further insight might be obtained by looking at the wake of the turbine blade, the meshes used for these simulations—including the WRLES mesh—do not have a sufficient resolution in the wake region to yield results of sufficient accuracy for meaningful comparison with experimental data. All the averaged profiles and fields presented in the following section include a spanwise average in addition to the time average, leveraging the periodicity of the setup in the spanwise direction.

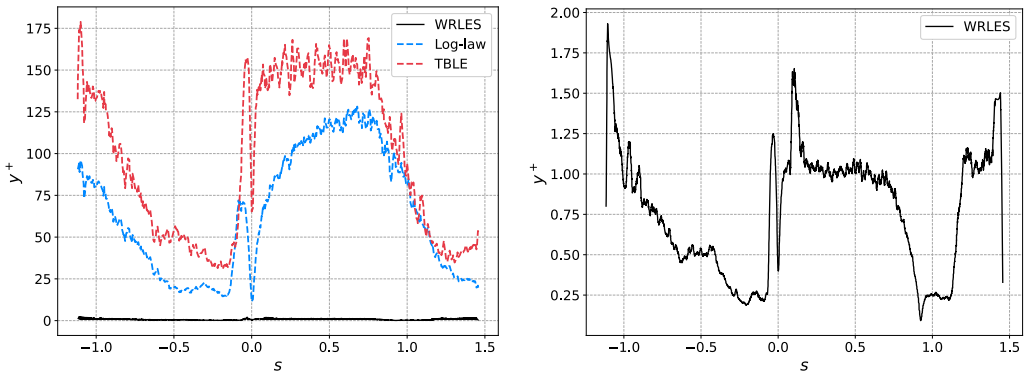

(a) WMLES compared to the WRLES (b) Wall Resolved LES

Figure 6.4: Wall mesh resolution in wall units along the turbine blade curvilinear coordinate s plotted from pressure side to suction side.

In both the WRLES and WMLES setups, the Navier–Stokes Characteristic Boundary Condition (NSCBC) formalism [137] is employed at the inlet to impose uniform total pressure, total temperature, and velocity angle [122] (see Table 6.1). At the outlet, an adapted NSCBC condition is applied to enforce atmospheric static pressure while accounting for transverse terms [63]. Periodic boundary conditions are imposed in the pitchwise direction to replicate the experimental turbine cascade, as well as in the spanwise direction. For the wall boundaries, both setups use isothermal boundary conditions, maintaining a fixed temperature of 300 K. The WRLES setup applies a no-slip boundary condition, whereas the WMLES computations use slip wall models. The performance of the TBLE model, incorporating the pressure gradient term —with and without the fluctuations model— is compared to the ones obtained with the logarithmic law of the wall. Due to the lack of a priori knowledge of the friction levels around the blade, as well as its variability around the blade profile, the time averaging cannot be determined with the expression $T_{av} = h_{wm}/(\kappa u_\tau)$ previously used. For this configuration, the time averaging constant was then fixed based on one flow-through time of the setup, approximated based on the inlet axial velocity and the axial length of the domain.

Inlet total pressure $P_{t,1}$	1022.7577 hPa
Inlet total temperature $T_{t,1}$	348.06 K
Inlet flow angle	127°
Outlet static pressure	1013.159 hPa

Table 6.1: Inlet and outlet boundary conditions of the T7.2 turbine setup.

Both the WRLES and WMLES setups employ the TTGC numerical scheme [37] for space and time discretization and the Sigma sub-grid scale (SGS) model to represent the effects of unresolved turbulence.

The WRLES setup is simulated over a period corresponding to 3 flow-through

times to achieve a stable operating state. After such an initial transient run, time-averaged values are gathered during a successive run over 2 more flow-through times. Regarding the WMLES case, a similar initialization is realized, followed by averaging operations spanning over 5 flow-through times.

6.1.2 Flow characteristics and results

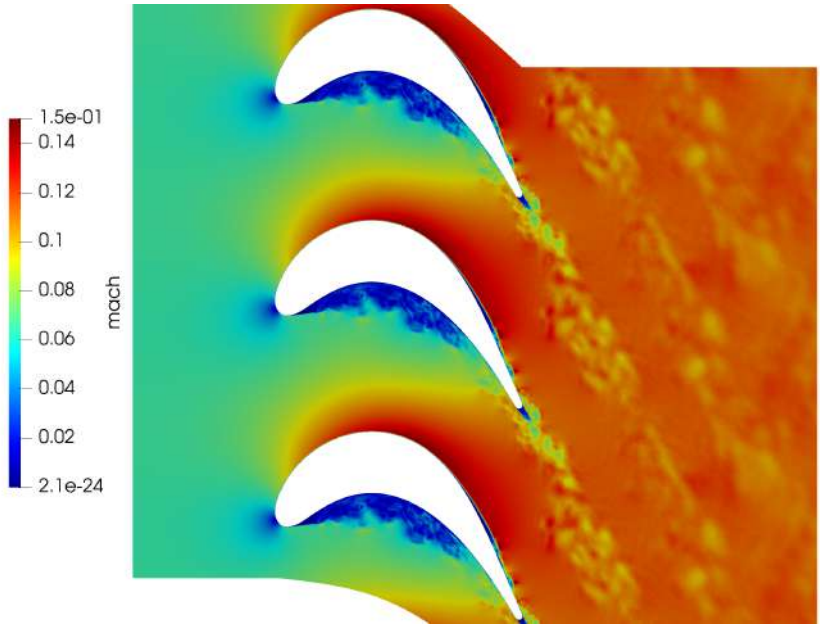

Figure 6.5: Instantaneous Mach number field around the T7.2 turbine cascade configuration simulated with WRLES.

The main features of the flow in the T7.2 turbine blade setup are revealed by analyzing both the Mach number field and the Q-criterion isosurface from the WRLES simulation.

First, analyzing the Mach number field presented in Fig. 6.5 clearly shows the acceleration of the flow through the cascade. The flow is highly unsteady with turbulent features and presents a massive separation on the pressure side. On the suction side, the flow remains laminar on most of the blade surface before experiencing a still laminar separation driven by an adverse pressure gradient followed by a transition to turbulent conditions.

The coherent structures of the flow are revealed by the plot of Q-criterion isosurfaces in Fig. 6.6, which highlights the presence of the separation on the pressure side as well as the laminar separation and the transition to turbulence on the suction side.

In this setup, the recirculation bubble on the pressure side serves as a critical benchmark for evaluating the performance of the different wall models tested. On the suction side, the laminar-to-turbulent transition region poses a serious challenge for the wall models tested here since all of them are designed and valid for fully turbulent flows only, and no specific transition modeling was considered in these simulations.

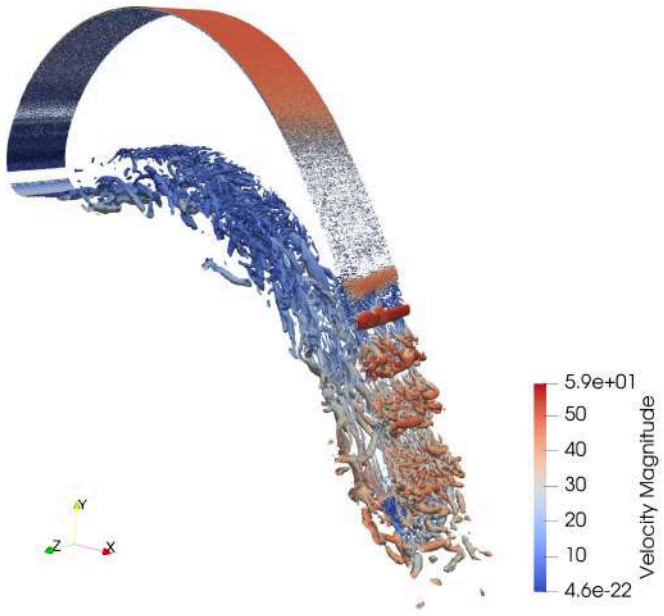

Figure 6.6: Q criterion isocontour of the T7.2 turbine configuration simulated with WRLES.

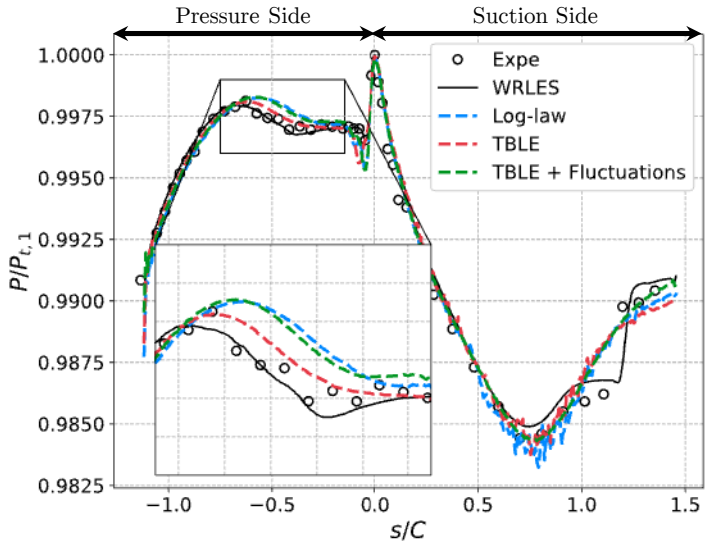

Figure 6.7: Pressure profile around the T72 blade.

The first results are analyzed by comparing the static pressure profiles around the blade along the non-dimensional curvilinear coordinate s/C, as shown in Figure 6.7.

The recirculation zone on the pressure side is accurately captured by the WRLES computation when compared to experimental data. In contrast, the WMLES using the logarithmic law of the wall fails to predict this region adequately. However, the

use of the TBLE model with the pressure gradient term improves the prediction, yielding pressure levels in better agreement with the WRLES results. In this region, however, the application of the fluctuations model leads to poorer performance, and the recirculation bubble is again poorly predicted, with inaccuracies comparable to those observed with the log-law model. This conclusion is consistent with the observations drawn from the periodic hill test case for which the fluctuations model showed deteriorated performance in low-velocity regions.

The second notable region, the transition zone on the suction side, is this time captured by the WRLES but missed by all WMLES computations. This outcome was expected, as no specific treatment for capturing the laminar-to-turbulent transition was included in these simulations, and the wall models were designed exclusively for fully turbulent conditions.

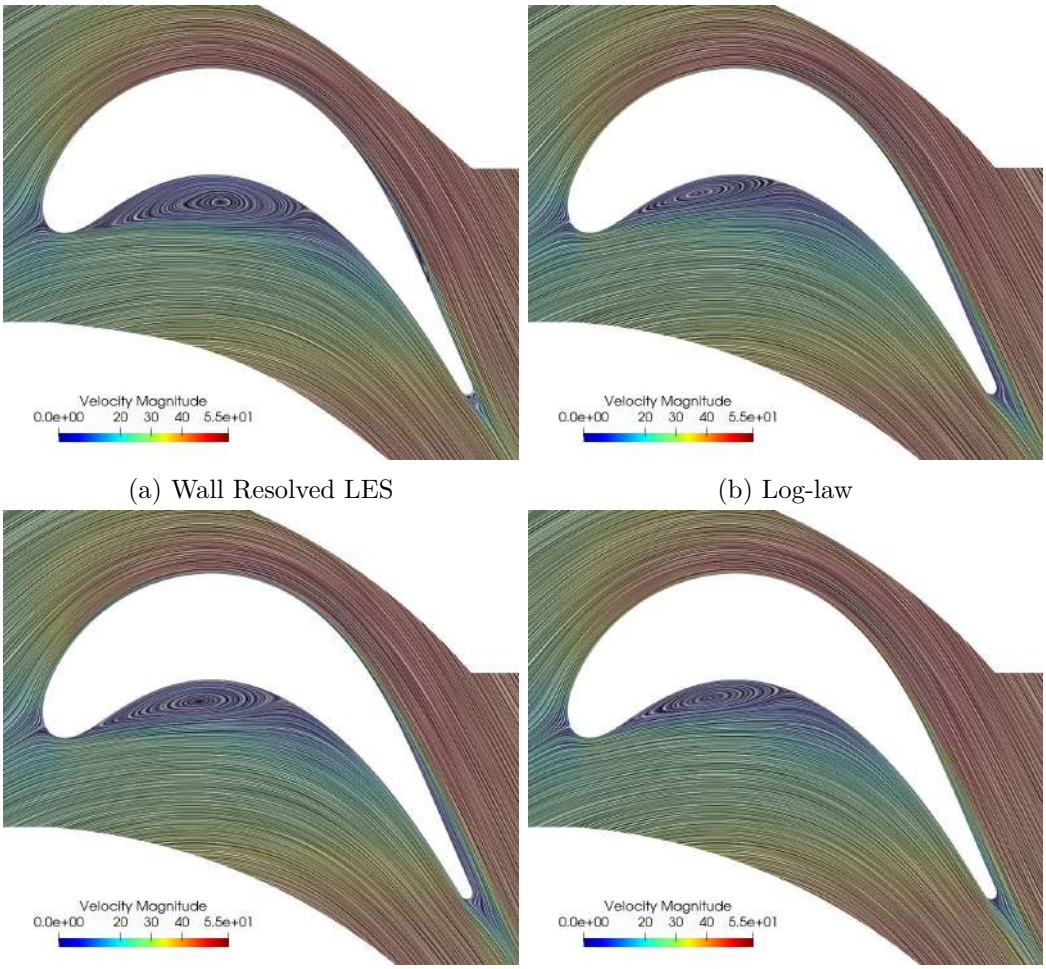

(a) Wall Resolved LES (b) Log-law

(c) TBLE (d) TBLE + Fluctuations

Figure 6.8: Streamlines around the T72 turbine blade.

The streamlines plotted around the turbine blade for each setup in Figure 6.8 give additional information on the performance of the different models on this configuration. In the case of the log-law computation, a small recirculation bubble on the pressure side is indeed predicted, but it is too small and positioned too far upstream relative to the WRLES reference. Conversely, when employing the TBLE model with the pressure gradient term, the streamlines show that the predicted recirculation bubble is larger and positioned further downstream. However, it is still a bit too small and remains too far upstream compared to the WRLES results, which explains the difference observed in the pressure profiles. It can also be noted here that this recirculation zone is better predicted without the fluctuations model than with it. This result is coherent with what was observed on the periodic hill.

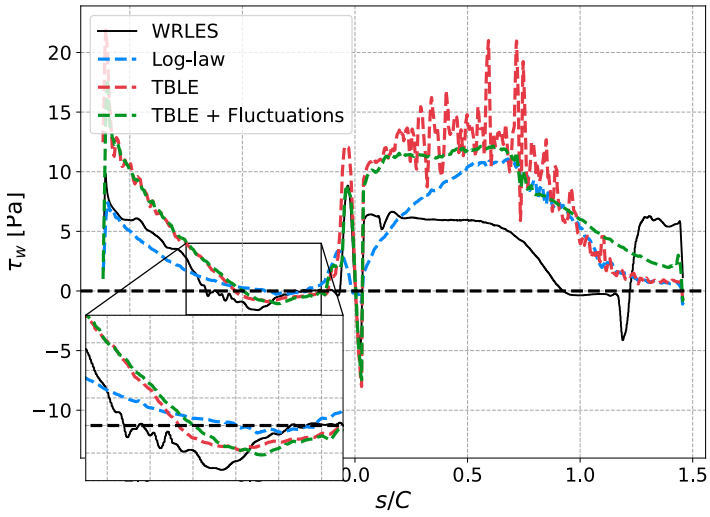

Figure 6.9: Friction levels around the T72 blade.

These observations are reinforced by the friction profiles, plotted in Figure 6.9, where the ability of the TBLE model with the pressure gradient to capture a much more realistic recirculation bubble is confirmed, although its size and exact position are still off by a small amount when compared to the WRLES results. Regarding the friction profile on the suction side, the WMLES computations generally give too high friction levels compared to the WRLES results. This is because the boundary layer on the suction side of the blade is largely laminar while the wall models used are designed to yield friction levels representative of fully turbulent conditions. It can still be noted in that region that the shapes of the friction profiles are more realistic using the TBLE approach than with the analytical law-of-the-wall, despite the overestimated levels, when compared to the reference.

Additionally, in all wall-modeled cases, the boundary layer is observed to stay laminar up to the trailing edge of the blade, and no laminar-to-turbulent transition is captured, whereas the friction profile of the WRLES clearly indicates this transition. This was expected, based on the nature of the models and the lack of

a transition model. It may also be possible that the too high friction predicted by the wall models on the suction side plays a role in the behavior of the boundary layer in this region, preventing it from separating and transitioning.

Regarding the role of the fluctuations model, the observation of the recirculation zone on the pressure side in Fig. 6.9 shows that the friction levels obtained seem insensitive to whether the fluctuations model is used or not. This suggests that the deterioration of the pressure profiles observed in Fig. 6.7 when using the fluctuations model is due to the excess levels of turbulent viscosity induced by the fluctuations model, and not to different friction levels predicted by the wall model. This behavior was already observed in the periodic hill test case and underlines the sensitivity of sub-grid scale viscosity models to the fluctuations model in low-friction regions.

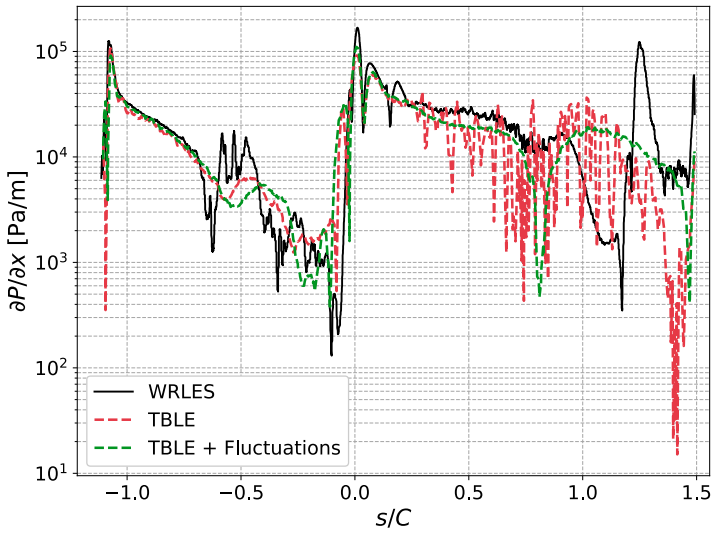

(a)

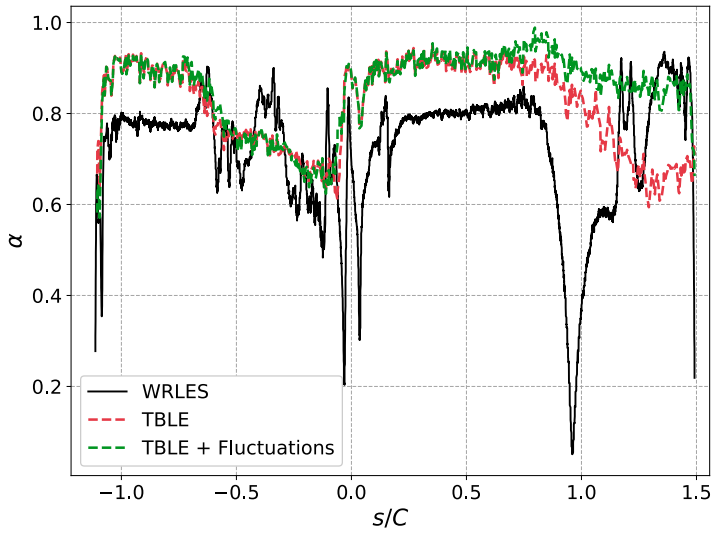

(b)

Figure 6.10: Pressure gradient importance along the streamwise direction plotted around the turbine blade both (a) in absolute value and (b) dimensionless α parameter.

Another remarkable observation from the friction profile is that, similarly to results obtained on the turbulent channel, the use of the fluctuations model smooths out the pressure gradient fluctuations near the wall when using the Sigma SGS model. This effect can be explained by the increase in turbulent viscosity close to the walls induced by the fluctuations model, which in turn leads to more homogeneous pressure gradient fields. This reasoning is further supported by the pressure gradient observations in Figure 6.10. In this figure, the WMLES pressure gradients are the time-averaged values of the input of the TBLE wall model. For the WRLES computation, the pressure gradient is extracted from the wall-neighboring cells of a time-averaged solution during a post-processing phase to provide a reference. When comparing the results, it can be seen that the pressure gradient used by the TBLE model in the absence of the fluctuations model appears noticeably noisier compared to the case with fluctuations on the suction side. Furthermore, it can be noted that the pressure gradient estimated with the TBLE model is in good agreement with the WRLES pressure gradient levels, except in the trailing edge area where, as already mentioned, the WMLES simulations don't predict the transition region. The non-dimensional pressure gradient in terms of $\alpha = u_\tau^2/u_{\tau p}^2$ based on the friction at the wall $u_{tau} = \sqrt{\frac{\tau_w}{\rho}}$ and pressure gradient at the wall via $u_{\tau p}^2 = u_\tau^2 + u_p^2 = u_\tau^2 + |(\nu/\rho)(\partial P/\partial x)|^{1/3}$ is also plotted in Figure 6.10b. The levels of α observed in this figure show this time different levels between the WRLES and the two different TBLE computations, which is caused in fact by the difference in wall friction predicted already discussed above, which is reflected here due to the non-dimensional form used.

As with the simpler academic cases discussed in sections 4.2 and 4.3, a summary of the computational costs associated with the different wall model approaches is provided in Table 6.2, including a comparison with the more computationally intensive WRLES. The computational costs for the various cases over the first five flow-through times of each simulation are presented. The additional cost incurred by the TBLE model is approximately 30% in that case, which is similar to what was noted in the periodic hill case. Furthermore, as anticipated, conducting a wall-resolved LES proves to be significantly more expensive than all WMLES, costing 587 times more than the logarithmic law simulation, due to both a higher number of cells and a lower time-step of the simulation. This striking contrast reinforces the relevance of studying and improving wall-modeled methodologies, as they offer a more affordable means of achieving rather accurate results in complex flow scenarios.

Case	Simulated flow-through times	Time-step (s)	Cost (h.CPU)	Add. Cost
Log Law	5	3.12×10^{-7}	197.7	
TBLE	5	3.12×10^{-7}	260.15	31.6%
TBLE + Fluctuations	5	3.12×10^{-7}	260.76	31.9%
WRLES	5	2.01×10^{-8}	116 100	58 624%

Table 6.2: Summary of the computational costs of the different setups of the T7.2 turbine.

The analysis of the T7.2 turbine blade gives much insight into the performance of wall models developed within this thesis for simulating complex flow phenomena associated with turbomachinery setups. These results confirm the trends observed in the simpler test cases. The WMLES computations using the logarithmic law of the wall fail to predict the recirculation zone and transition region, leading to significant friction and pressure profile discrepancies. In contrast, the TBLE model including the pressure gradient term shows significant improvements over the logarithmic law. It better predicts the separation and recirculation bubble on the pressure side, even if it still fails to capture the laminar separation and transition to turbulence. Moreover, the application of the fluctuations model in low-velocity regions leads to an overprediction of turbulent viscosity and thus deteriorates the simulation predictions. In other flow regions, however, the fluctuations model does allow the TBLE model to use a smoother pressure gradient compared to the case without a fluctuations model.

6.2 Fan of the DGEN-180 engine

6.2.1 Presentation

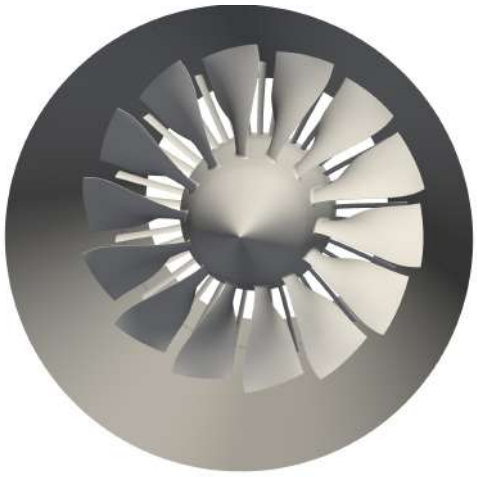

Figure 6.11: Front view of the fan of the DGEN engine.

The second turbomachinery configuration considered in this study is the fan stage of the DGEN-180 engine. This small geared turbofan engine was developed by AKIRA (formerly Price Induction) to be installed on light private aircraft in a twin-jet configuration. It presents a two-spool, unmixed flow design with a bypass ratio of 6 and a fan pressure ratio of 1.2 at maximum power. The engine is optimized for cruise at 4500 meters with a Mach number of 0.338. Under this condition, the thrust produced by the engine is 105 daN.

The fan stage of the engine, which is the object of this study, has a diameter of 352 mm with 14 rotor blades and 40 stator vanes, as shown in Figure 6.11. This

configuration presents a challenging case for wall modeling due to the complexity of the flow dynamics within the fan stage, including interactions between the rotor and stator components. Besides, it is particularly interesting to test a compressing stage of a turbomachine in this work after analyzing a turbine configuration in the previous test case, which gives a broader understanding of wall model performance across different turbomachinery stages.

This engine's fan configuration has been the subject of numerous experimental studies at ISAE Supaero, with key results presented by García Rosa et al. [56, 57], and Thacker and García Rosa [171]. The synoptic view of the full engine configuration, along with the location of the instrumentation used within these experiments, is presented in Figure 6.12. Besides, the fan stage was numerically simulated in earlier studies using the AVBP LES solver, as can be found in the works of Odier et al. [121] and Odier et al. [123].

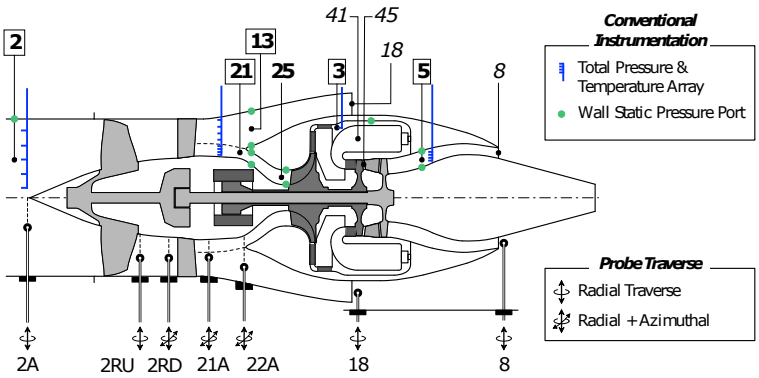

Figure 6.12: DGEN instrumentation cut, from García Rosa et al. [56].

In this work, the fan stage is simulated within a computational domain extending from an inlet located 3.28 rotor chord lengths C_R (at mid-span) upstream of the rotor to an outlet positioned 5.33 chord lengths downstream of the rotor, with the stator situated in between, as shown in Figure 6.13. Only one sector containing one rotor blade and three stator vanes is simulated to reduce the computational cost. Periodic boundary conditions are used to approximate the conditions of the full stage, which originally consists of 14 rotor blades and 40 stator vanes. This configuration however requires 42 stator vanes instead of 40 to accommodate for periodicity. To ensure a similar solidity of this modified stator, the blade stator chord is scaled down by a factor of $40/42 \approx 0.95$, thereby increasing the blade aspect ratio equivalently. This adaptation ensures that the aerodynamic characteristics of the stator remain consistent with the original design.

The computational domain is divided into two distinct regions: a rotating part containing the rotor blade and a stationary part containing the three stator blades. The Large Eddy Simulations (LES) of this configuration are performed using the TurboAVBP framework, as described by Wang et al. [179]. This framework couples the computations of two separate AVBP instances: one dedicated to the rotor and the other to the stator. The coupling of the two computational instances is done

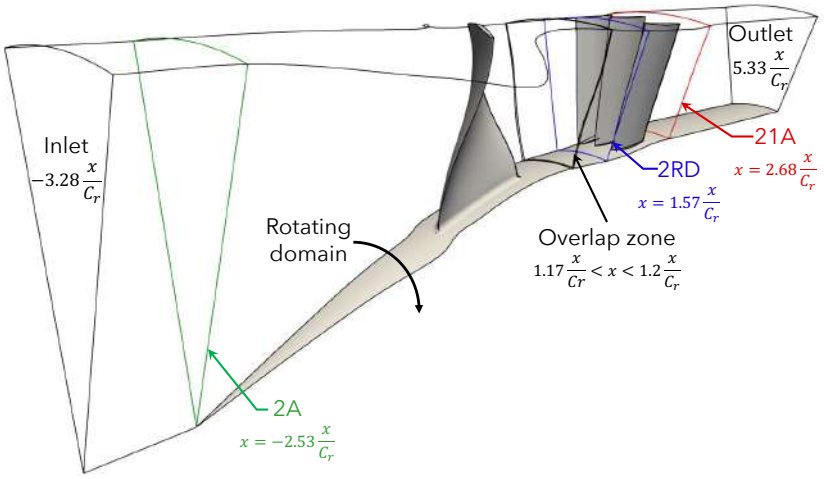

Figure 6.13: Geometry features of the simulated DGEN fan sector.

through an overlap zone between their respective meshes, as shown in Figure 6.13. In this overlap region, the coupling mechanism is implemented using the method detailed by Wang et al. [178], ensuring effective data exchange. Depending on the desired spatial accuracy, the coupling is performed using either a second-order [178] or a third-order interpolation [40]. This approach allows for an efficient and accurate simulation of the coupled rotor-stator interaction in the fan stage.

Inlet total pressure	99 306 Pa
Inlet total temperature	296.11 K
Rotating velocity N_{std}	11 460 rpm
Experimental total pressure ratio (21A/2A)	1.14
Experimental mass flow Q_{std}	12.1 kg/s
Rotor chord-based Reynolds number	700 000
Stator chord-based Reynolds number	322 000

Table 6.3: Operating point characteristics of the simulated DGEN fan.

The main characteristic of the operating point simulated during this work are reported in Table 6.3, with the standard rotating speed defined as

$$N_{std} = N\sqrt{\frac{T_{ref}}{T_{atm}}},$$

and the standard mass flow

$$Q_{std} = Q\sqrt{\frac{T_{atm}}{T_{\text{ref}}}}\frac{P_{\text{ref}}}{P_{\text{atm}}},$$

with N and Q respectively the absolute rotating velocity and mass flow, $P_{ref} = 101\,325$ Pa and $T_{ref} = 288.15$ K. This operating point corresponds to

85% of the engine's maximum power and an inlet Mach number of $Ma_{2A} = 0.32$. The inlet and outlet boundary conditions for this setup are imposed using the Navier-Stokes Characteristic Boundary Conditions (NSCBC) formalism [122, 137], as already applied in the T7.2 turbine case. At the inlet, the experimental total pressure and temperature are imposed along with an axial inlet velocity angle. At the outlet, the same boundary condition used for the turbine case is employed to impose the static pressure corresponding to the correct pressure ratio across the fan stage, while accounting for transverse flow terms [63]. All solid boundaries in the domain, including the casing, hub, and blades, are treated with adiabatic wall models.

Two sets of simulations are performed: one with the logarithmic law of the wall and one with the TBLE wall model implemented within this thesis. The TBLE model incorporates the pressure gradient term with temporal smoothing, as detailed in Section 4.1.2. However, similar to the T7.2 turbine blade cascade, no a priori knowledge of the friction in the setup is available, rendering the evaluation of the time characteristic $T_{av} = h_{wm}/(\kappa u_\tau)$ unusable. Instead, a characteristic time based on the duration of one full rotor rotation is used. The goal of this section is finally to enable a direct measurement of the performance of the TBLE model and an evaluation of any improvements achieved by the inclusion of pressure gradient effects in this fan configuration.

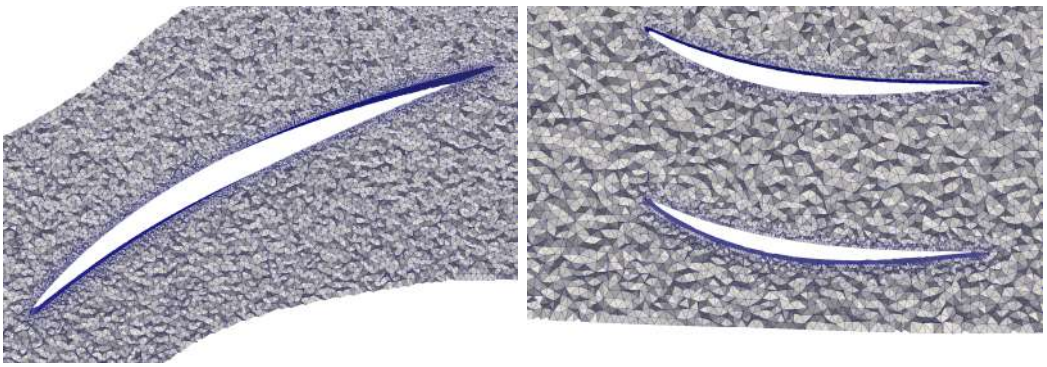

(a) Rotor (b) Stator

Figure 6.14: Side cuts of the near blade mesh of the DGEN setup.

The mesh used for the simulations is relatively coarse, balancing the requirement for the wall models to operate within their appropriate limits —specifically within the logarithmic region of the boundary layer— and the need to keep computational costs manageable. The stator mesh consists of 20 582 078 tetrahedral cells, while the rotor mesh comprises 26 758 529 tetrahedral cells. Representative cuts of both the rotor and stator meshes are given in Figure 6.14 to highlight the resolution and the overall structure of the computational domain at the mid-span of both rotor and stator blades.

The wall resolution obtained for both meshes, extracted at mid-span of the rotor and stator, is shown in Figure 6.15. The results indicate that the y^+ values

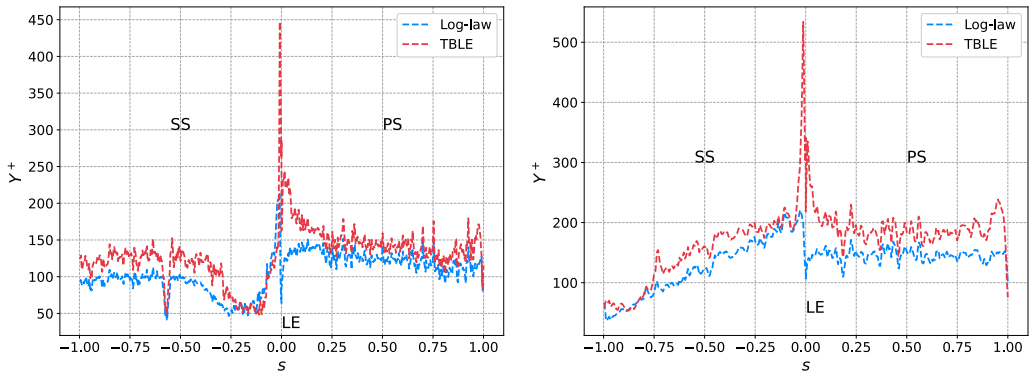

(a) Rotor (b) Stator

Figure 6.15: Mesh resolution in wall units of the blades of the DGEN at midspan.

are generally contained between 50 and 200. This range is sufficient to place the first wall cells within the logarithmic region of the boundary layer, thus justifying the appropriate use of the wall models in this setup.

The simulations performed for this case employ the second-order Lax-Wendroff scheme for time and space discretization [97] and the Sigma SGS model [118] to account for unresolved turbulent contributions. The computations ran for three complete engine rotations to ensure that the operating point was reached and stabilized, allowing any transient flow to dissipate. Following this stabilization phase, the simulations ran for two additional engine rotations to gather sufficient data for analyzing statistically representative time-averaged quantities.

6.2.2 Flow features

The main flow features of the simulated fan are first analyzed. The results of the TBLE model with pressure gradient inclusion are compared with those of the classical log-law. In both cases, the original Sigma SGS model is used. In terms of the operating point, Figure 6.16 illustrates that the correct pressure ratio at plane 21A is achieved for both computations. However, the mass flow rate is underpredicted by around 5% in the simulations when compared to the available experimental data. This implies that the simulations for both wall models do not correctly capture the appropriate level of losses within the setup. This observation has already been made in literature and it was shown that a mesh adaptation and refinement was an effective strategy to accurately reproduce both the correct mass flow and the corresponding pressure ratio simultaneously [123].

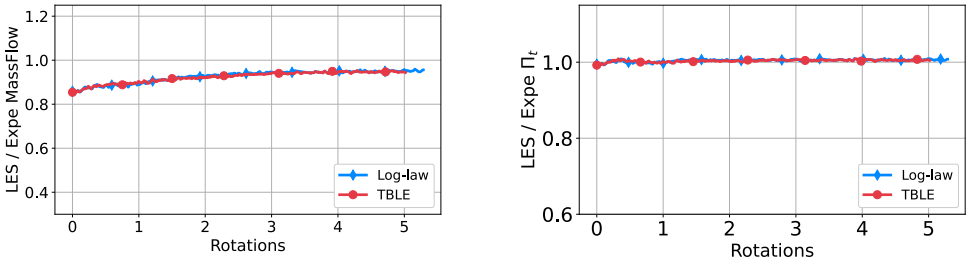

(a) Mass flow (b) Pressure ratio

Figure 6.16: 0D data of the DGEN at 21A plane.

To analyze the global flow structures, instantaneous contours of the Q-criterion are plotted in Figure 6.17 for the rotor and Figure 6.18 for the stator. Starting with the rotor, both computations—using either the log-law or the TBLE wall model—exhibit no distinct flow structures around the blades, suggesting the prediction of a predominantly laminar boundary layer. In both cases, a corner vortex-type flow is observed characterized by a coherent structure at the corner between the hub and suction side of the blade. Additionally, both simulations do not reveal any significant differences in the formation of the vortical structures developing at the rotor tip.

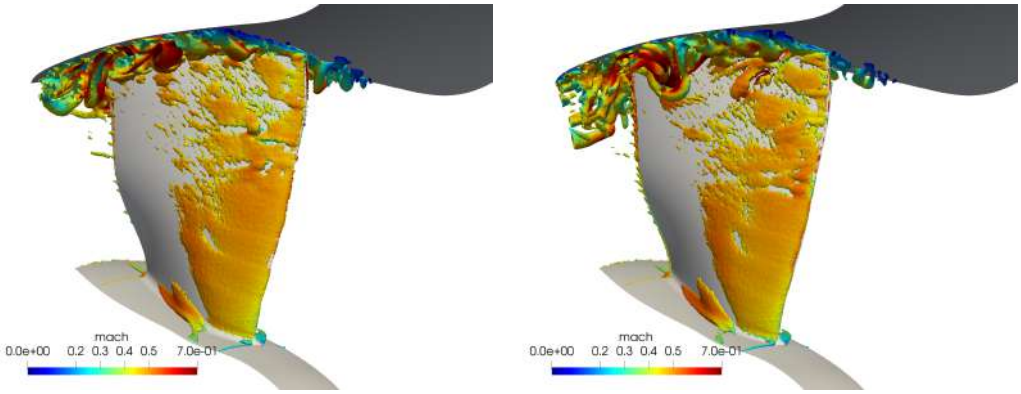

(a) Log-law (b) TBLE

Figure 6.17: Q-criterion isocontours on the rotor of the DGEN.

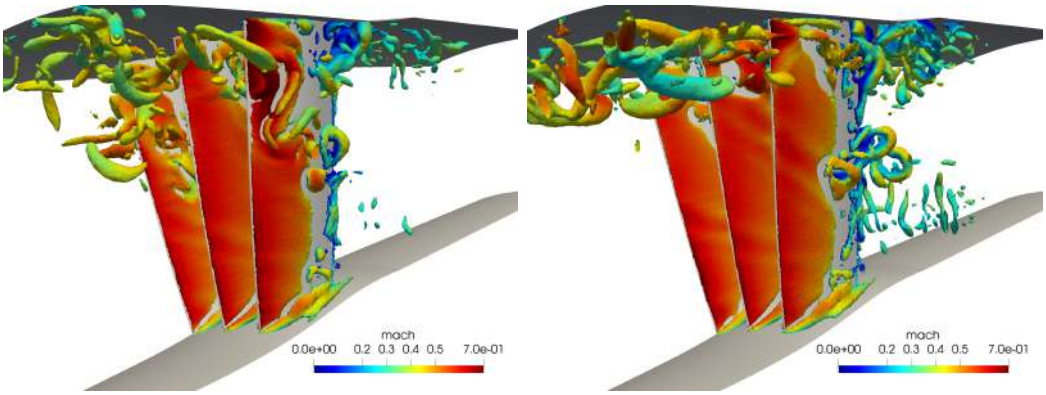

(a) Log-law (b) TBLE

Figure 6.18: Q-criterion isocontours on the stator of the DGEN.

Looking at the stator blade, no specific difference concerning either the structure of the incoming flow, characteristics of the boundary layers, or even wake structures developing past the stator blade could be obtained between the two models. In addition, the vortex forming at the corner between the suction side of the blades and the hub shows similar behaviors across both simulations.

Overall, no significant differences are observed in the results given by the classical log-law and the TBLE model accounting for pressure gradient concerning instantaneous flow structures and boundary layer behavior. In this regard, this case did not successfully demonstrate a notable contribution from the addition of the pressure gradient term in the TBLE wall model. It appears that further mesh refinement would be necessary in that case, or even some change in the wall modeling approach for the solution to fully represent flow behavior related to this particular fan.

6.2.3 Time-averaged results

After observing the main instantaneous flow characteristics, some time-averaged flow quantities are analyzed, with comparisons made to the experimental data at planes 2RD and 21A, as defined in Figures 6.12 and 6.13. Here again, the results obtained using the TBLE wall model with pressure gradient inclusion are compared to those obtained with the logarithmic law of the wall, with both sets of simulations employing the original Sigma SGS model.

6.2.3.1 Flow Fields Near the Blade Surface

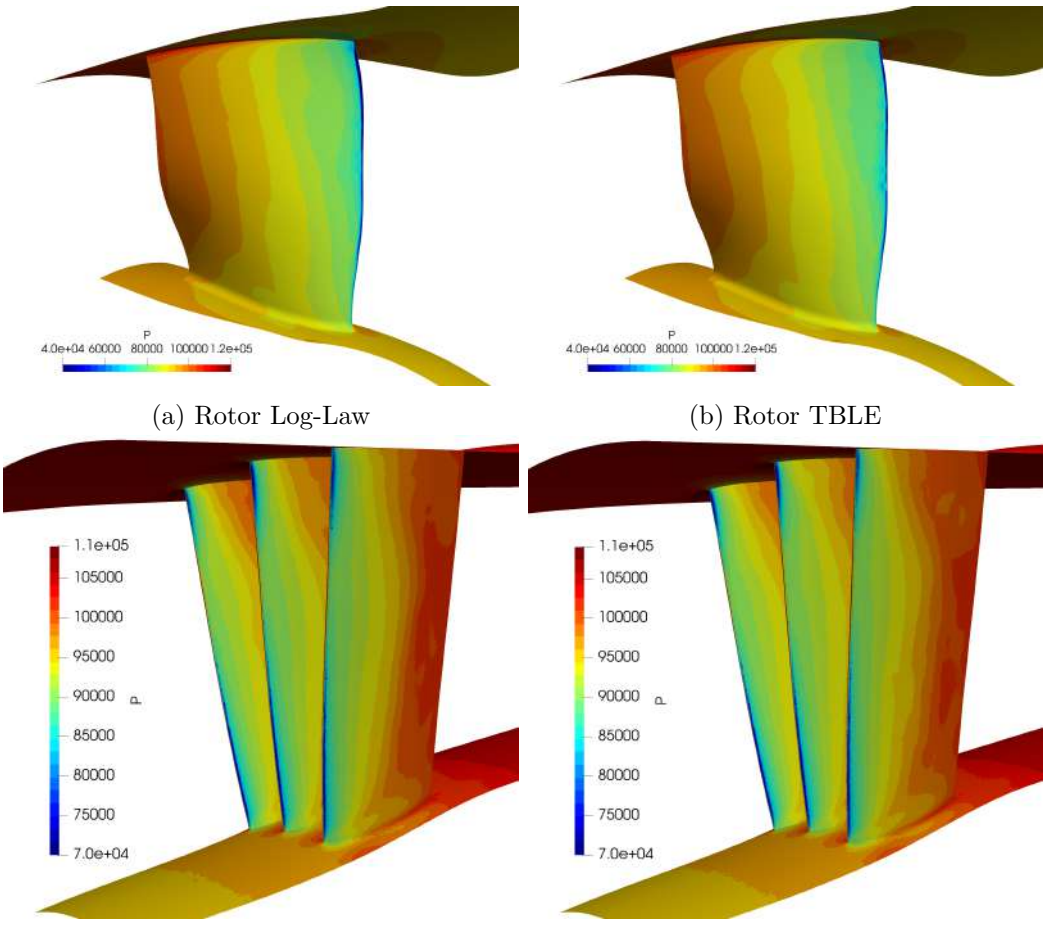

(a) Rotor Log-Law (b) Rotor TBLE

(c) Stator Log-Law (d) Stator TBLE

Figure 6.19: Time-averaged pressure field on the blades skin.

To begin with, the pressure field on the blades skin obtained with the different wall models is displayed for both the rotor and stator in Figure 6.19. Both wall models yield overall similar pressure distributions, which indicates that the general flow features and characteristics of pressure remain largely identical. One noticeable difference is visible however on the stator's suction side, above mid-span and near the casing. These observations are confirmed by the examination of pressure profiles plotted at constant channel height in Fig. 6.20, which additionally suggest the presence of flow separation on the suction side of the stator above mid-span.

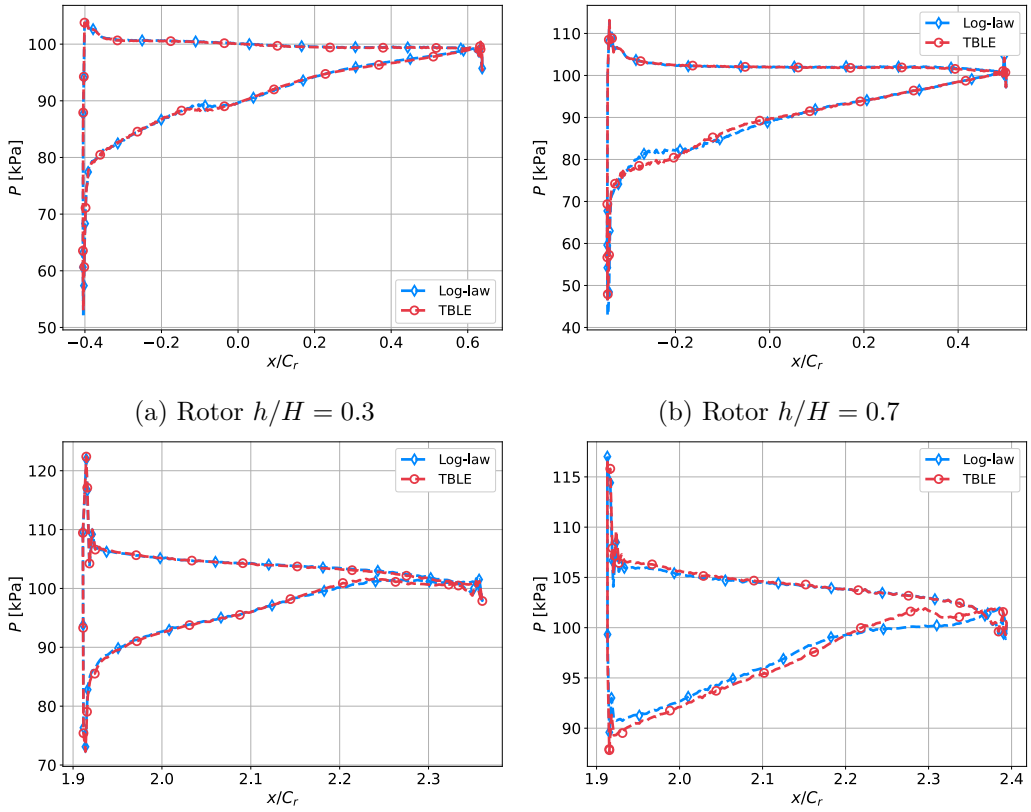

(a) Rotor $h/H = 0.3$

(b) Rotor $h/H = 0.7$

(c) Stator $h/H = 0.3$

(d) Stator $h/H = 0.7$

Figure 6.20: Time-averaged pressure profiles at iso height h/H along the rotor and stator blades.

Looking next at the time-averaged slip velocity fields on the suction-side of the stator blades in Fig. 6.21 confirms the presence of recirculation zones developing downstream of the mid-chord length both when using the log-law or the TBLE wall model with pressure gradient effects. While minor differences in the topology of the separation zones can be observed between the two models, both simulations produce overall similar regions of recirculation.

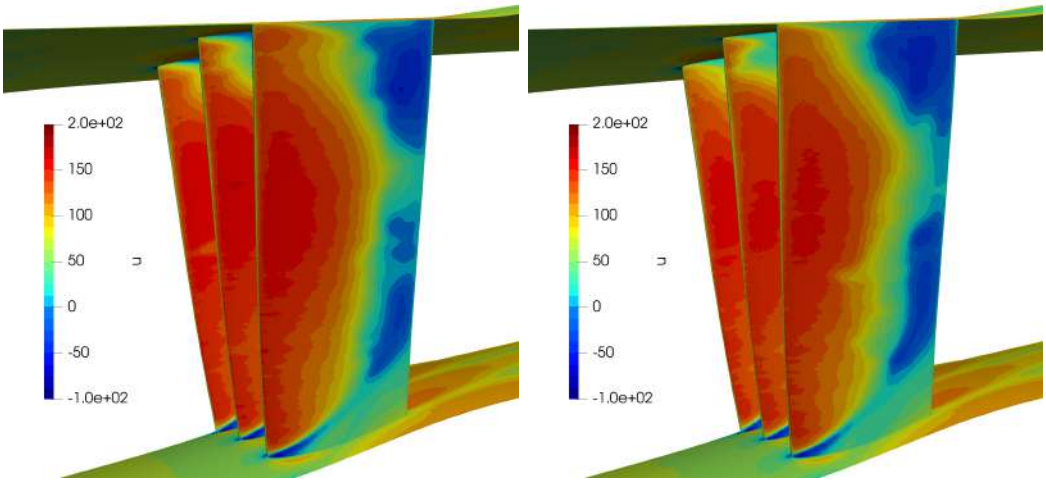

(a) Log-Law (b) TBLE

Figure 6.21: Time-averaged velocity field on the stator blades.

Turning to the wall friction produced by the different wall models, the results for both the rotor and stator are displayed in Figure 6.22. Focusing first on the rotor, some differences between the two models can be pointed out. The overall friction levels on the suction side are predicted to be higher when using the TBLE model with the pressure gradient term compared to the log-law model. In addition, the friction appears to be more uniform and at higher levels above half-span when the TBLE model is used. With the use of the TBLE model, the peak friction levels are also predicted to be higher at the leading edge.

Coming back to the stator, some more differences between the two models' friction level predictions come up. Similar to the rotor, the high friction area around the leading edge is also more concentrated when using the TBLE model; in that case, the friction levels are also notably higher. The TBLE model additionally predicts a high friction area on the hub and casing walls near the leading edge that is absent in the log-law computation, as well as increased friction at the corner between the suction side of the blade and the hub. This corresponds to the region where a corner vortex is identified in Figure 6.18 which leads to different levels of friction predicted depending on the wall model used.

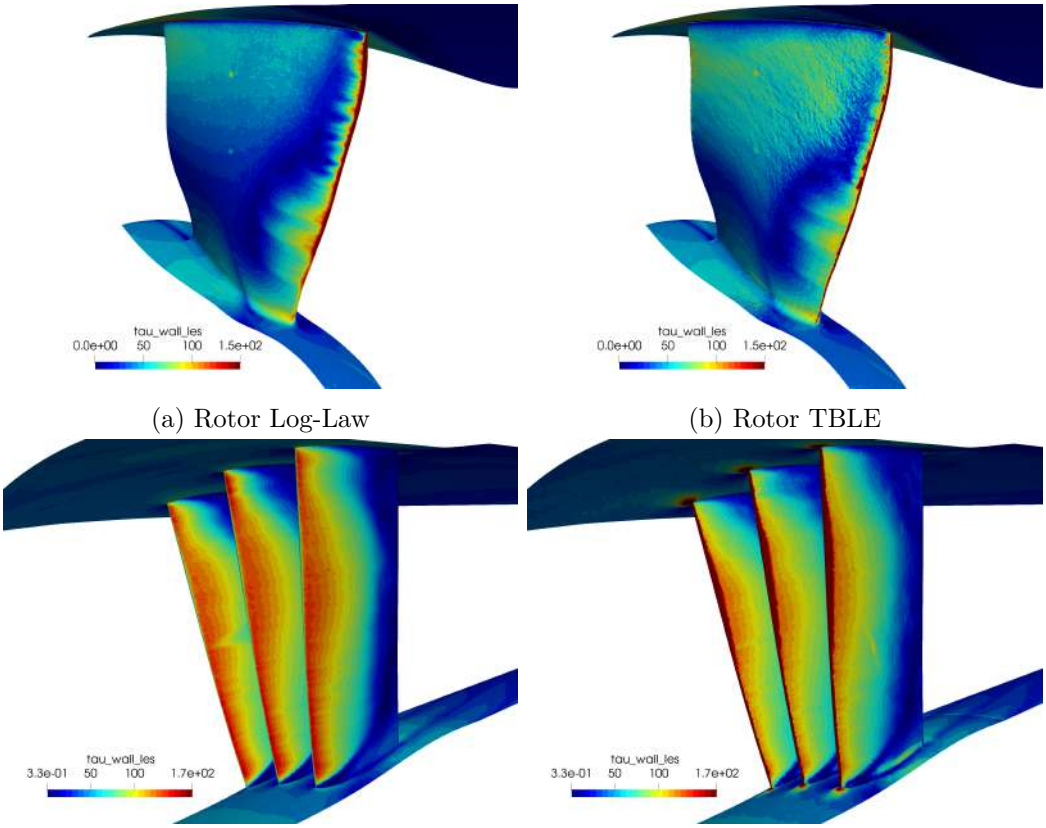

(a) Rotor Log-Law (b) Rotor TBLE

(c) Stator Log-Law (d) Stator TBLE

Figure 6.22: Time-averaged friction field on the blades skin.

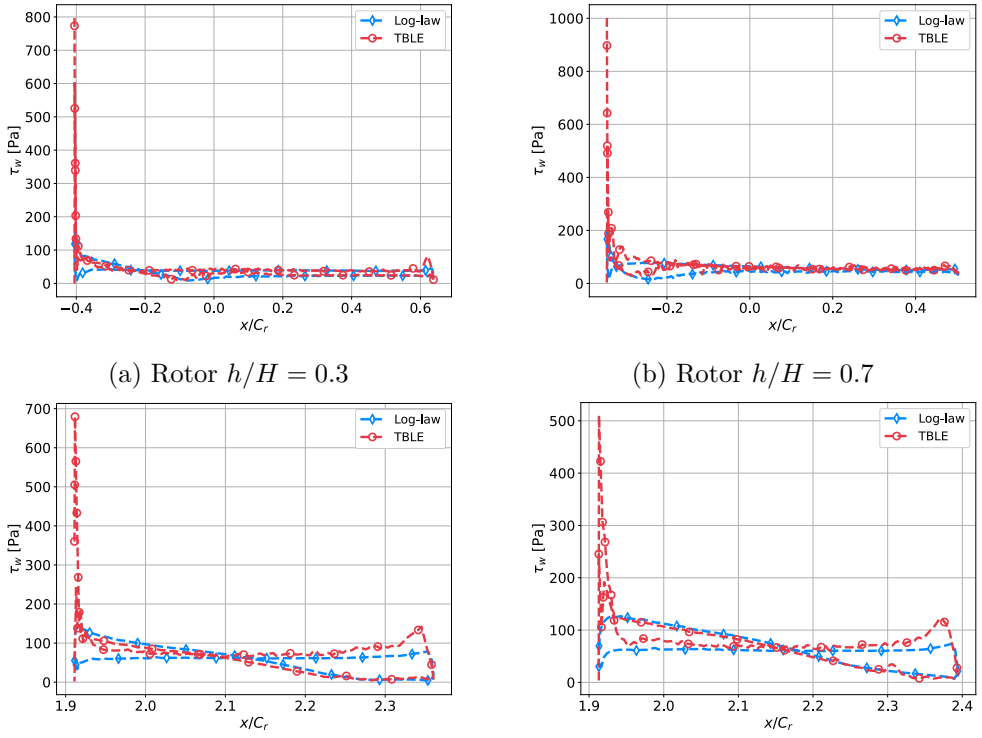

(a) Rotor $h/H = 0.3$ (b) Rotor $h/H = 0.7$

(c) Stator $h/H = 0.3$ (d) Stator $h/H = 0.7$

Figure 6.23: Time-averaged friction profiles at iso height h/H along the rotor and stator blades.

These differences in wall friction are also evident in the profiles plotted at iso-channel heights h/H, as shown in Fig. 6.23. On both the rotor and stator, the higher friction predicted by the TBLE wall model at the leading edge is noticeable at both heights presented, but appears to be unphysically high. The higher level of friction identified on the suction side above half channel can also be noted downstream of the leading edge, particularly visible at $x/C_r = -0.2$ and $h/H = 0.7$. Regarding the stator, consistent with observations on the blade surface the main visible difference between the results of the two wall models is the significantly higher friction predicted on the leading edge by the TBLE model.

Overall, the friction fields predicted by the two wall models differ in several regions on both the rotor and stator. However, the lack of available experimental data on friction, or higher-fidelity simulations for comparison, prevents us from definitively concluding whether these differences represent an improvement in the TBLE wall model with the integration of the pressure gradient effect. In addition to the differences observed in friction levels, no corresponding notable differences in flow behavior were noticed beforehand.

6.2.3.2 Flow Field Cross-Sections

After these observations of the blades' skin, time-averaged fields are compared at planes 2RD and 21A where experimental data is available.

Starting with the average axial velocity fields presented in Figures 6.24 and 6.25 for planes 2RD and 21A, respectively, no striking differences emerge between the results yielded by either wall model. This strengthens the conclusion that, in this case, no significant improvement can be attributed to the inclusion of pressure gradient effects within the wall model through the TBLE approach. Although this outcome may not meet initial expectations, it has to be noted that the relatively coarse mesh used could have limited the overall accuracy of the simulation, and could be the limiting factor in that instance.

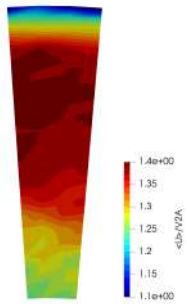

(a) Experiment

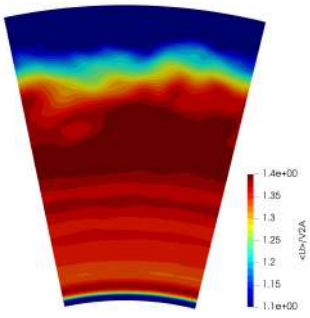

(b) Log-Law

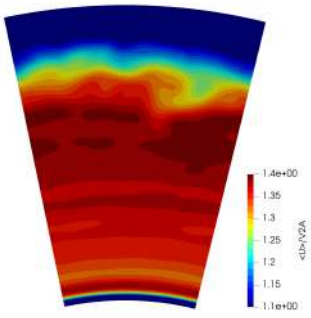

(c) TBLE

Figure 6.24: Time-averaged axial velocity at plane 2RD.

When comparing the LES results to the experimental data at plane 2RD, located between the rotor and the stator in Fig. 6.24, it is observed that near the hub, the velocity deficit is overestimated in the WMLES, while the secondary flow region is observed to be thicker in the experiments. Near the casing, on the other hand, the blockage area linked to the rotor clearance flow is predicted to be too thick by simulations. The flow near the casing is heavily dominated by the tip leakage vortex, which is overpredicted in size as well as impact compared to its real behavior in the experiments. A mesh adaptation strategy could be relevant in this case to better capture such phenomenon, as experimented in the work of Odier et al. [123].

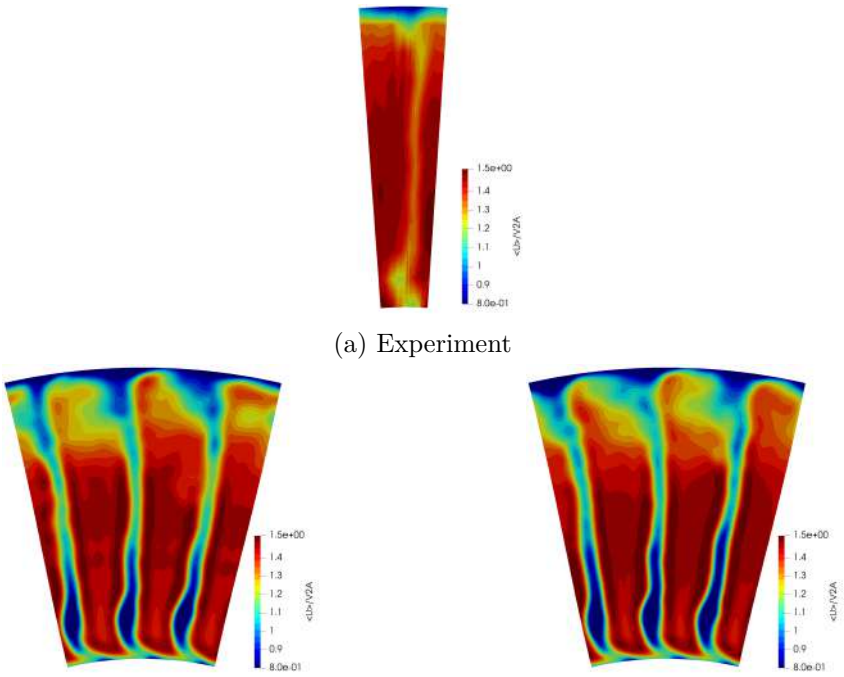

(a) Experiment

(b) Log-Law

(c) TBLE

Figure 6.25: Time-averaged axial velocity at plane 21A.

Turning to plane 21A in Fig. 6.25, located in the wake of the stator, the time-averaged axial velocity fields do not reveal noticeable differences between the two wall models, as mentioned previously. In this case, the velocity deficit present at the hub and casing is predicted to be greater by the LES than what is observed experimentally. Moreover, LES calculations overestimate the wake of the stator blades, and thus the wake region is thicker and with a more significant velocity deficit compared to the experimental findings. Such an observation shows again that the mesh used for this WMLES may be too coarse to resolve and transport the vortex structures accurately, which appear overpredicted in intensity for this setup. In this regard again, the use of mesh adaptation could improve this wake prediction.

Further investigation of the vortices and turbulent structures predicted by the LES can be done by analyzing the turbulence intensity fields. This can help in iden-

tifying deficiencies in the simulation as well as bringing in valuable insights about the global turbulence characteristics of the flow. The axial turbulence intensity is computed using the following formula:

$$I_u(\mathbf{x}) = \frac{u'_{RMS}(\mathbf{x})}{\bar{U}(\mathbf{x})} \tag{6.1}$$

the root mean square of the axial velocity u'_{RMS} is computed as

$$u'_{RMS}(\mathbf{x}) = \sqrt{\frac{1}{N}\sum_{i=1}^{N} u'^2(\mathbf{x}, i)}, \tag{6.2}$$

where N is the number of instantaneous samples. $N = 1\,080\,000$ in the experiment, while in both WMLES $N \approx 2000$.

In the turbulent velocity fields at planes 2RD and 21A, presented in Figures 6.26 and 6.27, respectively, no significant differences can be observed between the two WMLES setups. However, these turbulent fields suggest that the turbulent structures may not be accurately predicted, resolved, or transported in the simulations. At both planes, the turbulent activity near the casing is much higher compared to the experimental data. In the stator wake at plane 21A, both WMLES configurations predict excessive turbulent activity and vortices, which indicates again that a mesh refinement in the simulation would be needed to better capture the flow dynamics.

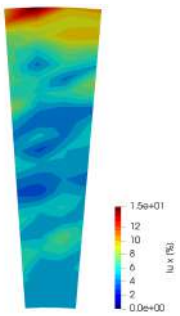

(a) Experiment

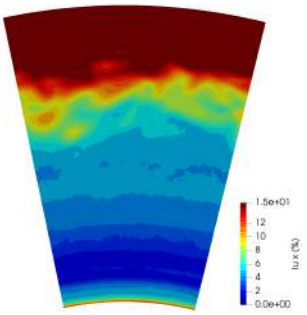

(b) Log-Law

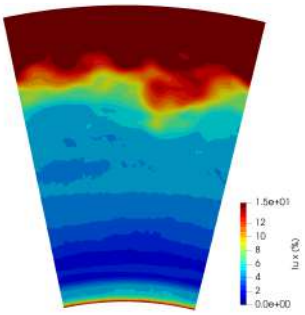

(c) TBLE

Figure 6.26: Turbulence intensity at plane 2RD.

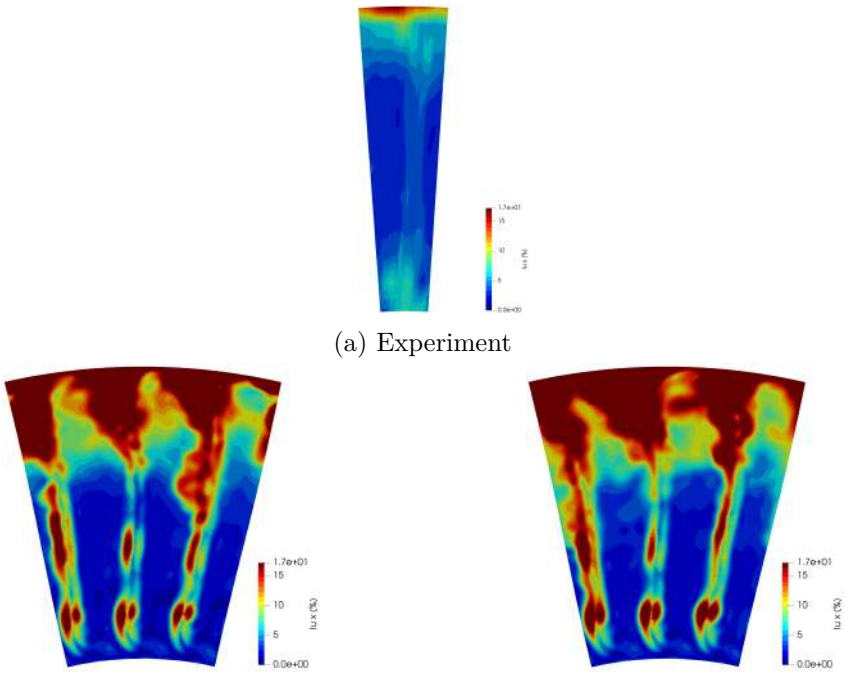

(a) Experiment

(b) Log-Law

(c) TBLE

Figure 6.27: Turbulence intensity at plane 21A.

In terms of computational costs, the simulations of the DGEN-180 fan needed around 12 000 CPU hours to run two complete engine rotations, as reported in Table 6.4. In that setup again, the additional computational cost added by running the TBLE model with the pressure gradient term fell within the range already observed in the previous test cases. In that particular instance, it required around 20% more CPU hours in total when compared to the simulation running the log-law model.

Case	Simulated fan rotations	Cost (h.CPU)	Add. Cost
Log Law	2	12 994	
TBLE	2	15 552	19.7%

Table 6.4: Summary of the computational costs of the different setups of the DGEN-180 fan.

As a conclusion, the fan of the DGEN-180 turbofan engine was successfully simulated using the TurboAVBP framework to compute the full compression stage, including the rotor and stator. This demonstrates the feasibility of applying the TBLE wall model developed in this thesis to such a complex configuration. Additionally, computations with this model exhibited the same extra computational cost that had been observed in simpler test cases, underlining the robustness and consistency of the implementation on setups with different levels of complexity.

However, the DGEN fan case did not evidence enough differences between the tested wall models to clearly demonstrate the improvements introduced by the pressure gradient term in the TBLE wall model. Although the friction levels on the blade, hub, and casing surfaces were notably different between the two wall models, these differences did not result in significant variations of overall flow features or averaged quantities. Comparisons of the average field at key planes with the experimental data showed that if any improvement is brought by the TBLE model, it is masked by large discrepancies between the WMLES results and the experiments.

These results are due to a number of factors, especially the coarse mesh. While intended to minimize computational cost while making the solution compatible with wall models, the mesh resolution was too poor to predict the behavior of the boundary layer, as well as the tip leakage development, and the wakes. The use of a finer mesh to capture complex flow physics and achieve closer agreement with experimental data may be one of the solutions to underline the improvements brought by the pressure gradient integration in the TBLE wall model. Additionally, the relatively low pressure ratio of the stage ($\Pi_t = 1.14$) limits the ability to distinguish the performance differences between the wall models. The use of a higher pressure ratio stage might help provide more conclusive results to identify the enhancements introduced by the TBLE wall model and the consideration of the pressure gradient.

Conclusion

This PhD work focused on wall-modeled Large Eddy Simulations (WMLES), particularly in the context of turbomachinery flows. Large Eddy Simulation (LES) is a numerical technique for simulating turbulent flows that falls between the highly detailed but very expensive Direct Numerical Simulation and the more affordable Reynolds-Averaged Navier-Stokes approach in terms of computational cost. LES achieves this by decomposing the fluid motion into large eddies which are resolved directly and small eddies which are not directly simulated but modeled through a sub-grid scale model. Despite its efficiency compared with DNS and the progress made in HPC over the last decades, the computational cost of LES remains considerable for high Reynolds numbers and large complex configurations. This is largely due to the high resolution required to accurately capture the near-wall region in turbulent boundary layers, which significantly increases the grid density and computational expense.

To mitigate the computational cost of Large Eddy Simulations of wall-bounded turbulent flows, wall models have been devised to provide an approximate representation of the intricate near-wall dynamics. By bypassing the need to resolve fine-scale turbulence directly at solid boundaries, wall models reduce the grid refinement requirements, as presented in Chapter 2. These models achieve significant savings in computational cost without compromising the acceptable level of accuracy for most engineering applications studying wall-bounded turbulent flows.

Over the past decades, various types of wall models have been developed and tested, with their characteristics and applications detailed in Chapter 2. This thesis focuses on wall stress models to fit within the context of the AVBP solver used in this work. These models provide the wall shear stress to the LES solver by solving some type of simplified equations in the near wall region.

The AVBP solver originally includes a logarithmic law of the wall model, a classical algebraic formulation frequently employed in LES and extensively documented in the literature. Although this model is widely used, it suffers from the same shortcomings as most wall models when dealing with LES. Broadly speaking, the problems that can arise fall into two categories: inaccuracies inherent in the wall model, and problems associated with coupling the wall model to the wider LES context.

First, the logarithmic law of the wall is based on strong assumptions about the boundary layer, which are mainly that the boundary layer is developing over a flat plate—thus is essentially 2D—, is incompressible, fully turbulent, stationary, and not subject to any pressure gradient. These simplifying assumptions limit its applicability to complex flow environments, such as turbomachinery configurations, where the influence of pressure gradients and other neglected physical phenomena become quite significant for accurate prediction, thus weakening the performance of the model.

Second, the integration of wall models into the LES framework is also challenging, as WMLES combines two frameworks that were not originally designed to interact seamlessly, namely the RANS context from which the wall model is derived on the one hand, and the LES equations on the other. This disparity is often identified as the source of the well-documented log-layer mismatch phenomenon, which can also be observed with the AVBP solver.

The primary objective of this thesis was to address both of these challenges by developing, implementing, and testing a complete approach that involved the following actions:

- Implementing a TBLE (Thin Boundary Layer Equations) wall model accounting for pressure gradient effects, a key feature in turbomachinery flows.
- Addressing the issue of the log-layer mismatch by improving, correcting, and increasing the robustness of the SGS correction model initiated by the work of Blanchard et al. [14].

Together, these advancements aim to improve the overall fidelity and robustness of WMLES simulations conducted within the AVBP framework for turbomachinery applications.

Results achieved during the thesis

During the present PhD work, a wall model based on solving the 1D Thin Boundary Layer Equations (TBLE) was implemented, enabling the inclusion of pressure gradient effects for more physically representative simulations. This model was combined with an eddy viscosity formulation that takes into account the influence of the pressure gradient, for more accurate physical representativeness. The inclusion of pressure gradient effects in this type of model has been identified in the literature as a useful feature to improve the predictions of turbomachinery WMLES, justifying the choice of this approach in this thesis.

The implementation of this model within the AVBP solver was evaluated through various test cases:

- A turbulent channel test case: The model was able to reproduce the canonical velocity profiles, similar to the logarithmic law of the wall in this case with no average pressure gradient. However, a temporal averaging filter had to be applied to the pressure gradient input to achieve these results, underlining the sensitivity of the model to pressure gradient fluctuations.
- A periodic hill test case: Over a range of Reynolds numbers, the TBLE wall model produced more accurate predictions than the log-law model in terms of the velocity profile, friction levels over the bottom wall, and characteristics of the recirculation bubble. These findings showcased the capability of this model to enhance the accuracy of WMLES under different conditions of friction and pressure gradient.

- A Turbine blade geometry (T7.2 turbine): On this first turbomachinery setup, the TBLE model showed improvements over the logarithmic law in predicting the recirculation region on the pressure side of the blade. However, as could be expected, it was unable to capture the laminar-to-turbulent transition on the suction side better than the log-law. Such a limitation is indeed inherent to this type of wall model.
- A Fan of a turbofan engine (DGEN-180): In that challenging test case, there was no evident improvement brought by the TBLE model compared to the log-law approach. Nevertheless, the successful application of the TBLE model within the TurboAVBP framework showed its robustness and adaptability to complex computational setups.

Alongside this development, the issue of the log-layer mismatch was also addressed within this thesis by improving the stochastic fluctuations model initially proposed by Blanchard et al. [14]. This fluctuation model originally aimed to enhance the coupling of a wall model with the SGS model—specifically the Sigma or WALE models—by modifying the SGS viscosity predictions in the near-wall regions, introducing stochastic velocity gradient fluctuations. During this thesis, this model was modified by restricting the fluctuations to the wall-normal component of velocity gradients and extending their application beyond the first wall-adjacent cells to a wider near-wall region. These changes were implemented to satisfy the theoretical and practical considerations outlined in part 5.2.2. The new version of the fluctuations model was tested on several cases in combination with either the log-law wall model or the TBLE wall model developed during this work:

- On the Turbulent channel case: The model effectively reduced the log-layer mismatch observed with both the Sigma and WALE SGS models. It also evidenced significant improvements in velocity profiles and SGS viscosity behavior over the original version of the fluctuations model. Additionally, its compatibility with the TBLE wall model was demonstrated. The modification of the SGS viscosity also induced a smoothing of the pressure gradient in the near wall region which proved to have a positive impact on the use of the TBLE wall model.
- On the periodic hill case: When combined with the TBLE wall model, the fluctuations model degraded predictions in low friction regions, particularly in the recirculation zone. However, in high-velocity regions with higher friction, the model improved the simulation quality, especially in the top wall region.
- On the T7.2 turbine blade: The use of the fluctuation model once again induced a smoothing of the near-wall pressure gradient, particularly on the suction side of the blade. However, in this transitional case, it did not improve predictions from either wall model, as these were not designed for laminar or transitional regions. In the recirculation bubble, the fluctuations model worsened the prediction accuracy of this region.

Future perspectives building on this thesis

The conclusions drawn from this PhD thesis naturally pave the way for potential advancements and future research directions:

- While the DGEN-180 fan study had inconclusive results, another study of a compressor stage may give better insight into the effect of introducing pressure gradient effects through the TBLE model and the fluctuations model. The study could consist of an investigation of the DGEN-180 fan on an adapted mesh or an entirely different compressor stage with a higher pressure ratio. Note that the compression ratio of this fan stage is quite limited ($\Pi = 1.15$). In either case, adequate mesh resolution for improved physical accuracy and access to reliable reference data will be required for meaningful comparisons.

- The TBLE model with pressure gradient effects implemented in this thesis is based on a number of simplifications, in which several significant terms have been neglected. However, the framework used for solving the 1D TBLE equations implemented in this work allows for additional physical terms to be included. In particular, one might consider including 3D convective terms since these are known to interact with the pressure gradient in boundary layer dynamics [17, 69, 96]. Accounting for these terms is however an important challenge since it requires a 3D computational framework to evaluate the spatial gradients in every direction. Some works, such as those of Hickel et al. [69], have proposed approximations to include these terms through a simplified 1D contribution. This approach could be investigated as a means to enhance the current model with minimal complexity.

- However, this model is still based on a one-dimensional RANS equation intrinsically ignoring 3D convective effects and is rigorously valid only for equilibrium boundary layer conditions (see part 2.3.1).

- The fluctuations model demonstrated limitations in low-friction regions, characterized by low velocities. In such regions, it has been shown to actually degrade the accuracy of the WMLES computations. A potential solution could involve disabling the fluctuations model in regions where the local values of y^+ fall below a predefined threshold that remains to be defined. This method could be implemented with minimal complexity, but rigorous testing would be required to confirm its ability to enhance predictions in low-friction regions while preserving the model's performance in the other regions of the domain.

Appendix

Appendix A

Applying the fluctuations model on the turbulent channel at different Reynolds numbers

---

This appendix presents some additional results of the application of the fluctuations model to turbulent channel at Reynolds numbers $\mathrm{Re}_\tau = 547$ and $\mathrm{Re}_\tau = 2003$. These complementary results reinforce and support the conclusions drawn in Chapter 5.

As was the case in Chapter 5, the results are first presented with the classical logarithmic law of the wall, and then with the TBLE model implemented during this thesis and detailed in Chapter 4. The results presented in the following are presented with a suffix corresponding to the models in use:

- "_F" when the fluctuations model is used
- (V) when the fluctuations model is applied to the wall-normal components of the velocity gradients only
- (2 cells) or ($y^+ < 500$) to distinguish the two implementations of the spatial extension of the model proposed in Chapter 5.

A.1 Results with the logarithmic law of the wall

Re_τ	Case	$Re_{b,Dh}$	$Re_{b,Dh,KNc}$	Error
	Smago	35520		<1%
	Sigma	32310		9%
	WALE	31418		11%
	Sigma_F	36204		2%
547	WALE_F	37107	35485	4%
	Sigma_F_V_2C	34826		1%
	WALE_F_V_2C	35465		<1%
	Sigma_F_V_yp	35275		<1%
	WALE_F_V_yp	36437		2%
	Smago	142974		<1%
	Sigma	130180		9%
	WALE	126518		11%
	Sigma_F	149011		4%
2003	WALE_F	154767	142816	8%
	Sigma_F_V_2C	140667		2%
	WALE_F_V_2C	144098		<1%
	Sigma_F_V_yp	139454		2%
	WALE_F_V_yp	142736		<1%

Table A.1: Wall friction results for the turbulent channel at $\mathrm{Re}_\tau = 547$ and $\mathrm{Re}_\tau = 2003$ comparing the different SGS models with and without the different enhancement of the fluctuations model.

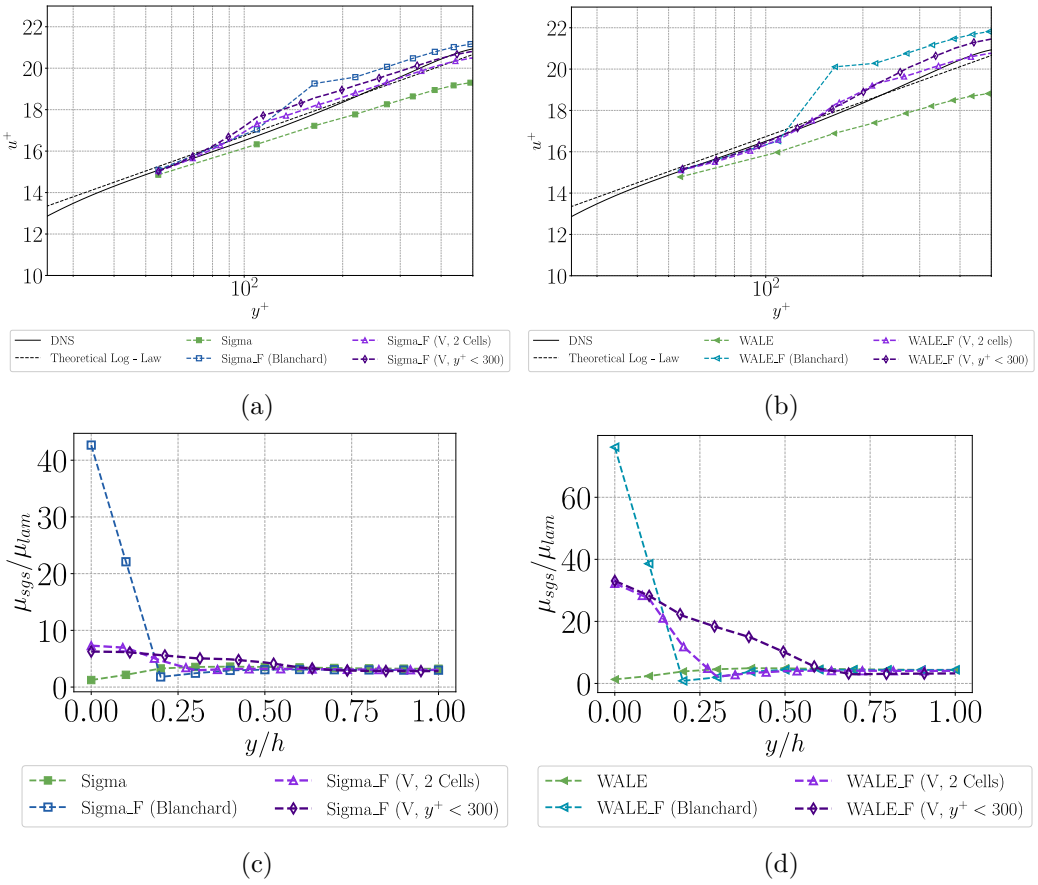

Figure A.1: Results of different versions of the fluctuations model on the turbulent channel ($\mathrm{Re}_\tau = 547$) in terms of velocity profiles for (a) Sigma and (b) WALE SGS models and SGS viscosity for (c) Sigma and (d) WALE.

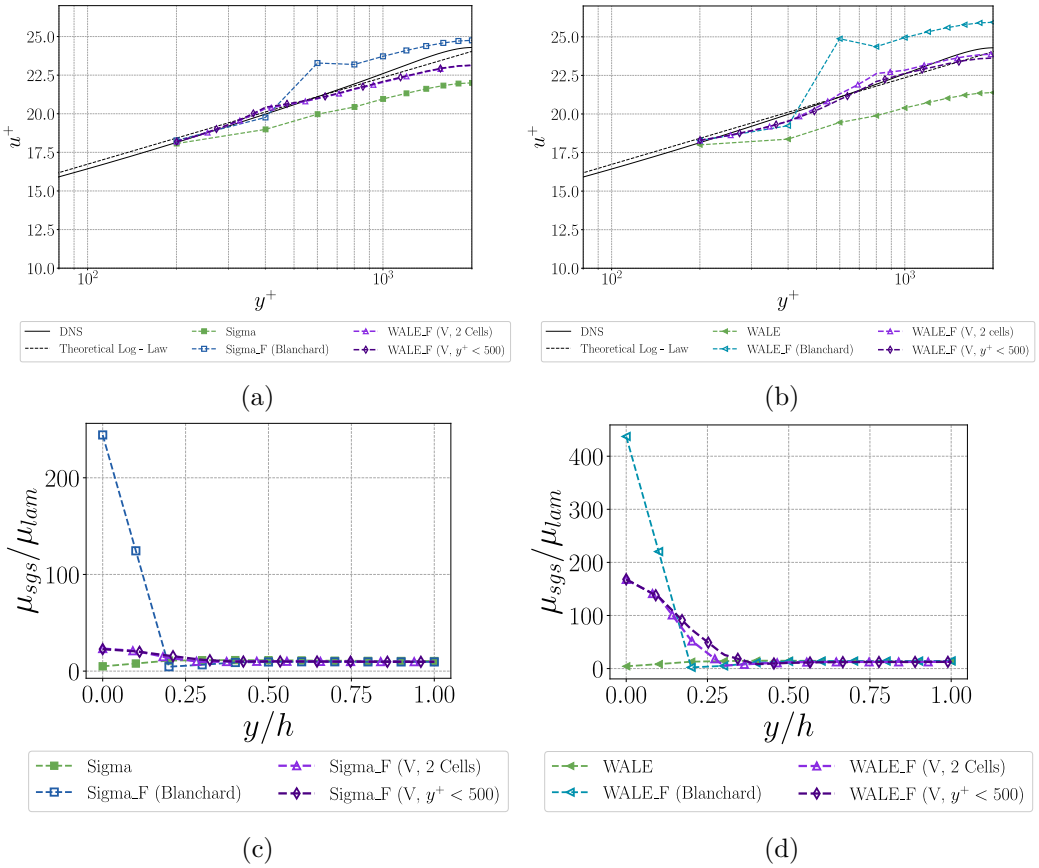

Figure A.2: Results of different versions of the fluctuations model on the turbulent channel ($\mathrm{Re}_\tau = 2003$) in terms of velocity profiles for (a) Sigma and (b) WALE SGS models and SGS viscosity for (c) Sigma and (d) WALE.

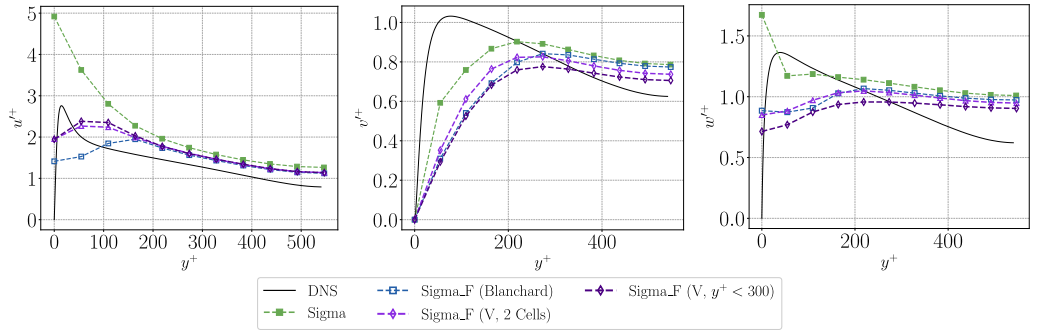

Figure A.3: RMS velocity profiles for the turbulent channel case at $\mathrm{Re}_\tau = 547$ and with different versions of the fluctuations model (with the Sigma SGS).

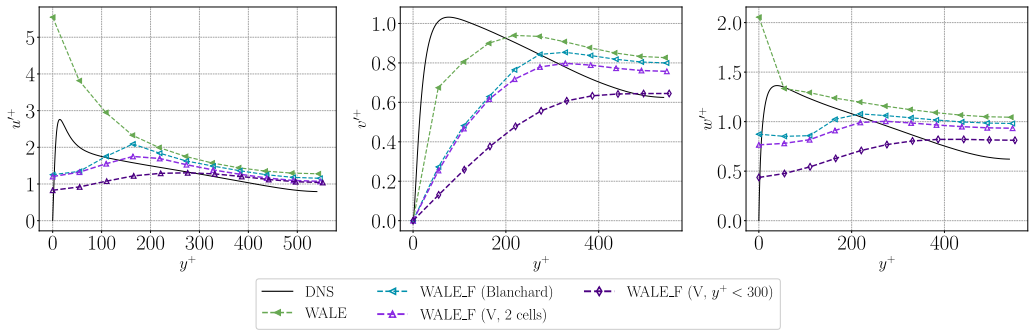

Figure A.4: RMS velocity profiles for the turbulent channel case at $\mathrm{Re}_\tau = 547$ and with different versions of fluctuations model (with the WALE SGS).

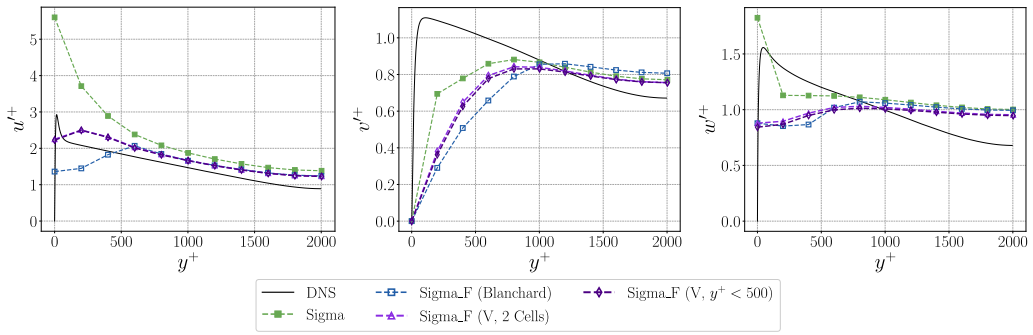

Figure A.5: RMS velocity profiles for the turbulent channel case at $\mathrm{Re}_\tau = 2003$ and with different versions of fluctuations model (with the Sigma SGS).

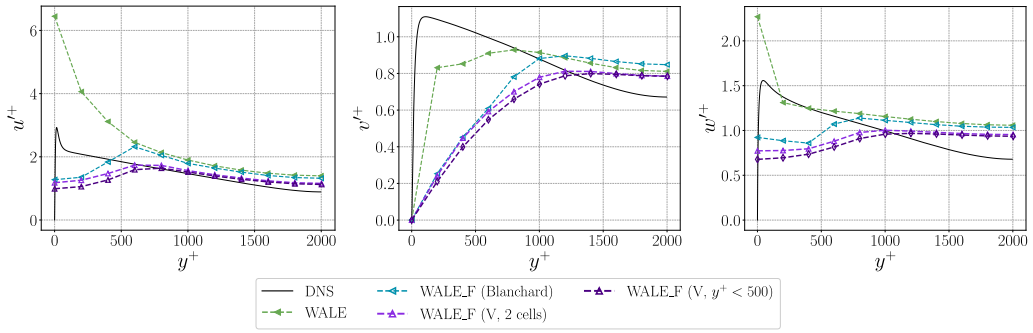

Figure A.6: RMS velocity profiles for the turbulent channel case at $\mathrm{Re}_\tau = 2003$ and with different versions of fluctuations model (with the WALE SGS).

A.2 Results with the TBLE wall model

Re_τ	Case	$Re_{b,Dh}$	$Re_{b,Dh,KNc}$	Error
	TBLE Smago	35667		<1%
	TBLE Sigma	25833		27%
	TBLE WALE	26363		25%
	TBLE Sigma (γ/100)	31156		12%
	TBLE WALE (γ/100)	31055		12%
547	TBLE Sigma_F	36000	35485	1%
	TBLE WALE_F	37304		4%
	TBLE Sigma_F_V_2C	34824		3%
	TBLE WALE_F_V_2C	35702		<1%
	TBLE Sigma_F_V_yp	35390		<1%
	TBLE WALE_F_V_yp	36775		3%
	TBLE Smago	144087		<1%
	TBLE Sigma	110516		22%
	TBLE WALE	110447		22%
	TBLE Sigma (γ/100)	128104		10%
	TBLE WALE (γ/100)	128443		10%
2003	TBLE Sigma_F	150276	142816	5%
	TBLE WALE_F	156290		9%
	TBLE Sigma_F_V_2C	144777		1%
	TBLE WALE_F_V_2C	145518		2%
	TBLE Sigma_F_V_yp	140382		2%
	TBLE WALE_F_V_yp	144168		1%

Table A.2: Wall friction results for the turbulent channel at $\mathrm{Re}_\tau = 934$ comparing the different SGS models with and without the different enhancement of the fluctuations model.

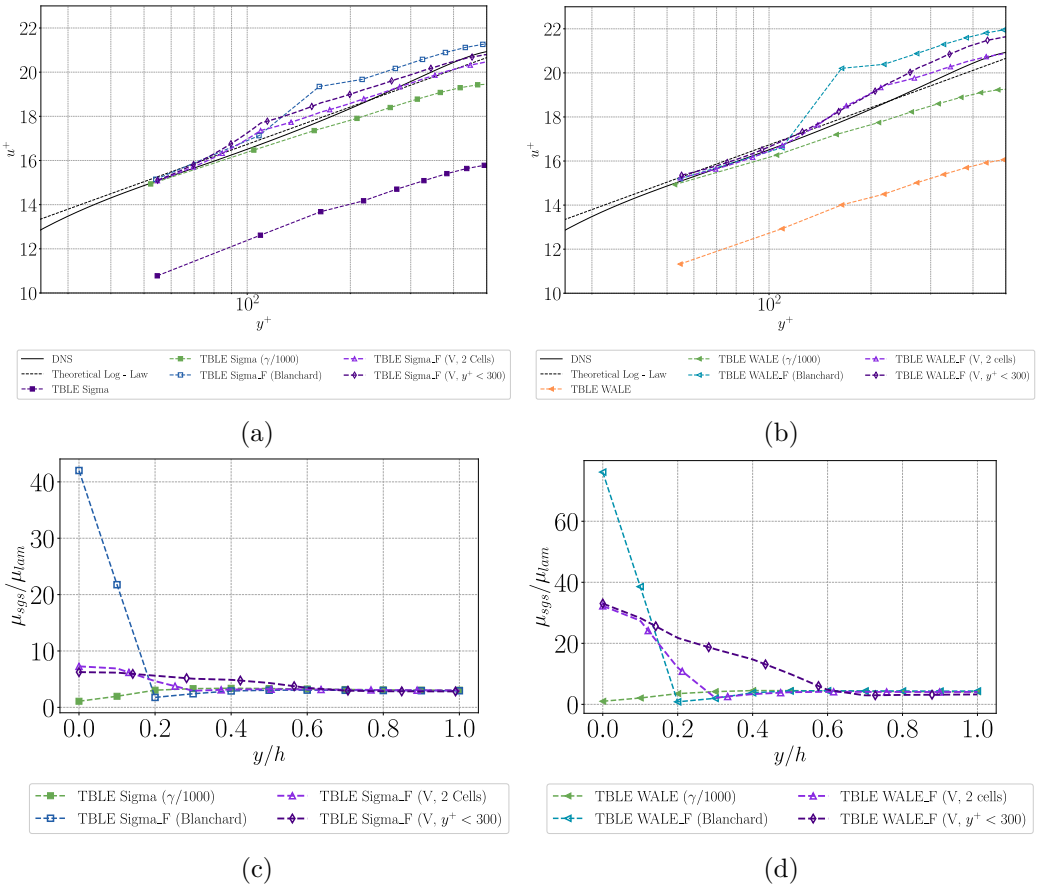

Figure A.7: Results of different versions of the fluctuations model in conjunction with the TBLE wall model on the turbulent channel ($\mathrm{Re}_\tau = 547$) in terms of velocity profiles for (a) Sigma and (b) WALE SGS models and SGS viscosity for (c) Sigma and (d) WALE.

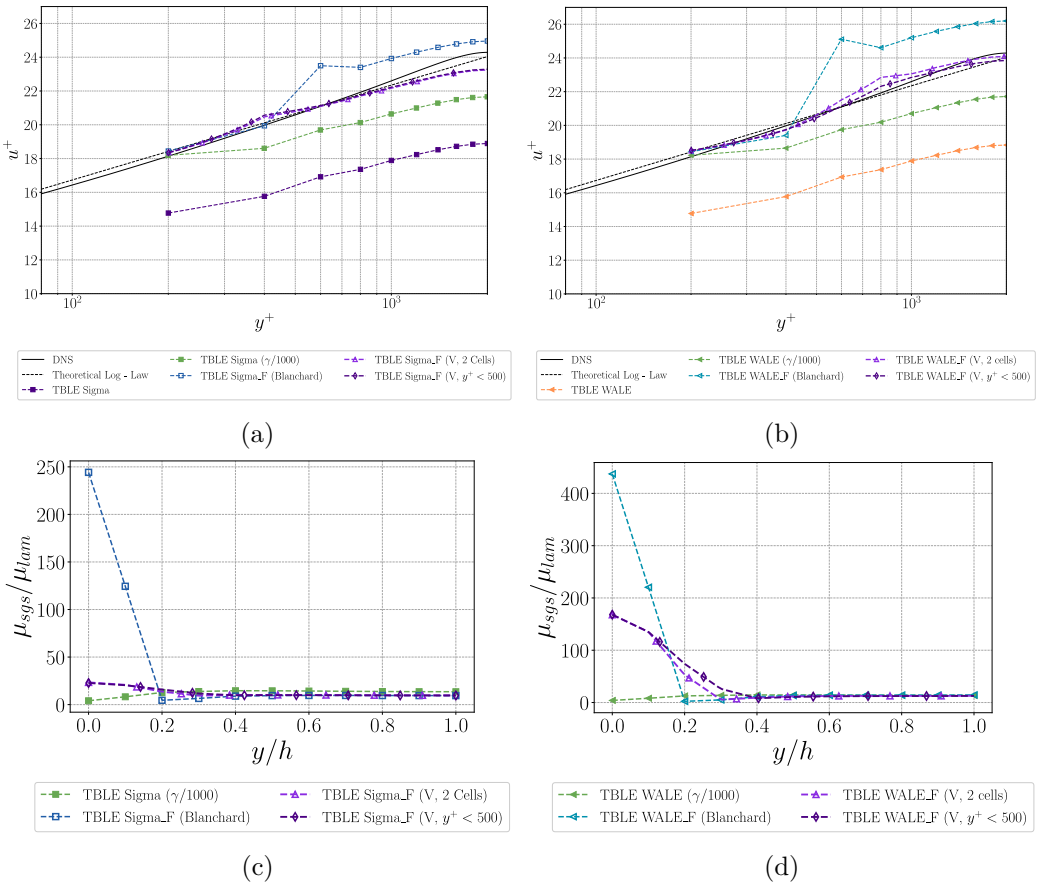

Figure A.8: Results of different versions of the fluctuations model in conjunction with the TBLE wall model on the turbulent channel ($\mathrm{Re}_\tau = 2003$) in terms of velocity profiles for (a) Sigma and (b) WALE SGS models and SGS viscosity for (c) Sigma and (d) WALE.

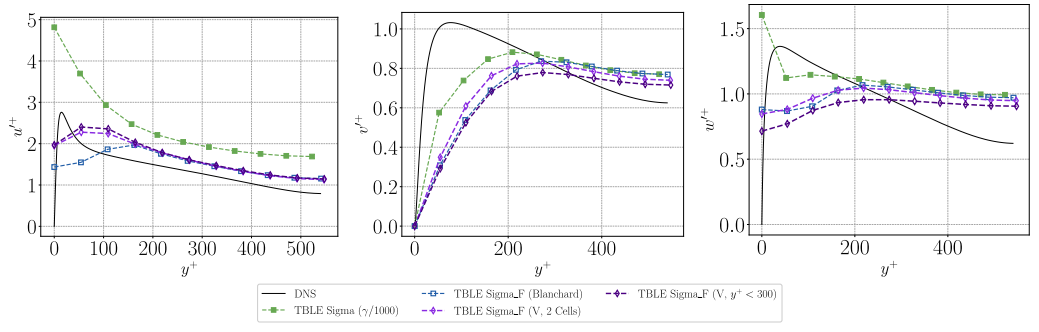

Figure A.9: RMS velocity profiles for the turbulent channel case at $\mathrm{Re}_\tau = 547$ and with the TLBE wall model and different versions of fluctuations model (with the Sigma SGS).

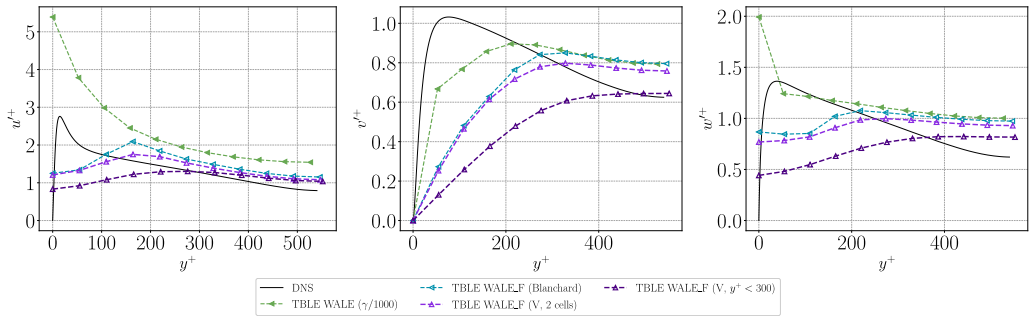

Figure A.10: RMS velocity profiles for the turbulent channel case at $\mathrm{Re}_\tau = 547$ and with the TLBE wall model and different versions of fluctuations model (with the WALE SGS).

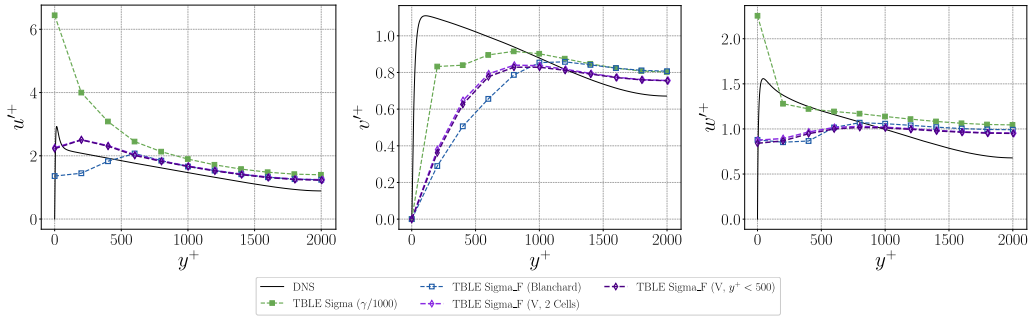

Figure A.11: RMS velocity profiles for the turbulent channel case at $\mathrm{Re}_\tau = 2003$ and with the TLBE wall model and different versions of fluctuations model (with the Sigma SGS).

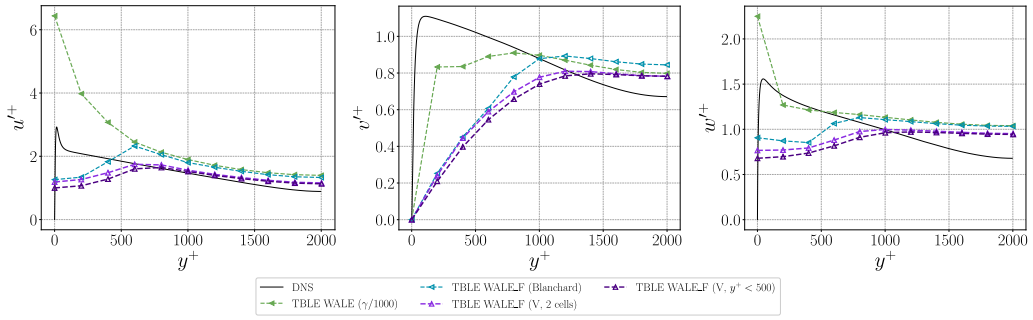

Figure A.12: RMS velocity profiles for the turbulent channel case at $\mathrm{Re}_\tau = 2003$ and with the TLBE wall model and different versions of fluctuations model (with the WALE SGS).

Appendix B

Applying the fluctuations model on the periodic hill at higher Reynolds numbers

This appendix presents the additional results of the application of the fluctuations model to the periodic hill setup at the higher Reynolds numbers $\mathrm{Re}_b = 19\,000$ and $\mathrm{Re}_b = 37\,000$. These complementary results reinforce and support the conclusions drawn in Chapter 5.

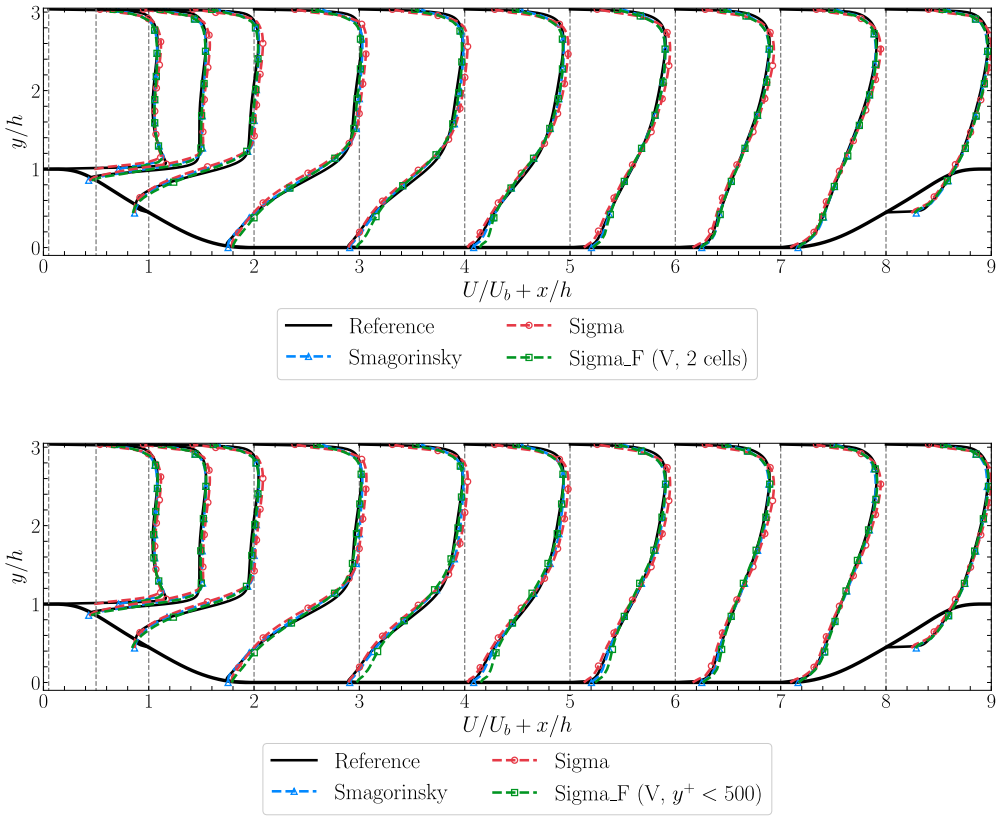

Figure B.1: Average streamwise velocity over the periodic hill case computed with the TBLE wall model and with or without the enhanced fluctuations model compared to WRLES reference [61] for $\mathrm{Re}_b = 19\,000$.

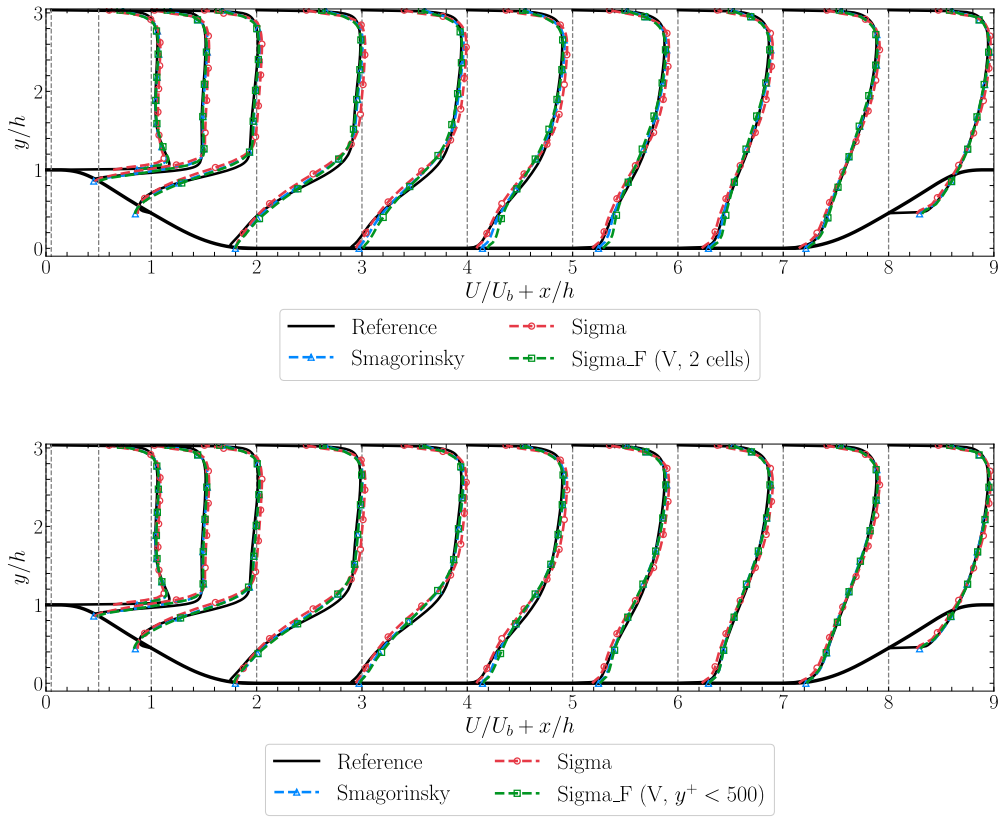

Figure B.2: Average streamwise velocity over the periodic hill case computed with the TBLE wall model and with or without the enhanced fluctuations model compared to WRLES reference [61] for $\mathrm{Re}_b = 37\,000$.

Re_b	Case	WRLES [61]	Exp. [142]	TBLE (Error)
19000	Smagorinsky	3.95	3.94	3.12 (21%)
	Sigma			3.34 (12%)
	Sigma_F (V, 2 cells)			2.67 (32%)
	Sigma_F (V, $y^+ < 500$)			2.67 (32%)
37000	Smagorinsky	4.0	3.76	2.89 (23%)
	Sigma			3.16 (16%)
	Sigma_F (V, 2 cells)			2.71 (28%)
	Sigma_F (V, $y^+ < 500$)			2.80 (26%)

Table B.1: Recirculation zone reattachment length on the Periodic Hill with relative errors computed with respect to the WRLES [61].

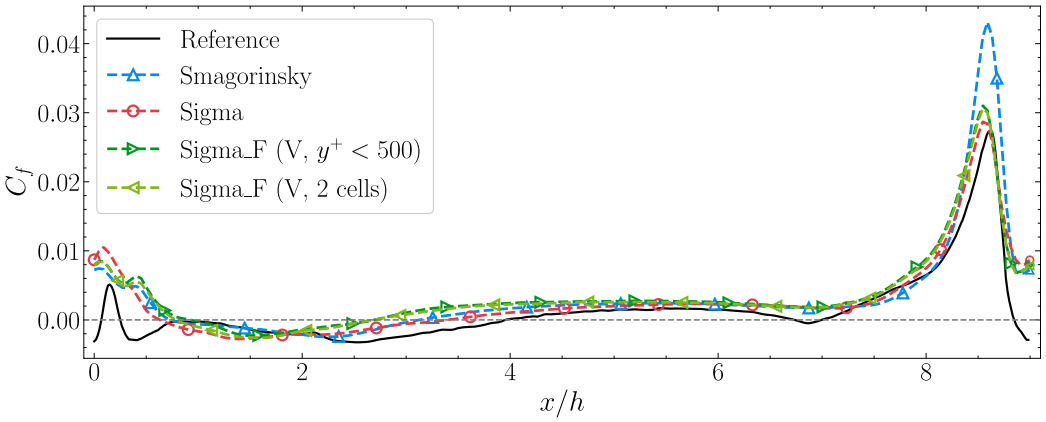

Figure B.3: Friction coefficient on the bottom wall of the periodic hill computed with the TBLE wall model and with or without the enhanced fluctuations model along the streamwise direction compared to the WRLES reference [61] at $\mathrm{Re}_b = 19000$.

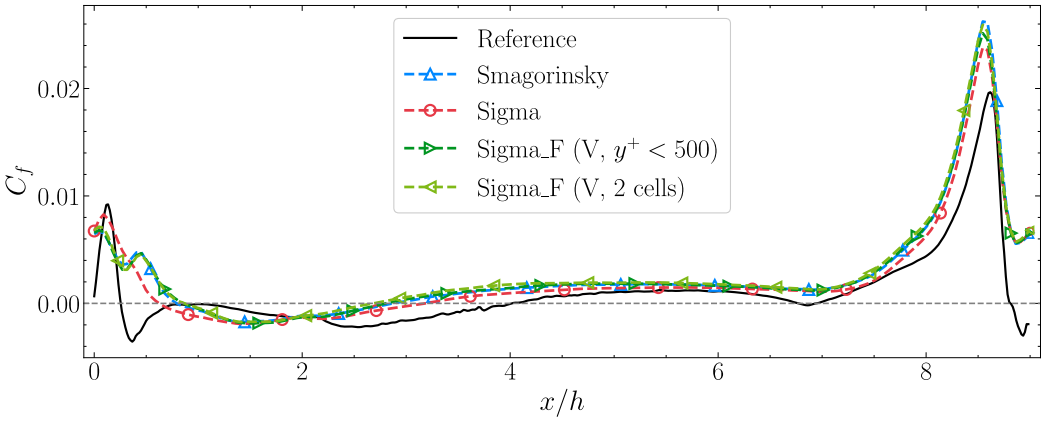

Figure B.4: Friction coefficient on the bottom wall of the periodic hill computed with the TBLE wall model and with or without the enhanced fluctuations model along the streamwise direction compared to the WRLES reference [61] at $\mathrm{Re}_b = 37000$.

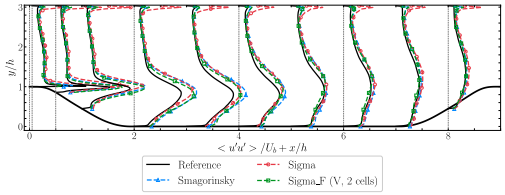

(a) $\langle u'u' \rangle / U_b^2$; Fluctuations on the first 2 cells

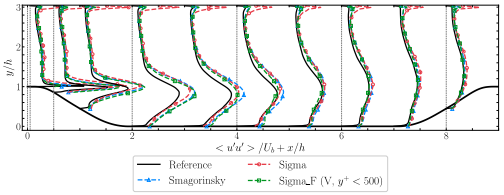

(b) $\langle u'u' \rangle / U_b^2$; Fluctuations for $y^+ < 500$

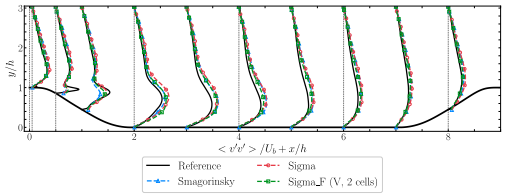

(c) $\langle v'v' \rangle / U_b^2$; Fluctuations on the first 2 cells

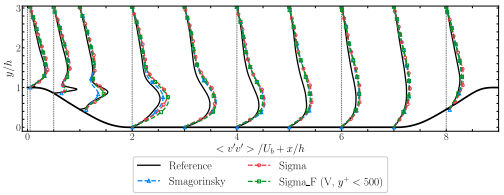

(d) $\langle v'v' \rangle / U_b^2$; Fluctuations for $y^+ < 500$

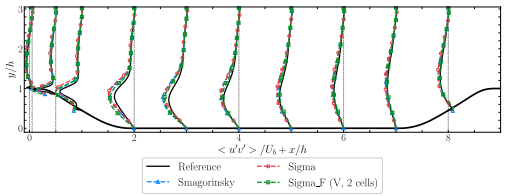

(e) $\langle u'v' \rangle / U_b^2$; Fluctuations on the first 2 cells

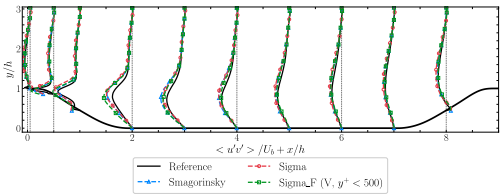

(f) $\langle u'v' \rangle / U_b^2$; Fluctuations for $y^+ < 500$

Figure B.5: Turbulence intensities over the periodic hill setup at $\mathrm{Re}_b = 19000$ computed with the TBLE wall model and with or without the enhanced fluctuations model compared to reference WRLES [61].

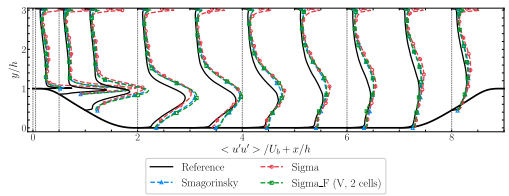

(a) $\langle u'u' \rangle / U_b^2$; Fluctuations on the first 2 cells

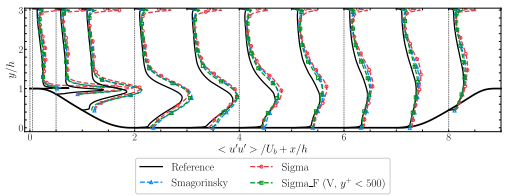

(b) $\langle u'u' \rangle / U_b^2$; Fluctuations for $y^+ < 500$

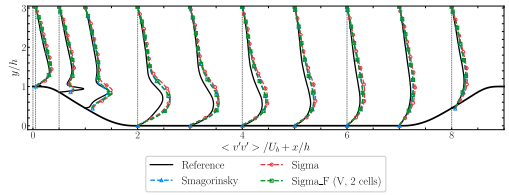

(c) $\langle v'v' \rangle / U_b^2$; Fluctuations on the first 2 cells

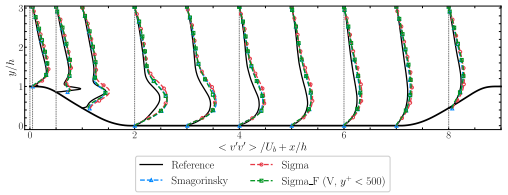

(d) $\langle v'v' \rangle / U_b^2$; Fluctuations for $y^+ < 500$

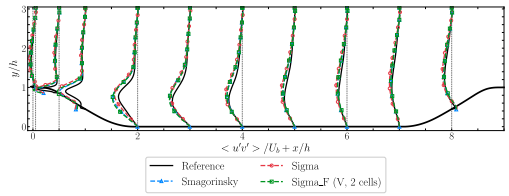

(e) $\langle u'v' \rangle / U_b^2$; Fluctuations on the first 2 cells

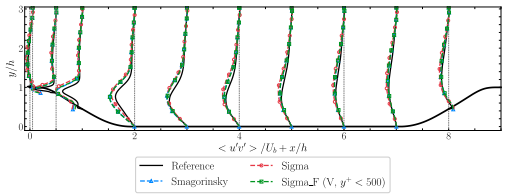

(f) $\langle u'v' \rangle / U_b^2$; Fluctuations for $y^+ < 500$

Figure B.6: Turbulence intensities over the periodic hill setup at $\mathrm{Re}_b = 37000$ computed with the TBLE wall model and with or without the enhanced fluctuations model compared to reference WRLES [61].

Appendix C

Coupling at a higher point

C.1 LLM Problem

As discussed in Section 2.3.2 of this thesis, the coupling between the LES solver and a RANS-type wall model can introduce discrepancies in the predicted results. A notable manifestation of this issue is the characteristic shift in velocity profiles within the boundary layer, commonly referred to as the *log-layer mismatch*.

To address this, as an alternative to the fluctuations model developed and implemented during this thesis, the classical and widely adopted approach of modifying the coupling point between the LES and the wall model, introduced in Section 2.3.2.3, was also implemented and evaluated. This solution was designed to be compatible with both the log-law and TBLE wall models, enabling a comparative analysis of its effectiveness within the AVBP solver framework.

C.2 Implementation

The implementation carried out in this thesis follows the work of Gelain [58] and involves the use of a user-defined wall distance h at which the coupling between the LES solver and the wall model is performed. The coupling process is structured as follows for each wall face:

- Compute the coordinate of the wall face x_{c_w}
- Extend the wall normal vector to the specified distance h
- Identify the coordinates of the corresponding point x_{off}
- Identify the cell and processor containing the off-wall point, as well as the points and weights needed to interpolate the data from the LES grid to the target point

This setup process is executed once during pre-processing, and the necessary information is stored for each wall face. After pre-processing, the LES solver operates as usual. During each solver iteration, the stored interpolation weights and nodes retrieve the off-wall velocity, density, and temperature values. These values are then provided to the wall model, ensuring its accurate operation.

A schematic representation of the general principle of the implemented coupling process is shown in Fig.C.1. While the approach is relatively straightforward on

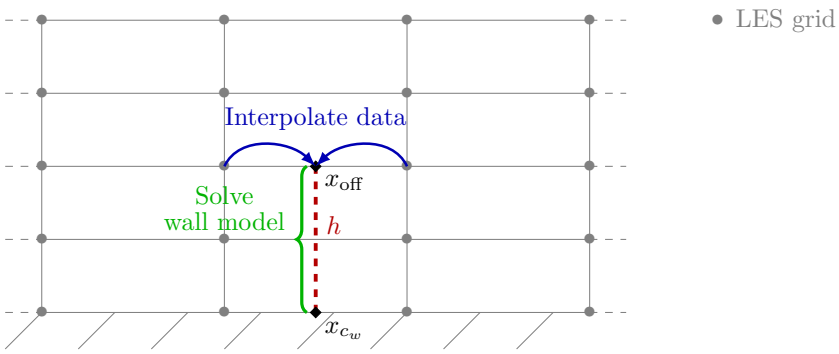

Figure C.1: Principle schematics of the off-wall implementation of the wall model.

a structured grid, it becomes significantly more complex when applied to fully unstructured grids, such as those used in AVBP, particularly in the context of parallelized computations. This complexity justifies the need for a user-defined wall distance to define the coupling points and the interpolation from surrounding grid nodes to obtain the required data. The process's working principle for unstructured grids is illustrated in Fig.C.2.

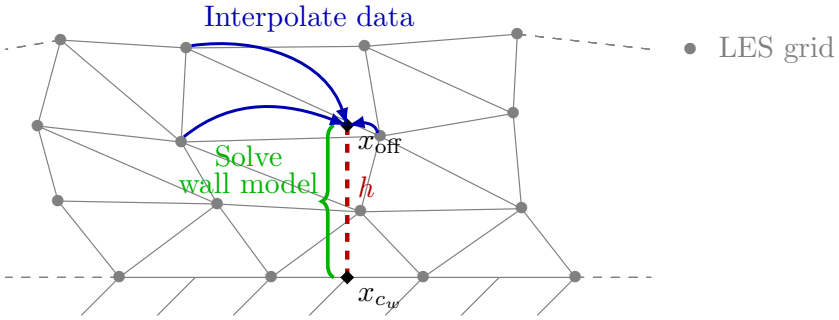

Figure C.2: Principle schematics of the off-wall implementation of the wall model on unstructured grids.

C.3 Results of the coupling on a turbulent channel

As was done in part 5.3 of this thesis for the fluctuations model, the implemenation of the off-wall coupling of the wall model is put to the test on the turbulent channel presented in part 3.2.1. The results in terms of velocity profiles are provided here, obtained both with the classical log-law and the TBLE model introduced in part 4.1.

C.3.1 Log-Law

The velocity profiles obtained on the turbulent channel at $\text{Re}_\tau = 934$ with the offwall implemenation described above are presented in Figs. C.3, C.4 and C.5 with the Smagorinsky, Sigma and WALE SGS models respectively. The results presented

are shown for coupling heights corresponding to 1, 2 or 3 points above the wall, noted 2PT or 3PT respectively.

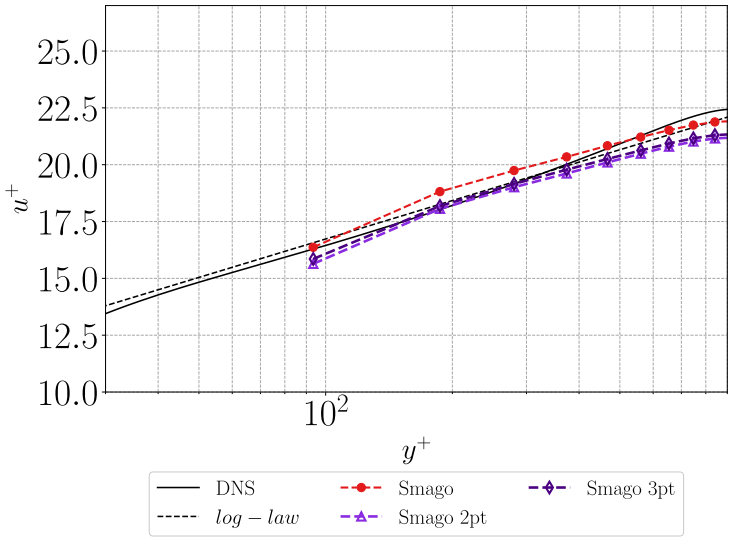

Figure C.3: Velocity profiles on the turbulent channel at $\mathrm{Re}_\tau = 934$ obtained with the Smagorinsky SGS model at different coupling heights with the wall model.

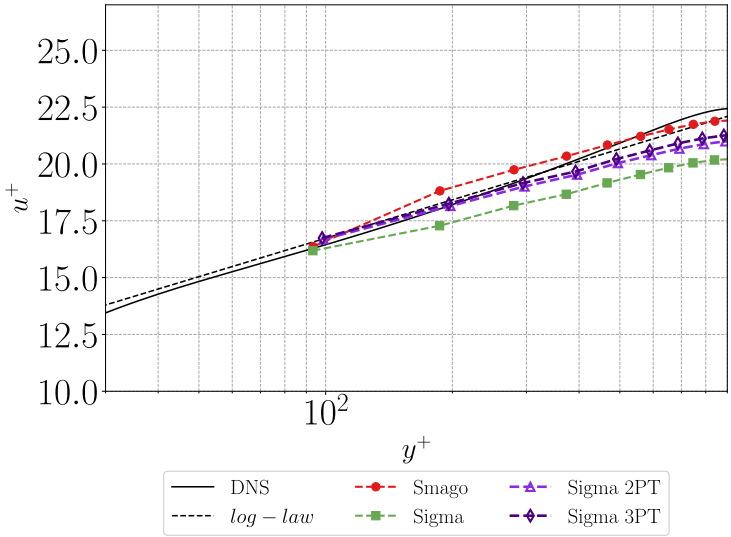

Figure C.4: Velocity profiles on the turbulent channel at $\mathrm{Re}_\tau = 934$ obtained with the Sigma SGS model at different coupling heights with the wall model.

On this setup, the obtained results prove to be quite satisfying, as this method is able to reduce the log-layer mismatch significantly in thes cases where the Sigma and WALE SGS models are employed. However, the fluctuations methodology introduced in thesis in chapter 5 is also able to achieve at least the same quality of results, while still maintaining the releveance of the LES data in the near wall region.

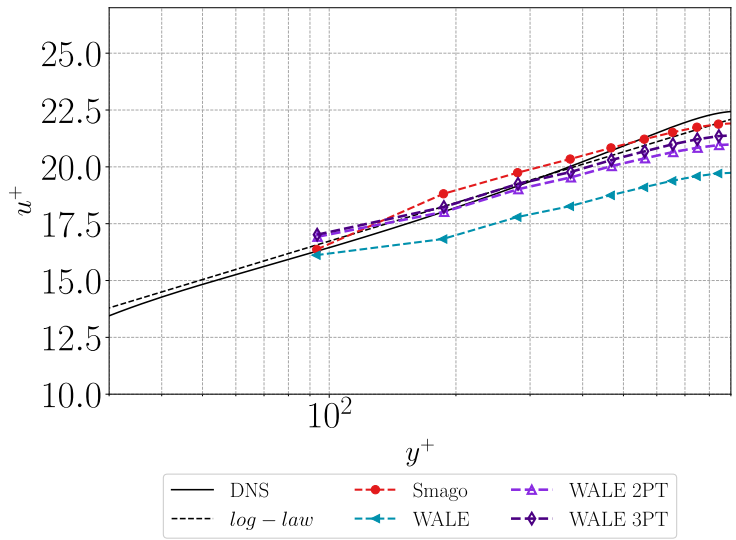

Figure C.5: Velocity profiles on the turbulent channel at $\mathrm{Re}_\tau = 934$ obtained with the WALE SGS model at different coupling heights with the wall model.

This is not the case with this method as the LES points below the coupling with the wall model may be irrelevant and should be discarded from the flow analysis as is particularly visible with the WALE SGS model in Fig. C.5.

C.3.2 TBLE

The velocity profiles obtained on the same turbulent channel with the offwall implemenation described above with the TBLE wall model are presented in Figs. C.6, C.7 and C.8 with the Smagorinsky, Sigma and WALE SGS models respectively. The results presented are shown for coupling heights corresponding to 1, 2 or 3 points above the wall, noted 2PT or 3PT respectively.

In the same manner as what was observed in part 5.3.5, the use of the TBLE wall model including the pressure gradient with the Sigma or WALE SGS models leads to overpredicted friction levels, resulting in shifted velocity profiles. This is again due to too high pressure gradient fluctuations leading to inaccurate predictions of the friction by the TBLE wall model. It can be seen however in Figs. C.7 and C.8 that the change in the coupling point between the LES and the wall model is able to somewhat move the velocity profiles in the right direction, without solving the problem, as was the case when triggering the fluctuations model.

In that case, increasing the time averaging time of the pressure gradient through reducing the γ factor in the EMA averaging described in part. 4.1.2 is the only solution to improve the results. This was done by reducing γ by a factor 1000, or equivalently increasing the time averaging characteristic T_{av} of the exponential moving average by the same factor 1000. The results with this time averaging of the pressure gradient are presented in Figs. C.9 and C.10 for the Sigma and WALE SGS models.

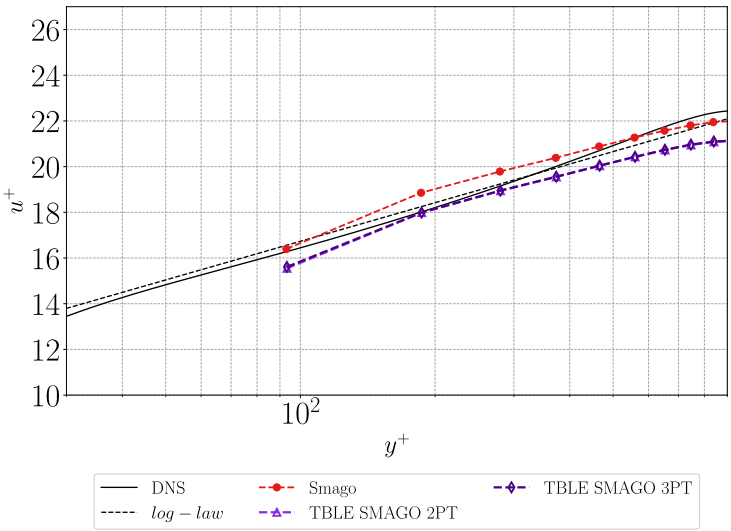

Figure C.6: Velocity profiles on the turbulent channel at $\mathrm{Re}_\tau = 934$ obtained with the Smagorinsky SGS model at different coupling heights with the wall model with the TBLE wall model.

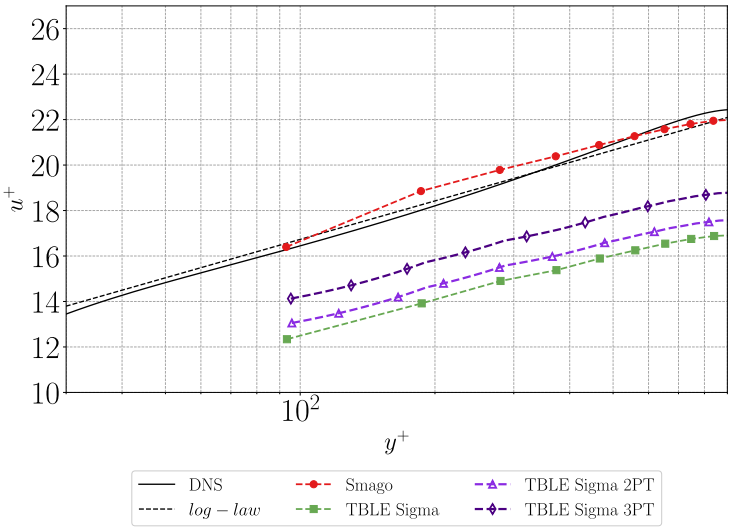

Figure C.7: Velocity profiles on the turbulent channel at $\mathrm{Re}_\tau = 934$ obtained with the Sigma SGS model at different coupling heights with the wall model with the TBLE wall model.

C.3.3 Conclusions

To conclude, the methodology which consists of changing the coupling points between the wall model and the LES solver has been implemented and tested during this thesis. However, the testing of this method was limited to the turbulent channel case. On this setup it showed that it is indeed capable of reducing the log-layer mismatch both when using the classical log-law model and the TBLE wall-model.

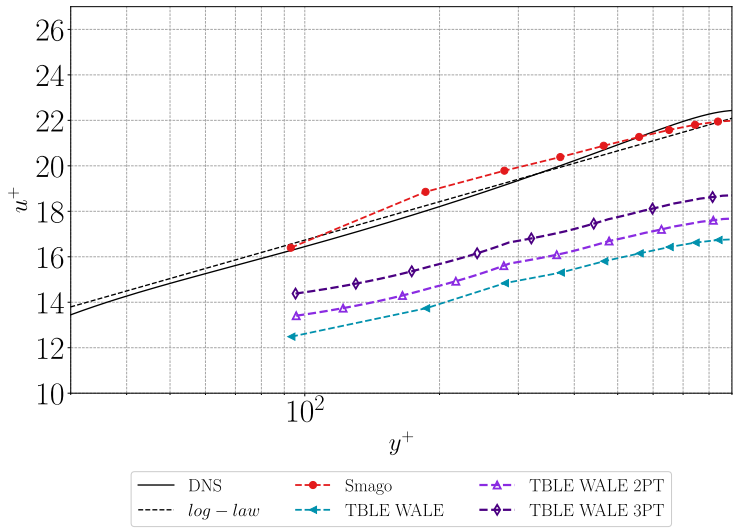

Figure C.8: Velocity profiles on the turbulent channel at $\mathrm{Re}_\tau = 934$ obtained with the WALE SGS model at different coupling heights with the wall model with the TBLE wall model.

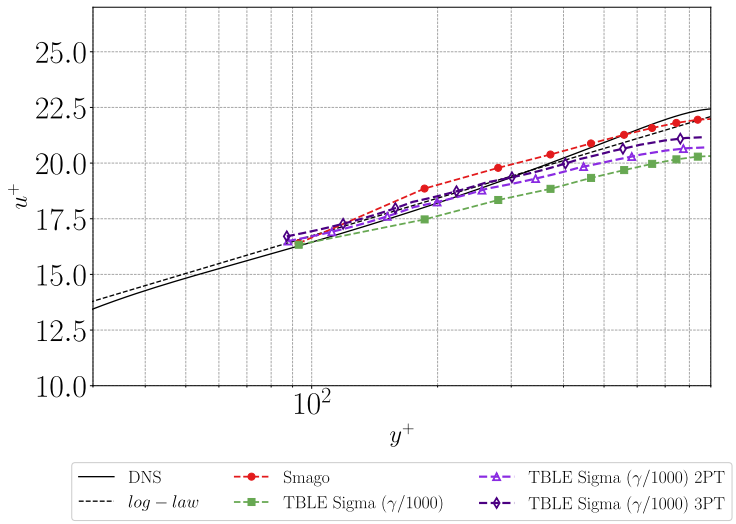

Figure C.9: Velocity profiles on the turbulent channel at $\mathrm{Re}_\tau = 934$ obtained with the Sigma SGS model at different coupling heights with the wall model with the TBLE wall model with more time averaging of the pressure gradient.

However, with the TBLE wall model, the use of the fluctuations model in part 5.3.5 proved to be more robust as it allows to use the same time avering conditions as the Samgorinsky model, while with this offwall coupling methodology, it required more time-avering with the Sigma and WALE SGS models. The assessment of this method should also require more testing on different setups or different Reynolds number to be able to compare its results with other works in literature, such as

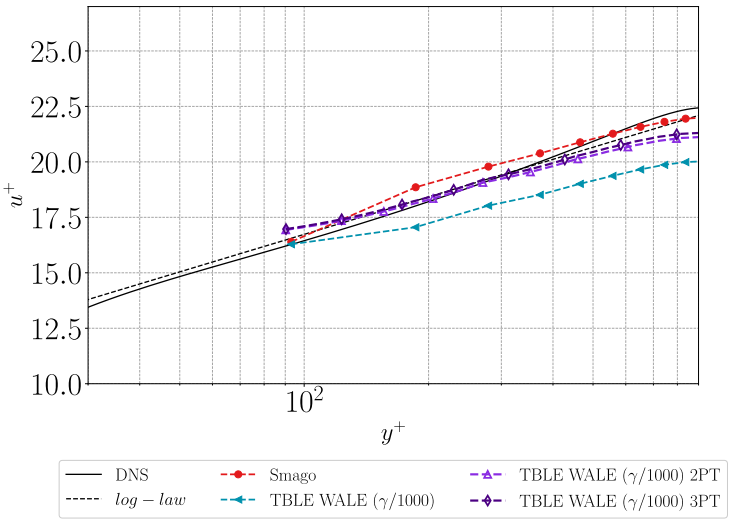

Figure C.10: Velocity profiles on the turbulent channel at $\mathrm{Re}_\tau = 934$ obtained with the WALE SGS model at different coupling heights with the wall model with the TBLE wall model with more time averaging of the pressure gradient.

those of Yang et al. [189] or Gelain [58].

Bibliography

[1] *Turbulent Shear Layers in Supersonic Flow*. Springer-Verlag, New York, 2006. ISBN 978-0-387-26140-9. doi: 10.1007/b137383. (Cited in page 26.)

[2] IATA Industry Statistics 2024, December 2024. (Cited in page 1.)

[3] N. Afzal. Wake Layer in a Turbulent Boundary Layer with Pressure Gradient: A New Approach. pages 95–118. Aix-Marseille Université, 1996. doi: 10.1007/978-94-009-1728-6_9. (Cited in page 47.)

[4] N. Afzal. Wake layer in a thermal turbulent boundary layer with pressure gradient. *Heat and Mass Transfer*, 35(4):281–288, September 1999. ISSN 1432-1181. doi: 10.1007/s002310050325. (Cited in page 47.)

[5] G. P. Almeida, D. F. G. Durão, and M. V. Heitor. Wake flows behind two-dimensional model hills. *Experimental Thermal and Fluid Science*, 7(1):87–101, July 1993. ISSN 0894-1777. doi: 10.1016/0894-1777(93)90083-U. (Cited in page 65.)

[6] Antares Development Team. Antares documentation release 2.3.0, October 2024. (Cited in page 6.)

[7] H. J. Bae, A. Lozano-Durán, S. T. Bose, and P. Moin. Dynamic slip wall model for large-eddy simulation. *Journal of Fluid Mechanics*, 859:400–432, January 2019. ISSN 0022-1120. doi: 10.1017/jfm.2018.838. (Cited in page 51.)

[8] J. S. Baggett. Some modeling requirements for wall models in large eddy simulation. *CTR Annual Research Briefs*, 1997:265–275, 1997. (Cited in page 51.)

[9] E. Balaras, C. Benocci, and U. Piomelli. Two-layer approximate boundary conditions for large-eddy simulations. *AIAA Journal*, 34(6):1111–1119, 1996. ISSN 00011452. doi: 10.2514/3.13200. (Cited in pages 6, 17, 49, and 69.)

[10] R. A. Baurle, C.-J. Tam, J. R. Edwards, and H. A. Hassan. Hybrid Simulation Approach for Cavity Flows: Blending, Algorithm, and Boundary Treatment Issues. *AIAA Journal*, 41(8):1463–1480, August 2003. ISSN 0001-1452. doi: 10.2514/2.2129. (Cited in page 53.)

[11] Y. Benarafa, O. Cioni, F. Ducros, and P. Sagaut. RANS/LES coupling for unsteady turbulent flow simulation at high Reynolds number on coarse meshes. *Computer Methods in Applied Mechanics and Engineering*, 195(23-24):2939–2960, April 2006. ISSN 00457825. doi: 10.1016/j.cma.2005.06.007. (Cited in page 49.)

[12] B. F. Blackwell, W. M. Kays, and R. J. Moffat. The Turbulent Boundary Layer on a Porous Plate: An Experimental Study of the Heat Transfer Behavior With Adverse Pressure Gradients. (Cited in pages 23 and 25.)

[13] S. Blanchard. *Multi-Physics Large-Eddy Simulation of Methane Oxy-Combustion in Liquid Rocket Engines*. PhD thesis, 2021. (Cited in pages 95 and 102.)

[14] S. Blanchard, N. Odier, L. Gicquel, B. Cuenot, and F. Nicoud. Stochastic forcing for sub-grid scale models in wall-modeled large-eddy simulation. *Physics of Fluids*, 33(9):095123, September 2021. ISSN 1070-6631. doi: 10.1063/5.0063728. (Cited in pages vi, 56, 61, 62, 92, 93, 96, 102, 115, 117, 118, 152, and 153.)

[15] A. Bobke, R. Vinuesa, R. Örlü, and P. Schlatter. History effects and near equilibrium in adverse-pressure-gradient turbulent boundary layers. *Journal of Fluid Mechanics*, 820:667–692, June 2017. ISSN 14697645. doi: 10.1017/jfm.2017.236. (Cited in page 31.)

[16] S. Bocquet, P. Sagaut, and J. Jouhaud. A compressible wall model for large-eddy simulation with application to prediction of aerothermal quantities. *Physics of Fluids*, 24(6):065103, June 2012. ISSN 1070-6631. doi: 10.1063/1.4729614. (Cited in pages 46, 50, 56, and 70.)

[17] S. T. Bose and P. Moin. A dynamic slip boundary condition for wall-modeled large-eddy simulation. *Physics of Fluids*, 26(1), 2014. ISSN 10897666. doi: 10.1063/1.4849535. (Cited in pages 6, 51, 53, and 154.)

[18] S. T. Bose and G. I. Park. Wall-Modeled Large-Eddy Simulation for Complex Turbulent Flows. *Annual Review of Fluid Mechanics*, 50:535–561, 2018. ISSN 00664189. doi: 10.1146/annurev-fluid-122316-045241. (Cited in pages 45, 48, and 51.)

[19] M. Boxho, M. Rasquin, T. Toulorge, G. Dergham, G. Winckelmans, and K. Hillewaert. Analysis of Space-Time Correlations to Support the Development of Wall-Modeled LES. *Flow, Turbulence and Combustion*, November 2022. ISSN 15731987. doi: 10.1007/s10494-022-00365-3. (Cited in page 53.)

[20] J. G. Brasseur and T. Wei. Designing large-eddy simulation of the turbulent boundary layer to capture law-of-the-wall scalinga). *Physics of Fluids*, 22(2): 021303, February 2010. ISSN 1070-6631. doi: 10.1063/1.3319073. (Cited in page 56.)

[21] M. Breuer, B. Kniazev, and M. Abel. Development of wall models for LES of separated flows using statistical evaluations. *Computers and Fluids*, 36(5): 817–837, June 2007. ISSN 00457930. doi: 10.1016/j.compfluid.2006.09.001. (Cited in page 65.)

[22] M. Breuer, N. Peller, C. Rapp, and M. Manhart. Flow over periodic hills – Numerical and experimental study in a wide range of Reynolds numbers. *Computers & Fluids*, 38(2):433–457, February 2009. ISSN 0045-7930. doi: 10.1016/j.compfluid.2008.05.002. (Cited in page 66.)

[23] W. Cabot and P. Moin. Approximate wall boundary conditions in the large-eddy simulation of high Reynolds number flow. *Flow, Turbulence and Combustion*, 63(1):269–291, 2000. ISSN 13866184. doi: 10.1023/a:1009958917113. (Cited in pages 6, 17, 46, 49, 69, 70, 71, 72, 73, 74, and 82.)

[24] O. Cabrit. *Modélisation Des Flux Pariétaux Sur Les Tuyères Des Moteurs à Propergol Solide*. PhD thesis, Université Montpellier II, 2009. (Cited in page 44.)

[25] L. Castillo and W. K. George. Similarity Analysis for Turbulent Boundary Layer with Pressure Gradient: Outer Flow. *AIAA Journal*, 39(1):41–47, January 2001. ISSN 0001-1452, 1533-385X. doi: 10.2514/2.1300. (Cited in page 30.)

[26] M. Catchirayer. *Modélisation de Paroi En Simulation Des Grandes Échelles Dans Une Turbomachine*. PhD thesis, Aix-Marseille Université, 2019. (Cited in page 47.)

[27] M. Catchirayer, J. F. Boussuge, P. Sagaut, M. Montagnac, D. Papadogiannis, and X. Garnaud. Extended integral wall-model for large-eddy simulations of compressible wall-bounded turbulent flows. *Physics of Fluids*, 30(6), 2018. ISSN 10897666. doi: 10.1063/1.5030859. (Cited in pages 42 and 50.)

[28] T. Cebeci and A. M. O. Smith. *Analysis of Turbulent Boundary Layers*. Number 15 in Applied Mathematics and Mechanics. Acad. Press, San Diego, 4. [print.] edition, 1990. ISBN 978-0-12-164650-9. (Cited in page 19.)

[29] D. R. Chapman. Computational Aerodynamics Development and Outlook. *AIAA Journal*, 17(12):1293–1313, December 1979. ISSN 0001-1452, 1533-385X. doi: 10.2514/3.61311. (Cited in page 41.)

[30] D. R. Chapman and G. D. Kuhn. The limiting behaviour of turbulence near a wall. *Journal of Fluid Mechanics*, 170:265–292, September 1986. ISSN 0022-1120, 1469-7645. doi: 10.1017/S0022112086000885. (Cited in page 36.)

[31] W. Cheng, D. I. Pullin, and R. Samtaney. Large-eddy simulation of separation and reattachment of a flat plate turbulent boundary layer. *Journal of Fluid Mechanics*, 785:78–108, 2015. ISSN 14697645. doi: 10.1017/jfm.2015.604. (Cited in page 51.)

[32] M. Cho, A. Lozano-Durán, P. Moin, and G. Ilhwan Park. Wall-Modeled Large-Eddy Simulation of Turbulent Boundary Layers with Mean-Flow Three-Dimensionality. *AIAA Journal*, 59(5):1707–1717, May 2021. ISSN 0001-1452, 1533-385X. doi: 10.2514/1.J059861. (Cited in page 48.)

[33] H. Choi and P. Moin. Grid-point requirements for large eddy simulation: Chapman's estimates revisited. *Physics of Fluids*, 24(1):30–35, 2012. ISSN 10706631. doi: 10.1063/1.3676783. (Cited in page 41.)

[34] D. Chung and D. I. Pullin. Large-eddy simulation and wall modelling of turbulent channel flow. *Journal of Fluid Mechanics*, 631:281–309, 2009. ISSN 00221120. doi: 10.1017/S0022112009006867. (Cited in page 51.)

[35] F. H. Clauser. Turbulent Boundary Layers in Adverse Pressure Gradients. *Journal of the Aeronautical Sciences*, 21(2):91–108, February 1954. ISSN 1936-9956. doi: 10.2514/8.2938. (Cited in pages 28 and 30.)

[36] F. H. Clauser. The Turbulent Boundary Layer. In H. L. Dryden and T. von Kármán, editors, *Advances in Applied Mechanics*, volume 4, pages 1–51. Elsevier, January 1956. doi: 10.1016/S0065-2156(08)70370-3. (Cited in page 21.)

[37] O. Colin and M. Rudgyard. Development of High-Order Taylor–Galerkin Schemes for LES. *Journal of Computational Physics*, 162(2):338–371, August 2000. ISSN 0021-9991. doi: 10.1006/jcph.2000.6538. (Cited in pages 61, 83, and 128.)

[38] T. J. Craft, A. V. Gerasimov, H. Iacovides, and B. E. Launder. Progress in the generalization of wall-function treatments. *International Journal of Heat and Fluid Flow*, 23(2):148–160, April 2002. ISSN 0142-727X. doi: 10.1016/S0142-727X(01)00143-6. (Cited in page 50.)

[39] M. de la Llave Plata, V. Couaillier, and M.-C. le Pape. On the use of a high-order discontinuous Galerkin method for DNS and LES of wall-bounded turbulence. *Computers & Fluids*, 176:320–337, November 2018. ISSN 0045-7930. doi: 10.1016/j.compfluid.2017.05.013. (Cited in page 66.)

[40] J. de Laborderie, F. Duchaine, O. Vermorel, L. Gicquel, and S. Moreau. Application of an Overset Grid Method to the Large Eddy Simulation of a High-Speed Multistage Axial Compressor. In *ASME Turbo Expo 2016: Turbomachinery Technical Conference and Exposition*. American Society of Mechanical Engineers Digital Collection, September 2016. doi: 10.1115/GT2016-56344. (Cited in page 137.)

[41] J. W. Deardorff. A numerical study of three-dimensional turbulent channel flow at large Reynolds numbers. *Journal of Fluid Mechanics*, 41(2):453–480, April 1970. ISSN 14697645. doi: 10.1017/S0022112070000691. (Cited in page 45.)

[42] J. D. Denton. Loss Mechanisms in Turbomachines. In *Volume 2: Combustion and Fuels; Oil and Gas Applications; Cycle Innovations; Heat Transfer; Electric Power; Industrial and Cogeneration; Ceramics; Structures and Dynamics; Controls, Diagnostics and Instrumentation; IGTI Scholar Award*,

page V002T14A001, Cincinnati, Ohio, USA, May 1993. American Society of Mechanical Engineers. ISBN 978-0-7918-7889-7. doi: 10.1115/93-GT-435. (Cited in pages 3 and 4.)

[43] W. J. Devenport and K. T. Lowe. Equilibrium and non-equilibrium turbulent boundary layers. *Progress in Aerospace Sciences*, 131(February):100807, 2022. ISSN 03760421. doi: 10.1016/j.paerosci.2022.100807. (Cited in pages 14, 16, 21, 29, 30, 31, 62, and 69.)

[44] S. L. Dixon and C. A. Hall. *Fluid Mechanics and Thermodynamics of Turbomachinery*. Butterworth-Heinemann is an imprint of Elsevier, Amsterdam ; Boston, seventh edition edition, 2014. ISBN 978-0-12-415954-9. (Cited in page 3.)

[45] F. Duchaine, N. Maheu, V. Moureau, G. Balarac, and S. Moreau. Large-Eddy Simulation and Conjugate Heat Transfer Around a Low-Mach Turbine Blade. *Journal of Turbomachinery*, 136(5):051015, May 2014. ISSN 0889-504X, 1528-8900. doi: 10.1115/1.4025165. (Cited in page 125.)

[46] C. Duprat, G. Balarac, O. Métais, P. M. Congedo, and O. Brugière. A wall-layer model for large-eddy simulations of turbulent flows with/out pressure gradient. *Physics of Fluids*, 23(1):015101, January 2011. ISSN 1070-6631, 1089-7666. doi: 10.1063/1.3529358. (Cited in pages 6, 50, 53, 65, 69, 70, 72, 73, 74, 78, 79, and 82.)

[47] D. Dupuy, L. Gicquel, N. Odier, F. Duchaine, and T. Arts. Analysis of the effect of intermittency in a high-pressure turbine blade. *Physics of Fluids*, 32 (9), September 2020. ISSN 10897666. doi: 10.1063/5.0018679. (Cited in page 61.)

[48] H. M. El-Batsh. Effect of the Radial Pressure Gradient on the Secondary Flow Generated in an Annular Turbine Cascade. *International Journal of Rotating Machinery*, 2012(1):509209, 2012. ISSN 1542-3034. doi: 10.1155/2012/509209. (Cited in page 62.)

[49] A. Elnahhas, A. Lozano-Duran, and P. Moin. Toward a flow-structure-based wall-modeled large-eddy simulation paradigm. *Center for Turbulence Research Annual Research Briefs*, 2020. (Cited in page 53.)

[50] European Commision. Aero-Thermal Investigation on Turbine EndWall and Blades. Technical Report AST4-CT-2005-516113, 2005. (Cited in page 125.)

[51] G. Fan, J. Zhu, W. Zhao, and D. Wan. A Comparative Study Between Wall-Resolved and Wall-Modeled Large Eddy Simulation of Turbulent Channel Flows. In *The 34th International Ocean and Polar Engineering Conference*. OnePetro, June 2024. (Cited in page 43.)

[52] K. A. Flack and M. P. Schultz. Roughness effects on wall-bounded turbulent flows. *Physics of Fluids*, 26(10):101305, October 2014. ISSN 1070-6631, 1089-7666. doi: 10.1063/1.4896280. (Cited in page 29.)

[53] K. A. Flack, M. P. Schultz, and T. A. Shapiro. Experimental support for Townsend's Reynolds number similarity hypothesis on rough walls. *Physics of Fluids*, 17(3):035102, March 2005. ISSN 1070-6631, 1089-7666. doi: 10.1063/1.1843135. (Cited in page 29.)

[54] L. S. Freire and M. Chamecki. Large-Eddy Simulation of smooth and rough channel flows using a one-dimensional stochastic wall model. *Computers and Fluids*, 230, November 2021. ISSN 00457930. doi: 10.1016/j.compfluid.2021.105135. (Cited in page 56.)

[55] J. Fröhlich, C. P. Mellen, W. Rodi, L. Temmerman, and M. A. Leschziner. Highly resolved large-eddy simulation of separated flow in a channel with streamwise periodic constrictions. *Journal of Fluid Mechanics*, 526:19–66, March 2005. ISSN 00221120. doi: 10.1017/S0022112004002812. (Cited in page 65.)

[56] N. García Rosa, G. Dufour, R. Barènes, and G. Lavergne. Experimental Analysis of the Global Performance and the Flow Through a High-Bypass Turbofan in Windmilling Conditions. *Journal of Turbomachinery*, 137(051001), May 2015. ISSN 0889-504X. doi: 10.1115/1.4028647. (Cited in page 136.)

[57] N. García Rosa, A. Thacker, and G. Dufour. Experimental analysis of the unsteady, turbulent flow through the fan stage of a high-bypass turbofan in windmilling conditions. In *12th European Conference on Turbomachinery Fluid Dynamics & Thermodynamics*. European Turbomachinery Society, 2017. doi: 10.29008/ETC2017-320. (Cited in page 136.)

[58] M. Gelain. *Caractérisation Aérothermique d'un Échangeur de Chaleur Surfacique Implémenté En Veine Secondaire*. PhD thesis, Université Paris-Saclay, 2021. (Cited in pages 6, 44, 54, 56, 70, 74, 76, 173, and 179.)

[59] M. Germano, U. Piomelli, P. Moin, and W. H. Cabot. A dynamic subgrid-scale eddy viscosity model. *Physics of Fluids A: Fluid Dynamics*, 3(7):1760–1765, July 1991. ISSN 0899-8213. doi: 10.1063/1.857955. (Cited in page 38.)

[60] L. Y. M. Gicquel, N. Gourdain, J. F. Boussuge, H. Deniau, G. Staffelbach, P. Wolf, and T. Poinsot. High performance parallel computing of flows in complex geometries. *Comptes Rendus Mécanique*, 339(2):104–124, February 2011. ISSN 1631-0721. doi: 10.1016/j.crme.2010.11.006. (Cited in page 61.)

[61] X. Gloerfelt and P. Cinnella. Large Eddy Simulation Requirements for the Flow over Periodic Hills. *Flow, Turbulence and Combustion*, 103(1):55–91, June 2019. ISSN 1573-1987. doi: 10.1007/s10494-018-0005-5. (Cited in

pages 65, 66, 83, 84, 85, 86, 87, 88, 89, 90, 119, 120, 121, 123, 167, 168, 169, 170, and 171.)

[62] N. Gourdain, L. Gicquel, M. Montagnac, O. Vermorel, M. Gazaix, G. Staffelbach, M. Garcia, J.-F. Boussuge, and T. Poinsot. High performance parallel computing of flows in complex geometries: I. Methods. *Computational Science & Discovery*, 2(1):015003, November 2009. ISSN 1749-4699. doi: 10.1088/1749-4699/2/1/015003. (Cited in page 61.)

[63] V. Granet, O. Vermorel, T. Léonard, L. Gicquel, and T. Poinsot. Comparison of Nonreflecting Outlet Boundary Conditions for Compressible Solvers on Unstructured Grids. *AIAA Journal*, 48(10):2348–2364, October 2010. ISSN 0001-1452. doi: 10.2514/1.J050391. (Cited in pages 128 and 138.)

[64] K. P. Griffin and L. Fu. A new ODE-based turbulence wall model accounting for pressure gradient and Reynolds number effects. October 2020. doi: 10.48550/arXiv.2010.04097. (Cited in page 69.)

[65] S. E. Guarini, R. D. Moser, K. Shariff, and A. Wray. Direct numerical simulation of a supersonic turbulent boundary layer at Mach 2.5. *Journal of Fluid Mechanics*, 414:1–33, July 2000. ISSN 0022-1120, 1469-7645. doi: 10.1017/S0022112000008466. (Cited in page 26.)

[66] A. G. Gungor, Y. Maciel, M. P. Simens, and J. Soria. Scaling and statistics of large-defect adverse pressure gradient turbulent boundary layers. *International Journal of Heat and Fluid Flow*, 59:109–124, June 2016. ISSN 0142-727X. doi: 10.1016/j.ijheatfluidflow.2016.03.004. (Cited in page 47.)

[67] F. R. Hama. Boundary Layer characteristics for smooth and rough surfaces. In *Trans. SNAME*, volume 62, pages 333–351, 1954. (Cited in page 28.)

[68] F. Haselbach and H. P. Schiffer. Aerothermal Investigations on Turbine Endwalls and Blades (AITEB). In *ASME Turbo Expo 2004: Power for Land, Sea, and Air*, pages 67–76. American Society of Mechanical Engineers Digital Collection, November 2008. doi: 10.1115/GT2004-53078. (Cited in page 125.)

[69] S. Hickel, E. Touber, J. Bodart, and J. Larsson. A parametrized non-equilibrium wall-model for large-eddy simulations. *International Symposium on Turbulence and Shear Flow Phenomena, TSFP 2013*, 2, 2013. doi: 10.13140/2.1.1281.6324. (Cited in page 154.)

[70] J. O. Hinze. *Turbulence*. McGraw-Hill, 1975. ISBN 978-0-07-029037-2. (Cited in pages 13 and 14.)

[71] C. Hirsch. *Numerical Computation of Internal and External Flows: Fundamentals of Computational Fluid Dynamics*. Elsevier/Butterworth-Heinemann, Oxford Burlington, MA, 2nd ed edition, 2007. ISBN 978-0-7506-6594-0. (Cited in page 32.)

[72] H. Hosseinzade and D. J. Bergstrom. Time-averaging and temporal-filtering in wall-modeled large eddy simulation. *Physics of Fluids*, 33(3):035108, March 2021. ISSN 1070-6631. doi: 10.1063/5.0039651. (Cited in pages 75, 76, and 80.)

[73] S. Hoyas and J. Jiménez. Reynolds number effects on the Reynolds-stress budgets in turbulent channels. *Physics of Fluids*, 20(10):101511, October 2008. ISSN 1070-6631. doi: 10.1063/1.3005862. (Cited in pages 21, 54, 64, 72, 73, 80, 91, 97, and 98.)

[74] P. G. Huang and G. N. Coleman. Van Driest transformation and compressible wall-bounded flows. *AIAA Journal*, 32(10):2110–2113, October 1994. ISSN 0001-1452, 1533-385X. doi: 10.2514/3.12259. (Cited in page 46.)

[75] P. G. Huang, P. Bradshaw, and T. J. Coakley. Skin friction and velocity profile family for compressible turbulentboundary layers. *AIAA Journal*, 31(9):1600–1604, September 1993. ISSN 0001-1452, 1533-385X. doi: 10.2514/3.11820. (Cited in page 27.)

[76] ICAO. Long term global aspirational goal (LTAG) for international aviation, 2022. (Cited in page 1.)

[77] M. Inoue, R. Mathis, I. Marusic, and D. I. Pullin. Inner-layer intensities for the flat-plate turbulent boundary layer combining a predictive wall-model with large-eddy simulations. *Physics of Fluids*, 24(7):0–17, 2012. ISSN 10706631. doi: 10.1063/1.4731299. (Cited in page 51.)

[78] F. Jaegle, O. Cabrit, S. Mendez, and T. Poinsot. Implementation methods of wall functions in cell-vertex numerical solvers. *Flow, Turbulence and Combustion*, 85(2):245–272, 2010. ISSN 13866184. doi: 10.1007/s10494-010-9276-1. (Cited in pages 43 and 61.)

[79] J. Jiménez. Turbulent Flows over Rough Walls. *Annual Review of Fluid Mechanics*, 36(1):173–196, January 2004. ISSN 0066-4189, 1545-4479. doi: 10.1146/annurev.fluid.36.050802.122103. (Cited in page 29.)

[80] J. Jimenez and C. Vasco. Approximate lateral boundary conditions for turbulent simulations. *CTR Proceedings of the Summer Program*, pages 399–412, 1998. (Cited in page 51.)

[81] B. A. Kader. Temperature and concentration profiles in fully turbulent boundary layers. *International Journal of Heat and Mass Transfer*, 24(9):1541–1544, September 1981. ISSN 0017-9310. doi: 10.1016/0017-9310(81)90220-9. (Cited in pages 23, 24, and 25.)

[82] C. J. Kähler, S. Scharnowski, and C. Cierpka. Highly resolved experimental results of the separated flow in a channel with streamwise periodic constrictions. *Journal of Fluid Mechanics*, 796:257–284, June 2016. ISSN 0022-1120, 1469-7645. doi: 10.1017/jfm.2016.250. (Cited in page 66.)

[83] S. Kawai and J. Larsson. Wall-modeling in large eddy simulation: Length scales, grid resolution, and accuracy. *Physics of Fluids*, 24(1), 2012. ISSN 10706631. doi: 10.1063/1.3678331. (Cited in pages 6, 50, 55, 57, and 70.)

[84] S. Kawai and J. Larsson. Dynamic non-equilibrium wall-modeling for large eddy simulation at high Reynolds numbers. *Physics of Fluids*, 25(1):015105, January 2013. ISSN 1070-6631. doi: 10.1063/1.4775363. (Cited in page 48.)

[85] H. Kawamura, H. Abe, and Y. Matsuo. DNS of turbulent heat transfer in channel flow with respect to Reynolds and Prandtl number effects. *International Journal of Heat and Fluid Flow*, 20(3):196–207, June 1999. ISSN 0142-727X. doi: 10.1016/S0142-727X(99)00014-4. (Cited in pages 23, 24, and 25.)

[86] W. M. Kays. Turbulent Prandtl Number—Where Are We? *Journal of Heat Transfer*, 116(2):284–295, May 1994. ISSN 0022-1481, 1528-8943. doi: 10.1115/1.2911398. (Cited in page 24.)

[87] W. M. Kays, M. E. Crawford, and B. Weigand. *Convective Heat and Mass Transfer*. McGraw-Hill Series in Mechanical Engineering. McGraw-Hill, Boston, 4. ed., [nachdr.], internat. ed edition, 20. ISBN 978-0-07-123829-8. (Cited in page 74.)

[88] A. Keating and U. Piomelli. A dynamic stochastic forcing method as a wall-layer model for large-eddy simulation. *Journal of Turbulence*, 7(12):1–24, 2006. ISSN 14685248. doi: 10.1080/14685240612331392460. (Cited in page 82.)

[89] A. Kharina and D. Rutherford. Fuel Efficiency Trends for New Commercial Jet Aircraft: 1960 to 2014. August 2015. (Cited in page 2.)

[90] P. S. Klebanoff and Z. W. Diehl. Some Features of Artificially Thickened Fully Developed Turbulent Boundary Layers with Zero Pressure Gradient, January 1952. (Cited in page 21.)

[91] A. N. Kolmogorov. The Local Structure of Turbulence in Incompressible Viscous Fluid for Very Large Reynolds Numbers. *Proceedings: Mathematical and Physical Sciences*, 434(1890):9–13, 1991. ISSN 0962-8444. (Cited in page 13.)

[92] B. Krank, M. Kronbichler, and W. A. Wall. Direct Numerical Simulation of Flow over Periodic Hills up to $\text {Re}_{H}=10{,}595$. *Flow, Turbulence and Combustion*, 101(2):521–551, September 2018. ISSN 1573-1987. doi: 10.1007/s10494-018-9941-3. (Cited in page 66.)

[93] A. Krein and G. Williams. Flightpath 2050: Europe's vision for aeronautics. In *Innovation for Sustainable Aviation in a Global Environment*, pages 63–71. IOS Press, 2012. doi: 10.3233/978-1-61499-063-5-63. (Cited in page 1.)

[94] H. Ladisch, A. Schulz, and H.-J.¨rg Bauer. Heat Transfer Measurements on a Turbine Airfoil With Pressure Side Separation. In *ASME Turbo Expo 2009: Power for Land, Sea, and Air*, pages 783–793. American Society of Mechanical Engineers Digital Collection, February 2010. doi: 10.1115/GT2009-59904. (Cited in page 125.)

[95] J. Larsson, S. Laurence, I. Bermejo-Moreno, J. Bodart, S. Karl, and R. Vicquelin. Incipient thermal choking and stable shock-train formation in the heat-release region of a scramjet combustor. Part II: Large eddy simulations. *Combustion and Flame*, 162(4):907–920, April 2015. ISSN 0010-2180. doi: 10.1016/j.combustflame.2014.09.017. (Cited in page 57.)

[96] J. Larsson, S. Kawai, J. Bodart, and I. Bermejo-Moreno. Large eddy simulation with modeled wall-stress: Recent progress and future directions. *Mechanical Engineering Reviews*, 3(1):15–00418–15–00418, January 2016. ISSN 2187-9753. doi: 10.1299/mer.15-00418. (Cited in pages 6, 45, 48, 56, 69, and 154.)

[97] P. Lax and B. Wendroff. Systems of conservation laws. *Communications on Pure and Applied Mathematics*, 13(2):217–237, 1960. ISSN 1097-0312. doi: 10.1002/cpa.3160130205. (Cited in pages 61, 79, and 139.)

[98] J. Lee, M. Cho, and H. Choi. Large eddy simulations of turbulent channel and boundary layer flows at high Reynolds number with mean wall shear stress boundary condition. *Physics of Fluids*, 25(11):110808, August 2013. ISSN 1070-6631. doi: 10.1063/1.4819342. (Cited in page 55.)

[99] M. Lee and R. D. Moser. Direct numerical simulation of turbulent channel flow up to. *Journal of Fluid Mechanics*, 774:395–415, July 2015. ISSN 0022-1120. doi: 10.1017/jfm.2015.268. (Cited in page 47.)

[100] M. Lesieur. *Turbulence in Fluids*. Number 84 in Fluid Mechanics and Its Applications. Springer, Dordrecht, 4th rev. and enl. ed edition, 2008. ISBN 978-1-4020-6434-0. (Cited in page 14.)

[101] M. Lesieur, O. Métais, and P. Comte. *Large-Eddy Simulations of Turbulence*. Cambridge University Press, Cambridge, reprint edition, 2008. ISBN 978-0-521-78124-4. (Cited in page 32.)

[102] D. K. Lilly. A proposed modification of the Germano subgrid-scale closure method. *Physics of Fluids A: Fluid Dynamics*, 4(3):633–635, March 1992. ISSN 0899-8213. doi: 10.1063/1.858280. (Cited in page 38.)

[103] G. Lodato, P. Castonguay, and A. Jameson. Structural Wall-modeled LES Using a High-order Spectral Difference Scheme for Unstructured Meshes. *Flow, Turbulence and Combustion*, 92(1):579–606, January 2014. ISSN 1573-1987. doi: 10.1007/s10494-013-9523-3. (Cited in pages 50, 57, and 65.)

[104] H. Ludwieg and W. Tillmann. Investigations of the wall-shearing stress in turbulent boundary layers, May 1950. (Cited in page 21.)

[105] T. Maeder, N. A. Adams, and L. Kleiser. Direct simulation of turbulent supersonic boundary layers by an extended temporal approach. *Journal of Fluid Mechanics*, 429:187–216, February 2001. ISSN 0022-1120, 1469-7645. doi: 10.1017/S0022112000002718. (Cited in page 26.)

[106] N. Maheu, V. Moureau, and P. Domingo. Large-Eddy Simulations of flow and heat transfer around a low-Mach number turbine blade. In *Proceeding of THMT-12. Proceedings of the Seventh International Symposium On Turbulence, Heat and Mass Transfer Palermo, Italy, 24-27 September, 2012*, page 12, Connecticut, 2012. Begellhouse. ISBN 978-1-56700-302-4. doi: 10.1615/ICHMT.2012.ProcSevIntSympTurbHeatTransfPal.810. (Cited in page 125.)

[107] M. Manhart, N. Peller, and C. Brun. Near-wall scaling for turbulent boundary layers with adverse pressure gradient : A priori tests on DNS of channel flow with periodic hill constrictions and DNS of separating boundary layer. *Theoretical and Computational Fluid Dynamics*, 22(3-4):243–260, May 2008. ISSN 09354964. doi: 10.1007/s00162-007-0055-0. (Cited in pages 69 and 70.)

[108] M. P. Martin. Direct numerical simulation of hypersonic turbulent boundary layers. Part 1. Initialization and comparison with experiments. *Journal of Fluid Mechanics*, 570:347–364, January 2007. ISSN 0022-1120, 1469-7645. doi: 10.1017/S0022112006003107. (Cited in page 26.)

[109] I. Marusic, B. J. McKeon, P. A. Monkewitz, H. M. Nagib, A. J. Smits, and K. R. Sreenivasan. Wall-bounded turbulent flows at high Reynolds numbers: Recent advances and key issues. *Physics of Fluids*, 22(6):065103, June 2010. ISSN 1070-6631, 1089-7666. doi: 10.1063/1.3453711. (Cited in page 22.)

[110] P. J. Mason and D. J. Thomson. Stochastic backscatter in large-eddy simulations of boundary layers. *Journal of Fluid Mechanics*, 242:51–78, September 1992. ISSN 1469-7645, 0022-1120. doi: 10.1017/S0022112092002271. (Cited in page 56.)

[111] T. Meyers, J. B. Forest, and W. J. Devenport. The wall-pressure spectrum of high-Reynolds-number turbulent boundary-layer flows over rough surfaces. *Journal of Fluid Mechanics*, 768:261–293, April 2015. ISSN 0022-1120, 1469-7645. doi: 10.1017/jfm.2014.743. (Cited in page 29.)

[112] D. Monfort, S. Benhamadouche, and P. Sagaut. Meshless approach for wall treatment in Large-Eddy Simulation. *Computer Methods in Applied Mechanics and Engineering*, 199(13-16):881–889, February 2010. ISSN 00457825. doi: 10.1016/j.cma.2009.04.013. (Cited in page 50.)

[113] M. V. Morkovin. Effects of compressibility on turbulent flows. *Mécanique de la Turbulence*, 367(380):26, 1962. (Cited in pages 15 and 26.)

[114] T. Mukha. *Modelling Techniques for Large-Eddy Simulation of Wall-Bounded Turbulent Flows*. PhD thesis, Uppsala Universitet, 2018. (Cited in page 46.)

[115] F. Nicoud and F. Ducros. Subgrid-Scale Stress Modelling Based on the Square of the Velocity Gradient Tensor. *Flow, Turbulence and Combustion*, 62(3): 183–200, September 1999. ISSN 1573-1987. doi: 10.1023/A:1009995426001. (Cited in pages 37 and 38.)

[116] F. Nicoud, G. Winckelmans, D. Carati, J. Baggett, and W. Cabot. Boundary conditions for LES away from the wall. *CTR Proceedings of the Summer Program*, 1998. (Cited in page 51.)

[117] F. Nicoud, J. S. Baggett, P. Moin, and W. Cabot. Large eddy simulation wall-modeling based on suboptimal control theory and linear stochastic estimation. *Physics of Fluids*, 13(10):2968–2984, October 2001. ISSN 1070-6631. doi: 10.1063/1.1389286. (Cited in pages 51, 53, and 55.)

[118] F. Nicoud, H. B. Toda, O. Cabrit, S. Bose, and J. Lee. Using singular values to build a subgrid-scale model for large eddy simulations. *Physics of Fluids*, 23(8):085106, August 2011. ISSN 1070-6631. doi: 10.1063/1.3623274. (Cited in pages 37, 39, and 139.)

[119] N. V. Nikitin, F. Nicoud, B. Wasistho, K. D. Squires, and P. R. Spalart. An approach to wall modeling in large-eddy simulations. *Physics of Fluids*, 12 (7):1629–1632, July 2000. ISSN 1070-6631. doi: 10.1063/1.870414. (Cited in page 53.)

[120] J. Nikuradse. Strömungsgesetze in rauben rohren. *Verein Deutsher Ingenieure - Forschungsheft*, page 361, 1933. (Cited in pages 28 and 64.)

[121] N. Odier, F. Duchaine, L. Gicquel, G. Staffelbach, A. Thacker, N. García Rosa, G. Dufour, and J.-D. Muller. Evaluation of Integral Turbulence Scale Through the Fan Stage of a Turbofan Using Hot Wire Anemometry and Large Eddy Simulation. In *Volume 2C: Turbomachinery*. American Society of Mechanical Engineers, June 2018. ISBN 978-0-7918-5101-2. doi: 10.1115/GT2018-75741. (Cited in page 136.)

[122] N. Odier, M. Sanjosé, L. Gicquel, T. Poinsot, S. Moreau, and F. Duchaine. A characteristic inlet boundary condition for compressible, turbulent, multi-species turbomachinery flows. *Computers & Fluids*, 178:41–55, January 2019. ISSN 00457930. doi: 10.1016/j.compfluid.2018.09.014. (Cited in pages 128 and 138.)

[123] N. Odier, A. Thacker, M. Harnieh, G. Staffelbach, L. Gicquel, F. Duchaine, N. García Rosa, and J. D. Müller. A mesh adaptation strategy for complex wall-modeled turbomachinery LES. *Computers and Fluids*, 214, January 2021. ISSN 00457930. doi: 10.1016/j.compfluid.2020.104766. (Cited in pages 136, 139, and 146.)

[124] C. Pantano, D. I. Pullin, P. E. Dimotakis, and G. Matheou. LES approach for high Reynolds number wall-bounded flows with application to turbulent channel flow. *Journal of Computational Physics*, 227(21):9271–9291, 2008. ISSN 10902716. doi: 10.1016/j.jcp.2008.04.015. (Cited in page 55.)

[125] G. I. Park and P. Moin. An improved dynamic non-equilibrium wall-model for large eddy simulation. *Physics of Fluids*, 26(1):0–21, 2014. ISSN 10897666. doi: 10.1063/1.4861069. (Cited in pages 48 and 76.)

[126] G. I. Park and P. Moin. Numerical aspects and implementation of a two-layer zonal wall model for LES of compressible turbulent flows on unstructured meshes. *Journal of Computational Physics*, 305:589–603, 2016. ISSN 10902716. doi: 10.1016/j.jcp.2015.11.010. (Cited in page 48.)

[127] S. Patankar. *Numerical Heat Transfer and Fluid Flow*. CRC Press, Boca Raton, October 2018. ISBN 978-1-315-27513-0. doi: 10.1201/9781482234213. (Cited in page 77.)

[128] V. C. Patel. Unified View of the Law of the Wall Using Mixing-Length Theory. *Aeron Q*, 24(Pt 1):55–70, 1973. ISSN 0001-9259. doi: 10.1017/s0001925900006429. (Cited in page 47.)

[129] V.C. Patel and F. Sotiropoulos. Longitudinal curvature effects in turbulent boundary layers. *Progress in Aerospace Sciences*, 33(1-2):1–70, January 1997. ISSN 03760421. doi: 10.1016/S0376-0421(96)00001-2. (Cited in pages 25 and 26.)

[130] W. W. Peng. *Fundamentals of Turbomachinery*. J. Wiley, Hoboken, N.J, 2008. ISBN 978-0-470-12422-2. (Cited in page 3.)

[131] J. E. Penner and IPCC, editors. *Aviation and the Global Atmosphere: A Special Report of IPCC Working Groups I and III in Collab. with the Scientific Assessment Panel to the Montreal Protocol on Substances That Deplete the Ozone Layer*. Cambridge University Press, Cambridge, 1. publ edition, 1999. ISBN 978-0-521-66404-2 978-0-521-66300-7. (Cited in page 2.)

[132] D. W. Perkins and F. Duchaine. Large-Eddy Simulations of a High-Speed Low-Pressure Turbine Cascade With Purge Flow. In *ASME Turbo Expo 2024: Turbomachinery Technical Conference and Exposition*. American Society of Mechanical Engineers Digital Collection, August 2024. doi: 10.1115/GT2024-122101. (Cited in page 61.)

[133] U. Piomelli and E. Balaras. Wall-Layer Models for Large-Eddy Simulations. *Annual Review of Fluid Mechanics*, 34(1):349–374, January 2002. ISSN 0066-4189, 1545-4479. doi: 10.1146/annurev.fluid.34.082901.144919. (Cited in pages 5, 44, 45, and 46.)

[134] U. Piomelli, J. Ferziger, P. Moin, and J. Kim. New approximate boundary conditions for large eddy simulations of wall-bounded flows. *Physics of Fluids A*, 1(6):1061–1068, 1989. ISSN 08998213. doi: 10.1063/1.857397. (Cited in page 55.)

[135] U. Piomelli, W. H. Cabot, P. Moin, and S. Lee. Subgrid-scale backscatter in turbulent and transitional flows. *Physics of Fluids A: Fluid Dynamics*, 3(7): 1766–1771, July 1991. ISSN 0899-8213. doi: 10.1063/1.857956. (Cited in page 37.)

[136] U. Piomelli, E. Balaras, H. Pasinato, K. D. Squires, and P. R. Spalart. The inner–outer layer interface in large-eddy simulations with wall-layer models. *International Journal of Heat and Fluid Flow*, 24(4):538–550, August 2003. ISSN 0142-727X. doi: 10.1016/S0142-727X(03)00048-1. (Cited in page 56.)

[137] T. J. Poinsot and S. K. Lele. Boundary conditions for direct simulations of compressible viscous flows. *Journal of Computational Physics*, 101(1):104–129, July 1992. ISSN 0021-9991. doi: 10.1016/0021-9991(92)90046-2. (Cited in pages 128 and 138.)

[138] S. B. Pope. *Turbulent Flows*. Cambridge University Press, August 2000. ISBN 978-0-511-84053-1. doi: 10.1017/CBO9780511840531. (Cited in pages 19, 20, 21, 32, 38, 41, 94, and 95.)

[139] F. Porté-Agel, C. Meneveau, and M. B. Parlange. A scale-dependent dynamic model for large-eddy simulation: Application to a neutral atmospheric boundary layer. *Journal of Fluid Mechanics*, 415:261–284, July 2000. ISSN 1469-7645, 0022-1120. doi: 10.1017/S0022112000008776. (Cited in page 56.)

[140] L. Prandtl. Über Flüssigkeitsbewegung bei sehr kleiner Reibung. Verhandlg. III. Intern. Math. Kongr. Heidelberg:484–491, 1904. (Cited in page 14.)

[141] L. Quartapelle and V. Selmin. High-order Taylor-Galerkin methods for non-linear multidimensional problems. *Finite Elements in Fluids*, 76(90):46, 1993. (Cited in page 61.)

[142] C. Rapp and M. Manhart. Flow over periodic hills: An experimental study. *Experiments in Fluids*, 51(1):247–269, July 2011. ISSN 1432-1114. doi: 10.1007/s00348-011-1045-y. (Cited in pages 66, 83, 88, 121, and 168.)

[143] H. Reichardt. Complete representation of the turbulent velocity distribution in smooth pipes. *Zeitschrift Fur Angewandte Mathematik Und Mechanik*, 31: 208, 1951. (Cited in page 46.)

[144] J. C. Rotta. Effect of Streamwise Wall Curvature on Compressible Turbulent Boundary Layers. *The Physics of Fluids*, 10(9):S174–S180, September 1967. ISSN 0031-9171. doi: 10.1063/1.1762440. (Cited in page 26.)

[145] J.C. Rotta. *Turbulent Boundary Layers with Heat Transfer in Compressible Flow*. AGARD Report. Advisory Group for Aeronautical Research and Development, 1960. (Cited in page 46.)

[146] J.C. Rotta. Turbulent boundary layers in incompressible flow. *Progress in Aerospace Sciences*, 2(1):1–95, January 1962. ISSN 03760421. doi: 10.1016/0376-0421(62)90014-3. (Cited in page 30.)

[147] P. Sagaut. *Large Eddy Simulation for Incompressible Flows: An Introduction*. Scientific Computation. Springer, Berlin ; New York, 3rd ed edition, 2006. ISBN 978-3-540-26344-9. (Cited in pages 32 and 36.)

[148] M. Schaefer. Forecast of Air Traffic's CO2 and NOx Emissions until 2030. June 2013. (Cited in page 1.)

[149] P. Schlatter, R. Örlü, Q. Li, G. Brethouwer, J. H. M. Fransson, A. V. Johansson, P. H. Alfredsson, and D. S. Henningson. Turbulent boundary layers up to Reϑ=2500 studied through simulation and experiment. *Physics of Fluids*, 21(5):051702, May 2009. ISSN 1070-6631. doi: 10.1063/1.3139294. (Cited in page 23.)

[150] P. Schlatter, Q. Li, G. Brethouwer, A. V. Johansson, and D. S. Henningson. Simulations of spatially evolving turbulent boundary layers up to Reϑ=4300. *International Journal of Heat and Fluid Flow*, 31(3):251–261, June 2010. ISSN 0142727X. doi: 10.1016/j.ijheatfluidflow.2009.12.011. (Cited in pages 22 and 23.)

[151] H. Schlichting and K. Gersten. *Boundary-Layer Theory*. Springer Berlin Heidelberg, Berlin, Heidelberg, 2017. ISBN 978-3-662-52917-1 978-3-662-52919-5. doi: 10.1007/978-3-662-52919-5. (Cited in pages 19 and 95.)

[152] T. Schonfeld and M. Rudgyard. Steady and Unsteady Flow Simulations Using the Hybrid Flow Solver AVBP. *AIAA Journal*, 37(11):1378–1385, November 1999. ISSN 0001-1452. doi: 10.2514/2.636. (Cited in page 61.)

[153] U. Schumann. Subgrid scale model for finite difference simulations of turbulent flows in plane channels and annuli. *Journal of Computational Physics*, 18(4):376–404, August 1975. ISSN 00219991. doi: 10.1016/0021-9991(75)90093-5. (Cited in page 45.)

[154] L. M. Segui, L. Gicquel, F. Duchaine, and J. de Laborderie. LES of the LS89 cascade: Influence of inflow turbulence on the flow predictions. In *Www.Euroturbo.Eu//*. EUROPEAN TURBOMACHINERY SOCIETY, 2017. doi: 10.29008/ETC2017-159. (Cited in page 61.)

[155] T.-H. Shih, L. A. Povinelli, N.-S. Liu, M. G. Potapczuk, and J. L. Lumley. A Generalized Wall Function. Technical report, NASA TM-1999-209398, 1999. (Cited in pages 47 and 53.)

[156] M. L. Shur, P. R. Spalart, M. K. Strelets, and A. K. Travin. A hybrid RANS-LES approach with delayed-DES and wall-modelled LES capabilities. *International Journal of Heat and Fluid Flow*, 29(6):1638–1649, December 2008. ISSN 0142-727X. doi: 10.1016/j.ijheatfluidflow.2008.07.001. (Cited in page 53.)

[157] M. Skote and D. S. Henningson. Direct numerical simulation of a separated turbulent boundary layer. *Journal of Fluid Mechanics*, 471:107–136, November 2002. ISSN 00221120. doi: 10.1017/S0022112002002173. (Cited in page 47.)

[158] J. Smagorinsky. General Circulation Experiments with the Primitive Equations: I. The Basic Experiment. *Monthly Weather Review*, 91(3):99–164, March 1963. ISSN 1520-0493, 0027-0644. doi: 10.1175/1520-0493(1963)091<0099:GCEWTP>2.3.CO;2. (Cited in pages 37, 79, and 83.)

[159] A. J. Smits. Some observations on Reynolds number scaling in wall-bounded flows. *Physical Review Fluids*, 5(11):110514, November 2020. ISSN 2469-990X. doi: 10.1103/PhysRevFluids.5.110514. (Cited in page 22.)

[160] A. J. Smits, B. J. McKeon, and I. Marusic. High–Reynolds Number Wall Turbulence. *Annual Review of Fluid Mechanics*, 43(1):353–375, January 2011. ISSN 0066-4189, 1545-4479. doi: 10.1146/annurev-fluid-122109-160753. (Cited in page 22.)

[161] R. M. C. So. A turbulence velocity scale for curved shear flows. *Journal of Fluid Mechanics*, 70(1):37–57, July 1975. ISSN 1469-7645, 0022-1120. doi: 10.1017/S0022112075001887. (Cited in page 26.)

[162] R. M.C. So, T. B. Gatski, and T. P. Sommer. Morkovin hypothesis and the modeling of wall-bounded compressible turbulent flows. *AIAA Journal*, 36 (9):1583–1592, 1998. ISSN 00011452. doi: 10.2514/2.584. (Cited in pages 15, 26, and 27.)

[163] P. R. Spalart. Direct simulation of a turbulent boundary layer up to Rϑ= 1410. *Journal of Fluid Mechanics*, 187:61–98, 1988. ISSN 14697645. doi: 10.1017/S0022112088000345. (Cited in pages 22 and 23.)

[164] D. B. Spalding. A Single Formula for the "Law of the Wall". *Journal of Applied Mechanics*, 28(3):455–458, September 1961. ISSN 0021-8936. doi: 10.1115/1.3641728. (Cited in page 46.)

[165] K. Suga, T. J. Craft, and H. Iacovides. An analytical wall-function for turbulent flows and heat transfer over rough walls. *International Journal of*

Heat and Fluid Flow, 27(5):852–866, October 2006. ISSN 0142727X. doi: 10.1016/j.ijheatfluidflow.2006.03.011. (Cited in page 50.)

[166] G. I. Taylor. Statistical theory of turbulence. *Proceedings of the Royal Society of London. Series A - Mathematical and Physical Sciences*, 151(873):421–444, September 1935. ISSN 0080-4630, 2053-9169. doi: 10.1098/rspa.1935.0158. (Cited in pages 95 and 96.)

[167] L. Temmerman, M. A. Leschziner, C. P. Mellen, and J. Fröhlich. Investigation of wall-function approximations and subgrid-scale models in large eddy simulation of separated flow in a channel with streamwise periodic constrictions. *International Journal of Heat and Fluid Flow*, 24(2):157–180, 2003. ISSN 0142727X. doi: 10.1016/S0142-727X(02)00222-9. (Cited in page 65.)

[168] L. Temmerman, M. Hadžiabdić, M. A. Leschziner, and K. Hanjalić. A hybrid two-layer URANS–LES approach for large eddy simulation at high Reynolds numbers. *International Journal of Heat and Fluid Flow*, 26(2):173–190, April 2005. ISSN 0142-727X. doi: 10.1016/j.ijheatfluidflow.2004.07.006. (Cited in pages 53 and 65.)

[169] J. A. Templeton, G. Medic, and G. Kalitzin. An eddy-viscosity based near-wall treatment for coarse grid large-eddy simulation. *Physics of Fluids*, 17(10): 105101, October 2005. ISSN 1070-6631, 1089-7666. doi: 10.1063/1.2084228. (Cited in page 56.)

[170] J. A. Templeton, M. Wang, and P. Moin. A predictive wall model for large-eddy simulation based on optimal control techniques. *Physics of Fluids*, 20 (6):065104, June 2008. ISSN 1070-6631. doi: 10.1063/1.2930673. (Cited in page 53.)

[171] A. Thacker and N. García Rosa. Measurements of fan efficiency at low pressure ratio. In *Www.Euroturbo.Eu//*. EUROPEAN TURBOMACHINERY SOCIETY, 2023. doi: 10.29008/ETC2023-232. (Cited in page 136.)

[172] L. C. Thomas and S. M. F. Hasani. Supplementary Boundary-Layer Approximations for Turbulent Flow. *Journal of Fluids Engineering*, 111(4):420–427, December 1989. ISSN 0098-2202, 1528-901X. doi: 10.1115/1.3243662. (Cited in page 69.)

[173] A. A. Townsend. *The Structure of Turbulent Shear Flow*. Cambridge Monographs on Mechanics and Applied Mathematics. Cambridge University Press, Cambridge [Eng.] ; New York, 2d ed edition, 1976. ISBN 978-0-521-20710-2. (Cited in pages 22 and 30.)

[174] J. Tyacke, P. Tucker, R. Jefferson-Loveday, N. Rao Vadlamani, R. Watson, I. Naqavi, and X. Yang. Large Eddy Simulation for Turbines: Methodologies, Cost and Future Outlooks. *Journal of Turbomachinery*, 136(061009),

November 2013. ISSN 0889-504X. doi: 10.1115/1.4025589. (Cited in pages 5 and 34.)

[175] E. R. VAN DRIEST. Turbulent Boundary Layer in Compressible Fluids. *Journal of the Aeronautical Sciences*, 18(3):145–160, 1951. doi: 10.2514/8.1895. (Cited in page 27.)

[176] T. Von Karman. Turbulence and Skin Friction. *Journal of the Aeronautical Sciences*, 1(1):1–20, January 1934. ISSN 1936-9956. doi: 10.2514/8.5. (Cited in page 94.)

[177] G. J. Walker and J. P. Gostelow. Effects of Adverse Pressure Gradients on the Nature and Length of Boundary Layer Transition. *Journal of Turbomachinery*, 112(2):196–205, April 1990. ISSN 0889-504X. doi: 10.1115/1.2927633. (Cited in page 62.)

[178] G. Wang, F. Duchaine, D. Papadogiannis, I. Duran, S. Moreau, and L. Y. M. Gicquel. An overset grid method for large eddy simulation of turbomachinery stages. *Journal of Computational Physics*, 274:333–355, October 2014. ISSN 0021-9991. doi: 10.1016/j.jcp.2014.06.006. (Cited in page 137.)

[179] L. Wang, R. Hu, and X. Zheng. A comparative study on the large-scale-resolving capability of wall-modeled large-eddy simulation. *Physics of Fluids*, 32(3):035102, March 2020. ISSN 1070-6631. doi: 10.1063/1.5144669. (Cited in page 136.)

[180] M. Wang and P. Moin. Dynamic wall modeling for large-eddy simulation of complex turbulent flows. *Physics of Fluids*, 14(7):2043–2051, 2002. ISSN 10706631. doi: 10.1063/1.1476668. (Cited in pages 49, 50, 70, and 78.)

[181] B. Weigand, J. R. Ferguson, and M. E. Crawford. An extended Kays and Crawford turbulent Prandtl number model. *International Journal of Heat and Mass Transfer*, 40(17):4191–4196, October 1997. ISSN 0017-9310. doi: 10.1016/S0017-9310(97)00084-7. (Cited in page 74.)

[182] C. Wenzel, T. Gibis, M. Kloker, and U. Rist. Self-similar compressible turbulent boundary layers with pressure gradients. Part 1. Direct numerical simulation and assessment of Morkovin's hypothesis. *Journal of Fluid Mechanics*, 880:239–283, December 2019. ISSN 14697645. doi: 10.1017/jfm.2019.670. (Cited in page 62.)

[183] H. Werner and H. Wengle. Large-Eddy Simulation of Turbulent Flow Over and Around a Cube in a Plate Channel. In F. Durst, R. Friedrich, B. E. Launder, F. W. Schmidt, U. Schumann, and J. H. Whitelaw, editors, *Turbulent Shear Flows 8*, pages 155–168, Berlin, Heidelberg, 1993. Springer. ISBN 978-3-642-77674-8. doi: 10.1007/978-3-642-77674-8_12. (Cited in page 46.)

[184] D. C. Wilcox. *Turbulence Modeling for CFD*. DCW Industries, La Cañada, Calif., 3. ed., 2. print edition, 2010. ISBN 978-1-928729-08-2. (Cited in pages 12, 14, and 19.)

[185] P. Wu and J. Meyers. A constraint for the subgrid-scale stresses in the logarithmic region of high Reynolds number turbulent boundary layers: A solution to the log-layer mismatch problem. *Physics of Fluids*, 25(1), January 2013. ISSN 10706631. doi: 10.1063/1.4774344. (Cited in page 56.)

[186] X. Wu and P. Moin. Direct numerical simulation of turbulence in a nominally zero-pressure-gradient flat-plate boundary layer. *Journal of Fluid Mechanics*, 630:5–41, July 2009. ISSN 0022-1120, 1469-7645. doi: 10.1017/S00221120090 06624. (Cited in page 21.)

[187] X. I. A. Yang and K. P. Griffin. Grid-point and time-step requirements for direct numerical simulation and large-eddy simulation. *Physics of Fluids*, 33 (1):015108, January 2021. ISSN 1070-6631. doi: 10.1063/5.0036515. (Cited in pages 41 and 42.)

[188] X. I. A. Yang, S. Bose, and P. Moin. A physics-based interpretation of the slip-wall LES model. *CTR Annual Research Briefs*, 2017. (Cited in page 51.)

[189] X. I.A. Yang, G. I. Park, and P. Moin. Log-layer mismatch and modeling of the fluctuating wall stress in wall-modeled large-eddy simulations. *Physical Review Fluids*, 2(10):1–13, 2017. ISSN 2469990X. doi: 10.1103/PhysRevFlu ids.2.104601. (Cited in pages 55, 56, 57, and 179.)

[190] X. I.A. A. Yang, J. Sadique, R. Mittal, and C. Meneveau. Integral wall model for large eddy simulations of wall-bounded turbulent flows. *Physics of Fluids*, 27(2):1–33, February 2015. ISSN 10897666. doi: 10.1063/1.4908072. (Cited in pages 48, 56, and 75.)

[191] B. Zebiri, A. Piquet, and A. Hadjadj. On the use of a two-layer model for large-eddy simulations of supersonic boundary layers with separation. *International Journal of Heat and Fluid Flow*, 90:108821, August 2021. ISSN 0142727X. doi: 10.1016/j.ijheatfluidflow.2021.108821. (Cited in pages 69 and 75.)

[192] Y. F. Zhang and R. Vicquelin. Controlling bulk Reynolds number and bulk temperature in channel flow simulations. *Journal of Computational Physics*, 305:208–216, January 2016. ISSN 0021-9991. doi: 10.1016/j.jcp.2015.10.051. (Cited in page 57.)

[193] Z. Zhou, T. Wu, and X. Yang. Reynolds number effect on statistics of turbulent flows over periodic hills. *Physics of Fluids*, 33(10):105124, October 2021. ISSN 1070-6631. doi: 10.1063/5.0062786. (Cited in pages 65, 66, and 83.)

RÉPUBLIQUE FRANÇAISE
Liberté
Égalité
Fraternité

Université de Toulouse

Titre : Modélisation de parois pour la Simulation aux Grandes Échelles d'écoulements de turbomachines

Mots clés : Simulation, Turbomachines, Modèle, Parois, SGE

Résumé : Les objectifs environnementaux et opérationnels ambitieux de l'industrie aéronautique nécessitent des avancées constantes dans les systèmes de propulsion, notamment en termes d'efficacité, d'émissions et de réduction de bruit. La dynamique des fluides numérique (*CFD* en anglais) joue un rôle essentiel dans la réalisation de ces objectifs en simulant les écoulements dans des composants tels que les compresseurs, les turbines, les chambres de combustion et les tuyères. Parmi les techniques de CFD, la simulation aux grandes turbulences (*SGE* ou *LES* en anglais) s'impose comme une approche de haute fidélité pour capturer la dynamique des écoulements turbulents et les mécanismes de perte dans les turbomachines. Cependant, le coût de calcul important de la LES, en particulier pour les écoulements à haut nombre de Reynolds dans des géométries complexes, reste un obstacle important à la généralisation de son applications pratique. Les modèles de paroi offrent une solution en modélisant l'écoulement près de la paroi plutôt qu'en le résolvant complètement, réduisant ainsi le coût de calcul tout en préservant les nombreux avantages de la LES.
L'objectif de cette thèse est de relever certains des défis de la modélisation de paroi afin d'assurer la pertinence physique des modèles de parois pour les turbomachines et d'améliorer leur intégration dans le cadre de la LES. Un modèle de paroi *TBLE* (Thin Boundary Layer Equations), conçu pour prendre en compte les effets du gradient de pression, a été implémenté dans le solveur massivement parallèle AVBP. En outre, un modèle de fluctuation stochastique utilisé pour corriger les modèles de sous-maille (*SGS*) près des murs a été étudié et amélioré pour traiter le décalage dans les profils de vitesse (*Log-Layer mismatch*) dû au couplage entre les modèles de paroi et le solveur LES.
Les principaux résultats présentés dans cette thèse comprennent la validation des modèles mis en œuvre, à la fois indépendamment et conjointement, sur les cas académiques du canal turbulent des collines périodiques. Les modèles ont ensuite été appliqués à des cas de turbomachines comprenant une cascade d'aubes de turbine haute pression et une configuration rotor/stator de fan.

Title: Wall modeling for Large-Eddy Simulations of turbomachinery flows

Key words: Simulation, Turbomachinery, Wall Model, LES, CFD

Abstract: The aviation industry's ambitious environmental and operational goals necessitate continuous advancements in propulsion systems, focusing on efficiency, emissions, and noise reduction. Computational Fluid Dynamics (*CFD*) plays a pivotal role in achieving these objectives by simulating flows in components like compressors, turbines, combustion chambers, and exhaust systems. Among CFD techniques, Large Eddy Simulation (*LES*) stands out as a high-fidelity approach for capturing turbulent flow dynamics and loss mechanisms in turbomachinery. However, the significant computational cost of LES, especially for high Reynolds number flows in complex geometries, remains a significant barrier to widespread practical applications. Wall models offer a solution by modeling near-wall behavior rather than fully resolving it, thus reducing computational demands while preserving numerous advantages of LES.
The objective of this thesis is to tackle some of the challenges of wall modeling to ensure the physical relevance of wall models for turbomachinery and improve their integration within the LES framework. A Thin Boundary Layer Equations (*TBLE*) wall model, designed to account for pressure gradient effects, was implemented in the massively parallel AVBP solver. Additionally, a stochastic fluctuation model used to correct sub-grid scale (*SGS*) models near walls was studied and enhanced to address the log-layer mismatch arising from the coupling between wall models and the LES solver.
Key results presented in this thesis include the validation of the implemented models, both independently and together, on the turbulent channel flow and periodic hill academic test cases. The models were subsequently applied to turbomachinery cases, including a high-pressure turbine blade cascade and a fan rotor/stator setup.